Mathematical Modeling and Numerical Simulations of the Extrinsic Pro-Apoptotic Signaling Pathway

Von der Fakultät Mathematik und Physik der Universität Stuttgart
zur Erlangung der Würde eines Doktors der Naturwissenschaften (Dr. rer. nat.)
genehmigte Abhandlung

Vorgelegt von

Markus Daub

aus Göppingen

Hauptberichter:	Prof. Dr. Guido Schneider
Mitberichter:	Prof. Dr. Johannes Müller
Tag der mündlichen Prüfung:	15. Januar 2013

Institut für Analysis, Dynamik und Modellierung der Universität Stuttgart

2013

Abstract

Apoptosis is an important physiological process that enables organisms to remove unneeded, damaged or infected cells and therefore, it plays an important role in diseases like cancer or neurodegenerative diseases. Apoptosis is induced amongst others by the extrinsic signaling pathway which is initiated by activation of ligand-receptor clusters located in the plasma membrane. The central network of the extrinsic signaling pathway is the caspase cascade in which two types of caspase are involved: the initiator caspase 8 and the effector caspase 3. Both types of caspase exist in cells in an active and inactive form. The initiator caspase becomes activated through death receptors in the plasma membrane and the effector caspase, which gets activated through initiator caspases, cleaves proteins that execute the apoptotic machinery. According to the structure of the extrinsic signaling pathway, we introduce mathematical models both for the caspase-3/8 feedback loop and the receptor clustering on the cellular membrane.

Two reactions are involved in the caspase-3/8 feedback loop: the activation of pro-caspase 8 by caspase 3 and the activation of pro-caspase 3 by caspase 8. Due to the spatial extension of a single cell and due to the occurrence of the stimulus of the reaction network at the cell membrane, we consider space and time dependent distributions of caspase concentrations. In order to describe the spatio-temporal evolution of the caspase concentrations in a single cell, we introduce a reaction-diffusion model.

First, we show that the reaction-diffusion system possesses three steady states: two asymptotically stable, namely the "life state" and the "death state", and one unstable steady state. Subsequently, we prove the local existence and uniqueness of a solution of the reaction-diffusion system with homogeneous Neumann boundary conditions and further state a bounded invariant region. The latter ensures that the solution remains bounded for all time once the solution resides inside the invariant region.

Second, we solve the reaction-diffusion system numerically for several initial conditions and investigate which of the two asymptotically stable stationary solutions is approached. Here, the initial condition corresponds to the strength of the external stimulus. The simulations show a switch-like behavior of the system concerning the size of the region initially occupied by the "death state". We conclude this part about the mathematical model of the caspase-3/8 feedback loop with the determination of a traveling wave solution connecting the two asymptotically stable steady states on a large spatial scale.

The third chapter of this thesis deals with the modeling of the receptor clustering on the cell membrane. The ligand-receptor clusters consist of death receptors glued by the respective death receptor ligands. The clusters result from the random motion of death re-

ceptors and death receptor ligands on the cell membrane and the association of molecules lying close to each other. We introduce a novel particle model where death receptors and death receptor ligands are modeled as disks with up to three binding sites. Thus, besides the location of the particles, their orientation is also taken into account. To model the motion of receptors and ligands at the cellular membrane, we introduce Langevin equations for the particle translation and rotation and derive a system of stochastic differential equations. This is nonlinearly coupled due to the interaction between the particles.

To solve the system of stochastic differential equations numerically, we apply the Euler-Maruyama approximation. Due to the high complexity of the simulation and the large number of simulations for various particle configurations, the algorithms are mapped on GPGPU architectures by Claus Braun, and we achieve a speed-up of up to 60x compared to a CPU implementation. This speed-up enables a numerical analysis of the time evolution of ligand-receptor clusters of different sizes for various particle configurations. In particular, we compare the formation of signal competent cluster units, i.e. two death receptor ligands bound to one death receptor dimer or two associated death receptor monomers, for death receptor dimers and monomers and observe that the formation of these units is more likely if the majority of death receptors exist as dimers. Moreover, we find that two associated death receptor monomers which are not bound to death receptor ligands can not be signal competent. Finally, the tool *cellVis* is used for the visualization of the simulation data. This powerful tool, developed by Martin Falk, is also helpful for the analysis of the structure and size of the ligand-receptor clusters.

Zusammenfassung

Apoptose ist ein bedeutender physiologischer Prozess, der es Organismen ermöglicht, defekte oder infektiöse Zellen zu entfernen, und spielt deshalb eine bedeutende Rolle bei Krebs oder neurodegenerativen Krankheiten wie Alzheimer. Apoptose wird durch den extrinsischen oder intrinsischen Signalweg ausgelöst, wobei der extrinsische Signalweg durch aktive Todesrezeptoren auf der Zellmembran und der intrinsische Signalweg in Mitochondrien innerhalb der Zelle initiiert wird. In dieser Arbeit beschränken wir uns auf den extrinsischen Signalweg. Das zentrale Reaktionsnetzwerk des extrinsischen Signalweges bildet die Caspase Kaskade, an der im Wesentlichen zwei Caspase-Typen beteiligt sind: die Initiator-Caspase 8 und die Effektor-Caspase 3, die jeweils in aktiver und inaktiver Form in der Zelle vorkommen. Die Initiator-Caspase wird durch Todesrezeptoren an der Zellmembran aktiviert und die Effektor-Caspase, die durch aktive Initiator-Caspasen aktiviert wird, spaltet Proteine innerhalb der Zelle, was letztlich zum Zelltod führt. Gemäß der Struktur des extrinsischen Signalweges führen wir mathematische Modelle für zwei Prozesse ein: zum einen zur Beschreibung der Caspase-3/8 Kaskade des extrinsischen apoptotischen Signalweges und zum anderen zur Beschreibung des Clusterprozesses von Rezeptoren auf der Zellmembran.

Das am extrinsischen Signalweg involvierte Reaktionsnetzwerk besteht in der einfachsten Form aus zwei Reaktionen: der Aktivierung von Pro-Caspase 8 durch Caspase 3 und der Aktivierung von Pro-Caspase 3 durch Caspase 8. Aufgrund der räumlichen Ausdehnung einer einzelnen Zelle und aufgrund der Initiierung des Reaktionsnetzwerks an der Zellmembran betrachten wir Caspase-Konzentrationen, die sowohl von der Zeit als auch vom Ort abhängen. Zur Beschreibung der räumlich-zeitlichen Entwicklung der Caspase-Konzentrationen in der Zelle führen wir deshalb ein Reaktions-Diffusions-Modell ein.

Im ersten Schritt zeigen wir, dass das Reaktions-Diffusions-System drei stationäre Lösungen besitzt, von denen eine instabil ist und zwei asymptotisch stabil sind. Die stabilen Zustände werden mit dem Lebens- bzw. Todeszustand bezeichnet. Anschließend zeigen wir, dass eine eindeutige Lösung dieses Systems existiert. Letztlich wird noch die Beschränktheit der Lösung durch die Existenz einer invarianten Region gewährleistet.

Im numerischen Teil der Arbeit lösen wir das Reaktions-Diffusions-System für verschiedene Anfangsbedingungen und untersuchen, welche der beiden asymptotisch stabilen, stationären Lösungen für die jeweilige Anfangsbedingung angenähert wird. Dabei entsprechen die verschiedenen Anfangsbedingungen unterschiedlich starken Stimuli des Signalweges. Die Simulationen zeigen ein schalterartiges Verhalten des Systems bezüglich der Größe der anfangs mit dem Todeszustand besetzten Region. In anderen

Worten: übersteigt die Größe der anfänglichen Todeszone einen gewissen Schwellenwert, wird der Todeszustand nach einer gewissen Zeit die gesamte Zelle besetzen, was dem Tod der Zelle entspricht. Wir schließen das Kapitel über das mathematische Modell der Caspase-3/8 Kaskade mit der Bestimmung einer Traveling-Wave-Lösung, die die zwei asymptotisch stabilen stationären Lösungen verbindet. Diese stellen eine typische Struktur für bistabile Reaktions-Diffusions-Systeme dar, existieren jedoch nur auf einer biologisch unrealistisch großen Ortsskala.

Das dritte Kapitel behandelt die Modellierung des Clusterprozesses auf der Zellmembran. Die sogenannten Ligand-Rezeptor-Cluster bestehen aus Todesrezeptoren und den dazugehörigen Liganden. Die Cluster entstehen durch die zufällige Bewegung der Rezeptoren und Liganden auf der Zelloberfläche und durch die Interaktion nahe beieinander liegender Rezeptoren und Liganden. Wir stellen ein Modell vor, bei dem die Rezeptoren und Liganden als Partikel modelliert werden, die bis zu drei Bindungsregionen besitzen. Also betrachten wir in diesem Modell neben der Position der Partikel auf der Zellmembran auch deren Orientierung. Für die Modellierung der Bewegung der Rezeptoren und Liganden führen wir Langevin Gleichungen für die Translation und Rotation der Partikel ein und leiten ein System von stochastischen Differentialgleichungen her. Dieses Gleichungssystem ist nichtlinear und aufgrund der Wechselwirkung zwischen den Partikeln gekoppelt. Um es numerisch zu lösen und damit die Clusterbildung zu simulieren, betrachten wir die Euler-Maruyama Approximation des Gleichungssystems. Aufgrund der hohen Komplexität der Simulationen und aufgrund der Erfordernis mehrerer Simulationsläufe für verschiedene Partikelkonfigurationen ist die Verwendung von Höchstleistungsrechnern notwendig. In diesem Fall sind die Algorithmen von Claus Braun auf die GPU abgebildet worden, was zu einer bis zu 60-fachen Beschleunigung für eine realistische biologische Partikelkonfiguration geführt hat. Diese Beschleunigung ermöglicht letztlich eine numerische Analyse der zeitlichen Entwicklung von Ligand-Rezeptor-Clustern verschiedener Größen. Insbesondere vergleichen wir die Bildung von signalübertragenden Einheiten, die aus zwei Liganden gebunden mit einem Dimer beziehungsweise zwei miteinander gebundenen Monomere bestehen, und zeigen, dass das Auftreten dieser signalübertragenden Einheiten wahrscheinlicher ist, wenn die Mehrheit der Rezeptoren als Dimere existiert. Außerdem finden wir, dass zwei gebundene Monomere ohne Ligandenbindung nicht für die Signalübertragung ausreichend sein können. Schließlich können die Simulationsdaten mittels des von Martin Falk entwickelten Visualisierungs-Tool *cellVis* veranschaulicht werden. Dieses Tool dient darüberhinaus der Analyse von Clusterstrukturen und Clustergrößen.

Danksagung

Diese Arbeit entstand am Institut für Analysis, Dynamik und Modellierung (IADM) an der Universität Stuttgart und wurde im Rahmen des Exzellenzclusters „Simulation Technology“ von der Deutschen Forschungsgemeinschaft gefördert. Den folgenden Personen gilt mein herzlicher Dank:

- Prof. Dr. Schneider, der mir die Möglichkeit gab, diese Arbeit im Rahmen des Exzellenzclusters SimTech zu schreiben und mir jederzeit mit Rat und Tat zur Seite stand. Ganz besonders möchte ich mich für das verständnisvolle Verhalten nach der schweren Erkrankung meiner Mutter bedanken.

- Prof. Dr. Scheurich für die Erklärungen der für diese Arbeit relevanten biologischen Grundlagen.

- Steffen Waldherr für die ergiebigen Diskussionen und die damit verbundene Bereicherung für die gemeinsame Publikation.

- Martin Falk für das Bereitstellen des Visualisierung-Tools *cellVis* zur Analyse des Partikelmodells.

- Claus Braun für die Abbildung der Algorithmen auf die GPU und die damit verbundene Beschleunigung der Simulation.

- Prof. Dr. Trebin und Dr. Roth für die *richtungs*weisenden Beiträge für das Partikelmodell.

- Tobias Häcker für das Korrekturlesen der Dissertation.

Mein Dank gilt auch meinen Freunden und meinen (ehemaligen) Kollegen am IADM:

- Christopher Chong für die Gastfreundschaft in Amherst.

- Tobias und Anita Häcker für die langjährige Motivation während des Studiums und der Promotion.

- Stefanie Siegert für die Unterstützung bei den Dienstreiseabrechnungen.

- Dominik Zimmermann für die lustige Zeit als Büronachbar.

Ebenfalls möchte ich mich bei den Kollegen am Institut für Stochastik und Anwendungen für die lustigen Kaffeerunden und die außeruniversitären Aktivitäten bedanken.

Insbesondere möchte ich mich bei meiner Partnerin Claudia Ruth für die tatkräftige Unterstützung während des Studiums und der Promotion bedanken.

Ganz besonderer Dank gilt natürlich meinen Eltern Lilian und Dieter Daub für die jahrelange bedingungslose Unterstützung und Förderung.

Contents

Abstract/Zusammenfassung **iii**

Danksagung **vii**

1 Introduction **1**

2 Mathematical Model of the Caspase-3/8 Feedback Loop **7**

2.1 Biological Background of the Caspase-3/8 Feedback Loop 8
2.2 Governing Equations for the Reaction Network 12
2.3 Spatially Extended Reaction-Diffusion Model of the Caspase-3/8 Feedback Loop 13
2.4 Stability Analysis for the Steady States of the Reaction System 16
2.5 Stability Analysis for the Stationary Solutions of the Reaction-Diffusion System 21
2.6 Local Existence and Uniqueness of a Solution of the Reaction-Diffusion System 30
2.7 Invariant Region for the Reaction-Diffusion System 31
2.8 Numerical Analysis of Spatial Inhibition Effects 41
2.9 Reaction-Diffusion Model on Large Spatial Scales 49
2.9.1 Existence of Nontrivial Spatio-Temporal Structures of Solutions . . 51
2.9.2 Spatial Inhibition Effects on Large Spatial Scales 56
2.10 Discussion 60

3 Mathematical Model of the Receptor Clustering on the Cell Membrane **63**

3.1 Biological Background of the Receptor Clustering 64
3.2 Particle Model of the Clustering Processes 66
3.3 Model of the Particle Translation and Particle Rotation 67
3.3.1 Derivation of Equations for the Particle Translation 68
3.3.2 Derivation of Equations for the Particle Rotation 71
3.3.3 Distinction of Cases for Different Death Receptor Structures 74
3.3.4 Modeling the Interaction between the Particles 76

3.3.5 Particle Model for the Different Particle Configurations 87
3.4 Euler-Maruyama Approximation of the Equations 90
3.5 The Linked-Cell Method 93
3.6 Results of the Numerical Simulations 106
3.7 Mapping of the Algorithms on GPGPU Architectures 128
3.8 Discussion 130

4 Outlook **133**

A Appendix **139**
A.1 Computation of Biological Quantities 139
A.1.1 Determination of the Typical Caspase Concentration 139
A.1.2 Determination of Diffusion Coefficients 139
A.2 Derivation of the Bessel Differential Equation for the 2D Laplace Operator 140
A.3 Unsuitable Invariant Region 141
A.4 Finite Difference Method for the Radially Symmetric Reaction-Diffusion System 144
A.5 Finite Difference Method for the Extended Reaction-Diffusion System . . . 147

Glossary **156**

List of Figures **164**

List of Tables **165**

Bibliography **172**

1. Introduction

Apoptosis is a common form of programmed cell death and represents an important physiological process in multicellular organisms that allows the removal of unneeded, damaged or infected cells [12, 56]. The apoptotic process occurs for instance during the embryonic development of mammalian limbs when the interstitial tissue between the limbs is removed. That is the reason why the human body forms fingers, toes and nares. Moreover, the apoptotic processes play an important role in many diseases like cancer or neurodegenerative diseases like Alzheimer's disease. One of the main focusses in cancer research is therefore to find the reason why the apoptotic process fails in cancerous cells. This knowledge is needed to initiate apoptotic processes in order to optimize clinical therapies.

Two major signaling pathways are involved in apoptotic processes: the extrinsic (death receptor) pathway and the intrinsic (mitochondrial) pathway. The extrinsic pathway is initiated by activation of so-called death receptors in the plasma membrane through binding of their respective death receptor ligands [12, 27]. The intrinsic pathway is activated by cellular damage caused by, e.g., ultraviolet irradiation at the DNA level or by toxic agents, which can lead to activation of the protein p53 and subsequent induction of apoptosis via mitochondria [27]. Both the extrinsic and the intrinsic pathways converge at the level of the caspase cascade, a network of caspases that is commonly recognized as the central and executing machinery of apoptosis [27, 52]. Both signaling pathways are interdigitated and the external activation at the cell membrane also influences the processes in the mitochondria. In apoptosis induction, two major types of caspases are distinguished: the initiator caspases, which get activated through death receptors at the cell membrane, and the effector caspases, which cleave multiple essential proteins thereby dismantling the cell [12, 52]. In contrast to necrosis, apoptosis allows for a structured decomposition of the apoptotic cell and prevents an inflammatory response to the surrounding cells.

Due to the relevance of the caspase cascade for apoptosis induction and execution, the development of mathematical models has grown in interest in recent years for a better

understanding of the regulation of cell death. In [19], a mathematical model of caspase function in apoptosis has been introduced that contains the clustering of Fas receptors at the cellular membrane and consider the activation of executioner caspases by the initiator caspases as well. Here, the dynamics only depends on time, while the spatial dimension of a single cell is completely disregarded. Thus, the model is described by a system of coupled ordinary differential equations. A more complex model of the Fas-induced apoptosis has been treated in [4]. Here, all known molecules and reactions which are directly or indirectly interacting with the components of the respective signaling pathway were incorporated into the model. By this, the model includes about 70 molecules, 80 reactions and more than 120 parameters which are not exactly known. In order to reduce the complexity of the model, "black boxes" replace parts of the reaction network whose input-output behavior is well-known. The resulting model contains 41 molecules, 32 reactions and 2 black boxes. Both models in [19] and [4] describe the two different signaling pathways whereas in [4] the mitochondrial pathway is replaced by a black box.
Further models of the signaling pathways have been introduced in [14] and [15]. Here, the focus turns to systems' theoretical aspects, for instance a bistability analysis for the reaction system with inhibitors for caspase 3 (IAP) and caspase 8 (BAR) in [14]. Bistability of the caspase cascade is essentially based on a positive feedback between initiator and effector caspases in the sense that not only initiator caspases can cleave and activate effector caspases, but also vice versa. Properties of bistability of the caspase cascade and the underlying mechanisms were further analyzed for similar models [15]. As one of their main conclusions, Eissing et al. found that model variants with cooperativity in caspase activation and binding of caspase 3 to an inhibitor are similarly able to generate bistability [15].

Recently, the spatial organization of caspase activation within cells has gained increased interest. While the switch-like behavior of effector caspase activation is well established for single cells in the dimension of time, this property is less clear in the spatial dimensions. In a first approach to investigate this issue, the organization of mitochondrial outer membrane permeabilization, an important initiating event in the intrinsic apoptotic pathway, has been studied [51]. In this study, the authors observed that mitochondrial membrane permeabilization occurs in a spatial wave within the cell. In a later study from the same group, it was additionally shown that caspase activation proceeds very quickly through the cell, apparently rendering the caspase substrate cleavage almost spatially homogeneous with respect to the relevant timescale [31]. These studies support the idea that caspase activation is also switch-like in the spatial dimension. Other mathematical models for intracellular pathways with spatial dependent protein concentrations, e.g. the MAPK cascade, have been studied for instance in [33] and [43].

We pick up the idea of a mathematical model describing the spatio-temporal evolution of caspase concentrations for the extrinsic pro-apoptotic signaling pathway and introduce a spatial extension of the model analyzed in [15]. Here, the interdigitated extrinsic and intrinsic signaling pathway have been unraveled and the reaction network is restricted to the initiator-caspase 8 and the effector-caspase 3. Due to the restriction and the associated simplification of the underlying reaction network, we are able to answer questions concerning the bistable behavior and the stability properties of the spatially homogeneous stationary solutions of the introduced reaction-diffusion system. This includes the local existence and uniqueness of a solution and the existence of an invariant region that guarantees the boundedness of the solution. Further questions concerning the switch-like behavior in the spatial dimension and the existence of a traveling wave solution will be answered subsequently.

Besides the modeling of the caspase cascade of the extrinsic pro-apoptotic signaling pathway, a deeper understanding of the external stimulus is desirable as well. Actually, some of the models mentioned above already include both aspects, the caspase cascade and the clustering of receptors at the cell membrane [19, 4], but all these models neglect the spatial extension of the cell. Concerning the formation of receptor clusters on the cell membrane, several models have been introduced recently. A mathematical model for the binding of multivalent ligands to mono- or multivalent cell surface receptors has been established in [49]. Here, the law of mass action has been applied yielding a system of ordinary differential equations. However, the spatial extension of the cell surface was disregarded in the model. This vulnerability could be eliminated in the thermodynamical approach to the modeling of receptor clustering in [24]. Here, the spatial extension of the cell surface has been taken into account and special types of receptors and ligands, namely tumor necrosis factor (TNF) and TNF receptor of type 1 (TNFR1), have been considered. Besides, the cell surface was treated as a lattice and the receptors were associated with the lattice sites. Finally, running Monte Carlo simulations, the formation of receptor clusters could be observed. In a later work, Guo and Levin introduced a statistical mechanics model for the clustering of receptors on the cell membrane [25]. Besides TNFR1 and TNF, other molecules like TNF receptor associated death domain (TRADD) and silencer of death domain (SODD) have been integrated into the lattice based model. On the other hand, the molecules that allow for clustering are TNFR1 monomers or ligated dimers or trimers. Thus, the model does not admit pre-assembled receptor homodimers and homotrimers. Another deficiency of the model is the fact that clusters are not allowed to move collectively. A further lattice based model for receptor clustering was established in [55]. Here, besides the cluster formation, the signaling of cell receptors was incorporated into the model.

In order to describe the clustering of the receptors on a lattice-free domain, we introduce in this thesis a particle model with receptors and ligands performing a free diffusion on the cellular membrane. In contrast to [25], we neglect cytoplasmic effects like binding of TRADD and SODD to TNFR1 and in contrast to [55], we omit the signaling of the receptors. Instead, the main focus of our particle model is the additional consideration of the particle orientation, that means we regard the rotation of the particles besides the sole particle translation like in [24, 25, 55]. Due to the particle rotation, the interaction between the particles also depends on the mutual orientation of the particles, cf. [32, 64]. Thereby, our model permits structural analysis of the receptor clusters as well as the determination of the time evolution of ligand-receptor clusters of different sizes.

This thesis is structured as follows. According to the two important processes involved in the extrinsic pro-apoptotic pathway, there are two main chapters: Chapter 2 deals with the mathematical model of the caspase-3/8 feedback loop of the extrinsic pro-apoptotic signaling pathway, Chapter 3 is about the particle model describing the receptor clustering on the cellular membrane. In the following, we briefly outline the content of the two main chapters.

In Chapter 2, we first give in Section 2.1 the biological background of the extrinsic signaling pathway before we state in Section 2.2 the equations modeling the underlying reaction network. Subsequently, we add the spatial extension of a single cell to the introduced model and present the reaction-diffusion system in Section 2.3. The determination of the steady states of the reaction system and the stability analysis follow in Section 2.4. As we expect from [15], the reaction system is bistable with two asymptotically stable steady states separated by one unstable steady state. In Section 2.5, we show that the stability properties of the steady states are transferred to the spatially homogeneous stationary solutions of the reaction-diffusion system. Afterward, we prove in Section 2.6 the local existence and uniqueness of a solution, before we state in Section 2.7 a positive invariant region that ensures the boundedness in the sense of L^∞. In Section 2.8, we numerically solve the reaction-diffusion system in case of radially symmetric concentration distributions and find a switch-like behavior concerning the initial condition. We conclude the chapter with Section 2.9 where we consider the reaction-diffusion system on a large spatial scale in order to find nontrivial spatio-temporal structures. For bistable reaction-diffusion systems, the typical structure is a traveling wave solution connecting the two asymptotically stable steady states. Some of the results of this chapter have already been published in [13].

At the beginning of Chapter 3, we state in Section 3.1 the biological background for the receptor clustering on the cell membrane before we introduce in Section 3.2 the general setting of the particle model. The mathematical model of receptor clustering is then de-

rived in Section 3.3: First, we consider the particle translation in Section 3.3.1 and derive a stochastic differential equation from a Langevin equation. Subsequently, we analogously derive a stochastic differential equation for the particle rotation in Section 3.3.2. Afterward, we present in Section 3.3.3 the distinction of the different scenarios with distinguishable binding structures of death receptors. To complete the particle model we introduce the interactions between the particles in Section 3.3.4 and summarize the particle model for the different scenarios in Section 3.3.5. In order to solve the nonlinearly coupled system of stochastic differential equations numerically, we present in Section 3.4 the Euler-Maruyama approximation. For an efficient implementation of the algorithms, we use the Linked-Cell Method explained in Section 3.5 and in Section 3.6, we present the numerical results of the simulation. Here, we investigate the different biological scenarios concerning the time evolution of the cluster formation. For the analysis of the receptor clustering, the visualization tool *cellVis* developed by the SimTech cooperation partner Martin Falk supports the determination of ligand-receptor cluster structures, and the application of GPU computing implemented by the SimTech cooperation partner Claus Braun enables the simulation for several particle configurations. The speed-up obtained with the mapping of the algorithms on the GPU is stated in Section 3.7. The first version of the particle model with only two particle types together with the visualization tool has been published in [17]. An extension of the particle model for three different particle types together with the mapping on a GPGPU architecture has been published in [8].
In the outlook (Chapter 4), we give ideas for an extension of the reaction-diffusion model with other boundary conditions and a more efficient analyzable model for the receptor clustering. Finally, the coupling of both processes would be desirable according to the biological structure of the extrinsic signaling pathway.
In the appendices, we state advisements for the computation of biological quantities (Appendix A.1) and the derivation of the Bessel differential equation for the Laplace operator in Appendix A.2 which is required for the stability analysis in Section 2.5. Furthermore, we present in Appendix A.3 an invariant region that has the typical structure for reaction-diffusion systems with a diagonal diffusion matrix. Last but not least, we state the Finite Difference method used for solving the reaction-diffusion system numerically. First, we explain the method for the case of radially symmetric concentrations (Appendix A.4) and afterward, for the reaction-diffusion system in two dimensions with parameter dependent boundary conditions on a rectangular domain (Appendix A.5) introduced in Chapter 4.

2. Mathematical Model of the Caspase-3/8 Feedback Loop

In recent years, the development of mathematical models for apoptotic processes has become of increased interest. In systems biology, models for the relationship and the interactions between proteins inside a cell are investigated and the models are described by huge systems of ordinary differential equations [19, 4]. The analysis of these systems give a detailed overview of the mutual inhibition and activation effects of the proteins. However, most of the models do not take into account the spatial extension of a cell.

Therefore, we introduce in Section 2.3 a spatially extended reaction-diffusion model, an extension of the reaction system replicated in Section 2.2, which forms the central machinery of the extrinsic pro-apoptotic signaling pathway. In Section 2.4, we determine the steady states of the underlying reaction system and study their stability. Afterward, we investigate in Section 2.5 whether the stability properties can be transferred to the respective stationary solutions of the reaction-diffusion system. In Section 2.6, we prove the existence and uniqueness of a solution of the reaction-diffusion system. Furthermore, we show that it is bounded in L^∞ by presenting an appropriate invariant region in Section 2.7. In the subsequent Section 2.8, we solve the reaction-diffusion system for different initial conditions numerically. We find a switch-like behavior of the system concerning the initial conditions, i.e., an initial activation beyond a certain threshold leads to the death of a cell whereas an initial activation beneath the threshold results in its survival. At the end, we find in Section 2.9 a nontrivial spatio-temporal structure of a solution under the assumption of a large spatial scale. Here, the solution has the form of a traveling wave connecting the two asymptotically stable steady states, the typical structure for bistable reaction-diffusion systems. Some of the results presented in this chapter have already been published in [13].

Before we introduce the mathematical model for the caspase-3/8 feedback loop in Section 2.2, we first provide in Section 2.1 the biological background of the apoptotic signaling pathway.

2.1 Biological Background of the Caspase-3/8 Feedback Loop

Apoptosis is a highly complex physiological process which is difficult to understand in detail. Two major signaling pathways are involved in the apoptotic process and therefore, they are object of research in recent decades: the mitochondrial or intrinsic signaling pathway and the death-receptor or extrinsic signaling pathway [27]. The interaction of the physiological processes is complicated due to the connection between the pathways [21, 27, 37]. Actually, the two pathways can not be considered separately. But, in order to enable the development of analyzable mathematical models of the apoptotic processes, the disentanglement of the two signaling pathways is necessary, especially if the point of interest is not the most realistic model with all possible interactions. The justification of the disentanglement is given for type I cell in [37, 4]. In this cell type, from death inducing signaling complex (DISC) released active caspase 8 simultaneously activate caspase 3 and the death of the cell occurs very quickly. A typical type I cell is the human rhabdomyosarcoma cell line KYM-1 which is highly sensitive to TNF-mediated cytotoxicity [44]. In this thesis, we focus on the extrinsic pro-apoptotic signaling pathway and introduce in this section the biological background of this signaling pathway.

A huge amount of proteins are involved in the reaction network of the extrinsic signaling pathway, whereby the so-called caspases play a central role in the apoptotic machinery. Caspases, which is the abbreviation for **c**ysteine-dependent **asp**artate-specific prote**ases** [59], are a special form of proteases, a type of proteins being able to cleave other proteins. Today, more than a dozen different caspases are known and subdivided into two groups [47]: the family of initiator caspases where caspase 8, 9 and 10 belong to, and the effector caspases including caspase 3, 4, 5, 6, 7, 11, 12, 13. The division of the caspases into two groups is according to their function: the effector caspases dismantle the cell and the initiator caspases initiate the degradation of the cell in response to pro-apoptotic signals. Caspases are present in mammalian cells as inactive pro-enzymes, so-called pro-caspases, and get activated upon proteolytic cleavage. The different forms of caspase activation will be explained below. For the extrinsic signaling pathway, caspase 8 is the key initiator caspase and caspase 3 is the most effective effector caspase. The other caspases do not play a major role in the central machinery of the extrinsic signaling pathway and thus, the effect of these caspases is not further explained. However, in the following we take a closer look at caspase 8 and caspase 3 as central proteases of the extrinsic pro-apoptotic signaling pathway.

Like any other caspase, caspase 8 is present in mammalian cells as pro-enzyme, called pro-caspase 8. Pro-caspase 8 has a mass of 55 kDa [37] and is composed of four distinct

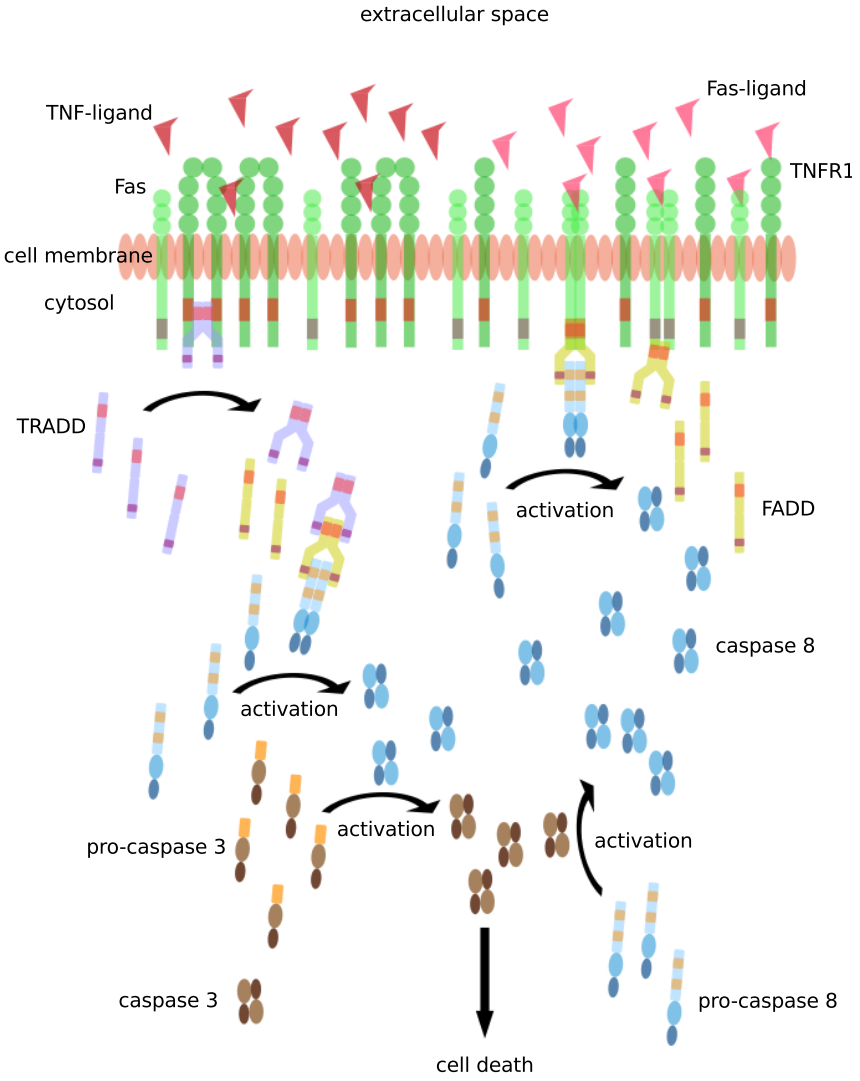

Figure 2.1: Sketch of the extrinsic pro-apoptotic signaling pathway. There are two ways to initiate the signaling pathway: by active TNF receptors of type 1 or by active Fas receptors. The caspase-3/8 feedback loop plays the central role of the extrinsic signaling pathway.

domains: the so-called pro-domain or N-terminal polypeptide, a large subunit of mass 20 kDa [37] or 18 kDa [11], a small subunit of mass 12 kDa [37] or 11 kDa [11], and a linker region between the large and the small subunit [47, 11]. At least, three mechanisms for caspase 8 activation exist in mammalian cells [37]: (a) transactivation, i.e. the activation of pro-caspase 8 by another caspase, for instance caspase 3; (b) recruitment activation via death receptors at the cell membrane; (c) autoactivation where pro-caspase 8 initiates its own activation.

(a) In case of transactivation, pro-caspase 8 gets activated through cleavage between the large and the small subunit and the removal of the pro-domain and the linker region [47, 21, 27]. The small and the large subunits are subsequently assembled to an active caspase which has a heterotetrameric structure composed of two small

subunits and two large subunits [37] with two active sites [27], and thus, has a mass of 64 kDa [37] and 58 kDa [11], respectively. Besides the structure of pro-caspase 8 with a large and a small subunit and the pro-domain, the composition of active caspase 8 is illustrated in Figure 2.1, whereas the special heterotetrameric structure of caspase 8 is omitted in Figure 2.1.

(b) In case of recruitment activation, pro-caspase 8 gets activated by death receptors at the cellular membrane. There are different ways of activating pro-caspase 8 by death receptors at the cellular membrane dependent on the type of death receptor [41, 37], see Figure 2.1. Considering Fas receptors, the Fas receptor binds to the Fas-associated death domain (FADD) adaptor protein via the death domain (DD) of FADD and the DD of the Fas receptor. By this, FADD molecules are brought together within the cell and a further death domain of FADD, the so-called death effector domain (DED), is exposed. By this, the DED of FADD binds to one of the two DEDs [21, 38] in the pro-domain of pro-caspase 8 resulting in the activation of pro-caspase 8, see Figure 2.1. The other DED in the pro-domain of pro-caspase 8 may be required for homodimerization or stabilization of the complex [38]. In summary, the activation occurs via dimerization, i.e., two pro-caspase 8 monomers are bound together and form a caspase dimer with a heterotetrameric structure [37].
Considering TNFR1, the activation process of pro-caspase 8 is more complex. First, ligated TNFR1 recruits TNFR-associated death domain (TRADD) adaptor proteins. The dimeric TRADD is subsequently released from the intracellular part of TNFR1 and enters the cytosol of the cell. There, the TRADD dimer recruits FADD enforcing the formation of FADD dimers which finally activate pro-caspase 8 by dimerization [37].

(c) In case of autoactivation of pro-caspase 8, the inactive pro-form of caspase 8, i.e. pro-caspase 8, has a small activity in the order of $1\%-2\%$ of the activity of caspase 8 [59]. This intrinsic enzymatic activity of the zymogens is also known for other caspase types, for instance pro-caspase 3 and pro-caspase 9. According to [27], the induced proximity model provides the sufficiency of a low intrinsic protease activity of pro-caspase 8 for a mutual activation of pro-caspase 8. Here, a high local concentration of pro-caspase 8 recruited by the adaptor proteins, for instance FADD, is required. More detailed information about the autoactivity of caspases is given in [59].

Once activated, caspase 8 is able to cleave effector pro-caspases, for instance pro-caspase 3 or pro-caspase 7, and initiates a cascade of effector caspases. Especially, the activation of pro-caspase 3 by caspase 8 occurs directly without an additional amplifier [58]. The activation of pro-caspase 3 by caspase 8 results in active caspase 3 and is also illustrated in Figure 2.1. According to [11], pro-caspase 3 has a mass of 32 kDa and consists of a large

subunit (17 kDa), a small subunit (12 kDa) and an additional pro-domain. Through the activation by caspase 8, pro-caspase 3 is cleaved into a small and a large subunit and the pro-domain is cutted. Two large and two small subunits are subsequently assembled to an active caspase 3 of mass 58 kDa with a heterotetrameric structure [11]. Caspase 3 itself is capable to cleave pro-caspase 8 [66] and thereby, a caspase cascade with a positive feedback loop is generated. Finally, caspase 3 is required for typical hallmarks of apoptosis. So, it is involved amongst others in the fragmentation of the DNA, the dismantling of the cell and the formation of apoptotic bodies that get engulfed by surrounding cells [50].

Remark 2.1. It seems that caspase 8, once activated, irrevocably leads to the death of the cell since nothing could stop this apoptotic machinery. Obviously, an accidental activation of pro-caspase 8 should not unstoppable lead to cell death. However, the processes in a single cell are more complex than described so far and other regulatory proteins exist. On the one hand, caspase 8 has also non-proteolytic functions, i.e. functions which do not induce apoptotic cascades, for instance the NFκB activation dependent on the cFLIP concentration [39]. Here, cFLIP prevents the dimerization of pro-caspase 8 at the adaptor protein FADD by forming heterodimers with pro-caspase 8 which then remain associated with FADD.
On the other hand, inhibitors for caspase 8, called BAR, and for caspase 3, called XIAP, exist [65, 15]. The functions of these inhibitors are not explained in detail as they do not play any role for the model in this work.

In order to formulate a mathematical model for the caspase-3/8 feedback loop, the most important facts of the reaction network of the extrinsic pro-apoptotic signaling pathway can be summarized as follows:
First, we emphasize that we only consider two caspase types in our model, namely caspase 8 and caspase 3, both in active and inactive form. Moreover, loosely speaking, pro-caspase 8 gets activated by active death receptors at the cell membrane and caspase 8 is capable to cleave pro-caspase 3. Conversely, caspase 3 cleaves pro-caspase 8 building an amplifier for the caspase cascade. Finally, high caspase 3 concentrations ensure the death of the cell.

In the subsequent Section 2.2, we replicate a reaction model of this caspase-3/8 feedback loop introduced in [15], before we present in Section 2.3 a spatial extension of this model.

2.2 Governing Equations for the Reaction Network

With the biological background of the extrinsic pro-apoptotic signaling pathway at hand, we recall the mathematical model of the caspase cascade introduced by Eissing et al. in [15]. This simplified model contains two caspase types: the initiator caspase 8 and the effector caspase 3. Both of them are present in most cells as pro-enzymes and get activated to fully functional proteases by cleavage. Hence, caspase 3 and caspase 8 exist in cells in an active and inactive form. In order to model the time evolution of the caspase concentrations, a simple four-dimensional system of ordinary differential equations (ODE) can be used if the spatial extension of the cell is ignored or if the caspase concentrations are assumed to be uniformly distributed in cells.

In the ODE model in [15], only two reactions involved in the caspase cascade are taken into account: the activation of pro-caspase 8 by caspase 3 upon cleavage and the activation of pro-caspase 3 by caspase 8:

$$\mathrm{C8} + \mathrm{C3}^* \longrightarrow \mathrm{C8}^* + \mathrm{C3}^*, \qquad \mathrm{C3} + n\,\mathrm{C8}^* \longrightarrow \mathrm{C3}^* + n\,\mathrm{C8}^*. \tag{2.1}$$

In (2.1), the asterisk denotes the active form of the corresponding caspase and n describes cooperativity effects in the activation of caspase 3. Cooperativity means that several molecules, say n, are involved in the reaction with another molecule. This phenomenon was first established by Hill in the year 1910 for the binding of oxygen to hemoglobin. Hill postulated that four oxygen molecules bind to one hemoglobin molecule [5, 18]. We assume that the caspases with their enzymatic properties show a similar cooperativity behavior [15].
We introduce the concentrations $X_i = [\mathrm{C8}]$, $Y_i = [\mathrm{C3}]$, $X_a = [\mathrm{C8}^*]$ and $Y_a = [\mathrm{C3}^*]$ of the four caspase types. The concentrations are measured in the unit Molar abbreviated with M. Another, more popular unit for molar concentrations is mol/l.
The reaction rates k_{c1} and k_{c2} are according to the law of mass action and it is assumed that pro-caspase 8 and pro-caspase 3 are produced in cells with a production rate k_{p1} and k_{p2}, respectively. Furthermore, (pro-) caspase 8 and (pro-) caspase 3 are degraded in cells with degradation rates k_{d1},k_{d2},k_{d3} and k_{d4}, respectively. If we further take cooperativity effects described by the exponent n into account, then we obtain the following system of ODEs, cf. [15]:

$$\begin{aligned}
\dot{X}_a &= k_{c1} X_i Y_a - k_{d1} X_a, \\
\dot{Y}_a &= k_{c2} Y_i X_a^n - k_{d2} Y_a, \\
\dot{X}_i &= -k_{c1} X_i Y_a - k_{d3} X_i + k_{p1}, \\
\dot{Y}_i &= -k_{c2} Y_i X_a^n - k_{d4} Y_i + k_{p2}.
\end{aligned} \tag{2.2}$$

We choose the parameter values

$$\begin{aligned} k_{c1} &= 8 \cdot 10^5\,\mathrm{M}^{-1}\mathrm{s}^{-1}, & k_{c2} &= 8 \cdot 10^{7n-2}\,\mathrm{M}^{-n}\mathrm{s}^{-1}, \\ k_{p1} &= k_{p2} = 1 \cdot 10^{-11}\,\mathrm{Ms}^{-1}, & k_{di} &= 0.03\,\mathrm{min}^{-1}, i = 1, \ldots, 4, \end{aligned} \tag{2.3}$$

close to the different values given in [14] and [15]. The exponent $n \geq 1$ for the cooperativity has no dimension and will be specified below. The reaction rate k_{c2} depends on the exponent n according to the units of the reaction system (2.2). In Section 2.3, the system (2.2) will be transferred to a dimensionless form. Then, the reaction rate k_{c2} will be independent of n.
Finally, we introduce the short form of the reaction system (2.2)

$$\dot{v}(t) = f(v(t)) \tag{2.4}$$

with $v(t) = (X_a(t), Y_a(t), X_i(t), Y_i(t))$ and the function $f(v(t))$ including the right-hand side of (2.2). The short form (2.4) simplifies the notation in the stability analysis of the reaction system in Section 2.4.

The nonlinearly coupled system of ordinary differential equations (2.2), briefly called reaction system, includes several parameters. These parameters influence the dynamical behavior of the system. A frequently occurrent phenomenon of nonlinear ODE systems is bistability, i.e. two stable steady states separated by one unstable steady state. Of course, the number and the location of steady states depend on the chosen parameter values.

In Section 2.4, we quantitatively determine the steady states of the reaction system (2.2) for the parameter setting in (2.3) for different values of n, and study their stability. But prior to that, we introduce in Section 2.3 a spatial extension of the reaction system (2.2).

2.3 Spatially Extended Reaction-Diffusion Model of the Caspase-3/8 Feedback Loop

The main disadvantage of the model introduced in Section 2.2 is the disregard of the spatial extension of a single cell. The different processes of the extrinsic pro-apoptotic signaling pathway occur at different places in a cell. For instance, the external stimulus of the signaling pathway is given by the activation of pro-caspase 8 by death receptors at the cell membrane.

Therefore, it makes sense to consider a spatially extended version of the ODE model introduced in [15]. The simplest way to do so is to incorporate diffusion of the caspases into the model. So, we introduce the spatial variable $x \in \mathbb{R}^d$, with d the space dimen-

sion, and extend (2.2) by adding the diffusion terms $(d_1\Delta_x X_a, d_2\Delta_x Y_a, d_3\Delta_x X_i, d_4\Delta_x Y_i)$, with diffusion coefficients d_1, d_2, d_3, d_4 similarly to other spatially extended models in mathematical biology, cf. for instance [46, Sec. 11.2]. We consider the spatial domain $\Omega = \{x \in \mathbb{R}^d, \|x\|_2 \leq L\}$, i.e., the cell is modeled as a d-dimensional sphere with radius L. Since the model introduced in [15] is best reflected in biology by a type I cell like KYM-1 and since a KYM-1 cell has a radius of approximately 10 µm, we assume a length scale of $L = 10\,\mu\text{m}$. We finally obtain the reaction-diffusion system

$$\begin{aligned}
\tfrac{\partial X_a}{\partial t} &= k_{c1} X_i Y_a - k_{d1} X_a + d_1 \Delta_x X_a, \\
\tfrac{\partial Y_a}{\partial t} &= k_{c2} Y_i X_a^n - k_{d2} Y_a + d_2 \Delta_x Y_a, \\
\tfrac{\partial X_i}{\partial t} &= -k_{c1} X_i Y_a - k_{d3} X_i + k_{p1} + d_3 \Delta_x X_i, \\
\tfrac{\partial Y_i}{\partial t} &= -k_{c2} Y_i X_a^n - k_{d4} Y_i + k_{p2} + d_4 \Delta_x Y_i.
\end{aligned} \tag{2.5}$$

First of all, we eliminate the units of the quantities with the transformation $\bar{x} = x/L$ and $\bar{t} = t/\tau$, where the time scale $\tau = L^2/d_1$ is coupled to the diffusion rate d_1 and the length scale L. We divide the equations of the reaction-diffusion system (2.5) by 100 nM, the order of the typical caspase concentration in KYM-1 cells, cf. Appendix A.1.1, and get the reaction-diffusion system in the dimensionless form

$$\begin{aligned}
\tfrac{\partial X_a}{\partial \bar{t}} &= \tilde{k}_{c1} X_i Y_a - \tilde{k}_{d1} X_a + D_1 \Delta_{\bar{x}} X_a, \\
\tfrac{\partial Y_a}{\partial \bar{t}} &= \tilde{k}_{c2} Y_i X_a^n - \tilde{k}_{d2} Y_a + D_2 \Delta_{\bar{x}} Y_a, \\
\tfrac{\partial X_i}{\partial \bar{t}} &= -\tilde{k}_{c1} X_i Y_a - \tilde{k}_{d3} X_i + \tilde{k}_{p1} + D_3 \Delta_{\bar{x}} X_i, \\
\tfrac{\partial Y_i}{\partial \bar{t}} &= -\tilde{k}_{c2} Y_i X_a^n - \tilde{k}_{d4} Y_i + \tilde{k}_{p2} + D_4 \Delta_{\bar{x}} Y_i
\end{aligned} \tag{2.6}$$

in $\bar{\Omega} := \{\bar{x} \in \mathbb{R}^d, \|\bar{x}\|_2 \leq 1\}, d = 1, 2, 3$, with $D_1 = 1, D_2 = d_2/d_1, D_3 = d_3/d_1, D_4 = d_4/d_1$. The values for the diffusion coefficients $d_1, \ldots, d_4$ are determined in Appendix A.1.2, namely

$$d_1 = 18.0\,\frac{\mu\text{m}^2}{\text{s}}, d_2 = 18.6\,\frac{\mu\text{m}^2}{\text{s}}, d_3 = 18.9\,\frac{\mu\text{m}^2}{\text{s}}, d_4 = 22.7\,\frac{\mu\text{m}^2}{\text{s}}. \tag{2.7}$$

Hence, the ratios of the diffusion coefficients are $D_2 = 1.03,\ D_3 = 1.05$ and $D_4 = 1.26$. Moreover, the reaction, production and degradation rates in the dimensionless form are

$$\begin{aligned}
&\tilde{k}_{c1} = k_{c1} \cdot \tau \cdot 100\,\text{nM} = 0.444, \quad \tilde{k}_{c2} = k_{c2} \cdot \tau \cdot (100\,\text{nM})^n = 0.444, \\
&\tilde{k}_{dj} = k_{dj} \cdot \tau/60 = 0.0028, \qquad\quad \tilde{k}_{pi} = k_{pi} \cdot \tau/100\,\text{nM} = 5.556 \cdot 10^{-4},
\end{aligned} \tag{2.8}$$

$i = 1, 2$ and $j = 1, \ldots, 4$. Actually, the concentrations in (2.6) do not agree with the concentrations in (2.5), since they are scaled by a factor 100 nM. For simplicity, we take the same notation for the dimensionless concentrations.

The reaction-diffusion system (2.6) has to be completed with appropriate boundary and initial conditions. Instead of mixed boundary conditions describing the activation of pro-caspase 8 by death receptors at the cell membrane, we assume that there is no flux of caspases through the cell membrane, but assume simultaneously that a region near the boundary is initially filled with high caspase 8 and caspase 3 concentrations, whereas the rest of the cell is initially filled with low caspase 8 and caspase 3 concentrations. This assumption corresponds to a fast activation of pro-caspase 8 and pro-caspase 3 at the cell membrane by death receptors and active caspase 8, respectively. Physiologically, this resembles a situation where death receptors are activated by a pulse stimulus and subsequently deactivated, for example by receptor internalization and turnover.

In detail our assumptions are as follows. The reaction-diffusion system (2.6) is completed with homogeneous Neumann boundary conditions at $\partial\bar{\Omega}$

$$\left.\frac{\partial X_a}{\partial n}\right|_{\partial\bar{\Omega}} = \left.\frac{\partial Y_a}{\partial n}\right|_{\partial\bar{\Omega}} = \left.\frac{\partial X_i}{\partial n}\right|_{\partial\bar{\Omega}} = \left.\frac{\partial Y_i}{\partial n}\right|_{\partial\bar{\Omega}} = 0 \tag{2.9}$$

due to the assumption that there is no flux of caspases through the cell membrane.

Moreover, we choose localized caspase concentrations as initial conditions

$$(X_a, Y_a, X_i, Y_i)(\bar{x}, 0) = \begin{cases} (X_a^{(d)}, Y_a^{(d)}, X_i^{(d)}, Y_i^{(d)}) & \text{for} \quad \bar{x} \in \bar{\Omega}_{\text{ext}}, \\ (X_a^{(l)}, Y_a^{(l)}, X_i^{(l)}, Y_i^{(l)}) & \text{for} \quad \bar{x} \in \bar{\Omega}_{\text{in}} \end{cases} \tag{2.10}$$

with

$$\bar{\Omega}_{\text{ext}} := \{\bar{x} \in \mathbb{R}^d, R_0 \leq \|\bar{x}\|_2 \leq 1\}, \quad \text{and} \quad \bar{\Omega}_{\text{in}} := \{\bar{x} \in \mathbb{R}^d, \|\bar{x}\|_2 < R_0\}$$

for a $R_0 \in (0, 1)$. Here, $(X_a^{(d)}, Y_a^{(d)}, X_i^{(d)}, Y_i^{(d)})$ denotes the state with high caspase 3/8 concentrations but low pro-caspase 3/8 concentrations, and $(X_a^{(l)}, Y_a^{(l)}, X_i^{(l)}, Y_i^{(l)})$ corresponds to the state with low caspase 3/8 concentrations and high pro-caspase 3/8 concentrations. These two states will correspond to the so-called death state and the life state in Section 2.4, respectively.

Finally, we introduce the short form of the reaction-diffusion system (2.6)

$$\frac{\partial u}{\partial \bar{t}} = D\Delta_{\bar{x}} u + f(u) \tag{2.11}$$

with $u(\bar{x}, \bar{t}) = (X_a(\bar{x}, \bar{t}), Y_a(\bar{x}, \bar{t}), X_i(\bar{x}, \bar{t}), Y_i(\bar{x}, \bar{t})), D = \text{diag}\{D_1, D_2, D_3, D_4\}$ and the function $f(u)$ containing the reaction kinetics of (2.6).

The initial conditions are according to (2.10)

$$u(\bar{x}, 0) = u_0(\bar{x}), \quad \bar{x} \in \bar{\Omega}, \tag{2.12}$$

and the boundary conditions are given by

$$\left.\frac{\partial u}{\partial n}\right|_{\partial\bar{\Omega}} = 0, \ \bar{t} \geq 0. \tag{2.13}$$

In order to enable an analysis of the reaction-diffusion system (2.11), we have to modify the diffusion rates. We set $\tilde{D}_1 = \tilde{D}_3 = 1, \tilde{D}_2 = \tilde{D}_4 = (D_2 + D_4)/2$ and $\tilde{D} = \mathrm{diag}\{\tilde{D}_1, \tilde{D}_2, \tilde{D}_3, \tilde{D}_4\}$, and obtain

$$\frac{\partial u}{\partial \bar{t}} = \tilde{D}\Delta_{\bar{x}} u + f(u). \tag{2.14}$$

Here, we assume for simplicity that the value of the diffusion coefficient for pro-caspase 8 agrees with that of caspase 8. For the corresponding values of pro-caspase 3 and caspase 3, we take the average of the diffusion rates D_2 and D_4. The discrepancy of $\tilde{D}_2$ and $\tilde{D}_4$ to the corresponding "exact" values is about 10%. Actually, performing an error propagation for the diffusion coefficient D_n given in formula (A.2) and assuming a measurement error of 5% for D_{GFP}, $\mathrm{m}_{\mathrm{GFP}}$ and m_{n} results in a relative error of about 8% for the diffusion coefficient D_n. This consideration justifies the simplification by averaging the values of the diffusion coefficients d_2 and d_4, and thereby the values of D_2 and D_4.

In the following and in the rest of this chapter, we only consider the dimensionless form of the reaction-diffusion system (2.14). Therefore, we omit the bars on top of the variables x and t, i.e., we replace $\bar{x}$ by x and $\bar{t}$ by t in order to simplify the notation.

2.4 Stability Analysis for the Steady States of the Reaction System

Before we analyze the reaction-diffusion system (2.14) with boundary and initial conditions, we first reproduce the results from Eissing et al. in [15]. In [15], a qualitative phase plane analysis shows bistable behavior for the reaction system (2.2). In contrast to [15], we present in the following a quantitative stability analysis of the numerically determined steady states of the reaction system.

The steady states for the reaction system (2.2) are time independent solutions $X^* = (X_a^*, Y_a^*, X_i^*, Y_i^*)$ of (2.2), i.e. $\frac{\mathrm{d}}{\mathrm{d}t}X^* = 0$. Therefore, X^* satisfies $f(X^*) = 0$ and we

obtain the steady states by solving the system of algebraic equations

$$0 = \tilde{k}_{c1} X_i^* Y_a^* - \tilde{k}_{d1} X_a^*, \tag{2.15}$$
$$0 = \tilde{k}_{c2} Y_i^* (X_a^*)^n - \tilde{k}_{d2} Y_a^*, \tag{2.16}$$
$$0 = -\tilde{k}_{c1} X_i^* Y_a^* - \tilde{k}_{d3} X_i^* + \tilde{k}_{p1}, \tag{2.17}$$
$$0 = -\tilde{k}_{c2} Y_i^* (X_a^*)^n - \tilde{k}_{d4} Y_i^* + \tilde{k}_{p2}. \tag{2.18}$$

First, we solve equation (2.15) for X_a^*, (2.16) for Y_a^*, (2.17) for X_i^*, (2.18) for Y_i^* and get

$$X_a^* = \frac{\tilde{k}_{c1} X_i^* Y_a^*}{\tilde{k}_{d1}}, \tag{2.19}$$
$$Y_a^* = \frac{\tilde{k}_{c2} Y_i^* (X_a^*)^n}{\tilde{k}_{d2}}, \tag{2.20}$$
$$X_i^* = \frac{\tilde{k}_{p1}}{\tilde{k}_{c1} Y_a^* + \tilde{k}_{d3}}, \tag{2.21}$$
$$Y_i^* = \frac{\tilde{k}_{p2}}{\tilde{k}_{c2} (X_a^*)^n + \tilde{k}_{d4}}. \tag{2.22}$$

If we put (2.22) into (2.20), we have

$$Y_a^* = \frac{\tilde{k}_{p2} \tilde{k}_{c2} (X_a^*)^n}{\tilde{k}_{d2} (\tilde{k}_{c2} (X_a^*)^n + \tilde{k}_{d4})}. \tag{2.23}$$

Together with (2.23), equation (2.21) leads to

$$X_i^* = \frac{\tilde{k}_{p1} \tilde{k}_{d2} (\tilde{k}_{c2} (X_a^*)^n + \tilde{k}_{d4})}{(\tilde{k}_{c1} \tilde{k}_{c2} \tilde{k}_{p2} + \tilde{k}_{c2} \tilde{k}_{d2} \tilde{k}_{d3}) (X_a^*)^n + \tilde{k}_{d2} \tilde{k}_{d3} \tilde{k}_{d4}}. \tag{2.24}$$

Finally, putting (2.24) together with (2.23) into (2.19), we obtain one equation for X_a^*

$$X_a^* = \frac{\tilde{k}_{c1} \tilde{k}_{p1} \tilde{k}_{p2} \tilde{k}_{c2} (X_a^*)^n}{\tilde{k}_{d1} ((\tilde{k}_{c1} \tilde{k}_{c2} \tilde{k}_{p2} + \tilde{k}_{c2} \tilde{k}_{d2} \tilde{k}_{d3}) (X_a^*)^n + \tilde{k}_{d2} \tilde{k}_{d3} \tilde{k}_{d4})}. \tag{2.25}$$

Equation (2.25) is equivalent to

$$\begin{aligned}(\tilde{k}_{c1} \tilde{k}_{c2} \tilde{k}_{d1} \tilde{k}_{p2} + \tilde{k}_{c2} \tilde{k}_{d1} \tilde{k}_{d2} \tilde{k}_{d3}) (X_a^*)^{n+1} &- \tilde{k}_{c1} \tilde{k}_{c2} \tilde{k}_{p1} \tilde{k}_{p2} (X_a^*)^n \\ &+ \tilde{k}_{d1} \tilde{k}_{d2} \tilde{k}_{d3} \tilde{k}_{d4} X_a^* = 0.\end{aligned} \tag{2.26}$$

Obviously, the first solution of (2.15)–(2.18) denoted with $X^{(l)} := (X_a^{(l)}, Y_a^{(l)}, X_i^{(l)}, Y_i^{(l)})$ is

given by

$$X^{(l)} = (0, 0, \frac{\tilde{k}_{p1}}{\tilde{k}_{d3}}, \frac{\tilde{k}_{p2}}{\tilde{k}_{d4}}) = (0, 0, 0.2, 0.2). \tag{2.27}$$

This solution exists independently of the choice of the parameter values and the exponent $n \geq 1$ as long as $\tilde{k}_{d3} \neq 0 \neq \tilde{k}_{d4}$. When there is no cooperativity, i.e. $n = 1$, then equation (2.26) has at most two real solutions and hence, the system exhibits no bistable behavior. Therefore, we only consider values for n larger than one. To find nontrivial solutions of (2.26), we consider

$$(\tilde{k}_{c1}\tilde{k}_{c2}\tilde{k}_{d1}\tilde{k}_{p2} + \tilde{k}_{c2}\tilde{k}_{d1}\tilde{k}_{d2}\tilde{k}_{d3})(X_a^*)^n - \tilde{k}_{c1}\tilde{k}_{c2}\tilde{k}_{p1}\tilde{k}_{p2}(X_a^*)^{n-1} + \tilde{k}_{d1}\tilde{k}_{d2}\tilde{k}_{d3}\tilde{k}_{d4} = 0. \tag{2.28}$$

According to [15], we first restrict the computation of the steady states and the stability analysis to the case $n = 2.5$ and close this section with results for other values of $n > 1$. We solve (2.28) numerically for $n = 2.5$ and obtain two real-valued positive solutions

$$X^{(d)} := (X_a^{(d)}, Y_a^{(d)}, X_i^{(d)}, Y_i^{(d)}) = (0.1917, 0.1440, 0.0083, 0.0560), \tag{2.29}$$
$$X^{(u)} := (X_a^{(u)}, Y_a^{(u)}, X_i^{(u)}, Y_i^{(u)}) = (0.0102, 3.3603 \cdot 10^{-4}, 0.1898, 0.1997). \tag{2.30}$$

Next, we analyze the stability of the three steady states. For this purpose, we cite the following well-known

Theorem 2.2 (Theorem 1.2.5 in [63]).
Let f be a $C^1(\mathbb{R}^d, \mathbb{R}^d)$ function. Suppose all eigenvalues of $J|_{X^*} = \nabla f(X^*)$ have negative real parts. Then the steady state $v = X^*$ of the nonlinear ordinary differential equation $\dot{v} = f(v)$ is asymptotically stable.

In order to analyze the stability of the steady states, we look at the Jacobian

$$J|_{X^*} = \begin{pmatrix} -\tilde{k}_{d1} & \tilde{k}_{c1}X_i & \tilde{k}_{c1}Y_a & 0 \\ n\tilde{k}_{c2}Y_iX_a^{n-1} & -\tilde{k}_{d2} & 0 & \tilde{k}_{c2}X_a^n \\ 0 & -\tilde{k}_{c1}X_i & -\tilde{k}_{c1}Y_a - \tilde{k}_{d3} & 0 \\ -n\tilde{k}_{c2}Y_iX_a^{n-1} & 0 & 0 & -\tilde{k}_{c2}X_a^n - \tilde{k}_{d4} \end{pmatrix}\Bigg|_{X^*} \tag{2.31}$$

of the right-hand side of the reaction system (2.2) evaluated at the steady state $X^* \in \{X^{(l)}, X^{(d)}, X^{(u)}\}$ and apply Theorem 2.2. The eigenvalues of the Jacobian for the three steady states in case $n = 2.5$ are given by

$$\begin{aligned} X^{(l)}: &\quad \lambda_{1,2,3,4}^{(l)} = -0.0028, \\ X^{(d)}: &\quad \lambda_1^{(d)} = \lambda_2^{(d)} = -0.0028, \lambda_3^{(d)} \approx -0.0184, \lambda_4^{(d)} \approx -0.0675, \\ X^{(u)}: &\quad \lambda_1^{(u)} = \lambda_2^{(u)} = -0.0028, \lambda_3^{(u)} \approx +0.0015, \lambda_4^{(u)} \approx -0.0072. \end{aligned} \tag{2.32}$$

Since the real parts of the eigenvalues $\lambda_i^{(l)}$ and $\lambda_i^{(d)}$, $i = 1, \ldots, 4$, are negative, Theorem 2.2 yields the asymptotic stability of the steady states $X^{(l)}$ and $X^{(d)}$. For $X^{(u)}$, the real part of one of the eigenvalues $\lambda_i^{(u)}$, $i = 1, \ldots, 4$, is positive, and therefore, the steady state $X^{(u)}$ is unstable. Thus, the reaction system (2.2) possesses bistable behavior for this special choice of parameter setting in case $n = 2.5$. The steady state $X^{(d)}$ with high caspase 3 concentration is identified with the death state and the state $X^{(l)}$ with low caspase 3 concentration corresponds to the life state. The unstable transition state has no biological relevance. The values for the life state and the transition state are located close to each other. More precisely, the difference in the concentrations is of the order 10^{-4} corresponding to dimensionally affected caspase concentrations of a few pM. Nevertheless, the difference of the concentrations in a cell with radius $10\,\mu\text{m}$ amounts to at least a few tens of molecules. The relationship between the concentration and the number of molecules is given by

$$N_{\text{mol}} = c \cdot V \cdot N_A, \tag{2.33}$$

where N_{mol} is the number of molecules, c denotes the caspase concentration, V is the volume of the domain and N_A is the Avogadro constant. Since the cell is modeled as a sphere with radius $L = 10\,\mu\text{m}$, the cell has a volume of $V \approx 10^{-12}\,\text{l}$. The difference between the life state concentration and the transition state concentration is about $3.36 \cdot 10^{-4}$ on a scale of $10^{-7}\,\text{M}$ for caspase 3, thus $c \approx 3 \cdot 10^{-11}\,\text{M} = 3 \cdot 10^{-11}\,\text{mol/l}$. If we insert V, c and $N_A = 6.022 \cdot 10^{23}\,1/\text{mol}$ into (2.33), we obtain $N_{\text{mol}} = 84$. So, the difference in the caspase 3 concentration corresponds to 84 molecules. The difference in the other components is much larger. Thus, the steady states are biologically distinguishable.

The bistable behavior of the reaction system is of biological relevance, since a small perturbation of the life state should not lead to the death of the cell for instance. Small perturbations of the life state correspond to a cell with a spontaneous, random activation of pro-caspase 8 by death receptors at the cellular membrane. Of course, in real life this tiny activation does not cause the death of the cell. The same perturbation arguments hold for the death state.

The qualitative behavior of the reaction system remains the same for other values of the exponent $n > 1$. We oppose the results of the case $n = 2.5$ to those of the exponents $n = 2$ and $n = 3$ in order to point out the differences in the quantitative behavior and confirm the similarities in the qualitative behavior of the system. For $n = 2$, we obtain the three steady states

$$X^{(l)} = (0, 0, 0.2, 0.2),$$

$$X^{(d)} = (0.1930, 0.1713, 0.0070, 0.0287),$$
$$X^{(u)} = (9.82 \cdot 10^{-4}, 3.08 \cdot 10^{-5}, 0.1990, 0.2000).$$

Again, the life state $X^{(l)}$ and the transition state $X^{(u)}$ lie close to each other in the phase space, in more detail, the difference in the caspase 3 concentration is $3.08 \cdot 10^{-12}$ M on the biological scale. With (2.33), this concentration corresponds to a number of 8 molecules. The differences in the other concentrations are larger than the difference in the caspase 3 concentration. Thus, the steady states $X^{(l)}$ and $X^{(u)}$ are biologically distinguishable. The same holds of course for the steady states $X^{(l)}$ and $X^{(d)}$. A stability analysis for the three steady states again yields the asymptotic stability of the life and the death state and the instability of the transition state, since the eigenvalues of the Jacobian are given by

$$\begin{aligned} X^{(l)}: &\quad \lambda^{(l)}_{1,2,3,4} = -0.0028, \\ X^{(d)}: &\quad \lambda^{(d)}_1 = \lambda^{(d)}_2 = -0.0028, \lambda^{(d)}_3 \approx -0.0191, \lambda^{(d)}_4 \approx -0.0791, \\ X^{(u)}: &\quad \lambda^{(u)}_1 = \lambda^{(u)}_2 = -0.0028, \lambda^{(u)}_3 \approx +0.0011, \lambda^{(u)}_4 \approx -0.0067. \end{aligned} \tag{2.34}$$

Hence, we again have a bistable behavior of the reaction system.
In case $n = 3$, we obtain the steady states

$$X^{(l)} = (0, 0, 0.2, 0.2),$$
$$X^{(d)} = (0.1886, 0.1036, 0.0114, 0.0964),$$
$$X^{(u)} = (0.0345, 0.0013, 0.1655, 0.1987).$$

Obviously, the three steady states are biologically distinguishable, since the differences in the concentrations are larger than in case $n = 2$ and $n = 2.5$. The eigenvalues of the Jacobian are

$$\begin{aligned} X^{(l)}: &\quad \lambda^{(l)}_{1,2,3,4} = -0.0028, \\ X^{(d)}: &\quad \lambda^{(d)}_1 = \lambda^{(d)}_2 = -0.0028, \lambda^{(d)}_3 \approx -0.0161, \lambda^{(d)}_4 \approx -0.0513, \\ X^{(u)}: &\quad \lambda^{(u)}_1 = \lambda^{(u)}_2 = -0.0028, \lambda^{(u)}_3 \approx +0.0017, \lambda^{(u)}_4 \approx -0.0079. \end{aligned} \tag{2.35}$$

Again, the life state and the death state are asymptotically stable. Thus, the reaction system possesses the desired bistable behavior.

Finally, we reveal the robustness of the bistable behavior of the reaction system under variations in the reaction kinetics. Actually, the given reaction system with the special form of reaction kinetics is a simple model of the reaction network of the caspase cascade. The biologically valid reactions are not known in detail but the cooperativity in the activation of caspase 3 is well established in physiology. Nevertheless, the correct exponent in the reaction kinetic can not exactly be measured in experiments. However,

we showed that the exponent $n > 1$ describing the cooperativity effect does not influence the qualitative behavior of the reaction system. On the other hand we demonstrated the necessity of cooperativity effects in the reaction system for the occurrence of bistability.

Next, we investigate the stability of the spatially homogeneous stationary solutions for the reaction-diffusion system (2.14) with homogeneous Neumann boundary conditions (2.13) introduced in Section 2.3.

2.5 Stability Analysis for the Stationary Solutions of the Reaction-Diffusion System

Since the steady states $X^{(l)}, X^{(u)}$, and $X^{(d)}$ are spatially homogeneous, they are also stationary solutions of the reaction-diffusion system (2.14). In order to analyze their stability, we follow the arguments of Casten and Holland in [9]. Thus, we study the linearized system and conclude the local stability properties of the nonlinear system from the stability properties of the linearized system.
In a first approach, we transform the reaction-diffusion system (2.14) via the linear substitution $z(x,t) = u(x,t) - \tilde{X}(x,t)$, where $\tilde{X}(x,t) = X^{(l,d,u)}$ denotes the spatially homogeneous, stationary solution. We obtain

$$\frac{\partial z}{\partial t} = \tilde{D}\Delta_x z + f(z + \tilde{X}) = \tilde{D}\Delta_x z + \tilde{f}(z) \tag{2.36}$$

with $\tilde{f}(z(x,t)) := f(z(x,t) + \tilde{X}(x,t))$. Here, as mentioned above, the variables x and t are dimensionless. Finally, we have $\tilde{f}(0) = f(\tilde{X}) = 0$ and the zero solution $z \equiv 0$ is a stationary solution of the transformed system (2.36). Actually, the transformed reaction-diffusion system (2.36) contains a hidden dependency on the stationary solution $\tilde{X}(x,t) = X^{(l,d,u)}$ in the function $\tilde{f}$. In the following, we omit the variables of the function $z(x,t)$, thus, we only write z instead of $z(x,t)$.
Next, we linearize the reaction-diffusion system (2.36) with respect to the zero solution $z \equiv 0$, i.e. $\tilde{f}(z) = \tilde{A}z + \tilde{g}(z)$, where $\tilde{A}$ denotes the Jacobian matrix of $\tilde{f}$ at $z \equiv 0$, and $\tilde{g}$ contains the higher order terms in z. Then, the linearized system becomes

$$\frac{\partial z}{\partial t} = \tilde{D}\Delta_x z + \tilde{A}z. \tag{2.37}$$

Obviously, $\tilde{A}$ agrees with the Jacobian matrix $J|_{X^*}$ of the function f evaluated at the steady states X^* of the reaction system (2.2). This circumstance will be used later in the stability analysis of the different steady states.

The stability of the zero solution of the linearized system is determined by the eigen-

values $\mu_i(\lambda_k), i = 1, \ldots, 4$, of the matrix $M(\lambda_k) := \tilde{A} - \lambda_k \tilde{D}$, where λ_k, $k \in \mathbb{N}_0$, are the eigenvalues to the eigenfunctions $\varphi_k \in \mathbb{R}$ of the Laplace operator, i.e., they fulfill the equation

$$-\Delta\varphi_k = \lambda_k \varphi_k \quad \text{in} \quad \Omega = \{x \in \mathbb{R}^d |, \|x\|_2 \leq 1\} \tag{2.38}$$

with homogeneous Neumann boundary conditions $\frac{\partial \varphi_k}{\partial n}|_{\partial\Omega} = 0$, cf. [9]. To see this, we cite the following

Theorem 2.3 (Theorem 1 in [9]).

(i) The zero solution $z \equiv 0$ of (2.37) is (globally) asymptotically stable if for each k the eigenvalues of the matrix $\tilde{A} - \lambda_k \tilde{D}$ have negative real part. Further, there exist positive constants K, ω such that for any $t > 0$

$$\|z(\cdot, t)\|_\infty \leq K \mathrm{e}^{-\omega t} \|z(\cdot, 0)\|_\infty.$$

(ii) The zero solution $z \equiv 0$ of (2.37) is unstable if for some k there exists an eigenvalue of $\tilde{A} - \lambda_k \tilde{D}$ with positive real part.

With this theorem, we obtain the stability statements for the linearized system. For stability results of the original nonlinear reaction-diffusion system (2.36), we need the following

Theorem 2.4 (Theorem 2 in [9]).

The zero solution of (2.36) is asymptotically stable if the zero solution of the linearized problem (2.37) is asymptotically stable.

The proofs of Theorem 2.3 and Theorem 2.4 are given in [9].

For the stability analysis we follow the strategy of the given theorems and study first the stability of the linearized system and conclude subsequently the stability property of the nonlinear system with Theorem 2.4. The main task for the stability analysis of the linearized system is the computation of the eigenvalues of the Laplace operator with homogeneous Neumann boundary conditions. Here, the difficulties of the eigenvalue problem strongly depend on the spatial dimension d. In the one-dimensional case, analytic expressions for the eigenvalues are available while in the two-dimensional case the eigenvalues are given by the zeros of the first derivative of the Bessel functions. The three-dimensional case is even more complicated. In the following, we state the discussion of the stability for the different dimensions in more detail.

First, we consider the eigenvalue problem in the one-dimensional case, i.e. $\Omega = [-1, 1]$, and the Laplace operator is replaced by the second derivative. Hence, the eigenvalue

problem becomes

$$-\varphi_k'' = \lambda_k \varphi_k \quad \text{in} \quad [-1,1] \tag{2.39}$$

with homogeneous Neumann boundary conditions $\varphi_k'(-1) = \varphi_k'(1) = 0$. The eigenvalues are $\lambda_k = \pi^2 k^2$, and the respective eigenfunctions read $\varphi_k(x) = \sqrt{2}/2 \cdot \cos(k\pi x)$, $k \in \mathbb{N}_0$.

Next, we compute the eigenvalues of the matrix $M(\lambda_k)$ in case $n = 2.5$ for the three steady states $X^{(l,d,u)}$.

i) For $\tilde{X}(x,t) = X^{(l)}$ the real part of each eigenvalue $\mu_i^{(l)}(\lambda_k), i = 1\ldots,4$, of the matrix $M(\lambda_k)$ takes negative values for all eigenvalues $\lambda_k, k \in \mathbb{N}_0$. The maxima of the eigenvalues of $M(\lambda_k)$ are reached for λ_0, cf. Figure 2.2, and take the values

$$\begin{aligned} &\max_{k\in\mathbb{N}_0}(\mathrm{Re}(\mu_1^{(l)}(\lambda_k))) \approx -0.0028, \quad \max_{k\in\mathbb{N}_0}(\mathrm{Re}(\mu_2^{(l)}(\lambda_k))) \approx -0.0028, \\ &\max_{k\in\mathbb{N}_0}(\mathrm{Re}(\mu_3^{(l)}(\lambda_k))) \approx -0.0028, \quad \max_{k\in\mathbb{N}_0}(\mathrm{Re}(\mu_4^{(l)}(\lambda_k))) \approx -0.0028. \end{aligned}$$

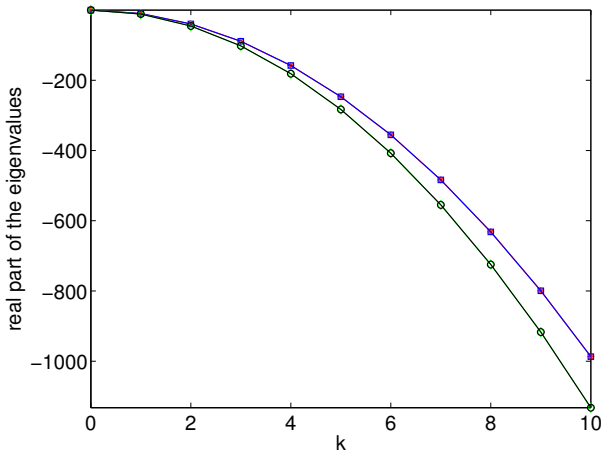

Figure 2.2: Eigenvalues $\mu_i^{(l)}(\lambda_k))), i = 1,\ldots,4$, of the matrix $M(\lambda_k)$ for $X^{(l)}$ depending on the mode k. According to the discrete spectrum of the Laplace operator, that means $k \in \mathbb{N}_0$, the matrix $M(\lambda_k)$ also possesses a discrete spectrum, illustrated by 'green diamonds', 'red stars', 'black circles' and 'blue squares'. The lines between the symbols only serves for the illustration of the progression of the eigenvalues. Actually, two curves coincide so that we only observe two curves instead of four. The range for the scale of the vertical axis is $[\min_{i=1,\ldots,4;k=1,\ldots,10}(\mathrm{Re}(\mu_i^{(l)}(\lambda_k))), \max_{i=1,\ldots,4;k=1,\ldots,10}(\mathrm{Re}(\mu_i^{(l)}(\lambda_k)))]$ and therefore, the real parts of the eigenvalues are negative.

Hence, the solution $z(x,t) = 0$ is asymptotically stable for the linearized system (2.37) and Theorem 2.4 yields the asymptotic stability of $\tilde{X}(x,t) = X^{(l)}$ for the reaction-diffusion system (2.14).

ii) For the steady state $\tilde{X}(x,t) = X^{(u)}$, the real part of one eigenvalue takes a positive value for λ_0, cf. Figure 2.3. The maxima of the real part of the eigenvalues $\mu_i^{(u)}(\lambda_k), i = 1, \ldots, 4$, are

$$\max_{k\in\mathbb{N}_0}(\mathrm{Re}(\mu_1^{(u)}(\lambda_k))) \approx -0.0028, \quad \max_{k\in\mathbb{N}_0}(\mathrm{Re}(\mu_2^{(u)}(\lambda_k))) \approx -0.0028,$$
$$\max_{k\in\mathbb{N}_0}(\mathrm{Re}(\mu_3^{(u)}(\lambda_k))) \approx +0.0015, \quad \max_{k\in\mathbb{N}_0}(\mathrm{Re}(\mu_4^{(u)}(\lambda_k))) \approx -0.0072.$$

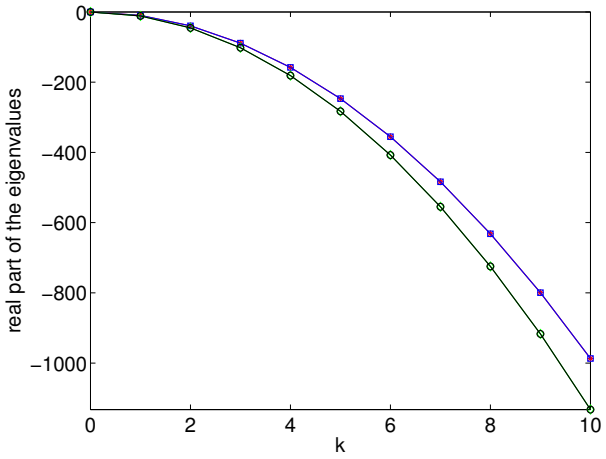

Figure 2.3: Eigenvalues of the matrix $M(\lambda_k)$ for the transition state $X^{(u)}$ depending on the mode k. Again, the range for the scale of the vertical axis is set to $[\min_{i=1,\ldots,4;k=1,\ldots,10}(\mathrm{Re}(\mu_i^{(u)}(\lambda_k))), \max_{i=1,\ldots,4;k=1,\ldots,10}(\mathrm{Re}(\mu_i^{(u)}(\lambda_k)))]$.

Hence, the solution $z(x,t) = 0$ is unstable for the linearized system (2.37) according to Theorem 2.3 and thereby the stationary solution $\tilde{X}(x,t) = X^{(u)}$ is unstable for the reaction-diffusion system (2.14).

iii) For $\tilde{X}(x,t) = X^{(d)}$ the real part of each eigenvalue $\mu_i^{(d)}(\lambda_k), i = 1, \ldots, 4$, of the matrix $M(\lambda_k)$ is negative, cf. Figure 2.4, and the maxima are reached for λ_0

$$\max_{k\in\mathbb{N}_0}(\mathrm{Re}(\mu_1^{(d)}(\lambda_k))) \approx -0.0028, \quad \max_{k\in\mathbb{N}_0}(\mathrm{Re}(\mu_2^{(d)}(\lambda_k))) \approx -0.0028,$$
$$\max_{k\in\mathbb{N}_0}(\mathrm{Re}(\mu_3^{(d)}(\lambda_k))) \approx -0.0184, \quad \max_{k\in\mathbb{N}_0}(\mathrm{Re}(\mu_4^{(d)}(\lambda_k))) \approx -0.0675.$$

Hence, the solution $z(x,t) = 0$ is asymptotically stable for the linearized system (2.37) and the stability of $\tilde{X}(x,t) = X^{(d)}$ for the reaction-diffusion system (2.14) follows from Theorem 2.4.

Again, we observe the same stability properties for the exponents $n = 2$ and $n = 3$. The maxima of the eigenvalues of $M(\lambda_k)$ are reached for $\lambda_0 = 0$, i.e. for the mode $k = 0$, just the same as in case $n = 2.5$. Therefore, the maxima of the eigenvalues

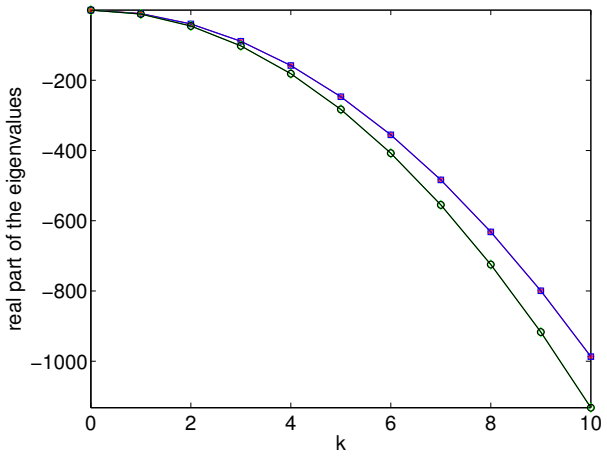

Figure 2.4: Eigenvalues of the matrix $M(\lambda_k)$ for $X^{(d)}$ depending on the mode k.

coincides with the eigenvalues of the Jacobian matrix $J|_{X^*}$ evaluated at the steady state $X^* \in \{X^{(l)}, X^{(d)}, X^{(u)}\}$ given by (2.34) and (2.35) since the Jacobian matrix $J|_{X^*}$ of f evaluated at $X^* \in \{X^{(l)}, X^{(d)}, X^{(u)}\}$ agrees with the Jacobian matrix $\tilde{A}$ of $\tilde{f}$ evaluated at $z = 0$. Hence, $X^{(l)}$ and $X^{(d)}$ are spatially homogeneous, asymptotically stable, stationary solutions of the reaction-diffusion system (2.14).

As mentioned above, the stability analysis is more complicated for the dimensions $d = 2$ and $d = 3$, since the computation of the eigenvalues of the Laplace operator on a union circle and a union ball, respectively, with homogeneous Neumann boundary conditions is more complex than in the one-dimensional case. For simplicity, we now restrict the stability analysis to the case $n = 2.5$ and assume that the stability behavior can be transferred to other values of n.

It is well-known that the Laplace operator is self-adjoint and possesses a point spectrum denoted again with $\lambda_k, k \in \mathbb{N}_0$. Obviously, $\lambda_0 = 0$ is an eigenvalue to the eigenfunction $\varphi_0 = const.$ independent of the domain $\tilde{\Omega}$ and the dimension d. Besides, the eigenvalues $\lambda_k, k \in \mathbb{N}$, are positive since

$$\lambda_k \underbrace{\int_{\tilde{\Omega}} \varphi_k^2 \mathrm{d}x}_{>0} = -\int_{\tilde{\Omega}} \Delta\varphi_k \cdot \varphi_k \mathrm{d}x = \underbrace{\int_{\tilde{\Omega}} \nabla\varphi_k \cdot \nabla\varphi_k \mathrm{d}x}_{>0 \text{ for } k>0} + \underbrace{\int_{\tilde{\Omega}} \nabla\varphi_k \cdot \mathbf{n} \mathrm{d}s}_{=0} > 0.$$

In [48], L. Payne and H. Weinberger proved an estimation for the first non-zero eigenvalue of the Laplace operator on convex domains $\tilde{\Omega} \subset \mathbb{R}^d$ with homogeneous Neumann boundary conditions, namely

$$\lambda_1(\tilde{\Omega}) \geq \left(\frac{\pi}{\mathrm{diam}}\right)^2, \tag{2.40}$$

where diam denotes the diameter of the convex domain $\tilde{\Omega}$. In particular, for the union circle and the union ball, respectively, we obtain $\lambda_1(\Omega) \geq \pi^2/4$. But for the stability analysis of the spatially homogeneous, stationary solutions of the reaction-diffusion system, the estimation (2.40) is useless since the assembling of the matrix $M(\lambda_k) = \tilde{A} - \lambda_k \tilde{D}$ requires "exact" values for the eigenvalues $\lambda_k, k \in \mathbb{N}_0$.

For $d = 2$, the transformation of the Laplace operator to polar coordinates leads to a Bessel differential equation and the eigenvalues of the Laplace operator are given by the zeros of the first derivative of the Bessel functions [28, Proposition 1.2.14]

$$\lambda_{\nu,\iota} = j_{\nu,\iota}^2,\ \nu \in \mathbb{N}_0, \iota \in \mathbb{N}, \tag{2.41}$$

where the eigenvalues for $\nu > 0$ are double. Here, $j_{\nu,\iota}$ denotes the ιth zero of the first derivative of the Bessel function J_ν. The derivation of the Bessel differential equation is performed in Appendix A.2. The zeros $j_{\nu,\iota}$ of the first derivative of the Bessel functions are computed numerically with the Matlab routine *BessDerivZerosBisect2* [1] and are listed in Table 2.1. With the zeros of the Bessel functions' first derivative at hand, we determine

$\nu \setminus \iota$	1	2	3	4	5	6	7	8	9	10
0	0	3.83	7.02	10.17	13.32	16.47	19.62	22.76	25.90	29.05
1	1.84	5.33	8.54	11.71	14.86	18.02	21.16	24.31	27.46	30.60
2	3.05	6.71	9.97	13.17	16.35	19.51	22.67	25.83	28.98	32.13
3	4.20	8.02	11.35	14.59	17.79	20.97	24.14	27.31	30.47	33.63
4	5.31	9.28	12.68	15.96	19.20	22.40	25.59	28.77	31.94	35.10
5	6.42	10.52	13.99	17.31	20.58	23.80	27.01	30.20	33.39	36.56
6	7.50	11.73	15.27	18.64	21.93	25.18	28.41	31.62	34.81	38,00
7	8.58	12.93	16.53	19.94	23.27	26.55	29.79	33.02	36.22	39.42
8	9.65	14.12	17.77	21.23	24.59	27.89	31.16	34.40	37.62	40.83
9	10.71	15.29	19.00	22.50	25.89	29.22	32.51	35.76	39.00	42.22
10	11.77	16.45	20.22	23.76	27.18	30.53	33.84	37.12	40.37	43.61

Table 2.1: The entries $j_{\nu,\iota}$ of the table show the ιth zero of the first derivative of the Bessel function J_ν. The values are rounded to two decimal places.

the eigenvalues of the Laplace operator according to (2.41). Finally, we compute the eigenvalues $\mu_i^{(l,d,u)}(\lambda_{\nu,\iota}), i = 1, \ldots, 4$, of the matrix $M(\lambda_{\nu,\iota}) = \tilde{A} - \lambda_{\nu,\iota}\tilde{D}$. For this, we restrict the computation to the first ten Bessel functions and the first ten zeros of the first derivative of the respective Bessel function. Again, we consider the three steady states $X^{(l,d,u)}$ and state the maximum of the eigenvalues.

[1] downloaded on 04/04/2012 from http://www.mathworks.com/matlabcentral/fileexchange/28001-bessel-derivative-zeros&watching=28001

i) For $\tilde{X}(x,t) = X^{(l)}$, the real part of each eigenvalue $\mu_i^{(l)}(\lambda_{\nu,\iota}), i = 1,\dots,4$, of the matrix $M(\lambda_{\nu,\iota})$ is negative and the maxima are given by

$$\max_{\nu\in\mathbb{N}_0,\iota\in\mathbb{N}}(\mathrm{Re}(\mu_1^{(l)}(\lambda_{\nu,\iota}))) \approx -0.0028, \max_{\nu\in\mathbb{N}_0,\iota\in\mathbb{N}}(\mathrm{Re}(\mu_2^{(l)}(\lambda_{\nu,\iota}))) \approx -0.0028,$$
$$\max_{\nu\in\mathbb{N}_0,\iota\in\mathbb{N}}(\mathrm{Re}(\mu_3^{(l)}(\lambda_{\nu,\iota}))) \approx -0.0028, \max_{\nu\in\mathbb{N}_0,\iota\in\mathbb{N}}(\mathrm{Re}(\mu_4^{(l)}(\lambda_{\nu,\iota}))) \approx -0.0028.$$

The real parts of the eigenvalues $\mu_i^{(l)}(\lambda_{\nu,\iota}), i = 1,\dots,4$, in dependence of ν and ι are illustrated in Figure 2.5. Again, the maxima are reached for $\lambda_{0,1} = 0$, thus,

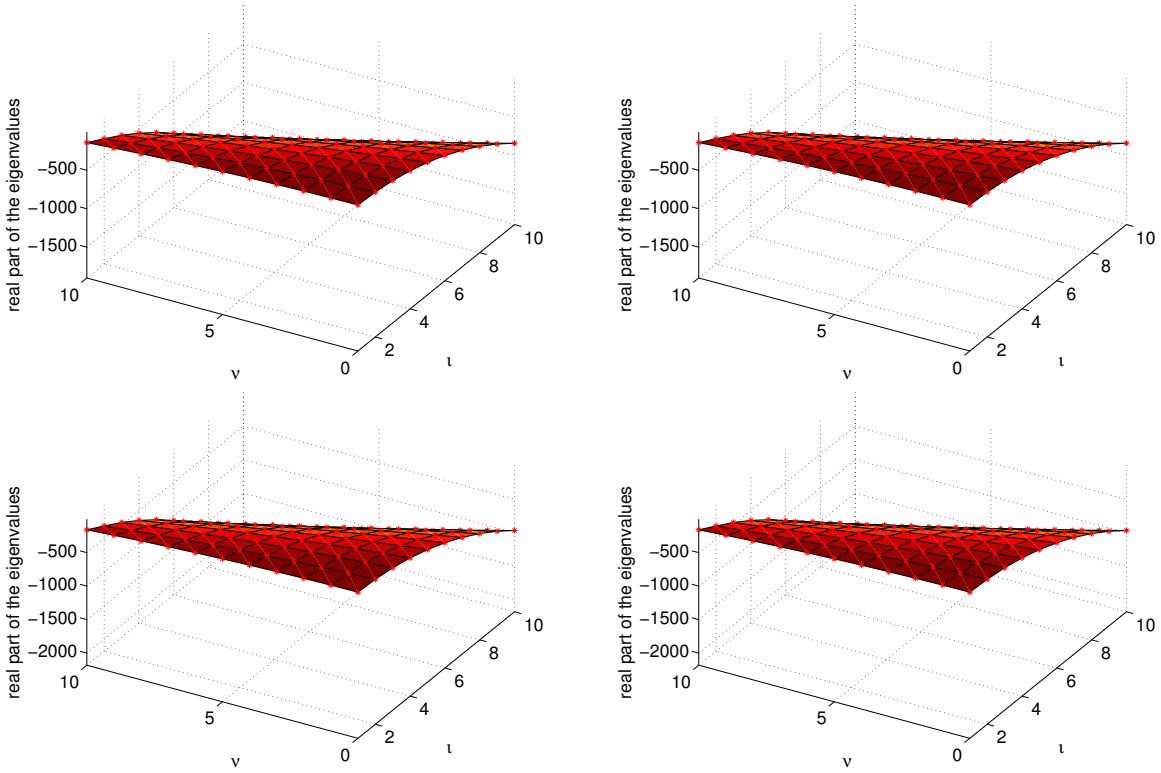

Figure 2.5: The real part of the eigenvalues $\mu_i(\lambda_{\nu,\iota}), i = 1,\dots,4$, of the matrix $M(\lambda_{\nu,\iota})$ for $\nu = 0,\dots,10$ and $\iota = 1,\dots,10$ for $X^{(l)}$. As in the one-dimensional case the matrix $M(\lambda_{\nu,\iota})$ possesses a discrete spectrum illustrated by the red asterisks. The continuous plot only serves for the illustration of the progression of the eigenvalues. The maximum is reached for $\nu = 0$ and $\iota = 1$, i.e. in the dark red vertices. Since we choose for the vertical axis the range $[\min_{\nu\in\mathbb{N}_0,\iota\in\mathbb{N}}(\mathrm{Re}(\mu_i(\lambda_{\nu,\iota}))), \max_{\nu\in\mathbb{N}_0,\iota\in\mathbb{N}}(\mathrm{Re}(\mu_i(\lambda_{\nu,\iota})))]$, we see that the real part of the eigenvalues are negative.

the asymptotic stability of the solution $z(x,t) = 0$ of the linearized system (2.37) is directly inherited from the asymptotic stability of the steady state $X^{(l)}$ of the reaction system. Finally, $\tilde{X}(x,t) = X^{(l)}$ is asymptotically stable for the reaction-diffusion system (2.14) according to Theorem 2.4.

ii) For $\tilde{X}(x,t) = X^{(u)}$, the real part of one of the eigenvalues $\mu_i^{(u)}(\lambda_{\nu,\iota}), i = 1,\dots,4$, of the matrix $M(\lambda_{\nu,\iota})$ becomes positive, see Figure 2.6. The maxima of the real part

are

$$\max_{\nu\in\mathbb{N}_0,\iota\in\mathbb{N}}(\mathrm{Re}(\mu_1^{(u)}(\lambda_{\nu,\iota}))) \approx -0.0028, \max_{\nu\in\mathbb{N}_0,\iota\in\mathbb{N}}(\mathrm{Re}(\mu_2^{(u)}(\lambda_{\nu,\iota}))) \approx -0.0028,$$
$$\max_{\nu\in\mathbb{N}_0,\iota\in\mathbb{N}}(\mathrm{Re}(\mu_3^{(u)}(\lambda_{\nu,\iota}))) \approx +0.0015, \max_{\nu\in\mathbb{N}_0,\iota\in\mathbb{N}}(\mathrm{Re}(\mu_4^{(u)}(\lambda_{\nu,\iota}))) \approx -0.0072.$$

Like in case $d = 1$, the real part of one eigenvalue is positive for $\lambda_{0,1}$ and the solution

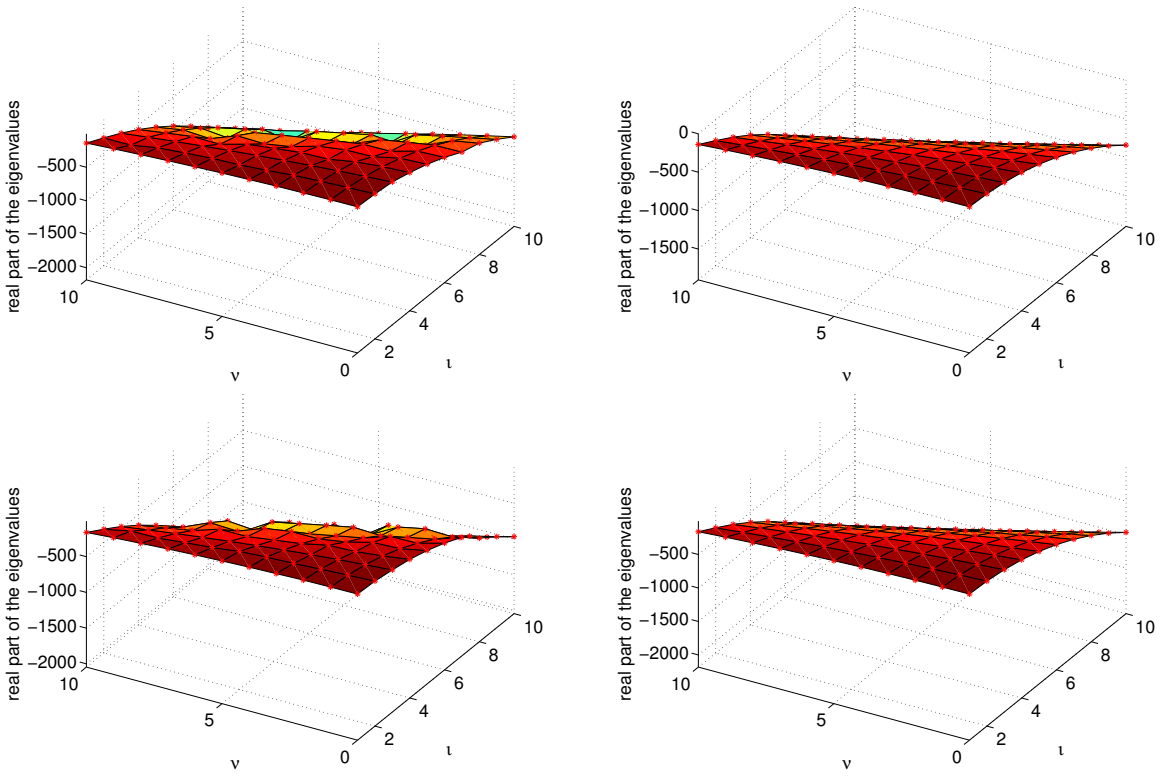

Figure 2.6: The real part of the eigenvalues $\mu_i(\lambda_{\nu,\iota}), i = 1,\dots,4$, of the matrix $M(\lambda_{\nu,\iota})$ for $\nu = 0,\dots,10$ and $\iota = 1,\dots,10$ for the transition state $X^{(u)}$. Again, we choose for the vertical axis the range $[\min_{\nu\in\mathbb{N}_0,\iota\in\mathbb{N}}(\mathrm{Re}(\mu_i(\lambda_{\nu,\iota}))), \max_{\nu\in\mathbb{N}_0,\iota\in\mathbb{N}}(\mathrm{Re}(\mu_i(\lambda_{\nu,\iota})))]$ and observe that the real part of the eigenvalue $\mu_i(\lambda_{0,1})$ is at least nonnegative (right top panel).

$z(x,t) = 0$ of the linearized system (2.37) is unstable. And therefore, $\tilde{X}(x,t) = X^{(u)}$ is unstable for the reaction-diffusion system (2.14).

iii) For $\tilde{X}(x,t) = X^{(d)}$, the real part of the eigenvalues $\mu_i^{(d)}(\lambda_{\nu,\iota}), i = 1,\dots,4$, of the matrix $M(\lambda_{\nu,\iota})$ is negative, see Figure 2.7. The maxima of the real part are

$$\max_{\nu\in\mathbb{N}_0,\iota\in\mathbb{N}}(\mathrm{Re}(\mu_1^{(d)}(\lambda_{\nu,\iota}))) \approx -0.0028, \max_{\nu\in\mathbb{N}_0,\iota\in\mathbb{N}}(\mathrm{Re}(\mu_2^{(d)}(\lambda_{\nu,\iota}))) \approx -0.0028,$$
$$\max_{\nu\in\mathbb{N}_0,\iota\in\mathbb{N}}(\mathrm{Re}(\mu_3^{(d)}(\lambda_{\nu,\iota}))) \approx -0.0184, \max_{\nu\in\mathbb{N}_0,\iota\in\mathbb{N}}(\mathrm{Re}(\mu_4^{(d)}(\lambda_{\nu,\iota}))) \approx -0.0675.$$

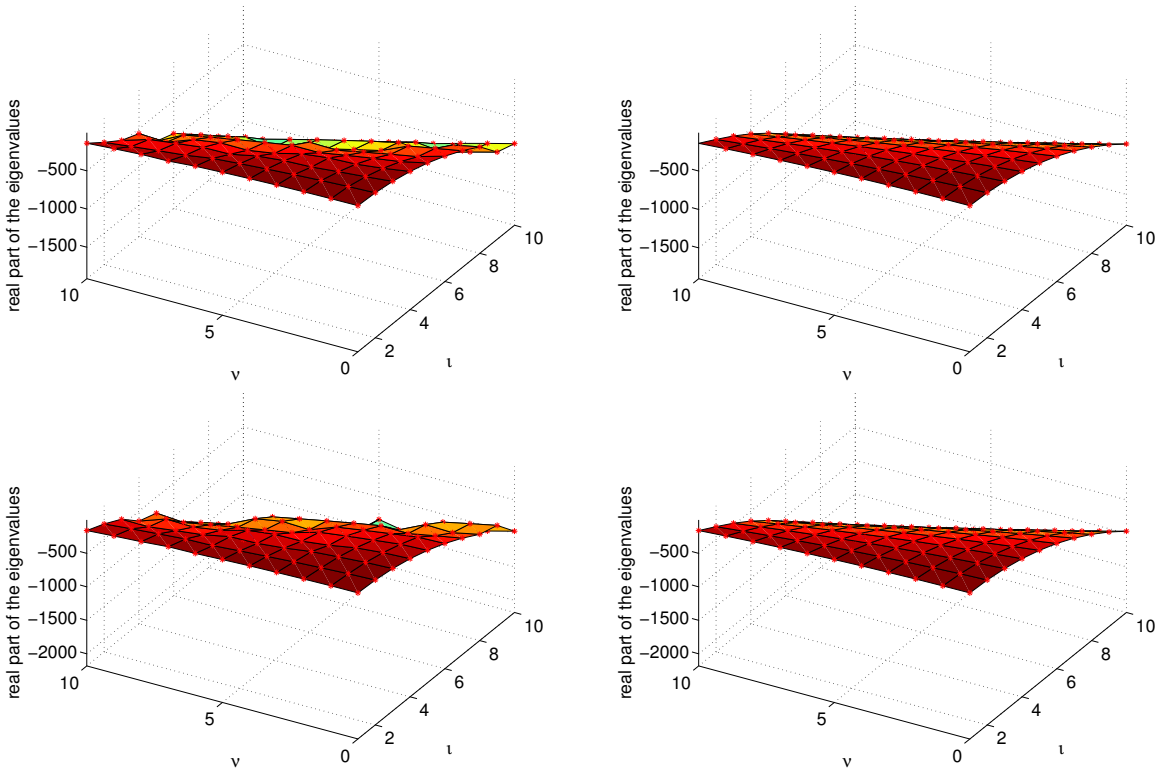

Figure 2.7: The real part of the eigenvalues $\mu_i(\lambda_{\nu,\iota}), i = 1, \ldots, 4$, of the matrix $M(\lambda_{\nu,\iota})$ for $\nu = 0, \ldots, 10$ and $\iota = 1, \ldots, 10$ for the death state $X^{(d)}$.

In the end, in case of the death state, the real part of all eigenvalues are negative and the solution $z(x,t) = 0$ of the linearized system (2.37) is asymptotically stable. Finally, Theorem 2.4 yields the asymptotic stability of the solution $\tilde{X}(x,t) = X^{(l)}$ of the reaction-diffusion system (2.14).

We conclude this section with some remarks on the stability of the spatially homogeneous, stationary solutions for $d = 3$. Obviously, $\lambda_0 = 0$ is an eigenvalue of the Laplace operator on the domain Ω with homogeneous Neumann boundary conditions. Thus, the eigenvalues of the matrix $M(\lambda_0) = \tilde{A} - \lambda_0 \tilde{D}$ coincide with the eigenvalues of the Jacobi matrix $\tilde{A}$ for $\lambda_0 = 0$. Furthermore, we mentioned that the Jacobi matrix $\tilde{A}$ of the linearization of $\tilde{f}$ with respect to $z \equiv 0$ agrees with the Jacobi matrix $J|_{X^*}$ evaluated at the corresponding steady state X^*. Since the real part of one eigenvalue of the Jacobian matrix $J|_{X^{(u)}}$ is positive, the real part of one eigenvalue of $M(\lambda_0)$ is positive as well. Thus, $\tilde{X}(x,t) = X^{(u)}$ is unstable for the reaction-diffusion system (2.14) for $d = 3$. For the two stable steady states $X^{(l,d)}$, the asymptotic stability of the steady states of the reaction system (2.2) is transferred to the asymptotic stability of the spatially homogeneous, stationary solution $\tilde{X}(x,t) = X^{(l,d)}$ of the reaction-diffusion system (2.14). The eigenvalue λ_0 yields for the matrix $M(\lambda_0)$ eigenvalues with a negative real part and the first nonzero eigenvalue λ_1 can be estimated according to (2.40). Thus, we suggest that the eigenvalues of the matrix $M(\lambda_k)$ for $d = 3$ show a similar behavior as in case

$d = 2$ illustrated in Figure 2.7 and Figure 2.5, respectively.

Before we solve the reaction-diffusion system numerically for several initial conditions in order to find out which of the two asymptotically stable, stationary solutions is approached, we first study the existence of a solution of the reaction-diffusion system (2.14).

2.6 Local Existence and Uniqueness of a Solution of the Reaction-Diffusion System

After studying the stability of the stationary solutions of the reaction-diffusion system (2.14), we take a closer look at the existence of a solution and its uniqueness. Since reaction-diffusion systems have been studied for several decades, adequate theoretical results can be found in literature. In the following, we briefly recall the results of H. Amann [1]. Before we state the main theorem that ensures the local existence and uniqueness of a solution, we first introduce the notations used in [1]. Let Ω be a bounded smooth domain in $\mathbb{R}^d$ and $u : \Omega \times \mathbb{R}_+ \to \mathbb{R}^N$. Further, let $\mathcal{A}$ be a general elliptic differential operator

$$\mathcal{A}(u)[u] := \partial_j(a_{jk}(\,\cdot\,, u)\partial_k u), \tag{2.42}$$

and $\mathcal{B}$ a boundary value operator in the general form

$$\mathcal{B}(u)[u] := \delta(a_{jk}(\,\cdot\,, u)n^j\partial_k u + b_0(\,\cdot\,, u)u) + (1-\delta)u = 0 \text{ on } \partial\Omega \times (0,\infty) \tag{2.43}$$

with $\delta = \operatorname{diag}(\delta^1, \ldots, \delta^N), \delta^r \in C(\partial\Omega, \{0,1\}), r = 1, \ldots, N$, and n^j denotes the jth component of the outer normal vector n. That means the different components of u may fulfill different types of boundary conditions. In the notations in (2.42) and (2.43), the indices j and k each run from 1 to d. Furthermore, $\mathcal{G}$ denotes an open subset of $\mathbb{R}^N$ and we assume that the function $f(x, u, \nabla u)$ satisfies

$$f \in C^\infty(\Omega \times \mathcal{G} \times \mathbb{R}^{dN}, \mathbb{R}^N)$$

besides some additional conditions on the gradient dependency of the function f, cf. [1]. Finally, we introduce the Sobolev space $H^{1,p}(\Omega, \mathbb{R}^N), p \in (d, \infty)$, and the open subset $\mathcal{V}$ of $H^{1,p}(\Omega, \mathbb{R}^N)$

$$\mathcal{V} := \{u \in H^{1,p}(\Omega, \mathbb{R}^N), u(\Omega) \subset \mathcal{G}\}.$$

With these notations, we have the following

Theorem 2.5 (p. 17 in [1]).
Given any $u_0 \in \mathcal{V}$, there exists a unique solution

$$u \in C([0, T(u_0)), \mathcal{V}) \cap C^\infty(\Omega \times (0, T(u_0)), \mathbb{R}^N)$$

of

$$\begin{aligned} \partial_t u + \mathcal{A}(u)[u] &= f(x, u, \nabla u) && \text{in } \Omega \times (0, \infty), \\ \mathcal{B}(u)[u] &= 0 && \text{on } \partial\Omega \times (0, \infty), \\ u(x, 0) &= u_0 && \text{on } \Omega, \end{aligned} \tag{2.44}$$

where $0 < T(u_0) \leq \infty$ and the operators $\mathcal{A}$ and $\mathcal{B}$ are given in (2.42) *and* (2.43).

The proof of Theorem 2.5 is given in [1]. Obviously, the reaction-diffusion system (2.14) with homogeneous Neumann boundary conditions is a special case of the system (2.44) in Theorem 2.5 and thus, we directly conclude the following

Theorem 2.6.
There exist a unique solution

$$u \in C([0, T(u_0)), \mathcal{V}) \cap C^\infty(\Omega \times (0, T(u_0)), \mathbb{R}^4)$$

of the reaction-diffusion system (2.12)-(2.14) *for a given $u_0 \in \mathcal{V}$ with $0 < T(u_0) \leq \infty$.*

Besides the existence of a unique solution of the reaction-diffusion system (2.14) with homogeneous Neumann boundary conditions, we even obtain a statement concerning the regularity of the solution, namely $u \in C^\infty(\Omega \times (0, T(u_0)), \mathbb{R}^4)$. In the subsequent section, we study the boundedness of the solution in the L^∞-norm. For this purpose, we construct a bounded invariant region, which is also required for the numerical analysis in Section 2.8.

2.7 Invariant Region for the Reaction-Diffusion System

Before we solve the reaction-diffusion system (2.14) numerically, we first check the boundedness of the solution in the L^∞-norm. For this purpose, we show in the following the existence of an invariant region and state it explicitly.

In order to apply the theory of invariant regions established in [57, Chapter 14.§B], we restrict ourselves to the one-dimensional case, i.e. $\Omega = [-1, 1]$, and the Laplace operator

is replaced by the second derivative $\frac{\partial^2}{\partial x^2}$. Thus, the reaction-diffusion system is written as

$$\begin{aligned}
\tfrac{\partial X_a}{\partial t} &= \tilde{D}_1 \tfrac{\partial^2 X_a}{\partial x^2} + \tilde{k}_{c1} X_i Y_a - \tilde{k}_{d1} X_a, \\
\tfrac{\partial Y_a}{\partial t} &= \tilde{D}_2 \tfrac{\partial^2 Y_a}{\partial x^2} + \tilde{k}_{c2} Y_i X_a^n - \tilde{k}_{d2} Y_a, \\
\tfrac{\partial X_i}{\partial t} &= \tilde{D}_3 \tfrac{\partial^2 X_i}{\partial x^2} - \tilde{k}_{c1} X_i Y_a - \tilde{k}_{d3} X_i + \tilde{k}_{p1}, \\
\tfrac{\partial Y_i}{\partial t} &= \tilde{D}_4 \tfrac{\partial^2 Y_i}{\partial x^2} - \tilde{k}_{c2} Y_i X_a^n - \tilde{k}_{d4} Y_i + \tilde{k}_{p2},
\end{aligned} \tag{2.45}$$

with the boundary conditions

$$\left.\frac{\partial X_a}{\partial x}\right|_{|x|=1} = \left.\frac{\partial Y_a}{\partial x}\right|_{|x|=1} = \left.\frac{\partial X_i}{\partial x}\right|_{|x|=1} = \left.\frac{\partial Y_i}{\partial x}\right|_{|x|=1} = 0 \tag{2.46}$$

and the initial condition

$$(X_a, Y_a, X_i, Y_i)(x, 0) = (X_{a,0}, Y_{a,0}, X_{i,0}, Y_{i,0}), \quad x \in \Omega. \tag{2.47}$$

Again, the reaction, degradation and production terms of (2.45) are summarized in the vector-valued function f, namely

$$f(X_a, Y_a, X_i, Y_i) = \begin{pmatrix} \tilde{k}_{c1} X_i Y_a - \tilde{k}_{d1} X_a \\ \tilde{k}_{c2} Y_i X_a^n - \tilde{k}_{d2} Y_a \\ -\tilde{k}_{c1} X_i Y_a - \tilde{k}_{d3} X_i + \tilde{k}_{p1} \\ -\tilde{k}_{c2} Y_i X_a^n - \tilde{k}_{d4} Y_i + \tilde{k}_{p2} \end{pmatrix}. \tag{2.48}$$

First of all, we state the definition of an invariant region for reaction-diffusion systems.

Definition 2.7. [57, Definition 14.5] A closed subset $\Sigma \subset \mathbb{R}^4$ is called a (positively) invariant region for the initial value problem (2.45), (2.47), if any solution $(X_a, Y_a, X_i, Y_i)(x, t)$ with initial values in Σ satisfies $(X_a, Y_a, X_i, Y_i)(x, t) \in \Sigma$ for all $x \in \Omega$ and for all $t \in [0, T)$.

According to [57, Corollary 14.8], a rectangular domain of the form

$$\begin{aligned}
\Sigma_R = \{(X_a, Y_a, X_i, Y_i) \in \mathbb{R}^4, & 0 \le X_a \le a, 0 \le Y_a \le b, \\
& 0 \le X_i \le c, 0 \le Y_i \le d\}
\end{aligned} \tag{2.49}$$

would be preferred for an invariant region for the reaction-diffusion system (2.45), since the diffusion matrix $\tilde{D}$ is diagonal. We show in Appendix A.3 that the domain Σ_R is unsuitable for the reaction-diffusion system (2.45) although the diffusion matrix is diagonal. Instead

of that, a suitable choice is

$$\Sigma := \{(X_a, Y_a, X_i, Y_i) \in \mathbb{R}^4,\ 0 \le X_i \le \frac{\tilde{k}_{p1}}{\tilde{k}_{d3}}, 0 \le X_a \le \frac{1}{m_x}(\frac{\tilde{k}_{p1}}{\tilde{k}_{d3}} - X_i), \\ 0 \le Y_i \le \frac{\tilde{k}_{p2}}{\tilde{k}_{d4}}, 0 \le Y_a \le \frac{1}{m_y}(\frac{\tilde{k}_{p2}}{\tilde{k}_{d4}} - Y_i)\} \tag{2.50}$$

with $1 \le m_x \le \tilde{k}_{d1}/\tilde{k}_{d3}$ and $1 \le m_y \le \tilde{k}_{d2}/\tilde{k}_{d4}$. Obviously, the concentrations Y_i of pro-caspase 3 and X_i of pro-caspase 8 are bounded from above by the concentration of the life state and from below by zero. The concentrations Y_a of caspase 3 and X_a of caspase 8 possess the same lower bound but the upper bound depends on the concentration of the corresponding pro-caspase. We have the following

Theorem 2.8.
Let $\tilde{k}_{d1} \ge \tilde{k}_{d3}$, $\tilde{k}_{d2} \ge \tilde{k}_{d4}$ and $\tilde{D} = \mathrm{diag}(\tilde{D}_1, \tilde{D}_2, \tilde{D}_1, \tilde{D}_2)$ with $\tilde{D}_3 = \tilde{D}_1, \tilde{D}_4 = \tilde{D}_2$. Then, the region Σ defined in (2.50) *is invariant for the reaction-diffusion system* (2.45)-(2.47).

In order to prove Theorem 2.8, we transfer the notation of the invariant region (2.50) to an abstract level to simplify the arguments and apply the general theory of invariant regions. Obviously, Σ defined by (2.50) can be written as

$$\Sigma = \cap_{i=1}^{8} \{(X_a, Y_a, X_i, Y_i) \in \mathbb{R}^4, G_i(X_a, Y_a, X_i, Y_i) \le 0\}, \tag{2.51}$$

where the functions $G_i, i = 1, \ldots, 8$, are given by

$$G_1 = -X_i, \tag{2.52}$$
$$G_2 = -Y_i, \tag{2.53}$$
$$G_3 = X_i - \frac{\tilde{k}_{p1}}{\tilde{k}_{d3}}, \tag{2.54}$$
$$G_4 = Y_i - \frac{\tilde{k}_{p2}}{\tilde{k}_{d4}}, \tag{2.55}$$
$$G_5 = -X_a, \tag{2.56}$$
$$G_6 = X_a - \frac{1}{m_x}(\frac{\tilde{k}_{p1}}{\tilde{k}_{d3}} - X_i), \tag{2.57}$$
$$G_7 = -Y_a, \tag{2.58}$$
$$G_8 = Y_a - \frac{1}{m_y}(\frac{\tilde{k}_{p2}}{\tilde{k}_{d4}} - Y_i). \tag{2.59}$$

With the notation of Σ stated in (2.51), we cite the following

Theorem 2.9 (Theorem 14.14 in [57]).
Let Σ defined by (2.51) *and consider system* (2.45) *with $\tilde{D}$ positive definite. Suppose*

that this system is f-stable. Then Σ is a positively invariant region for (2.45) *if and only if the following holds at each boundary point $(X_a^0, Y_a^0, X_i^0, Y_i^0)$ of Σ, i.e. $G_i((X_a^0, Y_a^0, X_i^0, Y_i^0)) = 0$ for some i:*

i) ∇G_i *is a left eigenvector of* $\tilde{D}$ *for all* $x \in \Omega$.

ii) G_i *is quasi-convex at* $(X_a^0, Y_a^0, X_i^0, Y_i^0)$.

iii) $\nabla G_i \cdot f(X_a, Y_a, X_i, Y_i) \leq 0$ *at* $(X_a^0, Y_a^0, X_i^0, Y_i^0)$,

where the function $f(X_a, Y_a, X_i, Y_i)$ is given in (2.48).

Before we prove Theorem 2.8 by applying Theorem 2.9, we first recall Gronwall's inequality in the form given in [16, p. 624].

Lemma 2.10 (Gronwall's inequality (differential form)).
Let η be a nonnegative, absolutely continuous function on $[0, T]$ which satisfies for a.e. t the differential inequality

$$\eta'(t) \leq \gamma(t)\eta(t) + \psi(t),$$

where $\gamma(t)$ and $\psi(t)$ are non-negative, summable functions on $[0, T]$. Then

$$\eta(t) \leq e^{\int_0^t \gamma(s)ds} \left[\eta(0) + \int_0^t \psi(s)ds \right]$$

for all $0 \leq t \leq T$.

This inequality is proven in [16].
In order to prove Theorem 2.8, we have to check whether the assumptions of Theorem 2.9 are satisfied. Then, we directly conclude that Σ is an invariant region for the reaction-diffusion system (2.45).

Proof of Theorem 2.8. To prove that Σ is invariant for the reaction-diffusion system (2.45) we have to check the conditions *i)*–*iii)* of Theorem 2.9 for the functions $G_i, i = 1, \ldots, 8$, defined in (2.52)–(2.59). However, condition *iii)* is weakened due to the f-stability of the reaction-diffusion system, i.e., the strict negativity of the scalar product of ∇G_i and f in [57, Theorem 14.11] is replaced by the condition that the respective scalar product in Theorem 2.9 is less than or equal to zero.

1) **f-stable**
   According to [57, Definition 14.10], system (2.45) is called f-stable if whenever f is the limit of functions f_n in the C^1-topology on compacta, then the solution of

the initial value problem (2.45), (2.47) is the limit in the compact-open topology of solutions of the initial value problem (2.45), (2.47) where f is replaced by f_n. We denote with u the solution of (2.45) and with u_n the solution of (2.45) with f_n instead of f, that means

$$\frac{\partial u}{\partial t} = \tilde{D}\frac{\partial^2 u}{\partial x^2} + f(u), \tag{2.60}$$

$$\frac{\partial u_n}{\partial t} = \tilde{D}\frac{\partial^2 u_n}{\partial x^2} + f_n(u_n). \tag{2.61}$$

Then, subtracting equation (2.61) from equation (2.60) yields

$$\frac{\partial (u-u_n)}{\partial t} = \tilde{D}\frac{\partial^2 (u-u_n)}{\partial x^2} + f(u) - f_n(u_n). \tag{2.62}$$

We introduce the notation $X = L^2(\Omega, \mathbb{R}^4)$ and make the ansatz

$$\begin{aligned}
\tfrac{\mathrm{d}}{\mathrm{d}t}\|u-u_n\|_X^2 &= \tfrac{\mathrm{d}}{\mathrm{d}t}\int_\Omega |u-u_n|^2 \mathrm{d}x \\
&= 2\langle u-u_n, \tfrac{\mathrm{d}}{\mathrm{d}t}(u-u_n)\rangle \\
&\overset{(2.62)}{=} 2\langle u-u_n, \tilde{D}\tfrac{\partial^2(u-u_n)}{\partial x^2} + f(u) - f_n(u_n)\rangle \\
&= 2\langle u-u_n, \tilde{D}\tfrac{\partial^2(u-u_n)}{\partial x^2}\rangle + 2\langle u-u_n, f(u)-f_n(u_n)\rangle
\end{aligned} \tag{2.63}$$

where $\langle \cdot, \cdot \rangle$ denotes the L^2-scalar product. Integration by parts yields with homogeneous Neumann boundary conditions

$$\begin{aligned}
\langle u-u_n, \tilde{D}\frac{\partial^2(u-u_n)}{\partial x^2}\rangle &= -\langle \frac{\partial(u-u_n)}{\partial x}, \tilde{D}\frac{\partial(u-u_n)}{\partial x}\rangle \\
&\leq -\tilde{d}|u-u_n|_{H^1(\Omega,\mathbb{R}^4)}
\end{aligned} \tag{2.64}$$

where $\tilde{d}$ denotes the smallest entry of the diagonal matrix $\tilde{D}$. If we put (2.64) into (2.63), we obtain

$$\begin{aligned}
\frac{\mathrm{d}}{\mathrm{d}t}\|u-u_n\|_X^2 \leq & -2\tilde{d}|u-u_n|_{H^1(\Omega,\mathbb{R}^4)} + 2\langle u-u_n, f(u)-f_n(u_n)\rangle \\
\leq & 2|\langle u-u_n, f(u)-f_n(u_n)\rangle|
\end{aligned}$$

$$\leq 2|\langle u-u_n, f(u)-f(u_n)\rangle| + 2|\langle u-u_n, f(u_n)-f_n(u_n)\rangle|$$

$$\leq 2\|u-u_n\|_X \cdot \|f(u)-f(u_n)\|_X +$$

$$+ 2|\langle u-u_n, f(u_n)-f_n(u_n)\rangle|$$

$$\leq 2\|u-u_n\|_X^2 \cdot \sup_{\rho\in[0,1]} \|\nabla f(u+\rho(u_n-u))\|_X +$$

$$+ 2|\langle u-u_n, \sup_{v_n}\|f_n(v_n)-f(v_n)\|_X\rangle|$$

$$\leq 2\|u-u_n\|_X^2 \cdot \sup_{\rho\in[0,1]} \|\nabla f(u+\rho(u_n-u))\|_X +$$

$$+ 2\sup_{v_n}\|f_n(v_n)-f(v_n)\|_X \cdot |\langle u-u_n, 1\rangle|$$

$$\leq 2\|u-u_n\|_X^2 \cdot \sup_{\rho\in[0,1]} \|\nabla f(u+\rho(u_n-u))\|_X +$$

$$+ \sup_{v_n}\|f_n(v_n)-f(v_n)\|_X \cdot (\|u-u_n\|_X^2 + \|1\|_X^2)$$

$$= \|u-u_n\|_X^2 (2 \sup_{\rho\in[0,1]} \|\nabla f(u+\rho(u_n-u))\|_X +$$

$$+ \sup_{v_n}\|f_n(v_n)-f(v_n)\|_X) + |\Omega|^2 \sup_{v_n}\|f_n(v_n)-f(v_n)\|_X.$$

Now, we apply Gronwall's inequality Lemma 2.10 for the function $\eta(t) = \|u-u_n\|_X^2$ and, with $u|_{t=0} = u_n|_{t=0}$, we get

$$\begin{aligned}\|u(t)-u_n(t)\|_X^2 \quad \leq \quad & \mathrm{e}^{\int_0^t 2\sup_{\rho\in[0,1]}\|\nabla f(u+\rho(u_n-u))\|_X + \sup_{v_n}\|f_n(v_n)-f(v_n)\|_X \mathrm{d}s} \times \\ & \times |\Omega|^2 \int_0^t \sup_{v_n}\|f_n(v_n)-f(v_n)\|_X \mathrm{d}s).\end{aligned}$$

Taking the supremum with respect to time, we have

$$\begin{aligned}
\sup_{t\in[0,T]} \|u(t)-u_n(t)\|_X^2 \leq & |\Omega|^2 \cdot \sup_{t\in[0,T]} \int_0^t \sup_{v_n} \|f_n(v_n)-f(v_n)\|_X \mathrm{d}s \times \\
& \times \sup_{t\in[0,T]} \mathrm{e}^{\int_0^t 2\sup_{\rho\in[0,1]}\|\nabla f(u+\rho(u_n-u))\|_X \mathrm{d}s} \times \\
& \times \sup_{t\in[0,T]} \mathrm{e}^{\int_0^t \sup_{v_n}\|f_n(v_n)-f(v_n)\|_X \mathrm{d}s} \\
\leq & |\Omega|^2 T \sup_{v_n} \|f_n(v_n)-f(v_n)\|_X \times \\
& \times \mathrm{e}^{T\cdot \sup_{v_n}\|f_n(v_n)-f(v_n)\|_X} \times \\
& \times \mathrm{e}^{2T\sup_{\rho\in[0,1]}\|\nabla f(u+\rho(u_n-u))\|_X} \\
\leq & |\Omega|^2 T \sup_{v_n} \|f_n(v_n)-f(v_n)\|_X \cdot \mathrm{e}^{2TC} \times \\
& \times \mathrm{e}^{T\sup_{v_n}\|f_n(v_n)-f(v_n)\|_X}.
\end{aligned}$$

Under the assumption that f_n converges to f in the C^1-topology, the limit $n \to \infty$ yields

$$\begin{aligned}
\lim_{n\to\infty} \sup_{t\in[0,T]} \|u(t)-u_n(t)\|_X^2 &\leq \tilde{C}(T) \lim_{n\to\infty} \sup_{v_n} \|f_n(v_n)-f(v_n)\|_X \times \\
&\quad \times \lim_{n\to\infty} \mathrm{e}^{T\cdot \sup_{v_n}\|f_n(v_n)-f(v_n)\|_X} \\
&= 0,
\end{aligned}$$

thus, the solution u_n of the reaction-diffusion system (2.45) with f_n instead of f converges to the solution u of the reaction-diffusion system (2.45) with the reaction kinetics f if the function f_n converges to f. Hence, the reaction-diffusion system (2.45) is f-stable.

2) **Condition** *i)*
The first condition *i)* provides for the gradient of the functions G_i to be a left eigenvector to the diffusion matrix $\tilde{D}$. Obviously, $\nabla G_i, i = 1, \dots, 8$, is either a multiple of a standard basis vector $e_1, \dots, e_4$ of $\mathbb{R}^4$ or one of the vectors $(1, 0, 1/m_x, 0)^\top = \nabla G_6$ and $(0, 1, 0, 1/m_y)^\top = \nabla G_8$. Of course, the standard basis vectors are left eigenvectors to the diffusion matrix and the vectors ∇G_6 and ∇G_8 are left eigenvalues due to the special choice $\tilde{D}_1 = \tilde{D}_3$ and $\tilde{D}_2 = \tilde{D}_4$.

3) **Condition** *ii)*
The second condition demands the quasi-convexity of the functions $G_i, i = 1, \dots, 8$, i.e., whenever $\nabla G_i \cdot \xi = 0$ then $\xi^\top \nabla^2 G_i \xi \geq 0$, cf. [57, Definition 14.6]. It is easy to see that the functions G_i are quasi-convex since they are linear and the second derivative of the functions $G_i, i = 1, \dots, 8$, vanishes identically. Therefore, the condition $\xi^\top \nabla^2 G_i \xi \geq 0$ is satisfied trivially for vectors ξ with $\nabla G_i \cdot \xi = 0, i = 1, \dots, 8$.

4) **Condition** *iii)*
Finally, to show that f points into Σ on $\partial\Sigma$, we check that $\nabla G_i \cdot f|_{G_i=0} \leq 0$ for $i = 1, \dots, 8$. Due to the f-stability of the reaction-diffusion system (2.45), we do not have to show that f points *strictly* into Σ on $\partial\Sigma$.
For the function $G_1 = -X_i$, the gradient is given by $\nabla G_1 = (0, 0, -1, 0)^\top$ and we obtain

$$\nabla G_1 \cdot f|_{G_1=0} = \tilde{k}_{c1} X_i Y_a + \tilde{k}_{d3} X_i - \tilde{k}_{p1}\Big|_{X_i=0} = -\tilde{k}_{p1} < 0.$$

Therefore, $X_i \geq 0$. Next, we consider the function $G_2 = -Y_i$ with the gradient $\nabla G_2 = (0, 0, 0, -1)^\top$. Similarly, we get

$$\nabla G_2 \cdot f|_{G_2=0} = \tilde{k}_{c2} Y_i X_a^n + \tilde{k}_{d4} Y_i - \tilde{k}_{p2}\Big|_{Y_i=0} = -\tilde{k}_{p2} < 0,$$

that implies $Y_i \geq 0$. For $G_3 = X_i - \frac{\tilde{k}_{p1}}{\tilde{k}_{d3}}$, the gradient is given by $\nabla G_3 = (0, 0, 1, 0)^\top$. Then, condition *iii)* for G_3 reads

$$\nabla G_3 \cdot f|_{G_3=0} = -\tilde{k}_{c1} X_i Y_a - \tilde{k}_{d3} X_i + \tilde{k}_{p1}\Big|_{X_i=\tilde{k}_{p1}/\tilde{k}_{d3}} = -\tilde{k}_{c1} \frac{\tilde{k}_{p1}}{\tilde{k}_{d3}} \cdot Y_a \leq 0,$$

and we get $X_i \leq \tilde{k}_{p1}/\tilde{k}_{d3}$. To complete the bounds for Y_i, we consider the function $G_4 = Y_i - \frac{\tilde{k}_{p2}}{\tilde{k}_{d4}}$ with the gradient $\nabla G_4 = (0, 0, 0, 1)^\top$. We obtain $Y_i \leq \tilde{k}_{p2}/\tilde{k}_{d4}$ since

$$\nabla G_4 \cdot f|_{G_4=0} = -\tilde{k}_{c2} Y_i X_a^n - \tilde{k}_{d4} Y_i + \tilde{k}_{p2}|_{Y_i=\tilde{k}_{p2}/\tilde{k}_{d4}} = -\tilde{k}_{c2} \frac{\tilde{k}_{p2}}{\tilde{k}_{d4}} \cdot X_a^n \leq 0.$$

The gradient of the function $G_5 = -X_a$ is given by $\nabla G_5 = (-1, 0, 0, 0)^\top$. Then, we get

$$\nabla G_5 \cdot f|_{G_5=0} = -\tilde{k}_{c1} X_i Y_a + \tilde{k}_{d1} X_a \Big|_{X_a=0} = -\tilde{k}_{c1} X_i Y_a \leq 0.$$

Thus, $X_a \geq 0$. The upper bound for X_a is described by the function $G_6 = X_a - \frac{1}{m_x}(\frac{\tilde{k}_{p1}}{\tilde{k}_{d3}} - X_i)$ with the gradient $\nabla G_6 = (1, 0, \frac{1}{m_x}, 0)^\top$. Now, the scalar product of the gradient and the function f reads

$$\begin{aligned}
\nabla G_6 \cdot f|_{G_6=0} &= \tilde{k}_{c1} X_i Y_a - \tilde{k}_{d1} X_a + \tfrac{1}{m_x}(-\tilde{k}_{c1} X_i Y_a - \tilde{k}_{d3} X_i + \tilde{k}_{p1}) \\
&= \tilde{k}_{c1} X_i Y_a (1 - \tfrac{1}{m_x}) - \tfrac{\tilde{k}_{d1}}{m_x}(\tfrac{\tilde{k}_{p1}}{\tilde{k}_{d3}} - X_i) - \tfrac{\tilde{k}_{d3}}{m_x} X_i + \tfrac{\tilde{k}_{p1}}{m_x} \\
&= \tilde{k}_{c1} X_i Y_a \underbrace{(1 - \frac{1}{m_x})}_{\leq 0} + \tfrac{1}{m_x} \underbrace{(\tilde{k}_{d1} - \tilde{k}_{d3})}_{\geq 0} \underbrace{(X_i - \frac{\tilde{k}_{p1}}{\tilde{k}_{d3}})}_{\leq 0} \\
&\leq 0.
\end{aligned}$$

It follows $X_a \leq \frac{1}{m_x}(\frac{\tilde{k}_{p1}}{\tilde{k}_{d3}} - X_i)$. The bounds for Y_a are on the one side given by the function $G_7 = -Y_a$ with the gradient $\nabla G_7 = (0, -1, 0, 0)^\top$. Then, condition *iii)* yields

$$\nabla G_7 \cdot f|_{G_7=0} = -\tilde{k}_{c2} Y_i X_a^n + \tilde{k}_{d2} Y_a \Big|_{Y_a=0} = -\tilde{k}_{c2} Y_i X_a^n \leq 0,$$

that implies $Y_a \geq 0$. On the other side, the function $G_8 = Y_a - \frac{1}{m_y}(\frac{\tilde{k}_{p2}}{\tilde{k}_{d4}} - Y_i)$ determines the upper bound for Y_a. With the gradient $\nabla G_8 = (0, 1, 0, \frac{1}{m_y})^\top$, we obtain

$$\begin{aligned}
\nabla G_8 \cdot f|_{G_8=0} &= \tilde{k}_{c2} Y_i X_a^n - \tilde{k}_{d2} Y_a + \tfrac{1}{m_y}(-\tilde{k}_{c2} Y_i X_a^n - \tilde{k}_{d4} Y_i + \tilde{k}_{p2}) \\
&= \tilde{k}_{c2} Y_i X_a^n (1 - \tfrac{1}{m_y}) - \tfrac{\tilde{k}_{d2}}{m_y}(\tfrac{\tilde{k}_{p2}}{\tilde{k}_{d4}} - Y_i) - \tfrac{\tilde{k}_{d4}}{m_y} Y_i + \tfrac{\tilde{k}_{p2}}{m_y} \\
&= \tilde{k}_{c2} Y_i X_a^n \underbrace{(1 - \frac{1}{m_y})}_{\leq 0} + \tfrac{1}{m_y} \underbrace{(\tilde{k}_{d2} - \tilde{k}_{d4})}_{\geq 0} \underbrace{(Y_i - \frac{\tilde{k}_{p2}}{\tilde{k}_{d4}})}_{\leq 0} \\
&\leq 0.
\end{aligned}$$

Finally, the estimate $Y_a \leq \frac{1}{m_y}(\frac{\tilde{k}_{p2}}{\tilde{k}_{d4}} - Y_i)$ holds. So, we showed that f points into Σ on $\partial\Sigma$.

In summary, we checked conditions *i)*–*iii)* of Theorem 2.9 for the region Σ and further confirmed the f-stability of the reaction-diffusion system. The positive definiteness of the diffusion matrix $\tilde{D}$ holds trivially and all assumptions of Theorem 2.9 are satisfied. Thus, Σ is invariant for the reaction-diffusion system (2.45) with $\tilde{D} = \mathrm{diag}(\tilde{D}_1, \tilde{D}_2, \tilde{D}_1, \tilde{D}_2)$ for

$\tilde{k}_{d1} \geq \tilde{k}_{d3}$ and $\tilde{k}_{d2} \geq \tilde{k}_{d4}$. □

Remark 2.11. In the proof of Theorem 2.8, the lower bound of the parameters m_x and m_y are revealed. Actually, the upper bounds for m_x and m_y do not play a role in the proof. Nevertheless, the values for m_x and m_y have to guarantee that the invariant region contains the death state $X^{(d)} = (X_a^{(d)}, Y_a^{(d)}, X_i^{(d)}, Y_i^{(d)})$. Thus, we ask for the conditions

$$(i) \quad X_a^{(d)} \leq \frac{1}{m_x}(\frac{\tilde{k}_{p1}}{\tilde{k}_{d3}} - X_i^{(d)}),$$
$$(ii) \quad Y_a^{(d)} \leq \frac{1}{m_y}(\frac{\tilde{k}_{p2}}{\tilde{k}_{d4}} - Y_i^{(d)}).$$

For (i), we obtain with (2.24)

$$m_x X_a^{(d)} \leq \frac{\tilde{k}_{p1}}{\tilde{k}_{d3}} - \frac{\tilde{k}_{p1}\tilde{k}_{d2}(\tilde{k}_{c2}(X_a^{(d)})^n + \tilde{k}_{d4})}{(\tilde{k}_{c1}\tilde{k}_{c2}\tilde{k}_{p2} + \tilde{k}_{c2}\tilde{k}_{d2}\tilde{k}_{d3})(X_a^{(d)})^n + \tilde{k}_{d2}\tilde{k}_{d3}\tilde{k}_{d4}}.$$

Multiplying by the denominator yields

$$\begin{aligned}
&m_x \left[(\tilde{k}_{c1}\tilde{k}_{c2}\tilde{k}_{p2} + \tilde{k}_{c2}\tilde{k}_{d2}\tilde{k}_{d3})(X_a^{(d)})^{n+1} + \tilde{k}_{d2}\tilde{k}_{d3}\tilde{k}_{d4}X_a^{(d)}\right] \\
&\leq \frac{\tilde{k}_{p1}}{\tilde{k}_{d3}}\left[(\tilde{k}_{c1}\tilde{k}_{c2}\tilde{k}_{p2} + \tilde{k}_{c2}\tilde{k}_{d2}\tilde{k}_{d3})(X_a^{(d)})^n + \tilde{k}_{d2}\tilde{k}_{d3}\tilde{k}_{d4}\right] - \tilde{k}_{p1}\tilde{k}_{d2}\tilde{k}_{c2}(X_a^{(d)})^n - \tilde{k}_{p1}\tilde{k}_{d2}\tilde{k}_{d4}) \\
&= \frac{\tilde{k}_{p1}}{\tilde{k}_{d3}}\tilde{k}_{c1}\tilde{k}_{c2}\tilde{k}_{p2}(X_a^{(d)})^n.
\end{aligned}$$

Since $X_a^{(d)}$ is a solution of equation (2.26), we obtain

$$m_x \left(\frac{\tilde{k}_{p1}}{\tilde{k}_{d1}}\tilde{k}_{c1}\tilde{k}_{c2}\tilde{k}_{p2}(X_a^{(d)})^n\right) \leq \frac{\tilde{k}_{p1}}{\tilde{k}_{d3}}\tilde{k}_{c1}\tilde{k}_{c2}\tilde{k}_{p2}(X_a^{(d)})^n,$$

which is equivalent to $m_x \leq \tilde{k}_{d1}/\tilde{k}_{d3}$.
For (ii), we have with (2.22) and (2.23)

$$m_y \cdot \frac{\tilde{k}_{p2}\tilde{k}_{c2}(X_a^{(d)})^n}{\tilde{k}_{d2}(\tilde{k}_{c2}(X_a^{(d)})^n + \tilde{k}_{d4})} \leq \frac{\tilde{k}_{p2}}{\tilde{k}_{d4}} - \frac{\tilde{k}_{p2}}{\tilde{k}_{c2}(X_a^{(d)})^n + \tilde{k}_{d4}}. \tag{2.65}$$

Again, multiplying (2.65) by the denominator on the right-hand side of (2.65) and simultaneously dividing (2.65) by $\tilde{k}_{p2}$ yields

$$m_y \frac{\tilde{k}_{c2}(X_a^{(d)})^n}{\tilde{k}_{d2}} \leq \frac{\tilde{k}_{c2}(X_a^{(d)})^n + \tilde{k}_{d4}}{\tilde{k}_{d4}} - 1,$$

which is equivalent to $m_y \leq \tilde{k}_{d2}/\tilde{k}_{d4}$.

Thus, we see that the parameters m_x and m_y have to be bounded from above dependent on the degradation rates $\tilde{k}_{di}, i = 1, \ldots, 4$.

Remark 2.12. In case $\tilde{D}_1 \neq \tilde{D}_3$, $\tilde{D}_2 \neq \tilde{D}_4$, condition i) in Theorem 2.9 is not satisfied and Theorem 2.9 can not be applied to prove that Σ is an invariant region for the reaction-diffusion system (2.45). Thus, the proof of the existence of an invariant region is more difficult in this case, and one has to pursue a totally different strategy.

Hence, we proved that if the solution $(X_a, Y_a, X_i, Y_i)(x, t)$ once resides in the region Σ, it remains in Σ for all time. Besides the boundedness of the solution of the reaction-diffusion system (2.45), we further obtain an important result for the numerical analysis, since the existence of an invariant region belongs to the conditions of a theorem in Section 2.8.

Remark 2.13. Concluding, we note that the conditions for the concentrations X_a, Y_a, X_i and Y_i, namely $X_a \geq 0$, $Y_a \geq 0$, $X_i \geq 0$ and $Y_i \geq 0$, are natural for the caspase concentrations due to the positivity of concentrations.

After analyzing the reaction-diffusion system (2.45) with respect to the existence and uniqueness of a solution and after determining an invariant region, we solve the reaction-diffusion system in case of radially symmetric concentration distributions numerically in the subsequent section.

2.8 Numerical Analysis of Spatial Inhibition Effects

With the steady states at hand, we come back to the initial value problem introduced in Section 2.3. For the numerical simulations, we simplify the model and restrict ourselves to radially symmetric caspase concentrations. So, the reaction-diffusion system (2.14) with d space dimensions and one time dimension is reduced to an effective model with one dimensionless spatial coordinate r and one time coordinate t. The Laplace operator Δ_x in polar coordinates is given by

$$\Delta_x w = \frac{1}{r^{d-1}} \frac{\partial}{\partial r} \left(r^{d-1} \frac{\partial w}{\partial r} \right) = \frac{\partial^2 w}{\partial r^2} + \frac{d-1}{r} \frac{\partial w}{\partial r}, \; w \in \{X_a, Y_a, X_i, Y_i\}, \tag{2.66}$$

$d = 1, 2, 3$. The reaction-diffusion system (2.14) reads now

$$\begin{aligned}
\tfrac{\partial X_a}{\partial t} &= \tilde{k}_{c1} X_i Y_a - \tilde{k}_{d1} X_a + \tilde{D}_1 \tfrac{1}{r^{d-1}} \tfrac{\partial}{\partial r} (r^{d-1} \tfrac{\partial X_a}{\partial r}), \\
\tfrac{\partial Y_a}{\partial t} &= \tilde{k}_{c2} Y_i X_a^n - \tilde{k}_{d2} Y_a + \tilde{D}_2 \tfrac{1}{r^{d-1}} \tfrac{\partial}{\partial r} (r^{d-1} \tfrac{\partial Y_a}{\partial r}), \\
\tfrac{\partial X_i}{\partial t} &= -\tilde{k}_{c1} X_i Y_a - \tilde{k}_{d3} X_i + \tilde{k}_{p1} + \tilde{D}_3 \tfrac{1}{r^{d-1}} \tfrac{\partial}{\partial r} (r^{d-1} \tfrac{\partial X_i}{\partial r}), \\
\tfrac{\partial Y_i}{\partial t} &= -\tilde{k}_{c2} Y_i X_a^n - \tilde{k}_{d4} Y_i + \tilde{k}_{p2} + \tilde{D}_4 \tfrac{1}{r^{d-1}} \tfrac{\partial}{\partial r} (r^{d-1} \tfrac{\partial Y_i}{\partial r}).
\end{aligned} \tag{2.67}$$

The radially symmetric reaction-diffusion system (2.67) is completed with homogeneous Neumann boundary conditions at the boundaries $r = 0$ and $r = 1$, thus

$$\left.\frac{\partial X_a}{\partial r}\right|_{r\in\{0,1\}} = \left.\frac{\partial Y_a}{\partial r}\right|_{r\in\{0,1\}} = \left.\frac{\partial X_i}{\partial r}\right|_{r\in\{0,1\}} = \left.\frac{\partial Y_i}{\partial r}\right|_{r\in\{0,1\}} = 0; \tag{2.68}$$

at the boundary $r = 0$ because of the smoothness of the radially symmetric concentration distribution at the center and at the boundary $r = 1$ due to the assumption that there is no flux of caspases through the cell membrane. Moreover, we consider localized caspase concentrations as initial conditions, cf. (2.10),

$$(X_a, Y_a, X_i, Y_i)(r, 0) = \begin{cases} (X_a^{(d)}, Y_a^{(d)}, X_i^{(d)}, Y_i^{(d)}) & \text{for} \quad R_0 \le r \le 1, \\ (X_a^{(l)}, Y_a^{(l)}, X_i^{(l)}, Y_i^{(l)}) & \text{for} \quad r < R_0 \end{cases} \tag{2.69}$$

for a $R_0 \in (0, 1)$.
Hence, we study the competition between a spatially localized death state corresponding to high active caspase concentrations close to the cell membrane and the life state corresponding to low active caspase concentrations in the interior of the cell. For this purpose, we solve the reaction-diffusion system (2.67) with an implicit Euler scheme, where the spatial derivatives are discretized with a first order centered Finite Difference method [30]. The implementation of the implicit Euler method is explained in Appendix A.4.

We observe the following behavior. The dynamics of the reaction-diffusion system (2.67) can roughly be separated into two steps. At the beginning, the diffusion process is much faster than the reaction kinetics. After about three seconds, the diffusion process has balanced the gradient in the caspase concentrations and leads to an almost homogeneous distribution of caspase molecules, see Figure 2.8. It is not astonishing that the exponent n in the reaction kinetic does not influence the diffusion time measurably. Therefore, we only present the diagram for $n = 2.5$, see Figure 2.9, and mention that those for $n = 2$ and $n = 3$ are identical. Afterward, the diffusion process is almost irrelevant for the dynamics and the reaction kinetics determines the behavior of the system. Thus, we solve the reaction-diffusion system (2.67) with homogeneous Neumann boundary conditions (2.68) and initial conditions (2.69) until the gradient in the concentrations is almost vanished and solve subsequently the ODE system corresponding to the reaction kinetics with the values of the almost homogeneously distributed caspase concentrations as initial conditions.

To give a theoretical motivation for this behavior, we state an important result for the description of the large time behavior of reaction-diffusion systems. First of all, we remind us of the short form of the reaction-diffusion system (2.14) with the abbreviation $u = (X_a, Y_a, X_i, Y_i)$ for the subsequent analysis. Then, we introduce some new quantities.

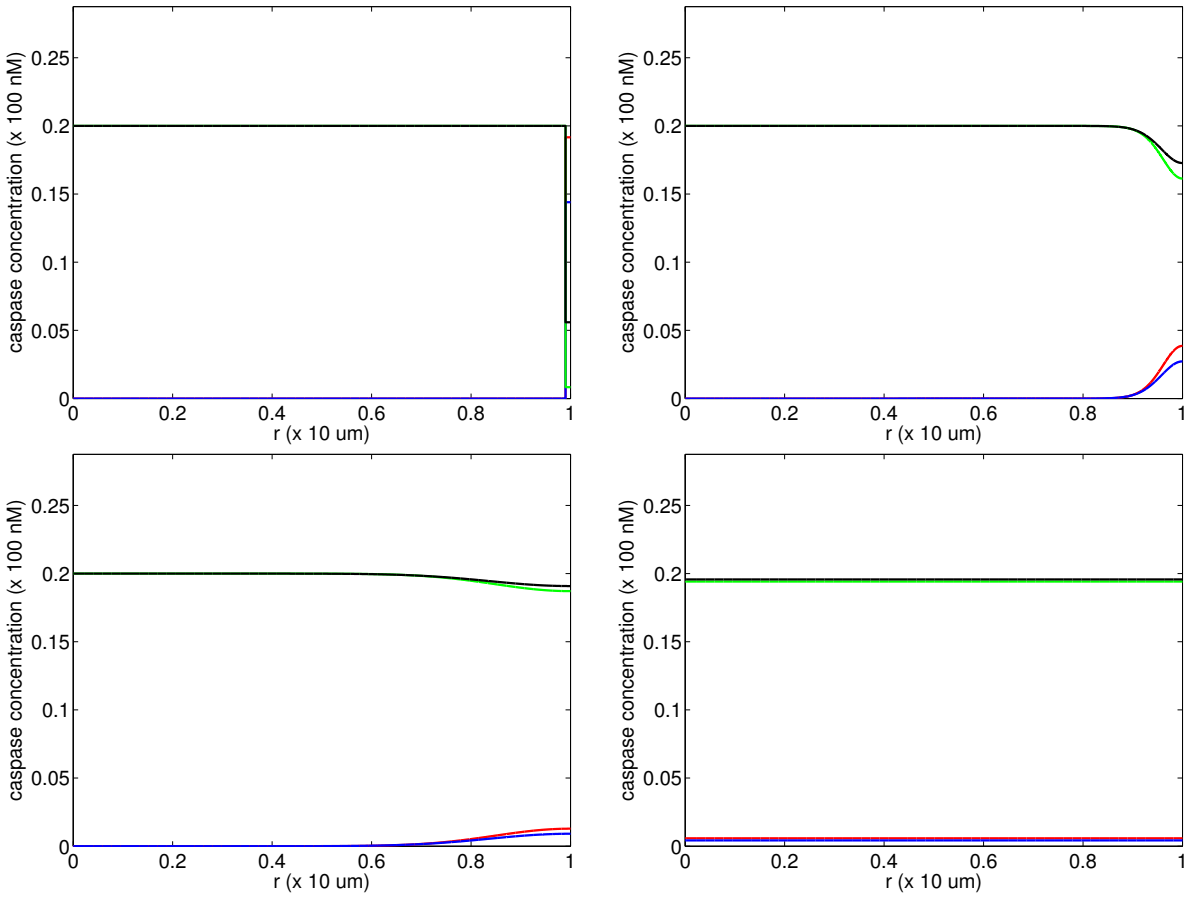

Figure 2.8: Numerical solution of the radially symmetric reaction-diffusion system (2.67) with homogeneous Neumann boundary conditions (2.68) after 1 (left top), 10 (right top), 100 (left bottom) and 4900 (right bottom) time steps in case $d = 3$ and $n = 2.5$. The step size in time is $\Delta t = 0.0001$, multiplied with $\tau = 50/9$ s yields a "homogenization time" of about 2.5 s. The mesh size for the spatial discretization is $\Delta r = 0.0001$ and we choose $R_0 = 0.99$. Red line: caspase 8, blue line: caspase 3, green line: pro-caspase 8, black line: pro-caspase 3.

The most important quantity for the large time behavior is σ which is given by

$$\sigma = \tilde{d} \cdot \zeta - \mathcal{M}, \tag{2.70}$$

where ζ is the first nonzero eigenvalue of $-\Delta_x$ on Ω with homogeneous Neumann boundary conditions and $\tilde{d}$ is the smallest eigenvalue of the diffusion matrix $\tilde{D}$. Furthermore, let $\mathcal{M}$ be given by $\mathcal{M} := \max\{\|\nabla_u f(u)\|_{\max}, u \in \Sigma\}$, where Σ is the invariant region defined in (2.50) in Section 2.7. Obviously, the existence of an invariant region and the boundedness of the Jacobian on the invariant region are essential for the definition of σ. With σ at hand, we want to describe the large time behavior of the reaction-diffusion system (2.14). For this purpose, we cite a theorem which holds in a more general setting, namely the situation where the caspase concentration distribution is not radially symmetric.

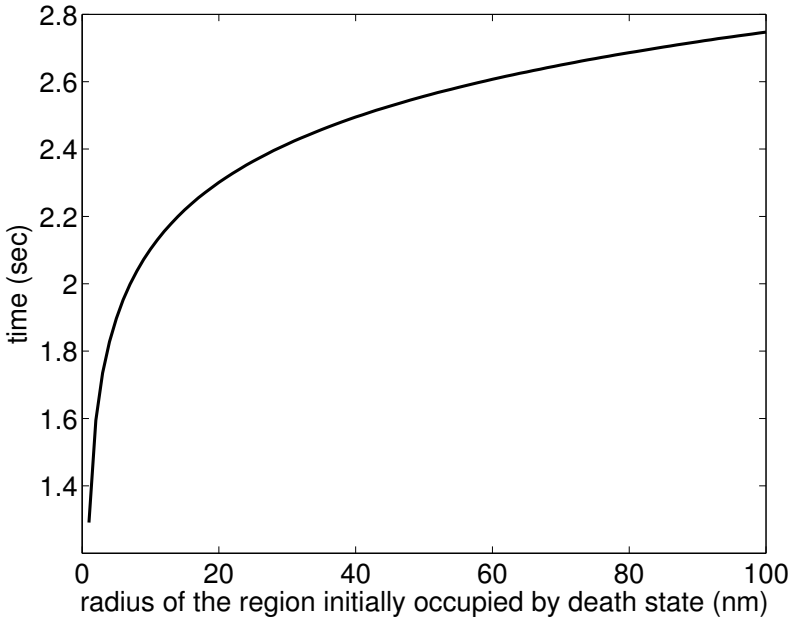

Figure 2.9: The time passed until the gradient in the caspase concentrations is balanced by the diffusion process depends on the size of the region initially occupied by the death state. We present the diagram for $n = 2.5$ and $d = 3$. For $n = 2$ and $n = 3$, the graphs are identical.

Theorem 2.14 (Theorem 14.17 in [57]).
Consider problem (2.14), (2.12) *with boundary conditions* (2.13). *Assume that* (2.14) *admits a bounded invariant region* Σ, *and that* $\{u_0(x), x \in \Omega\} \subset \Sigma$. *If* σ *is positive, then there exist constants* $c_i > 0, i = 1, \ldots, 4$, *such that the following holds for* $t > 0$

1) $\|\nabla_x u(\cdot, t)\|_{L_2(\Omega)} \leq c_1 \mathrm{e}^{-\sigma t}$,

2) $\|u(\cdot, t) - \bar{u}(t)\|_{L_2(\Omega)} \leq c_2 \mathrm{e}^{-\sigma t}$, *where*

$$\bar{u}(t) = \frac{1}{|\Omega|} \int_{\Omega} u(x, t) \mathrm{d}x \tag{2.71}$$

and $\bar{u}$ *satisfies*

$$\frac{\mathrm{d}\bar{u}}{\mathrm{d}t} = f(\bar{u}) + h(t), \ \bar{u}(0) = \frac{1}{|\Omega|} \int_{\Omega} u_0(x) \mathrm{d}x, \tag{2.72}$$

with

$$|h(t)| \leq c_3 \mathrm{e}^{-\sigma t}. \tag{2.73}$$

If $\tilde{D}$ *is a diagonal matrix, then* 2) *can be strengthened to*

2') $\|u(\cdot, t) - \bar{u}(t)\|_{L^\infty(\Omega)} \leq c_4 \mathrm{e}^{-\sigma t}$.

The proof of Theorem 2.14 is given in [57].
Before we apply the cited theorem, we first check the positivity of σ for the invariant region Σ defined in (2.50), the diffusion matrix $\tilde{D}$ and the eigenvalue ζ of the Laplace operator with homogeneous Neumann boundary conditions. The smallest eigenvalue of $\tilde{D}$ is $\tilde{d} = 1$ and the first non-negative eigenvalue of $-\Delta_x$ is $\zeta = \pi^2$ for $d = 1$ and $\zeta = 1.84^2$, cf. Table 2.1, for $d = 2$. For $d = 3$, we know that $\zeta \geq \pi^2/4$, cf. (2.40). Furthermore, we regard the Jacobian matrix $\nabla_u f(u)$ in (2.31), but without the evaluation at the steady states, and compute the maximum norm

$$\begin{aligned}\mathcal{M} &= \max\{\|\nabla_u f(u)\|_{\max}, u \in \Sigma\} \\ &\leq \sup\{\tilde{k}_{d1}, \tilde{k}_{d2}, \tilde{k}_{c1} X_{i,\max}, \tilde{k}_{c1} Y_{a,\max}, n\tilde{k}_{c2} Y_{i,\max} X_{a,\max}^{n-1}, \\ &\qquad \tilde{k}_{c2} X_{a,\max}^{n}, \tilde{k}_{c1} Y_{a,\max} + \tilde{k}_{d3}, \tilde{k}_{c2} X_{a,\max}^{n} + \tilde{k}_{d4}\},\end{aligned} \tag{2.74}$$

where $X_{i,\max} = X_{a,\max} = \tilde{k}_{p1}/\tilde{k}_{d3} = 0.2$, $Y_{i,\max} = Y_{a,\max} = \tilde{k}_{p2}/\tilde{k}_{d4} = 0.2$. With the values for $X_{i,\max}$, $Y_{i,\max}$, $X_{a,\max}$ and $Y_{a,\max}$, estimate (2.74) results in $\mathcal{M} \leq 0.0917$ for $n = 2.5$. Finally, we obtain lower bounds for σ, namely $\sigma = \pi^2 - \mathcal{M} \geq 9.7779$ in the one-dimensional case, $\sigma \geq 3.2939$ in the two-dimensional case and $\sigma \geq 2.3757$ for $d = 3$. For the other values of n, we summarize the lower bounds for σ in Table 2.2 and find

n \ d	1	2	3
2	9.7779	3.2939	2.3757
3	9.7779	3.2939	2.3757

Table 2.2: Lower bounds for σ for the two exponents $n = 2$ and $n = 3$ and the dimensions $d = 1, 2, 3$.

that σ is the same. Hence, all assumptions of Theorem 2.14 are satisfied, and thus, the gradient of the solution $u(x,t)$ gets balanced exponentially, and the solution $u(x,t)$ decays exponentially to the spatial average $\bar{u}(t)$ of the solution $u(x,t)$.

The simulation of the reaction system is stopped at time $t = t^*$ if $\text{dist}^{(l)}(t^*) < 10^{-1}$ or $\text{dist}^{(d)}(t^*) < 10^{-1}$, where $\text{dist}^{(*)}(t) := \max_{v \in \{X_a, Y_a, X_i, Y_i\}}\{|v(t) - v^*|/|v^{(u)} - v^*|\}$, and the asterisk is replaced either by 'd' for the death state or 'l' for the life state. The stopping criterion $\text{dist}^{(l)}(t^l) < 10^{-1}$ defines the "life time" t^l and the criterion $\text{dist}^{(d)}(t^d) < 10^{-1}$ the "death time" t^d. We briefly state the algorithm for the numerical simulation.

Algorithm 2.1.

```
Loop over R_0
  Set initial conditions
  While (max_{v ∈ {X_a,Y_a,X_i,Y_i}} (max_{x ∈ Ω} (v(x,t)) − min_{x ∈ Ω} (v(x,t)) > 1e−6))
    Solve reaction-diffusion system for v(x,t)
  end
  Set initial condition v̄ = (max_{x ∈ Ω} (v(x)) + min_{x ∈ Ω}(v(x)))/2 for ODE
  While (max_{v ∈ {X_a,Y_a,X_i,Y_i}} ( |v(t) − v^(l)| / |v^(u) − v^(l)| ) > 0.1) &&
        (max_{v ∈ {X_a,Y_a,X_i,Y_i}} ( |v(t) − v^(d)| / |v^(u) − v^(d)| ) > 0.1)
    Solve reaction system for v(t)
  end
  Decide whether death state or life state is approached
end
```

With numerical simulations, we finally find the critical value

$$R_c = \sup\{R_0, \text{where } R_0 \text{ is the size of the region where the life state finally wins}\}$$

for the initial condition of the reaction-diffusion system (2.67). The value for R_c depends on the dimension d and the reaction kinetics, especially the exponent n. For $n = 2.5$, the physical values for R_c are $R_c^{1d} = 50\,\text{nm}$ in one dimension, $R_c^{2d} = 25\,\text{nm}$ in two dimensions and $R_c^{3d} = 17\,\text{nm}$ in three dimensions. The spherical shell with an initial thickness of R_c^{3d} homogeneously filled with caspase 3 and caspase 8 approximately has a volume of $V_{\text{shell}} \approx 21.33\,\mu\text{m}^3$. Since we consider a cell modeled by a sphere with radius $10\,\mu\text{m}$ and volume $V_{\text{cell}} \approx 4188\,\mu\text{m}^3$, the death state initially occupies less than 1% of the cell. For this size of death region, the death state does not succeed to invade the region occupied by the life state, but for larger regions of initial caspase activation, the death state will ultimately cover the complete cellular volume. With the volume of the initially occupied death region at hand, we compute the corresponding number of activated caspase 3 and caspase 8. We apply (2.33) and obtain for the three-dimensional case $N_{C8^*} = 246$ molecules of caspase 8 and $N_{C3^*} = 184$ molecules of caspase 3 homogeneously distributed in a spherical shell of thickness $R_c^{3d} = 17\,\text{nm}$. That means, $N_{C8^*} = 246$ caspase 8 molecules and $N_{C3^*} = 184$ caspase 3 molecules homogeneously distributed at the cellular membrane are not sufficient to kill the cell. But, if the spherical shell initially filled with active caspase has a thickness of 18 nm, the cell is finally filled with the death state. This initial concentration of caspase 8 and caspase 3 corresponds to $N_{C8^*} = 260$ and $N_{C3^*} = 195$, respectively. The reason for the jump in the number of molecules from 246 to 260 and 184 to 195, respectively, is the resolution in the spatial discretization Δr in the order of nanometers. A

finer resolution for values between 17 nm and 18 nm in the order of angstrom would result in a continuous variation in the number of molecules. Again, we regard the exponents $n = 2$ and $n = 3$ and oppose the results for these two exponents to the case $n = 2.5$.

For $n = 2$, we obtain for the critical value R_c in one dimension $R_c^{1d} = 4\,\text{nm}$, in the two-dimensional case $R_c^{2d} = 2\,\text{nm}$, and for $d = 3$ we have $R_c^{3d} = 1\,\text{nm}$. Here, the spherical shell initially occupied by the death state has a volume of approximately $V_{\text{shell}} \approx 1.26\,\mu\text{m}^3$. For this size of initial death region, the death state does not succeed to invade the region occupied by the life state. But for larger initial death domains, the death state will ultimately cover the complete cellular volume. Relationship (2.33) finally yields the number of caspase 8 and caspase 3 molecules $N_{C8^*} = 14$ and $N_{C3^*} = 12$. But this amount of active caspase molecules is not sufficient to kill the cell. If the death state initially occupies a spherical shell with a thickness of 2 nm, the whole cell will be finally filled with the death state. Thus, 29 molecules of caspase 8 and 25 molecules of caspase 3 are necessary for the death of the cell.

In case $n = 3$, the critical values for R_c are determined to be $R_c^{1d} = 258$ nm in one dimension, $R_c^{2d} = 130$ nm in two dimensions and $R_c^{3d} = 87$ nm in three dimensions. The critical value R_c^{3d} in three dimensions yields a spherical shell with a volume of approximately $V_{\text{shell}} \approx 108.38\,\mu\text{m}^3$. Again, this size of region initially occupied by the death state is not sufficient for the occurrence of cell death. If the spherical shell has a thickness of 88 nm, the complete cell is finally filled with the death state. With this, we obtain a number of $N_{C3^*} = 683$ caspase 3 molecules and $N_{C8^*} = 1244$ caspase 8 molecules being necessary for cell death.

Obviously, the values $R_c^{1d/2d/3d}$ strongly varies with the exponent n. More precisely, the size of the initial death region required for the death of the cell increases for an increasing exponent n. In other words, the size of the region initially occupied by the death state, where the cell finally survives, increases with the exponent n. This can be seen as follows: The fast diffusion balances the gradient in the concentrations on a very short time scale and thus, the size of the initial death region corresponds to a certain averaged caspase concentration which serves as initial condition for the reaction system. The larger the region initially occupied by the death state the larger the averaged caspase concentration in the cell. Initial conditions for the reaction system 'close' to the life state leads to the survival of the cell. Here, the expression 'close' is relative since the transition state is also located in close proximity to the life state. According to Section 2.4, the location of the steady states varies with the exponent n, more precisely, for increasing values of n the distance between the life state and the transition state increases. Therefore, we expect that the ω-limit set for the life state gets larger for increasing n, i.e., the amount of initial conditions for the reaction system, for which the system finally approaches the life state,

becomes larger. On the other hand, each of these initial conditions for the reaction system corresponds to a certain size of the initial death region.

In addition to the value for R_c, we numerically obtain the dependence of the "death time" on the size of the region initially occupied by the death state, see Figure 2.10. The time passed until the cell dies is of a realistic biological order, since in living cells or in manipulated cells produced for experiments, it takes more than 15 minutes from stimulation of the signaling pathway to the occurrence of cell death (data from personal discussions with Peter Scheurich). The simulations yield in the three-dimensional case for $n = 2.5$ for radially symmetric concentration distributions a death time of 50 to 250 minutes dependent on the strength of the initial activation, i.e. the size of the region initially filled with the death state. Moreover, the "death time" depends on the exponent n, i.e. the strength of the reaction kinetics. For $n = 2$ the "death time" is 30 to 250 minutes. We obtain similar results for initial conditions different from the death

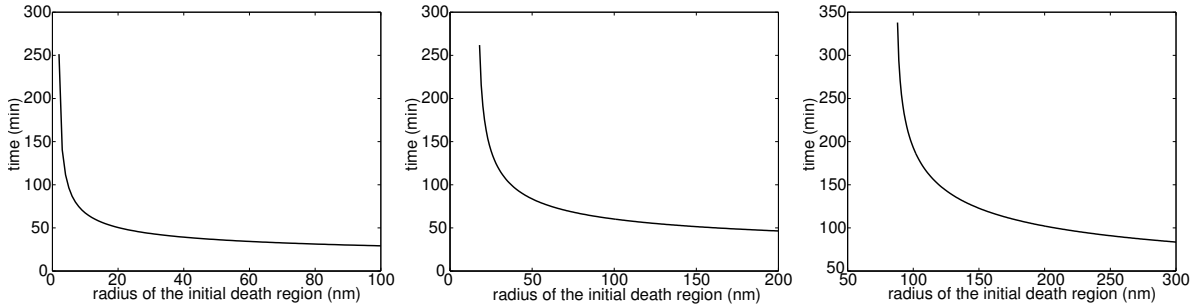

Figure 2.10: The figure shows the dependence of the "death time" on the size of the region initially occupied by the death state in the three-dimensional case for $n = 2$ (left panel), $n = 2.5$ (middle panel) and $n = 3$ (right panel). Again, we choose $\Delta r = 0.0001$ and the thickness of the spherical shell is varied from 1 nm to 100 nm (left panel), from 1 nm to 200 nm (middle panel) and from 50 nm to 300 nm (right panel).

state close to the boundary: taking arbitrary initial conditions where the caspase 8 and caspase 3 concentrations are high close to the boundary of the cell and where the rest of the cell is filled with the life state, we obtain the same effects. Again, diffusion will homogenize the caspase concentrations within a few seconds. Afterward, the concentrations will be governed by the original reaction system. To study the switch-like behavior for initial concentrations different from the steady state concentration, we choose for the initial concentration a range of 50% to 200% of the death state concentration and besides, we vary the thickness of the initial death region. Both variations influence the switch-like behavior of the system significantly, cf. Figure 2.11, Figure 2.12 and Figure 2.13. Therefore, the important variable is the averaged initial concentration of caspase 8 and caspase 3, i.e. for a fixed cell the total number of caspase 8 and caspase 3 molecules at the beginning of the apoptotic process. We observe that for averaged concentrations beneath a certain threshold, the cell survives instead of getting killed.

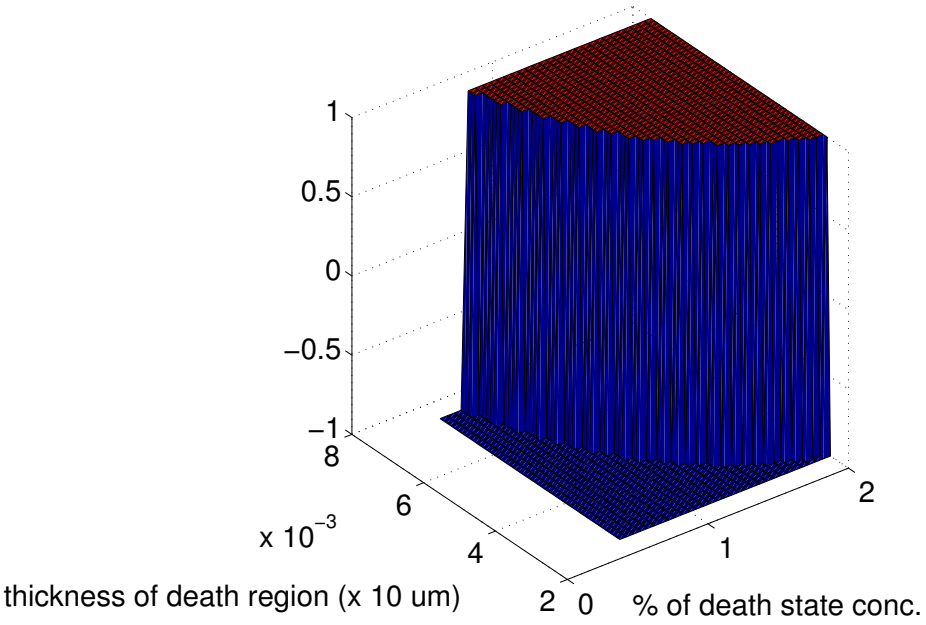

Figure 2.11: The figure shows the switch-like behavior of the reaction-diffusion system (2.67) for different initial configurations for $d = 1$ in case $n = 2.5$. Besides the size of the initial death region, different initial concentrations of (pro-) caspase 8 and (pro-) caspase 3 are taken into account. The value -1 in z-direction stands for the survival of the cell, the value 1 in z-direction means cell death.

In this section, we analyzed inhibition effects of apoptosis through the spatial extension of a single cell. We found a threshold for the size of the initial death domain, above which the death state invades the region occupied by the life state. And we saw that the spatially extended model presents a robustness of the cell concerning an accidental activation of pro-caspase at the cell membrane, although no inhibitors for caspase 3 and caspase 8 are incorporated into the model as we mentioned in Remark 2.1 in Section 2.1.

2.9 Reaction-Diffusion Model on Large Spatial Scales

In Section 2.8, we solved the radially symmetric reaction-diffusion system (2.67) with homogeneous Neumann boundary conditions for several initial conditions numerically. Depending on the initial condition, the system approaches one of the spatially homogeneous, asymptotically stable stationary solutions. In summary, we observed a switch-like behavior of the reaction-diffusion system with respect to the size of the region initially occupied by the death state. The domain modeling the biological single cell was the interval $[-1, 1]$ in one dimension, a union circle in two dimensions and a union ball in three dimensions on a length scale of $L = 10^{-5}$ m. Hence, the domain size was of a realistic biological order.

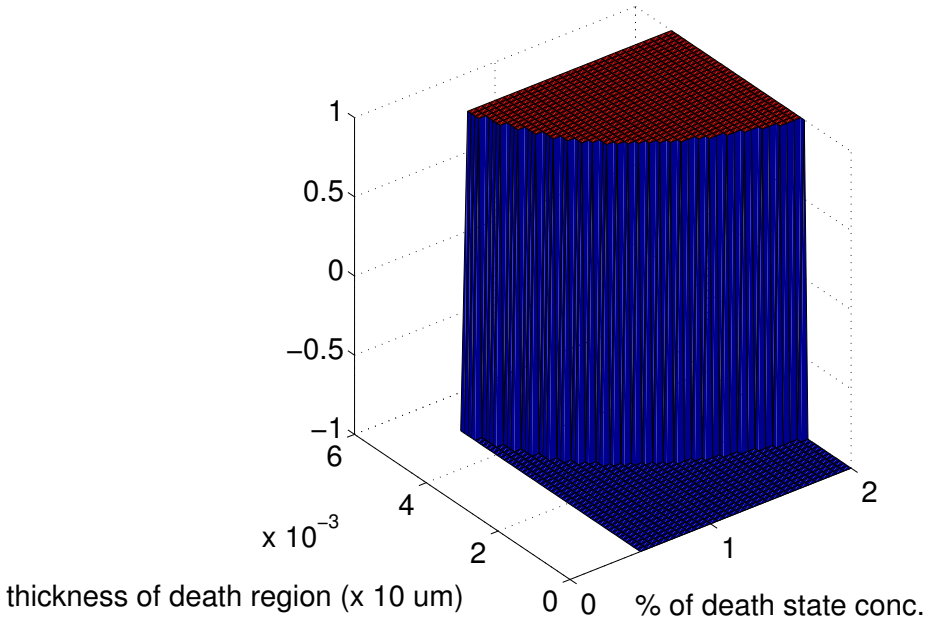

Figure 2.12: The figure shows the switch-like behavior of the reaction-diffusion system (2.67) for different initial configurations for $d = 2$ in case $n = 2.5$.

On the other hand, a typical characteristic of bistable reaction-diffusion systems in one spatial dimension is the existence of traveling wave solutions [29]. Thus, in Section 2.9.1 we study nontrivial spatio-temporal structures of solutions of the radially symmetric reaction-diffusion system

$$\begin{aligned}
\tfrac{\partial X_a}{\partial t} &= \tilde{k}_{c1} X_i Y_a - \tilde{k}_{d1} X_a + \tilde{D}_1 \tfrac{1}{r^{d-1}} \tfrac{\partial}{\partial r}(r^{d-1} \tfrac{\partial X_a}{\partial r}), \\
\tfrac{\partial Y_a}{\partial t} &= \tilde{k}_{c2} Y_i X_a^n - \tilde{k}_{d2} Y_a + \tilde{D}_2 \tfrac{1}{r^{d-1}} \tfrac{\partial}{\partial r}(r^{d-1} \tfrac{\partial Y_a}{\partial r}), \\
\tfrac{\partial X_i}{\partial t} &= -\tilde{k}_{c1} X_i Y_a - \tilde{k}_{d3} X_i + \tilde{k}_{p1} + \tilde{D}_3 \tfrac{1}{r^{d-1}} \tfrac{\partial}{\partial r}(r^{d-1} \tfrac{\partial X_i}{\partial r}), \\
\tfrac{\partial Y_i}{\partial t} &= -\tilde{k}_{c2} Y_i X_a^n - \tilde{k}_{d4} Y_i + \tilde{k}_{p2} + \tilde{D}_4 \tfrac{1}{r^{d-1}} \tfrac{\partial}{\partial r}(r^{d-1} \tfrac{\partial Y_i}{\partial r}),
\end{aligned} \tag{2.75}$$

$r \in [0, R]$, with homogeneous Neumann boundary conditions

$$\left.\frac{\partial X_a}{\partial r}\right|_{r\in\{0,R\}} = \left.\frac{\partial Y_a}{\partial r}\right|_{r\in\{0,R\}} = \left.\frac{\partial X_i}{\partial r}\right|_{r\in\{0,R\}} = \left.\frac{\partial Y_i}{\partial r}\right|_{r\in\{0,R\}} = 0. \tag{2.76}$$

Now, $R \gg 1$ describes the size of the cell. Afterward, we analyze in Section 2.9.2 the switch-like behavior of the reaction-diffusion system (2.75) with homogeneous Neumann boundary conditions (2.76) on a large spatial scale similar to the numerical analysis in Section 2.8.

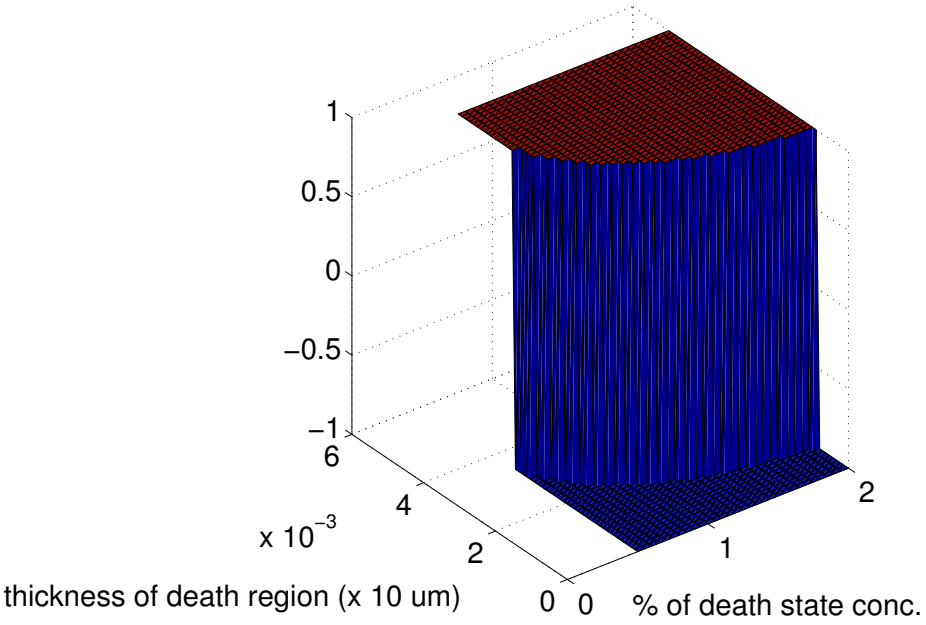

Figure 2.13: The figure shows the switch-like behavior of the reaction-diffusion system (2.67) for different initial configurations for $d = 3$ in case $n = 2.5$.

2.9.1 Existence of Nontrivial Spatio-Temporal Structures of Solutions

To motivate the expectation of the existence of traveling wave solutions, we first consider a reaction-diffusion equation in one spatial dimension

$$\partial_t u = \partial_x^2 u + f(u), \ x \in \mathbb{R}, t > 0, \tag{2.77}$$

with

$$f(u) = u(1-u)(u-\alpha), 0 < \alpha < \frac{1}{2}. \tag{2.78}$$

Equation (2.77) together with (2.78) is a simple form of the Fitzhugh-Nagumo equation. The traveling wave ansatz $u(x,t) = \phi(x+ct) =: \phi(s)$ leads to the ODE

$$\phi''(s) - c\phi'(s) + f(\phi(s)) = 0, \quad -\infty < s < \infty. \tag{2.79}$$

In [29, Section 5.4], the existence of a solution $\phi(s)$ to (2.79) for $c > 0$ with $\phi(s) \to 1$ for $s \to \infty$ and $\phi(s) \to 0$ for $s \to -\infty$ has been proven. This solution corresponds to a heteroclinic orbit between the two steady states $u_0 = 0$ and $u_1 = 1$, and is given by

$$\phi(s) = \frac{1}{1 + \exp(-s/\sqrt{2})} \quad \text{and} \quad c = \sqrt{2}\left(\frac{1}{2} - \alpha\right). \tag{2.80}$$

The two steady states u_0 and u_1 are separated by the steady state $u = \alpha, 0 < \alpha < 1/2$. Now, the reaction-diffusion system (2.14) established in Section 2.3 possesses a similar structure as (2.77), (2.78) and the existence of a traveling wave solution connecting the two asymptotically stable steady states can be expected.

In order to analyze the spatio-temporal structure of the solution, we solve the reaction-diffusion system (2.75) with homogeneous Neumann boundary conditions (2.76) and the initial conditions

$$X(r,0) = X^{(l)} \text{ for } 0 \leq r < 1000 \text{ and } X(r,0) = X^{(d)} \text{ for } 1000 \leq r \leq 2000$$

in the domain $[0, 2000]$ numerically. For solving the system, we again use the implicit Euler method together with the Finite Difference method for the spatial, equidistant discretization introduced in Appendix A.4. We set the distance between two nodes of the spatial discretization to $\Delta r = 0.1$ and the size of the time step is $\Delta t = 50 \cdot \Delta r^2 = 0.5$. This choice is possible since the CFL condition does not need to be satisfied for the implicit Euler method. We consider the one-dimensional case and the parameter setting given in (2.8). The numerical solution of the reaction-diffusion system presents a traveling wave solution connecting the two asymptotically stable steady states, see Figure 2.14. We observe that the traveling wave solution moves from the right to the left, i.e., the death state invades the region initially occupied by the life state. Actually, the existence of a traveling wave solution does not depend on the exponent n. For this purpose, we solve the reaction-diffusion system (2.75) for $n = 2$ and $n = 3$ numerically, see Figure 2.15 and Figure 2.16. Obviously, the shape of the traveling wave solution depends on the exponent n since the death state concentrations depend on n but the life state concentrations do not depend on n, cf. Section 2.4. Besides the shape, the velocity of the traveling wave solution varies with the exponent n. To measure the velocity, we consider the smallest value for r where the concentration X_a of active caspase 8 takes a value larger than $X_a^{\max}/2$. Every 60 time steps, the coordinate of this point is stored and the comparison of two consecutive coordinates yields the velocity of the traveling wave for each time interval. Since we determine the velocity for different times, we first ascertain that the velocity remains constant except for numerical inaccuracies. Averaging all the computed velocities, the numerical experiments finally give an approximate velocity $|\bar{c}| \approx 0.2118$ for $n = 2$, $|\bar{c}| \approx 0.1452$ for $n = 2.5$ and $|\bar{c}| \approx 0.0935$ for $n = 3$. Then, taking $L = 10\,\mu\text{m}$, the corresponding physical velocities are $|c_{\text{phys}}| \approx 0.3813\,\mu\text{m/s}$ for $n = 2$, $|c_{\text{phys}}| \approx 0.2614\,\mu\text{m/s}$ for $n = 2.5$ and $|c_{\text{phys}}| \approx 0.1684\,\mu\text{m/s}$ for $n = 3$. We see that the velocity decreases with an increasing exponent n and that the physical velocities are of a realistic biological order. In order to study the robustness concerning variations in the parameter values we hold the parameter values $\tilde{k}_{c1} = \tilde{k}_{c2} = 0.444, \tilde{k}_{p1} = \tilde{k}_{p2} = 5.556 \cdot 10^{-4}$ and choose four

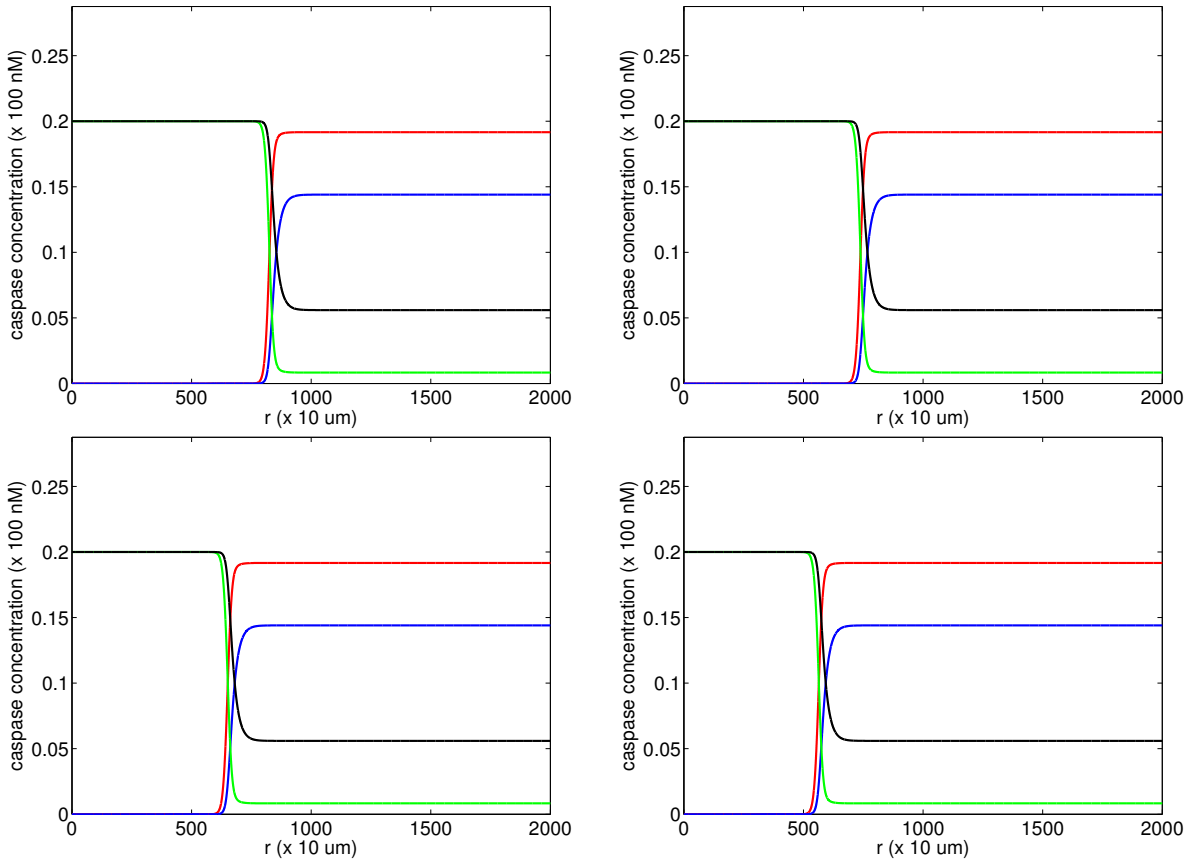

Figure 2.14: Traveling wave solution which moves from the right to the left for $n = 2.5$ in case $d = 1$ for the radially symmetric reaction-diffusion system (2.75) after 2400 (left top), 3600 (right top), 4800 (left bottom) and 6000 (right bottom) time steps. Red line: caspase 8, blue line: caspase 3, green line: pro-caspase 8, black line: pro-caspase 3

arbitrary degradation rates $\tilde{k}_{d1} = 0.0028, \tilde{k}_{d2} = 0.0033, \tilde{k}_{d3} = 0.0022$ and $\tilde{k}_{d4} = 0.0028$. Again, the numerical simulation shows for $d = 1$ the existence of traveling wave solutions connecting the two asymptotically stable steady states. But for this special choice of degradation rates, we observe a non-monotone traveling wave solution, see Figure 2.17. For $n = 2$ and $n = 3$, the traveling wave solution has a similar structure but, due to the difference in the death state concentrations, the traveling wave solutions differ in their shape. Again, we determine the velocity of the traveling waves. We obtain the approximate velocities $|\bar{c}| \approx 0.2347$ for $n = 2$, $|\bar{c}| \approx 0.1658$ for $n = 2.5$ and $|\bar{c}| \approx 0.1113$ for $n = 3$. The corresponding physical velocities are $|c_{\text{phys}}| \approx 0.4225\,\mu\text{m/s}$ for $n = 2$, $|c_{\text{phys}}| \approx 0.2985\,\mu\text{m/s}$ for $n = 2.5$ and $|c_{\text{phys}}| \approx 0.2004\,\mu\text{m/s}$ for $n = 3$. Thus, for fixed exponent n, the traveling wave solution is faster in case of different degradation rates than in case of equal degradation rates. This is not surprising since the steady states depend on the degradation rates and on the other hand, the steady states influence the velocity of the traveling wave, cf. (2.80).

Remark 2.15. In Section 2.8, we stated Theorem 2.14 with the proposition that the

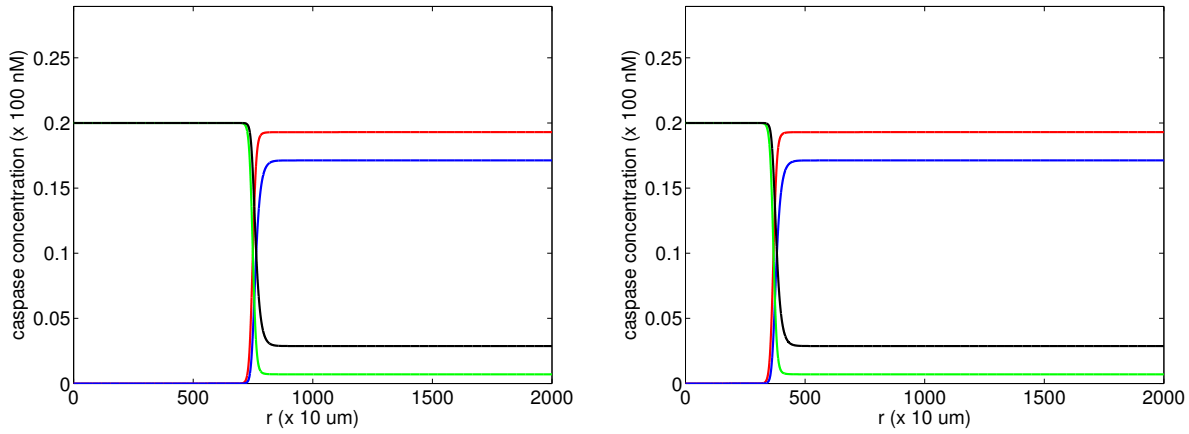

Figure 2.15: Traveling wave solution which moves from the right to the left for $n = 2$ in case $d = 1$ for the radially symmetric reaction-diffusion system (2.75) after 2400 (left) and 6000 (right) time steps. Red line: caspase 8, blue line: caspase 3, green line: pro-caspase 8, black line: pro-caspase 3.

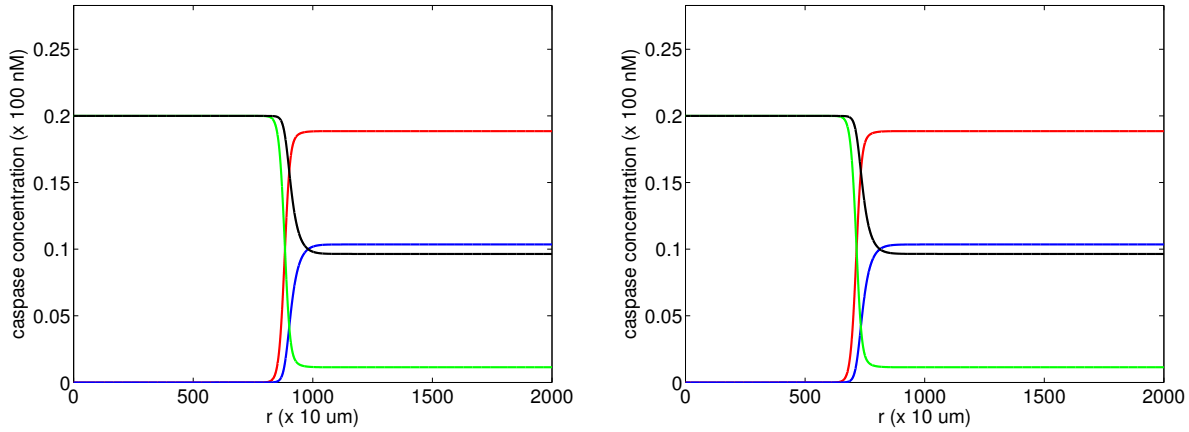

Figure 2.16: Traveling wave solution which moves from the right to the left for $n = 3$ in case $d = 1$ for the radially symmetric reaction-diffusion system (2.75) after 2400 (left) and 6000 (right) time steps. Red line: caspase 8, blue line: caspase 3, green line: pro-caspase 8, black line: pro-caspase 3.

gradient of the caspase concentrations is balanced by the diffusion on a small time scale. But now, the eigenvalues of the one-dimensional Laplace operator with homogeneous Neumann boundary conditions on the domain $\Omega = [0, 2000]$ are $\lambda_k = k^2 \cdot \pi^2/2000^2$, especially $\lambda_1 = \pi^2/2000^2 \approx 2.4674 \cdot 10^{-6}$ and with $\mathcal{M} = 0.0917$ and $\tilde{d} = 1$, we obtain $\sigma = \tilde{d} \cdot \lambda_1 - \mathcal{M} \approx -0.0917 < 0$ and thus, the assumptions for Theorem 2.14 are not fulfilled. So, the numerical result that shows the existence of a traveling wave does not contradict the theoretical results from Section 2.8.

Remark 2.16. In case $d = 2$ and $d = 3$, we obtain solutions with a similar structure as the traveling wave solution. We call them front-like solutions. But we expect that the velocity of the solution is not constant anymore due to the curvature in the two- and three-dimensional space.

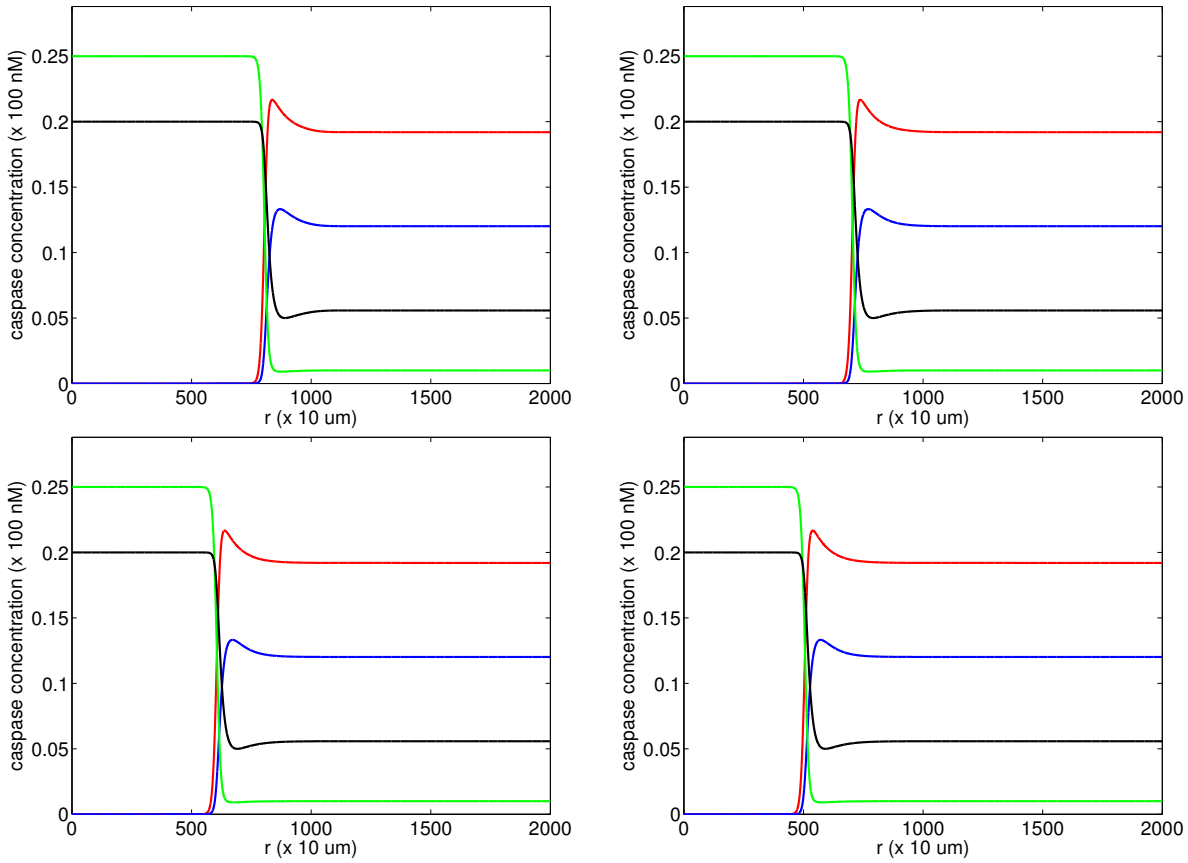

Figure 2.17: Traveling wave solution which moves from the right to the left for $n = 2.5$ in case $d = 1$ for the radially symmetric reaction-diffusion system (2.75) with $\tilde{k}_{d1} > \tilde{k}_{d3}$ and $\tilde{k}_{d2} > \tilde{k}_{d4}$ after 2400 (left top), 3600 (right top), 4800 (left bottom) and 6000 (right bottom) time steps. Red line: caspase 8, blue line: caspase 3, green line: pro-caspase 8, black line: pro-caspase 3.

Remark 2.17. The numerical simulation shows in the one-dimensional case the existence of a traveling wave solution connecting the two asymptotically stable steady states. We notice that the structure of the traveling wave solution is by a factor 100 too large to fit into a cell of size 10 µm. Scaling the spatial variable by a factor 100, i.e. setting $y = x/100$, leads to the scaled second derivative $u_{yy} = 100^2 u_{xx}$ and so, we obtain

$$u_t = \tilde{D}u_{xx} + f(u) = \tilde{D}/100^2 u_{yy} + f(u) = D^* u_{yy} + f(u)$$

with $D^* = \tilde{D}/10000$. Thus, in the rescaled equation, the diffusion rate is by a factor 10000 smaller than in the original equation. However, the velocity of the traveling wave then will be so small that execution of cell death would take an unphysiologically long time.

At the end, we switch the region initially occupied by the death state and the region initially filled with the life state, respectively, i.e., we choose the initial conditions

$$X(r,0) = X^{(d)} \text{ for } 0 \le r < 1000 \text{ and } X(r,0) = X^{(l)} \text{ for } 1000 \le r \le 2000.$$

Again, we observe through numerical simulations a traveling wave solution. But this time, the solution moves from the left to the right, that means, the death state again invades the region initially occupied by the life state, see Figure 2.18.

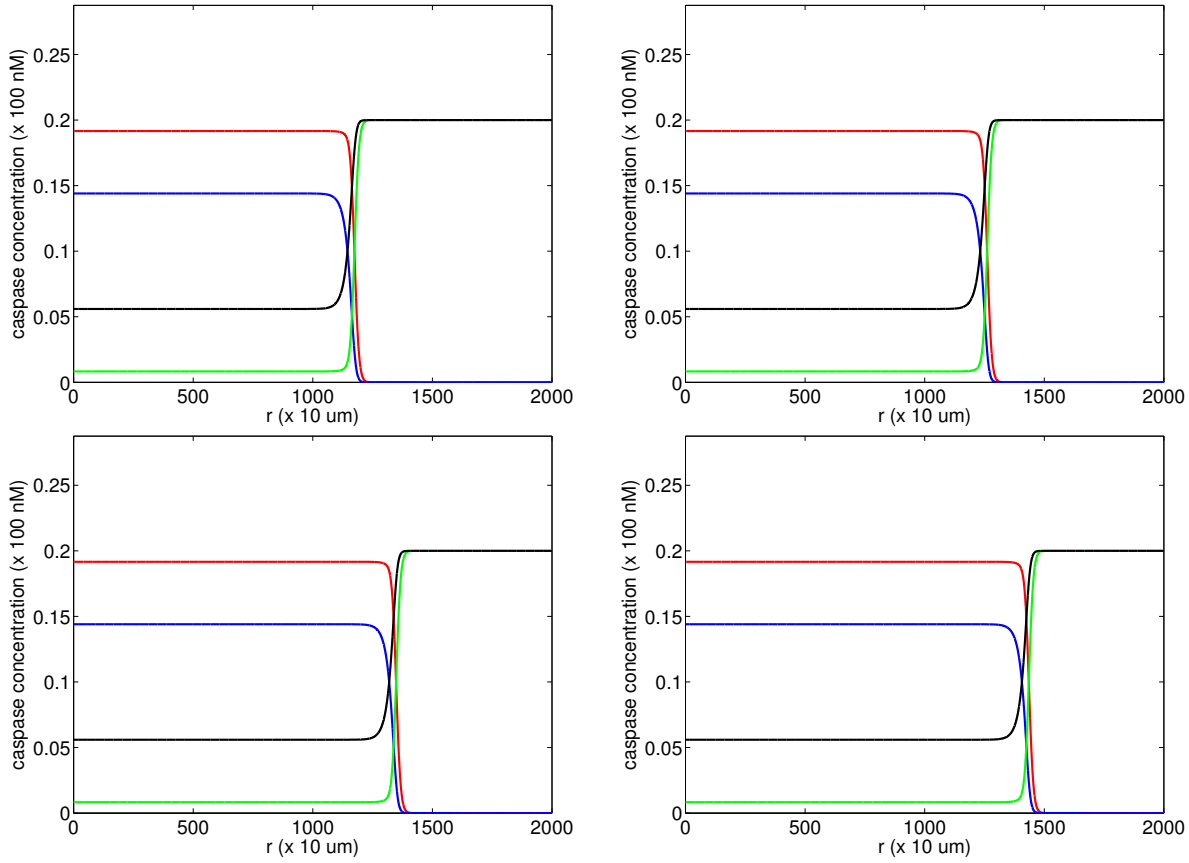

Figure 2.18: Traveling wave solution which moves from the left to the right for $n = 2.5$ in case $d = 1$ for the radially symmetric reaction-diffusion system (2.75) with $\tilde{k}_{d1} = \tilde{k}_{d2} = \tilde{k}_{d3} = \tilde{k}_{d4}$ after 2400 (left top), 3600 (right top), 4800 (left bottom) and 6000 (right bottom) time steps. Red line: caspase 8, blue line: caspase 3, green line: pro-caspase 8, black line: pro-caspase 3.

However, this behavior depends on the special choice of initial condition. For initial conditions of the form

$$X(r,0) = X^{(d)} \text{ for } 0 \leq r < r^* \text{ and } X(r,0) = X^{(l)} \text{ for } r^* \leq r \leq 2000,$$

$0 < r^* < 2000$, the formation of a traveling wave solution is observable if r^* is larger than a critical value r_c. In the next section, we investigate the situation when $r^* < r_c$ and determine the critical value r_c, so it exists.

2.9.2 Spatial Inhibition Effects on Large Spatial Scales

In Section 2.9.1, we studied the existence of traveling wave solutions on a large spatial scale and found that the death state invades the region initially occupied by the life state.

For the first numerical simulations, we chose a spherical shell of a certain thickness filled by the death state as initial condition. At the end of Section 2.9.1, we inverted the initial conditions and considered a ball of a certain diameter occupied by the death state whereas the spherical shell was filled with the life state. In both cases, the death state invades the region initially occupied by the life state. But the formation of a traveling wave solution and the associated invasion of the death state should not be possible for all initial conditions: according to Figure 2.19, the ball filled with the death state can be regarded as a small spot located close to the cell membrane instead of the center of the cell. If there was no threshold for r^*, i.e. for the size of the ball initially filled with the death state, then the tiniest activation would lead to the formation of a traveling wave and the invasion of the death state.

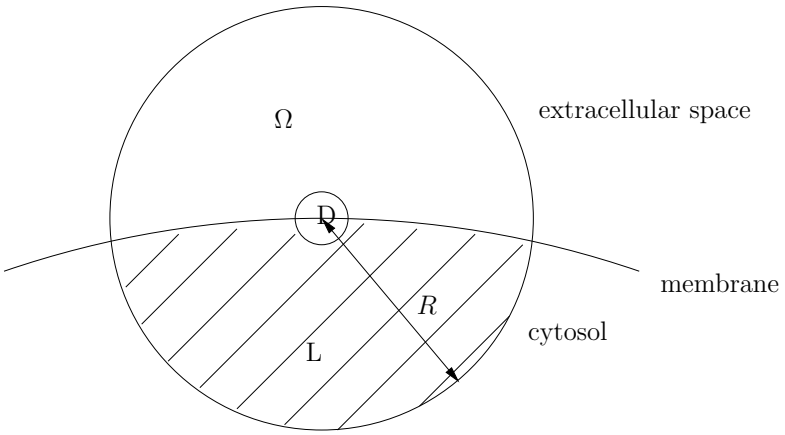

Figure 2.19: The domain Ω modeling a circle ($2d$) or a ball ($3d$) with radius R. The initial condition for the reaction-diffusion system is defined by the death state (D) in a small ball and the life state (L) in a spherical shell, i.e. the rest of the domain Ω. Here, Ω does not reflect a model for the cell but a ball with center on the cell membrane. Thus, the death state occupies a small region located close to the cell membrane. Considering radially symmetric concentrations, we only focus on the dynamics within the cell, i.e. in the cytosol.

In order to determine the critical value r^c for r^*, we solve the radially symmetric reaction-diffusion system (2.75) with homogeneous Neumann boundary conditions and initial conditions

$$X(r,0) = X^{(d)} \text{ for } 0 \leq r < r^* \text{ and } X(r,0) = X^{(l)} \text{ for } r^* \leq r \leq 2000.$$

To find the critical value r_c for r^* that enables the formation of a traveling wave solution, we superpose a bisection algorithm. In the following, the notation $r_{d,\cdot}$ denotes the value for r^* for which the formation of a traveling wave solution succeeds and $r_{l,\cdot}$ denotes the value for r^* where the formation of a traveling wave solution fails.

Algorithm 2.2.

```
Choose r_{l,0} and r_{d,0}
while | r_{l,i} − r_{d,i} | ≥ 2
    compute z = 0.5 · (r_{l,i} + r_{d,i})
    solve initial value problem for r* = z
    if { traveling wave is built }
      r_{d,i+1} = z; r_{l,i+1} = r_{l,i};
    else
      r_{l,i+1} = z; r_{d,i+1} = r_{d,i};
    end
    i = i + 1;
end
```

It remains to explain the decision whether the formation of a traveling wave is performed. In Figure 2.20, we see that for a certain initial condition, the concentrations initially get balanced and the maxima of the active caspase concentrations are decreasing. However,

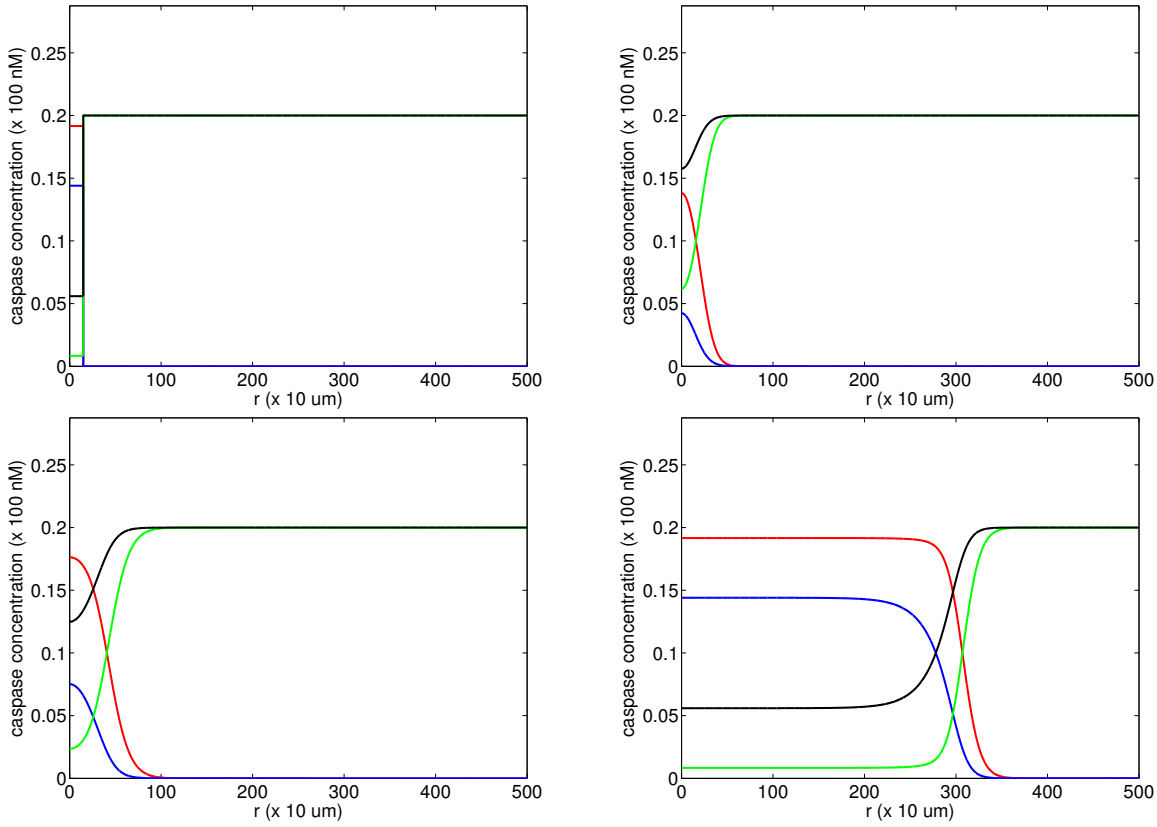

Figure 2.20: The formation of a traveling wave depends on the special choice of initial condition. For values beneath a critical value r_c, the system does not allow the formation of traveling waves. Red line: caspase 8, blue line: caspase 3, green line: pro-caspase 8, black line: pro-caspase 3.

there is a time point $t^\dagger$ where the maximum of the active caspase concentrations reaches a minimum and afterward, it is increasing and approaches the death state concentration of active caspase 3 and 8. Finally, a traveling wave solution is built. Thus, we expect the formation of a traveling wave if there exist $t_1, t_2 > 0$ with $t_2 > t_1$ such that

$$\max_{r\in[0,2000]} X_a(r, t_2) > \max_{r\in[0,2000]} X_a(r, t_1).$$

For the algorithm, we use the condition

$$\exists k \in \mathbb{N} : \max_{r\in[0,2000]} X_a(r, (k+1)\cdot 100\cdot \Delta t) - \max_{r\in[0,2000]} X_a(r, k\cdot 100\cdot \Delta t) > 10^{-3},$$

thus, the monotony of the maximum of X_a on a discretized time interval. With this condition at hand, we complete the algorithm and a simulation of the algorithm yields series $\{r_{l,i}\}_{i\in\mathbb{N}}$ and $\{r_{d,i}\}_{i\in\mathbb{N}}$ of initial conditions where the formation of traveling waves fails or succeeds. Besides, the series converge towards the critical value r_c.

Again, we run the simulation for different scenarios, i.e. for $n = 2, n = 2.5, n = 3$, and for $d = 2, 3$. We define the function

$$\mathcal{R}(r) = \begin{cases} 1, & r \in \{r_{d,i}\}_{i\in\mathbb{N}}, \\ -1, & r \in \{r_{l,i}\}_{i\in\mathbb{N}}, \end{cases}$$

where the value 1 stands for the formation of a traveling wave and, thereby, the death of the cell, and the value -1 stands for the survival of the cell. The numerical simulation yields the critical values $r_c^{2d} \approx 9\,\mu\text{m}$ and $r_c^{3d} \approx 41\,\mu\text{m}$ for $n = 2$, $r_c^{2d} \approx 34\,\mu\text{m}$ and $r_c^{3d} \approx 101\,\mu\text{m}$ for $n = 2.5$, and $r_c^{2d} \approx 67\,\mu\text{m}$ and $r_c^{3d} \approx 191\,\mu\text{m}$ for $n = 3$, see Figure 2.21, Figure 2.22 and Figure 2.23. For values larger than r_c, a traveling wave is built. We have to mention that the resolution in space is of the order of micrometers, that means, for instance in case $n = 2$, a value of $r^{2d} = 10\,\mu\text{m}$ allows for the formation of a traveling wave. Values between $9\,\mu\text{m}$ and $10\,\mu\text{m}$ are not investigated due to the resolution of the spatial discretization with step size $\Delta r = 0.1$ on a scale of $L = 10^{-5}\,\text{m}$. Again, we obtain a switch-like behavior concerning the initial condition similar to the situation in Section 2.8 on a realistic biological scale. Here, we have the switch-like behavior on a large spatial scale and the critical values for r^* are of the size of several micrometers.

Remark 2.18. Similar to the study of the switch-like behavior in Section 2.8, we found in this section critical values r_c for the initial death region, above which the formation of traveling wave solution succeeds. With this critical values at hand, we would be able to compute the volume of the region initially occupied by the death state and with equation (2.33), we would find the corresponding amount of molecules. But, since we consider a large spatial scale, i.e. a cell of size two centimeters, the result for the amount of molecules

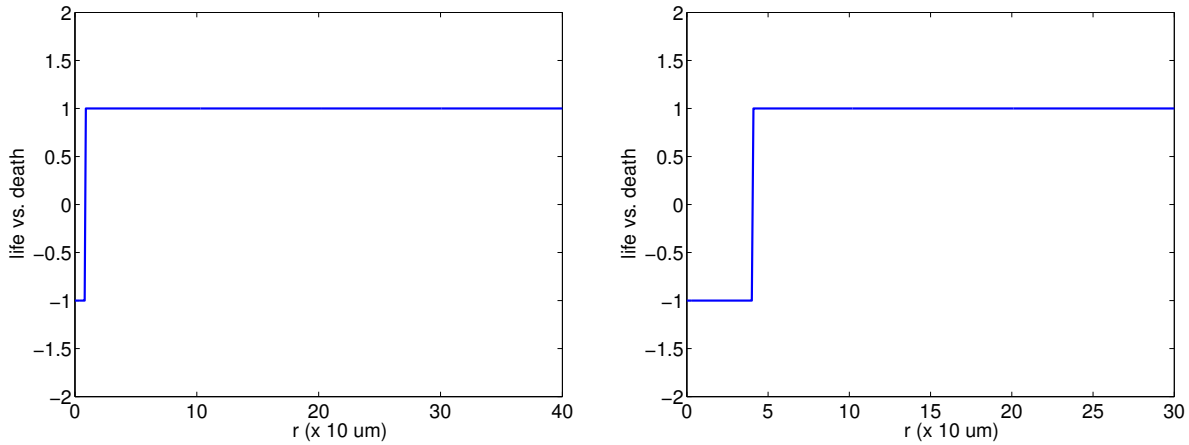

Figure 2.21: Illustration of the switch-like behavior of the reaction-diffusion system (2.75) on a large spatial scale for $d = 2$ (left) and $d = 3$ (right) in case $n = 2$. The value 1 in the y-direction means the death of the cell, the value -1 denotes the survival of the cell.

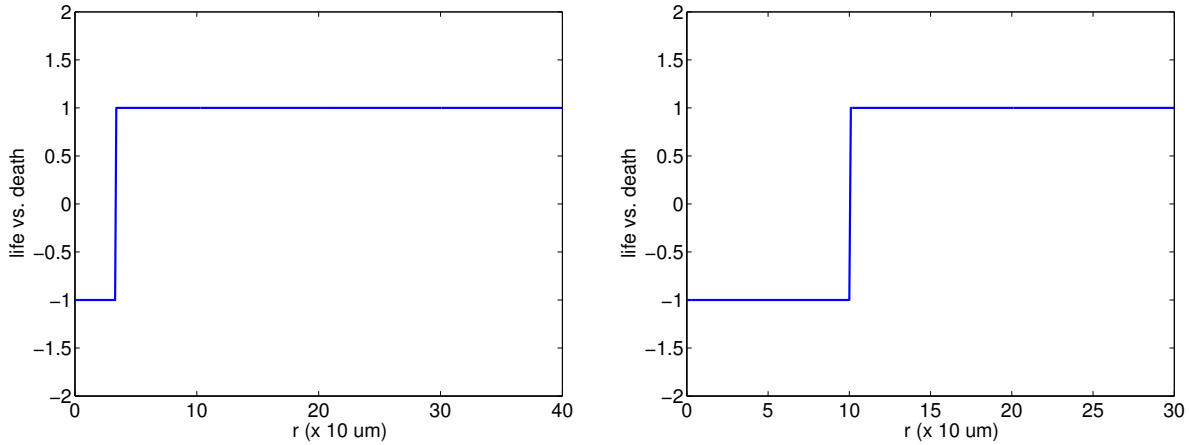

Figure 2.22: Illustration of the switch-like behavior of the reaction-diffusion system (2.75) on a large spatial scale for $d = 2$ (left) and $d = 3$ (right) in case $n = 2.5$.

would be on a very large biological scale. Thus, we restrict ourselves to a qualitative study concerning the switch-like behavior on the large spatial scale.

2.10 Discussion

In Chapter 2, we introduced a spatial extension of a model of the caspase-3/8 feedback loop established in [15]. Similar to [15], we computed the steady states of the reaction system and analyzed the stability properties. For our chosen parameter setting, we found two asymptotically stable and one unstable steady state, thus, the reaction system possesses bistable behavior.

For the spatial extension of the model introduced in [15], we assumed for simplicity that the dynamics of the caspase molecules in space obeys a diffusion process. We showed stability properties of spatially homogeneous stationary solutions and found

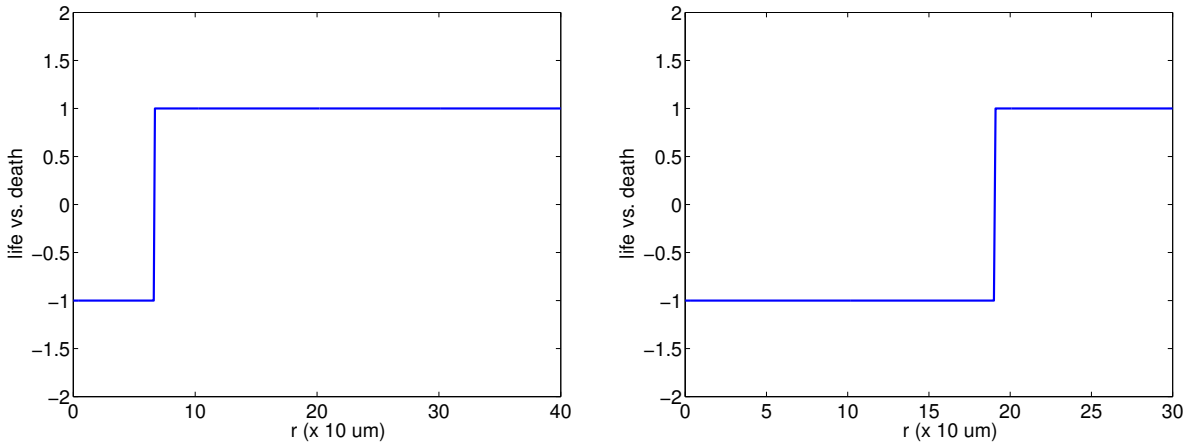

Figure 2.23: Illustration of the switch-like behavior of the reaction-diffusion system (2.75) on a large spatial scale for $d = 2$ (left) and $d = 3$ (right) in case $n = 3$.

two asymptotically stable and one unstable stationary solution. Furthermore, we found an invariant region for the reaction-diffusion system and obtained the boundedness of the solutions. Finally, in Section 2.8 and Section 2.9, we solved the reaction-diffusion system with homogeneous Neumann boundary conditions and certain initial conditions in case of radially symmetric concentration distributions numerically. We found that the gradient of the concentrations is rapidly balanced by the diffusion and we saw that the reaction kinetics finally decides which of the two asymptotically stable stationary solutions is approached depending on the averaged initial caspase concentration. On a realistic biological scale, the numerical simulations showed a switch-like behavior of the system concerning the initial conditions, and on a large spatial scale, we found traveling wave solutions – a typical structure for bistable reaction-diffusion systems. In this thesis, all simulations were run for a certain choice of parameter values which were taken from literature [14, 15]. On the other hand, according to Theorem 2.8, we varied the diffusion rates, i.e., we needed for the invariant region $\tilde{D}_1 = \tilde{D}_3$ and $\tilde{D}_2 = \tilde{D}_4$ instead of pairwise different diffusion rates. But in [13], we published the results of the numerical simulations with the original diffusion rates taken from literature and given in Appendix A.1.2. The results in [13] confirm that the results are qualitatively indistinguishable and quantitatively close to each other.

However, all results we obtained in this thesis and in [13] have been computed for radially symmetric concentration distributions, thus, we reduced the spatially extended reaction-diffusion system in d dimensions, $d = 1, 2, 3$, to one spatial dimension, namely the distance to the center of the cell. Of course, this is a rough simplification of the model, since, amongst others, it only allows for homogeneously distributed initial activations at the cellular membrane. Despite the simplification of the model, the qualitative results obtained from the numerical simulations are meaningful. On the other hand, the concept

of a radially symmetric reaction-diffusion system has already been used for modeling the MAPK pathway in [43] and phosphorylation waves traveling over long distances with constant amplitude and high velocity have been found. We discussed the nontrivial spatio-temporal structure of the numerical solution of the reaction-diffusion system (2.75) in Section 2.9.1.

Besides the simplification through the reduction of the spatial dimension, we further assumed that the activation of pro-caspase 8 by death receptors at the cell membrane occurs on a very small time scale in relation to the diffusion process, such that the activation of pro-caspase 8 by death receptors is integrated into the model as initial condition. Thereby, this reaction at the cell membrane has been omitted the rest of the time. Physiologically, this pulse stimulus corresponds to a death receptor internalization and turnover. Indeed, the activation of pro-caspase 8 by death receptors at the cell membrane can be incorporated into the model through time and parameter dependent boundary conditions. One possibility for this ansatz is presented in the Outlook (Chapter 4).

Although we made several simplifications in the reaction-diffusion model of the extrinsic signaling pathway, the quantitative results of the simulations are biologically realistic, especially the sizes of the initial death regions in Section 2.8 are of a realistic biological order. Furthermore, we observe inhibitory effects through the spatial extension of the model. As mentioned in Remark 2.1, we did not incorporate inhibitors for caspase 8 and caspase 3 like cFLIP, BAR or XIAP into the model, and the structure of the reaction network with its positive feedback suggests a behavior of the system where a tiny activation of pro-caspase ultimately leads to the death of the cell. However, the spatially extended reaction-diffusion system shows a robustness towards an accidental activation of pro-caspase 8. Besides, the simulation of the model enables the determination of the threshold for initially active caspase 8 and caspase 3 being necessary for the death of the cell. In particular, the value of the threshold is bounded away from zero.

3. Mathematical Model of the Receptor Clustering on the Cell Membrane

In Chapter 2, we introduced a mathematical model of the caspase-3/8 feedback loop and analyzed the evolution of caspase concentrations in a domain modeling the interior of a single cell. The investigated caspase cascade is the executive machinery of the apoptotic signaling pathway, and it is initiated at the cellular membrane by ligand-receptor clusters, cf. Figure 2.1. Hence, the knowledge about the clustering of receptors at the cell membrane is an essential part for the understanding of the extrinsic pro-apoptotic signaling pathway.

Before we introduce a mathematical model for the motion of receptors on the cellular membrane and describe the formation of ligand-receptor clusters, we first state the biological aspects of the receptors and ligands involved in the extrinsic pro-apoptotic signaling pathway in Section 3.1. Afterward, we introduce in Section 3.2 and Section 3.3 a particle model for the motion of receptors and ligands which consists of a system of nonlinearly coupled system of stochastic differential equations describing the translation and rotation of the receptors and ligands. In the subsequent Section 3.4, an approximated solution of the system of stochastic differential equations for the evolution of the ligand-receptor clusters is stated. By numerical simulations we are able to determine their size and structure. An overview of the implementation aspects is given in Section 3.5 followed by the results of the simulations in Section 3.6. Here, we also present the visualization of ligand-receptor clusters obtained through the visualization tool *cellVis*. Finally, we close Chapter 3 with some results concerning the speed-up we achieved through the mapping of the algorithms on GPGPU architectures in Section 3.7. Some parts of the particle model together with the mapping of the algorithms onto GPGPU architectures [8] and the description of the visualization tool [17] have already been published.

But before we derive the particle model, we first state the biological aspects of the death receptors and the corresponding ligands required for the particle model.

3.1 Biological Background of the Receptor Clustering

The extrinsic pro-apoptotic signaling pathway is triggered by signal competent ligand-receptor clusters on the cell membrane which are composed of so-called death receptors and the respective death receptor ligands. The receptors under consideration belong to the Tumor Necrosis Factor (TNF) receptor superfamily and the respective ligand is TNF. In the subsequent section, we first introduce the receptors TNFR1 and TNFR2 and describe their functions. Afterward, we present two types of TNF ligands, namely the soluble and the membrane-bound TNF. To complete the list of important particles for the initiation of the extrinsic signaling pathway, we introduce the so-called TNFR1/2-Fas chimeras and motivate subsequently the choice of particles being relevant for our particle model. Finally, we establish the binding behavior for the molecules under consideration.

The TNF receptor of type 1, briefly called TNFR1, and the TNF receptor of type 2, briefly denoted with TNFR2 belong to the most important representatives of the TNF receptor superfamiliy. Other notations for the TNF receptors are TNF-R55, TNFRβ, p55 or CD120a for TNFR1 and TNF-R75, TNFRα, p75 or CD120b for TNFR2 [62]. In the following, we adopt the notation TNFR1 and TNFR2 from [2, 6]. In other publications, for instance [10], the receptors are denoted with p60 and p80, according to the receptor masses of 60 kDa and 80 kDa, respectively.

While the two TNF receptors differ in their structure as well as in their function, they both consist of an extracellular part that contains four cysteine rich domains (CRD), a transmembrane region and an intracellular part, where different cellular responses are facilitated [62, 6]. In contrast to TNFR2, the intracellular part of TNFR1 contains a death domain that initiates the apoptotic signaling pathway [36]. Explaining the different biological activities of the two TNF receptors in detail would go beyond the scope of this thesis. We only mention that TNFR2 initiates the NFκB-pathway through the intracellular binding of TRAF2, for instance in endothelial cells [36], or regulates the rate of TNF association with TNFR1 in non-lymphoid cells by increasing the local concentration of TNF [60]. For this, TNFR2 has a higher affinity to TNF and a higher dissociating rate than TNFR1 that enables a ligand passing from TNFR2 to TNFR1 [60, 62, 22]. On the other hand, the intracellular part of TNFR1 contains a death domain and the recruitment of TRADD or FADD leads to the activation of caspases [36] and thereby to the stimulation of the extrinsic pro-apoptotic signaling pathway.

Besides the TNF receptors, TNF ligands are required for the initiation of the extrinsic pro-apoptotic signaling pathway. Two types of TNF ligands exist, a soluble cytokine and a membrane-integrated type II precursor [36]. The latter one has a weight of 26 kDa and

releases the soluble TNF which has a weight of 17 kDa [62]. Both types of TNF ligands interact with both TNF receptors, but in different ways and with different responses. Actually, the cellular responses also depend on the cell type under consideration and a generalization should be avoided. According to [22], most cell lines coexpress both TNF receptors, and the cellular responses to the soluble TNF seems to be dominated by the interaction with TNFR1.

Besides the wild type TNFR1 and TNFR2, other structures of composed receptors, so-called chimeras, have been investigated in [36]. These are composed of the cytoplasmic part of Fas and the extracellular domains of TNFR1 or TNFR2. The TNFR1-Fas chimera shows responsiveness to both TNF forms, the soluble and the membrane-bound TNF, whereas only the membrane-bound TNF induces apoptosis via the TNFR2-Fas chimera [36]. However, the soluble TNF is only capable to initiate the NFκB pathway via the TNFR2-Fas chimera [36].

Thus, for the investigation of the extrinsic pro-apoptotic signaling pathway, the consideration of TNFR1 and TNFR1-Fas chimeras besides the soluble TNF is of interest.

After introducing the most important particles for the clustering process on the cellular membrane, we take a look at their binding behavior. The soluble TNF exists in a homotrimeric pre-assembled form being able to bind up to three TNFR1 or TNFR1-Fas chimeras. The binding of TNFR1 with TNF occurs in the grooves between two of its three promoters in the broader half of the pyramidal structure [62, 7] and at TNFR1 via the domains CRD2 and CRD3 of the extracellular part of TNFR1 [10]. The interaction between two TNFR1 and between two TNFR1-Fas chimeras takes place via the membrane distal domain CRD1 of the extracellular part of TNFR1, more precisely through the pre-ligand binding assembly domain [7, 10]. Concerning the oligomerization behavior of TNF receptors, the opinions in biology differ. In [41], the scenario of trimerized TNFR1 is established, i.e., TNFR1 exist in a pre-assembled homotrimeric form. This opinion concerning the association behavior of TNFR1 is supported by the results published in [10]. On the other hand, the results published in [6] suggest the existence of homodimeric TNFR1-Fas besides monomeric TNFR1-Fas whereas the majority of the receptors exist as pre-assembled homodimers. Here, it must be mentioned that the cytoplasmic part of the corresponding receptors does not influence the association behavior of the receptors.

In summary, we consider in the following the wild type TNFR1, the receptor analyzed in [10], TNFR1-Fas in a dimeric and monomeric pre-form, the receptors investigated in [6], and the respective soluble TNF that is able to bind both receptor types. We further assume that TNFR1 and TNFR1-Fas are not located fixed at the cell membrane but

perform a random motion on the cell surface. Moreover, the soluble TNF also diffuses through the extracellular space. For simplicity, we assume that the soluble TNF stays in a two-dimensional plane directly above the cell membrane.

In the following section, we introduce a flexible particle model for the motion and the binding of TNF receptors, namely TNFR1 and TNFR1-Fas, and TNF ligands that allows for the treatment of various scenarios with the different receptor types. Hence, we study with this model the situation postulated in [10] with trimerized TNFR1 and the scenario with monomeric and dimeric TNFR1-Fas described in [6]. Finally, the results of these two hypotheses can be compared concerning the number of signal-competent cluster units.

3.2 Particle Model of the Clustering Processes

In this section, we introduce the general framework for the particle model. First, we note that the cell membrane can be considered as a two-dimensional area in the three-dimensional space. Thus, we model the cell surface as a two-dimensional domain, for simplicity without curvature, and take the simplest form, namely a square. Furthermore, the simulation domain is completed with periodic boundary conditions. Here, we assume that particles that leave the domain at one side due to the Brownian motion enters the domain opposite. So, the number of particles located on the cell membrane remains fix.

According to the dimension of the simulation domain, TNFR1, TNFR1-Fas and TNF are modeled as spatially extended particles, more precisely, as two-dimensional disks, see Figure 3.1, with a certain number of sectors modeling the binding sites, see Figure 3.2. The wild type TNFR1 exists in a homotrimeric pre-form and, thus, has three binding sites for TNF ligands, cf. [10]. Hence, the wild type TNFR1 is modeled by a disk with three sectors, each of them for the association with TNF ligands. TNFR1-Fas receptors exist as monomers being able to self-associate and as dimers that associate only with TNF ligands. A TNFR1-Fas monomer has two binding sites; one for a self-association

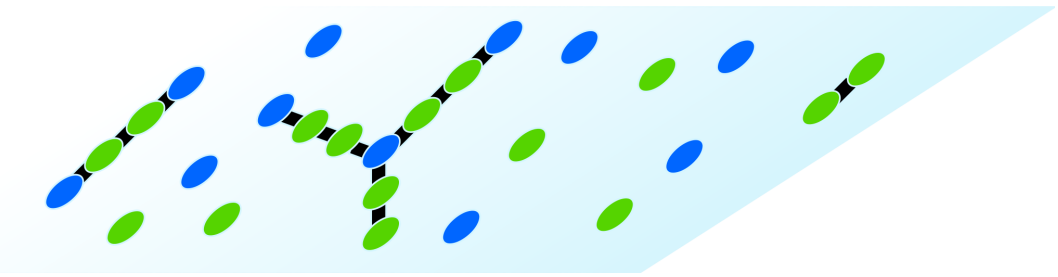

Figure 3.1: Two-dimensional simulation domain for the particle model. The green ellipses illustrate death receptor monomers and the blue ellipses describe death receptor ligands.

with another monomer and the other for an association with a TNF ligand. The disk which models a TNFR1-Fas monomer accordingly possesses two distinguishable sectors, cf. Figure 3.2. One can be occupied by a TNFR1-Fas monomer and the other by a TNF ligand. The dimeric TNFR1-Fas has two binding sites, both for the association with TNF ligands. The disk for the TNFR1-Fas dimer consequently has two indistinguishable sectors, see Figure 3.2. Finally, a TNF ligand is modeled by a disk with three sectors describing the three binding sites for the two receptor types, see Figure 3.2. In the following, the receptors TNFR1 and TNFR1-Fas in summary are called death receptors and the respective ligand is denoted with death receptor ligand. The motion of death receptors

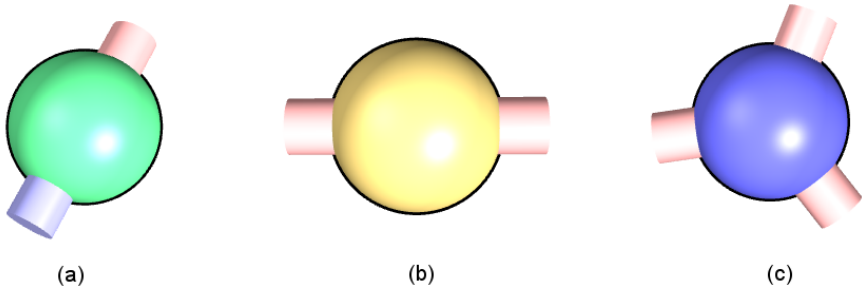

Figure 3.2: Illustration of three different particle types - (a) TNFR1-Fas monomer, (b) TNFR1-Fas dimer and (c) TNF ligand. The trimeric TNFR1 has the same structure as the TNF ligand. The blue binding site of the TNFR1-Fas monomer indicates the binding site for the association with another TNFR1-Fas monomer and the red one marks the binding site for the association with a TNF ligand. The TNFR1-Fas dimer has two red binding sites for the association with TNF ligands. The three particles are illustrated with the visualization tool *cellVis*.

and death receptor ligands in two spatial dimensions has three degrees of freedom: two for the particle translation of the center of mass and one for the particle rotation around the center of mass. Considering z_{P} death receptors and z_{L} death receptor ligands, we derive in the next two sections a system of $3(z_{\mathrm{P}} + z_{\mathrm{L}})$ equations for the description of the particle motion.

3.3 Model of the Particle Translation and Particle Rotation

In the subsequent section, we introduce a model for the particle translation and rotation. First, we look at the translation of a single particle. This motion is influenced by an interaction force effected by the vicinity of two particles and by impulses of the environmental lipids modeled by a Brownian motion. These assumptions finally yield one stochastic differential equation describing the translation of a single particle. Secondly, we consider the rotation of a single particle which again is influenced by the environmental particles and

the environmental lipids. Therefore, we obtain for the particle rotation an equation with a similar structure as for the particle translation. Afterward, we present scenarios with the different particle types introduced in Section 3.1 and Section 3.2. We regard the case where death receptors are pre-associated as trimers and the other case where monomeric and dimeric death receptors coexist. Actually, the latter will be splitted into three parts. To complete the mathematical model, we subsequently introduce the interactions between the particles for the different particle types, before we assemble the equations for a single particle to a nonlinearly coupled system of stochastic differential equations to obtain a mathematical model for a large amount of particles.

3.3.1 Derivation of Equations for the Particle Translation

The particle translation is described by the particle coordinates $\mathbf{x}$ and the velocity $\mathbf{v}$, whereas the relationship $\mathbf{v} = \dot{\mathbf{x}}$ holds. The momentum $\mathbf{p}$ is given by $\mathbf{p} = m \cdot \mathbf{v}$ and a variation in the momentum is caused by a force $\mathbf{F}$, thus $\frac{\mathrm{d}}{\mathrm{d}t}(m\mathbf{v}) = \mathbf{F}$. The mass m of the particles is constant, hence $m \cdot \dot{\mathbf{v}} = \mathbf{F}$. We assume that the force which affects the particles is composed of a random force $\sigma_{\text{trans}}\tilde{\mathbf{X}}_t$, a friction force $\mathbf{F}_{\text{fric}}$ and a force $\mathbf{F}_{\text{interact}}$ for the interaction between the particles. The friction force is proportional to the particle velocity and has the form $\mathbf{F}_{\text{fric}} = -\beta\mathbf{v}$ with the friction coefficient β. Thus, the particle translation is modeled by the Langevin equation

$$m\dot{\mathbf{v}} = \mathbf{F}_{\text{interact}} - \beta\mathbf{v} + \sigma_{\text{trans}}\tilde{\mathbf{X}}_t. \tag{3.1}$$

We assume that the components of the random force $\tilde{\mathbf{X}}_t$ describe a white noise. Then, the relation between the fluctuation of the random force σ_{trans} and β is given by the Einstein relation $\sigma_{\text{trans}} = \sqrt{2k_BT\beta}$, cf. [54, Chapter 8], where k_B is the Boltzmann constant and T is the temperature. Besides, we assume that the friction force is of Stokes type, so that the coefficient β has the form $\beta = 6\pi\eta R$, where η is the viscosity of the cell membrane and R is the radius of the particle. The masses of the death receptors and death receptor ligands are $m_{\text{receptor}} \approx 55\,\text{kDa}$ and $m_{\text{ligand}} \approx 51\,\text{kDa}$, respectively. With $1\,\text{kDa} \approx 1.6605 \cdot 10^{-24}\,\text{kg}$, these masses correspond to $m_{\text{receptor}} \approx 9.133 \cdot 10^{-23}\,\text{kg}$ and $m_{\text{ligand}} \approx 8.469 \cdot 10^{-23}\,\text{kg}$. By the way, we do not distinguish the masses of monomeric, dimeric and trimeric pre-forms of death receptors since the masses of the particles do not play any role in the model as we will see later.

In order to transform equation (3.1) into a dimensionless form, we introduce the magnitudes $\bar{\mathbf{x}} = \mathbf{x}/L, \bar{t} = t/\tau$ and $\bar{\mathbf{F}}_{\text{interact}} = L/\varepsilon \cdot \mathbf{F}_{\text{interact}}$, where ε is the binding energy between the particles, L is the length scale of the cell and τ is the time scale. Thus, the dimensionless velocity is $\bar{\mathbf{v}} = \tau/L \cdot \mathbf{v}$ and the dimensionless acceleration is $\bar{\mathbf{v}}' = \tau^2/L \cdot \dot{\mathbf{v}}$,

where the prime denotes the derivative with respect to $\bar{t}$. The binding energy between two death receptors is approximately $\varepsilon_{\mathrm{RR}} \approx 6k_BT$, and for a death receptor and a death receptor ligand we have $\varepsilon_{\mathrm{RL}} \approx 60k_BT$ [24]. Thus, we set $\varepsilon = 6k_BT$ and multiply the external force by a factor ten, if the interaction occurs between a death receptor and a death receptor ligand.
With these magnitudes, we obtain from (3.1)

$$\frac{L}{\tau^2} m \cdot \bar{\mathbf{v}}' = \frac{\varepsilon}{L} \cdot \bar{\mathbf{F}}_{\mathrm{interact}} - \beta \frac{L}{\tau} \cdot \bar{\mathbf{v}} + \sqrt{2k_BT\beta} \cdot \tilde{\mathbf{X}}_t. \tag{3.2}$$

The length scale of the cell is assumed to be $L = 10\,\mu\mathrm{m}$ and for the time scale we choose $\tau = 1\,\mathrm{s}$. The coefficient on the left-hand side of equation (3.2) is of the order 10^{-27} for the chosen length scale and the given masses, and the coefficients on the right-hand side of (3.2) are of the order 10^{-15} to 10^{-12}. Thus, we simplify (3.2) by omitting the left-hand side. Hence, equation (3.2) becomes

$$\bar{\mathbf{v}} = \frac{\varepsilon\tau}{L^2\beta} \cdot \bar{\mathbf{F}}_{\mathrm{interact}} + \sqrt{\frac{2k_BT\tau^2}{L^2\beta}} \cdot \tilde{\mathbf{X}}_t = \frac{6k_BT\tau}{L^2\beta} \cdot \bar{\mathbf{F}}_{\mathrm{interact}} + \sqrt{\frac{2k_BT\tau^2}{L^2\beta}} \cdot \tilde{\mathbf{X}}_t. \tag{3.3}$$

Introducing the parameter μ defined by $\mu^2 := \frac{k_BT\tau}{L^2\beta}$, we obtain from (3.3)

$$\bar{\mathbf{v}} = \frac{\mathrm{d}\bar{\mathbf{x}}}{\mathrm{d}\bar{t}} = 6\mu^2 \cdot \bar{\mathbf{F}}_{\mathrm{interact}} + \sqrt{2}\,\mu \cdot \tilde{\mathbf{X}}_{\bar{t}} \quad \text{with} \quad \tilde{\mathbf{X}}_{\bar{t}} := \sqrt{\tau}\tilde{\mathbf{X}}_t. \tag{3.4}$$

Integration of (3.4) with respect to time yields

$$\begin{aligned} \bar{\mathbf{x}}_{\bar{t}} &= \bar{\mathbf{x}}_0 + \int_0^{\bar{t}} 6\mu^2 \cdot \bar{\mathbf{F}}_{\mathrm{interact}} \mathrm{d}\bar{s} + \int_0^{\bar{t}} \sqrt{2}\mu \cdot \tilde{\mathbf{X}}_{\bar{s}} \mathrm{d}\bar{s} \\ &= \bar{\mathbf{x}}_0 + \int_0^{\bar{t}} 6\mu^2 \cdot \bar{\mathbf{F}}_{\mathrm{interact}} \mathrm{d}\bar{s} + \int_0^{\bar{t}} \sqrt{2}\mu \mathrm{d}\widetilde{\mathbf{W}}_{\mathrm{trans},\bar{s}} \end{aligned} \tag{3.5}$$

with $\mathrm{d}\widetilde{\mathbf{W}}_{\mathrm{trans},\bar{s}} = \tilde{\mathbf{X}}_{\bar{s}}\mathrm{d}\bar{s}$. The second integral on the right-hand side of (3.5) is an Itô stochastic integral with respect to the Wiener process $\widetilde{\mathbf{W}}_{\mathrm{trans}} = \{\widetilde{\mathbf{W}}_{\mathrm{trans},\bar{t}}, \bar{t} \geq 0\}$. We abbreviate the integral equation (3.5) as an Itô stochastic differential equation

$$\mathrm{d}\bar{\mathbf{x}} = 6\mu^2 \cdot \bar{\mathbf{F}}_{\mathrm{interact}} \mathrm{d}\bar{t} + \sqrt{2}\mu \cdot \mathrm{d}\widetilde{\mathbf{W}}_{\mathrm{trans},\bar{t}}, \tag{3.6}$$

where $\mathrm{d}\widetilde{\mathbf{W}}_{\mathrm{trans},\bar{t}}$ are increments of the Wiener process $\widetilde{\mathbf{W}}_{\mathrm{trans}} = \{\widetilde{\mathbf{W}}_{\mathrm{trans},\bar{t}}, \bar{t} \geq 0\}$ and $\bar{\mathbf{x}}$ are the coordinates of the particles, cf. [20].

To model the interaction between two particles, a potential which describes the inter-

action between uncharged and chemically unbounded atoms is necessary. This is typically done with a Lennard-Jones potential, which has an attractive impact given by the Van-der-Waals force and a repulsive impact for very small distances between the particles affected by the Pauli repulsion. For simplicity, we choose for our model the Lennard-Jones-$(2n, n)$ potential

$$V_{\mathrm{LJ}}^{\mathrm{P}}(r) = \varepsilon\gamma_n \left(\left(\frac{\sigma_{\mathrm{LJ}}^{\mathrm{P}}}{r} \right)^{2n} - \alpha_n \left(\frac{\sigma_{\mathrm{LJ}}^{\mathrm{P}}}{r} \right)^{n} \right), \tag{3.7}$$

where r is the distance between two particles, $\sigma_{\mathrm{LJ}}^{\mathrm{P}}$ describes the size of the particles, and ε is the depth of the potential and corresponds to the binding energy. The parameters γ_n and α_n are determined below under suitable conditions for the potential $V_{\mathrm{LJ}}^{\mathrm{P}}$. The dimensionless form of the Lennard-Jones potential is

$$\bar{V}_{\mathrm{LJ}}^{\mathrm{P}}(\bar{r}) = \gamma_n \left(\left(\frac{\bar{\sigma}_{\mathrm{LJ}}^{\mathrm{P}}}{\bar{r}} \right)^{2n} - \alpha_n \left(\frac{\bar{\sigma}_{\mathrm{LJ}}^{\mathrm{P}}}{\bar{r}} \right)^{n} \right), \tag{3.8}$$

with $\bar{r} = r/L$ and $\bar{\sigma}_{\mathrm{LJ}}^{\mathrm{P}} = \sigma_{\mathrm{LJ}}^{\mathrm{P}}/L$. The interaction force $\bar{\mathbf{F}}_{\mathrm{interact}}$ is given by the negative gradient of the potential $\bar{V}_{\mathrm{LJ}}^{\mathrm{P}}(\bar{r})$. First, we ask for the potential that its minimum is $-\varepsilon$, the binding energy of the particles under consideration. The minimum of the potential $V_{\mathrm{LJ}}^{\mathrm{P}}$ is determined by the condition

$$\frac{\partial V_{\mathrm{LJ}}^{\mathrm{P}}}{\partial r} = \varepsilon\gamma_n \left(-2n \cdot \frac{1}{r} \cdot \left(\frac{\sigma_{\mathrm{LJ}}^{\mathrm{P}}}{r} \right)^{2n} + \alpha_n \cdot n \cdot \frac{1}{r} \cdot \left(\frac{\sigma_{\mathrm{LJ}}^{\mathrm{P}}}{r} \right)^{n} \right) \stackrel{!}{=} 0.$$

With this, we obtain for the minimizing distance

$$-2 \left(\frac{\sigma_{\mathrm{LJ}}^{\mathrm{P}}}{r} \right)^{2n} + \alpha_n \left(\frac{\sigma_{\mathrm{LJ}}^{\mathrm{P}}}{r} \right)^{n} = 0, \quad \text{that implies} \quad \alpha_n = 2 \left(\frac{\sigma_{\mathrm{LJ}}^{\mathrm{P}}}{r} \right)^{n}.$$

Now, we demand on the potential to reach its minimum for $r^* = 2\sigma_{\mathrm{LJ}}^{\mathrm{P}}$. Thus, we have $\alpha_n = 2^{1-n}$. The condition $V_{\mathrm{LJ}}^{\mathrm{P}}(r^*) = -\varepsilon$ finally yields the value for γ_n,

$$V_{\mathrm{LJ}}^{\mathrm{P}}(r^*) = \gamma_n\varepsilon \left(\left(\frac{1}{2} \right)^{2n} - 2^{1-n} \left(\frac{1}{2} \right)^{n} \right) = \varepsilon\gamma_n \left(-2^{-2n} \right) \stackrel{!}{=} -\varepsilon \;\Rightarrow\; \gamma_n = 2^{2n}.$$

With the values for α_n and γ_n, the Lennard-Jones potential (3.8) reads

$$\bar{V}_{\mathrm{LJ}}^{\mathrm{P}}(\bar{r}) = 2^{2n} \left(\left(\frac{\bar{\sigma}_{\mathrm{LJ}}^{\mathrm{P}}}{\bar{r}} \right)^{2n} - 2^{1-n} \left(\frac{\bar{\sigma}_{\mathrm{LJ}}^{\mathrm{P}}}{\bar{r}} \right)^{n} \right). \tag{3.9}$$

For the interaction between particles of the same type, except death receptor

monomers, we introduce a further potential with a sole repulsive impact. For this purpose, we consider the repulsive part of the Lennard-Jones potential in (3.9) and define

$$\bar{W}_{\mathrm{LJ}}^{\mathrm{P}}(\bar{r}) = 2^{2n} \left(\frac{\bar{\sigma}_{\mathrm{LJ}}^{\mathrm{P}}}{\bar{r}} \right)^{2n}. \tag{3.10}$$

Since the interaction between the particles is short-ranged, i.e. on a length scale of several nanometers, we introduce a cut-off radius r_{cut} for the potentials $\bar{V}_{\mathrm{LJ}}^{\mathrm{P}}(\bar{r})$ and $\bar{W}_{\mathrm{LJ}}^{\mathrm{P}}(\bar{r})$. For this purpose, we set

$$\bar{V}_{\mathrm{LJ,cut}}^{\mathrm{P}}(\bar{r}) := \begin{cases} \bar{V}_{\mathrm{LJ}}^{\mathrm{P}}(\bar{r}), & \text{for } \bar{r} \leq r_{\mathrm{cut}}, \\ 0, & \text{for } \bar{r} > r_{\mathrm{cut}} \end{cases} \tag{3.11}$$

and

$$\bar{W}_{\mathrm{LJ,cut}}^{\mathrm{P}}(\bar{r}) := \begin{cases} \bar{W}_{\mathrm{LJ}}^{\mathrm{P}}(\bar{r}), & \text{for } \bar{r} \leq r_{\mathrm{cut}}, \\ 0, & \text{for } \bar{r} > r_{\mathrm{cut}}. \end{cases} \tag{3.12}$$

With these potentials at hand and with the fact that the force acting on a particle is given by the negative gradient of the potential, all the ingredients of the stochastic differential equation (3.6) are determined. The structure of the interaction forces for the different particle types will be given later in Section 3.3.4.

In order to describe the motion of the particles in more detail, we introduce a further equation for the particle rotation in the following section.

3.3.2 Derivation of Equations for the Particle Rotation

Besides the translation, the particles also perform a rotation described by the angle of rotation φ and the angular velocity ω. Here, φ describes the direction of one particle binding site and thereby defines the orientation of a particle. The directions of the other binding sites can be simply derived from φ. The relationship between the angle of rotation and the angular velocity is given by $\omega = \dot{\varphi}$. The angular momentum $\mathcal{L}$ of a rotating particle is given by $\mathcal{L} = I \cdot \omega$, where I is the moment of inertia of the particle depending on its mass and radius. A variation of the angular momentum is caused by a torsional moment D, i.e. $\dot{\mathcal{L}} = D$. With a constant moment of inertia I it follows $I\dot{\omega} = D$. We assume that the torsional moment is composed of a random torsional moment $\sigma_{\mathrm{rot}}\tilde{D}_t$ describing the white noise for the particle rotation, a friction torsional moment D_{fric} and an additional torsional moment D_{drill} similarly to the composition of the force for the particle translation. The friction torsional moment D_{fric} has the same form as the friction force and is thereby proportional to the angular velocity, i.e. $D_{\mathrm{fric}} = -\gamma_{\mathrm{rot}} \cdot \omega$, with the

friction coefficient γ_{rot}. In summary, the particle rotation is modeled by a Langevin equation analogously to the Langevin equation for the particle translation, i.e.

$$I\dot{\omega} = D_{\text{drill}} - \gamma_{\text{rot}}\omega + \sigma_{\text{rot}}\tilde{D}_t. \tag{3.13}$$

The torsional moment D_{drill} cares for the correct mutual orientation of particles lying close to each other, relative to the orientation of the binding sites. It will be specified later in Section 3.3.4.

The relation between the diffusion coefficient σ_{rot} and the friction coefficient γ_{rot} has the same structure as the relation for the coefficients of the translation, i.e. $\sigma_{\text{rot}} = \sqrt{2k_BT\gamma_{\text{rot}}}$. The coefficient γ_{rot} is given by $\gamma_{\text{rot}} = 8\pi\eta R^3$ [53], where η is the viscosity of the cell membrane and R is the radius of the particle. Furthermore, we write equation (3.13) in a dimensionless form by introducing the magnitudes $\bar{\varphi} = \varphi$ and $\bar{\omega} = \omega \cdot \tau$, which yields $\bar{\omega}' := \frac{\mathrm{d}\bar{\omega}}{\mathrm{d}\bar{t}} = \tau^2 \frac{\mathrm{d}\omega}{\mathrm{d}t}$. Thus, equation (3.13) becomes

$$\frac{I}{\tau^2}\bar{\omega}' = D_{\text{drill}} - \frac{\gamma_{\text{rot}}}{\tau} \cdot \bar{\omega} + \sqrt{2k_BT\gamma_{\text{rot}}} \cdot \tilde{D}_t. \tag{3.14}$$

We write D_{drill} as a function of particle coordinates and orientations, namely $D_{\text{drill}} = D_r \cdot g(\bar{\mathbf{x}}, \bar{\varphi})$, where the constant coefficient D_r is proportional to the thermal energy k_BT, i.e. $D_r = \kappa k_BT$, and the function $g(\bar{\mathbf{x}}, \bar{\varphi})$ describes the mutual influence of the particles on the torsional moment. Thus, equation (3.14) can be written as

$$\frac{I}{\tau^2}\bar{\omega}' = \kappa k_BT \cdot g(\bar{\mathbf{x}}, \bar{\varphi}) - \frac{\gamma_{\text{rot}}}{\tau} \cdot \bar{\omega} + \sqrt{2k_BT\gamma_{\text{rot}}} \cdot \tilde{D}_t. \tag{3.15}$$

Before we will define the function $g(\bar{\mathbf{x}}, \bar{\varphi})$ for the different particle types in Section 3.3.4, we first simplify equation (3.15) by studying its coefficients.
First of all, we will give a rude estimation for I. The moment of inertia of a molecule is given by the sum over all squared distances of each atom from the rotational axis multiplied by the mass of the respective atom, i.e.

$$I = \sum_{i=1}^{\#\,\text{atoms}} m_{\text{atom},i} \cdot r_i^2.$$

Defining by $r_{\max}$ the largest possible distance of an atom to the rotational axis, we obtain

$$I \leq \sum_{i=1}^{\#\,\text{atoms}} m_{\text{atom},i} \cdot r_{\max}^2 = r_{\max}^2 \cdot m_{\text{particle}}.$$

Since the total mass of a TNFR1 is about $55\,\text{kDa} \approx 9.133 \cdot 10^{-23}\,\text{kg}$ and the size of the

receptor is assumed to be 1 nm, the estimation of the moment of inertia I yields

$$I \leq 10^{-18}\,\mathrm{m}^2 \cdot 9.133 \cdot 10^{-23}\,\mathrm{kg} = 9.133 \cdot 10^{-41}\,\mathrm{kg\,m}^2.$$

The other particles have a moment of inertia of the same order due to their similar mass and size. With this parameter setting, the coefficient on the left-hand side of equation (3.15) is of the order 10^{-40}, the terms on the right-hand side are of the order 10^{-19} to 10^{-15}. Thus, analogously to the derivation of the equation for the particle translation, the left-hand side of equation (3.15) is negligible, which gives

$$\bar{\omega} = \frac{\tau \kappa k_B T}{\gamma_{\mathrm{rot}}} \cdot g(\bar{\mathbf{x}}, \bar{\varphi}) + \sqrt{\frac{2 k_B T \tau}{\gamma_{\mathrm{rot}}}} \tilde{D}_{\bar{t}} \text{ with } \tilde{D}_{\bar{t}} := \sqrt{\tau} \tilde{D}_t. \tag{3.16}$$

Finally, we obtain

$$\frac{\mathrm{d}\bar{\varphi}}{\mathrm{d}\bar{t}} = \bar{\omega} = \kappa \frac{k_B T \tau}{\beta L^2} \cdot \frac{\beta L^2}{\gamma_{\mathrm{rot}}} \cdot g(\bar{\mathbf{x}}, \bar{\varphi}) + \sqrt{2} \sqrt{\frac{k_B T \tau}{\beta L^2}} \cdot \sqrt{\frac{\beta L^2}{\gamma_{\mathrm{rot}}}} \cdot \tilde{D}_{\bar{t}},$$

which can be written as

$$\frac{\mathrm{d}\bar{\varphi}}{\mathrm{d}\bar{t}} = \kappa \mu^2 \zeta^2 \cdot g(\bar{\mathbf{x}}, \bar{\varphi}) + \sqrt{2} \mu \zeta \cdot \tilde{D}_{\bar{t}}, \tag{3.17}$$

with the abbreviations $\mu^2 = \frac{k_B T \tau}{\beta L^2}$ and $\zeta^2 = \frac{\beta L^2}{\gamma_{\mathrm{rot}}}$. Integration of equation (3.17) with respect to time yields

$$\begin{aligned} \bar{\varphi}_{\bar{t}} &= \bar{\varphi}_0 + \int_0^{\bar{t}} \kappa \mu^2 \zeta^2 \cdot g(\bar{\mathbf{x}}, \bar{\varphi})\,\mathrm{d}\bar{s} + \int_0^{\bar{t}} \sqrt{2} \mu \zeta \cdot \tilde{D}_{\bar{s}}\,\mathrm{d}\bar{s} \\ &= \bar{\varphi}_0 + \int_0^{\bar{t}} \kappa \mu^2 \zeta^2 \cdot g(\bar{\mathbf{x}}, \bar{\varphi})\,\mathrm{d}\bar{s} + \int_0^{\bar{t}} \sqrt{2} \mu \zeta\,\mathrm{d}\widetilde{W}_{\mathrm{rot},\bar{s}} \end{aligned} \tag{3.18}$$

with $\mathrm{d}\widetilde{W}_{\mathrm{rot},\bar{s}} = \tilde{D}_{\bar{s}}\,\mathrm{d}\bar{s}$. The second integral on the right-hand side of (3.18) is again an Itô stochastic integral with respect to the Wiener process $\widetilde{W}_{\mathrm{rot}} = \{\widetilde{W}_{\mathrm{rot},\bar{t}}, \bar{t} \geq 0\}$. Again, we rewrite the stochastic integral equation as an Itô stochastic differential equation

$$\mathrm{d}\bar{\varphi} = \kappa \mu^2 \zeta^2 \cdot g(\bar{\mathbf{x}}, \bar{\varphi})\mathrm{d}\bar{t} + \sqrt{2} \mu \zeta \cdot \mathrm{d}\widetilde{W}_{\mathrm{rot},\bar{t}}, \tag{3.19}$$

where $\mathrm{d}\widetilde{W}_{\mathrm{rot},\bar{t}}$ are increments of the Wiener process $\widetilde{W}_{\mathrm{rot}}$ and $\bar{\varphi}$ is the angle defining the orientation of the particle binding site. To complete the stochastic differential equation (3.19), the function $g(\bar{\mathbf{x}}, \bar{\varphi})$ has to be specified for the different particle types. This

will be done in Section 3.3.4. But before, we oppose the scenarios with the different death receptor structures in Section 3.3.3.

3.3.3 Distinction of Cases for Different Death Receptor Structures

After deriving stochastic differential equations for the particle translation and rotation in Section 3.3.1 and Section 3.3.2, we present here the configurations for the different death receptors. In order to compare the cluster formation for the different death receptor types, we develop a particle model for each of the configurations listed below, starting with the equations derived in Section 3.3.1 and Section 3.3.2. For the different configurations, we distinguish the cases where

a) the death receptors are TNFR1-Fas chimeras which exist in a monomeric or dimeric pre-form,

b) the death receptors are TNFR1 which exist in a trimeric pre-form,

c) the death receptors are pre-associated with death receptor ligands and form so-called cluster units.

We specify the three cases in more detail and split the first case into three parts.

a.i) First, we assume that the death receptors initially exist as monomers being able to bind to another death receptor monomer and a death receptor ligand at the opposite binding site.

a.ii) Second, we consider death receptors in a dimeric pre-form. These death receptor dimers have two binding sites and only bind to the respective death receptor ligand.

a.iii) Third, we think about the more general scenario where death receptor monomers and dimers coexist. Again, death receptor monomers can associate with another death receptor monomer and with a death receptor ligand at the opposite binding site. The death receptor dimers have two binding sites for the association with death receptor ligands.

b) Regarding death receptors in a trimeric pre-form, we follow the arguments of [10]. Since TNFR1 are fixed bound to two other TNFR1 and thereby form death receptor trimers, these trimers have three binding sites for the association with the respective death receptor ligand.

c) Finally, we consider so-called cluster units consisting of three death receptor monomers bound to one death receptor ligand. This formation stays fix during

the whole time. This assumption is made due to the fact that the binding energy for the association of a TNFR1 and a TNF ligand is by a factor ten larger than for the self-association of two TNFR1.

Due to the Brownian motion, a fragmentation of a bond between associated particles within a ligand-receptor cluster, which consists of several death receptors and death receptor ligands, can occur. However, pre-associated particles like dimeric or trimeric death receptors or the cluster units in case *c*) are not decomposed. In fact, these structures remain fixed.

Obviously, the binding behavior of the different death receptors differ. So, death receptor monomers and death receptor dimers have two binding sites whereas death receptor trimers have three binding sites. According to the different number of binding sites, the orientation of the binding sites vary. That is why the structure of the ligand-receptor cluster depends on the type of death receptor under consideration. But we are not only interested in the structure of large ligand-receptor clusters. A more significant aspect to analyze is the amount of signal competent cluster units for the given particle configurations. Of course, the structure of the signal competent cluster unit depends on the death receptor type.

First, we give the structure of signal competent cluster units in case of dimeric death receptors. According to [6], the signal competent cluster unit consists of one death receptor dimer bound to two death receptor ligands. Since a death receptor dimer can be understood as self-associated death receptor monomers, we assume that the signal competent cluster unit in case of death receptor monomers consists of two death receptor monomers, each bound to a death receptor ligand. In case of the coexistence of death receptor monomers and death receptor dimers, we assume that both structures are signal competent. However, in previous years, other hypotheses about the signal competent cluster units have been proposed. In [3], it was suggested that three death receptors bound to one death receptor ligand is signal competent. Here, a TNF receptor of type I has a monomeric structure. Thus, we analyze the structure where three death receptor monomers are bound to one death receptor ligand which forms the center of this complex. Nevertheless, in [10], the existence of trimeric TNF receptors of type I was postulated. However, in case of death receptor trimers, the structure of signal competent cluster units is rather unclear. We think of two structures that would be eligible for signal transduction. The first possibility for a signal competent structure in case of death receptor trimers could be three death receptor trimers bound to one death receptor ligand which again is located in the center of the complex similar to the scenario introduced in [3]. A second suggestion for the signal competent unit in case of death receptor trimers

picks up the idea of the scenario with dimeric death receptors. In case of death receptor dimers, the two binding sites of the death receptor dimer are occupied by a death receptor ligand. The corresponding structure for death receptor trimers would be one death receptor trimer bound to three death receptor ligands, where the death receptor trimer is located in the center of the complex.
The last scenario deals with fixed cluster units consisting of one death receptor ligand bound to three death receptor monomers. According to [3], this structure is supposed to be signal competent. Indeed, this assumption makes it unnecessary to analyze the scenario with pre-associated cluster units. However, following the arguments of [6], the signal competent cluster unit in case of death receptor monomers is given by two associated death receptor monomers each bound to a death receptor ligand. Finally, this structure evolves from the binding of two cluster units. Hence, in case of pre-associated cluster units, we suggest that two bonded cluster units are signal competent.

In summary, we have six different structures that are supposed to be signal competent depending on the particle configuration. For death receptor monomers and death receptor trimers, we even have two possible structures for a signal competent cluster unit. In order to study the time evolution of the signal competent cluster units for the given particle configurations, we first complete the particle model. For this purpose, we introduce the interactions between the particles given by the interaction force $\bar{\mathbf{F}}_{\text{interact}}$ and the function g for each particle type in Section 3.3.4.

3.3.4 Modeling the Interaction between the Particles

In the following, we introduce the force $\bar{\mathbf{F}}_{\text{interact}}$ and the function g for the different particle types. These quantities are required for the completion of the particle model. But first of all, we introduce abbreviations for the particle types, namely M for death receptor monomers, D for death receptor dimers, T for death receptor trimers, L for death receptor ligands and U for cluster units. Additionally, to make the definition of the force $\bar{\mathbf{F}}_{\text{interact}}$ and the function g more simple, we summarize the particle coordinates and the angles of the binding sites in matrices and vectors, respectively, i.e.

$$\begin{aligned}
\bar{\boldsymbol{\xi}}_{\mathrm{M}} &= (\bar{\mathbf{x}}_{\mathrm{M}_1},\ldots,\bar{\mathbf{x}}_{\mathrm{M}_{z_{\mathrm{M}}}}), \quad \bar{\boldsymbol{\varphi}}_{\mathrm{M}} = (\bar{\varphi}_{\mathrm{M}_1},\ldots,\bar{\varphi}_{\mathrm{M}_{z_{\mathrm{M}}}}),\\
\bar{\boldsymbol{\xi}}_{\mathrm{D}} &= (\bar{\mathbf{x}}_{\mathrm{D}_1},\ldots,\bar{\mathbf{x}}_{\mathrm{D}_{z_{\mathrm{D}}}}), \quad \bar{\boldsymbol{\varphi}}_{\mathrm{D}} = (\bar{\varphi}_{\mathrm{D}_1},\ldots,\bar{\varphi}_{\mathrm{D}_{z_{\mathrm{D}}}}),\\
\bar{\boldsymbol{\xi}}_{\mathrm{T}} &= (\bar{\mathbf{x}}_{\mathrm{T}_1},\ldots,\bar{\mathbf{x}}_{\mathrm{T}_{z_{\mathrm{T}}}}), \quad \bar{\boldsymbol{\varphi}}_{\mathrm{T}} = (\bar{\varphi}_{\mathrm{T}_1},\ldots,\bar{\varphi}_{\mathrm{T}_{z_{\mathrm{T}}}}),\\
\bar{\boldsymbol{\xi}}_{\mathrm{L}} &= (\bar{\mathbf{x}}_{\mathrm{L}_1},\ldots,\bar{\mathbf{x}}_{\mathrm{L}_{z_{\mathrm{L}}}}), \quad \bar{\boldsymbol{\varphi}}_{\mathrm{L}} = (\bar{\varphi}_{\mathrm{L}_1},\ldots,\bar{\varphi}_{\mathrm{L}_{z_{\mathrm{L}}}}),\\
\bar{\boldsymbol{\xi}}_{\mathrm{U}} &= (\bar{\mathbf{x}}_{\mathrm{U}_1},\ldots,\bar{\mathbf{x}}_{\mathrm{U}_{z_{\mathrm{U}}}}), \quad \bar{\boldsymbol{\varphi}}_{\mathrm{U}} = (\bar{\varphi}_{\mathrm{U}_1},\ldots,\bar{\varphi}_{\mathrm{U}_{z_{\mathrm{U}}}}).
\end{aligned} \tag{3.20}$$

Here, z_{M}, z_{D}, z_{T}, z_{L} and z_{U} denote the numbers of death receptor monomers, death receptor dimers, death receptor trimers, death receptor ligands and cluster units, respectively.

Interaction forces and the function g for the different particle types

First, we itemize the forces and the functions g according to the particle type starting with death receptor monomers. Subsequently, we state $\bar{\mathbf{F}}_{\text{interact}}$ and g for death receptor dimers, and proceed with the interaction terms for death receptor trimers and death receptor ligands and conclude this section with the terms for cluster units. In each item, we first introduce some angles required for the angular dependency of the interaction terms due to the orientation of the binding sites.

1) In case of death receptor monomers, the two binding sites are distinguishable, i.e., one of the two binding sites is for the association with death receptor monomers while the other one is for the association with death receptor ligands. Therefore, we arbitrarily identify the angles $\bar{\varphi}_{\mathrm{M}_i}, i = 1, \dots, z_{\mathrm{M}}$, in (3.20) with the binding site for the association with death receptor monomers. Then, the binding site for death receptor ligands is given by $\bar{\varphi}_{\mathrm{M}_i} + \pi$. We further consider the vectors $\mathbf{e}_{\mathrm{M}_k\mathrm{M}_i}$, $\mathbf{e}_{\mathrm{D}_k\mathrm{M}_i}$ and $\mathbf{e}_{\mathrm{L}_k\mathrm{M}_i}$ connecting the center of mass of M_k and M_i, D_k and M_i, and L_k and M_i, respectively, and define $\bar{\varphi}_{\mathbf{e}_{\mathrm{M}_k\mathrm{M}_i}}$ as the angle between the vector $\mathbf{e}_{\mathrm{M}_k\mathrm{M}_i}$ and the positive real line. Analogously, we define $\bar{\varphi}_{\mathbf{e}_{\mathrm{L}_k\mathrm{M}_i}}$. With the angles $\bar{\varphi}_{\mathbf{e}_{\mathrm{M}_k\mathrm{M}_i}}$ and $\bar{\varphi}_{\mathbf{e}_{\mathrm{L}_k\mathrm{M}_i}}$ at hand, we introduce the angles $\psi_{\mathrm{M}_k;\mathrm{M}_i} := \bar{\varphi}_{\mathbf{e}_{\mathrm{M}_k\mathrm{M}_i}} - \bar{\varphi}_{\mathrm{M}_k}$ and $\psi_{\mathrm{L}_k;\mathrm{M}_i} := \bar{\varphi}_{\mathbf{e}_{\mathrm{L}_k\mathrm{M}_i}} - \bar{\varphi}_{\mathrm{L}_k;\mathrm{M}_i}$. Here, the angle $\bar{\varphi}_{\mathrm{L}_k;\mathrm{M}_i}$ is given by

$$\bar{\varphi}_{\mathrm{L}_k;\mathrm{M}_i} := \underset{\zeta\in\Lambda_{\mathrm{L}_k}}{\operatorname{argmin}}\{|\bar{\varphi}_{\mathbf{e}_{\mathrm{L}_k\mathrm{M}_i}} - \zeta|\} \text{ with } \Lambda_{\mathrm{L}_k} := \{\bar{\varphi}_{\mathrm{L}_k}, \bar{\varphi}_{\mathrm{L}_k} + \frac{2\pi}{3}, \bar{\varphi}_{\mathrm{L}_k} + \frac{4\pi}{3}\}.$$

With this notation, the force for death receptor monomers is given by

$$\begin{aligned}
\bar{\mathbf{F}}_{\mathrm{M}_i}(\bar{\boldsymbol{\xi}}_{\mathrm{M/D/L}}, \bar{\boldsymbol{\varphi}}_{\mathrm{M/D/L}}) = &- \sum_{k=1}^{z_{\mathrm{D}}} \frac{\mathrm{d}}{\mathrm{d}r}\bar{W}^{\mathrm{D}}_{\mathrm{LJ,cut}}(|\bar{\mathbf{x}}_{\mathrm{D}_k} - \bar{\mathbf{x}}_{\mathrm{M}_i}|)\mathbf{e}_{\mathrm{D}_k\mathrm{M}_i} \\
&- \sum_{k=1,k\neq i}^{z_{\mathrm{M}}} \Bigg(\frac{\mathrm{d}}{\mathrm{d}r}\bar{V}^{\mathrm{M}}_{\mathrm{LJ,cut}}(|\bar{\mathbf{x}}_{\mathrm{M}_k} - \bar{\mathbf{x}}_{\mathrm{M}_i}|) \cdot H(\delta - |\psi_{\mathrm{M}_k;\mathrm{M}_i}|) \\
&+ \frac{\mathrm{d}}{\mathrm{d}r}\bar{W}^{\mathrm{M}}_{\mathrm{LJ,cut}}(|\bar{\mathbf{x}}_{\mathrm{M}_k} - \bar{\mathbf{x}}_{\mathrm{M}_i}|) \cdot H(|\psi_{\mathrm{M}_k;\mathrm{M}_i}| - \delta) \Bigg) \mathbf{e}_{\mathrm{M}_k\mathrm{M}_i} \\
&- \sum_{k=1}^{z_{\mathrm{L}}} \Bigg(\frac{\mathrm{d}}{\mathrm{d}r}\bar{V}^{\mathrm{L}}_{\mathrm{LJ,cut}}(|\bar{\mathbf{x}}_{\mathrm{L}_k} - \bar{\mathbf{x}}_{\mathrm{M}_i}|) \cdot H(\delta - |\psi_{\mathrm{L}_k;\mathrm{M}_i}|) \\
&+ \frac{\mathrm{d}}{\mathrm{d}r}\bar{W}^{\mathrm{L}}_{\mathrm{LJ,cut}}(|\bar{\mathbf{x}}_{\mathrm{L}_k} - \bar{\mathbf{x}}_{\mathrm{M}_i}|) \cdot H(|\psi_{\mathrm{L}_k;\mathrm{M}_i}| - \delta) \Bigg) \mathbf{e}_{\mathrm{L}_k\mathrm{M}_i},
\end{aligned}$$

$i = 1, \dots, z_{\mathrm{M}}$, where z_{M} denotes the number of death receptor monomers. Here, the

gradient of the potential is the derivative with respect to the variable r since the potentials $\bar{V}^{\mathrm{P}}_{\mathrm{LJ,cut}}$ and $\bar{W}^{\mathrm{P}}_{\mathrm{LJ,cut}}$ are assumed to be radially symmetric. Furthermore, δ is the apex angle of the binding site and $H(\,\cdot\,)$ is the Heaviside function. Here, the definition of $\bar{\mathbf{F}}_{\mathrm{M}_i}, i = 1, \ldots, z_{\mathrm{M}}$, is given in a general form: in case of the sole existence of death receptor monomers, the number of death receptor dimers z_{D} is set to zero. In case of the coexistence of death receptor dimers and death receptor monomers, the sum over all death receptor monomers and the sum over all death receptor dimers is taken into account.

To define the function g for death receptor monomers, we introduce further abbreviations for the distance between the particles, namely $R_{\mathrm{M}_i;\mathrm{M}_k} := |\mathbf{e}_{\mathrm{M}_i\mathrm{M}_k}|$ and $R_{\mathrm{M}_i;\mathrm{L}_k} := |\mathbf{e}_{\mathrm{M}_i\mathrm{L}_k}|$ where $\mathbf{e}_{\mathrm{M}_i\mathrm{M}_k} := -\mathbf{e}_{\mathrm{M}_k\mathrm{M}_i}$ and $\mathbf{e}_{\mathrm{M}_i\mathrm{L}_k} := -\mathbf{e}_{\mathrm{L}_k\mathrm{M}_i}$. Then, for death receptor monomers we define

$$\begin{aligned} g_{\mathrm{M}_i}(\bar{\boldsymbol{\xi}}_{\mathrm{M/L}}, \bar{\boldsymbol{\varphi}}_{\mathrm{M/L}}) := & \frac{1}{z_{\mathrm{M}} + z_{\mathrm{L}}} \left(\sum_{k=1, k\neq i}^{z_{\mathrm{M}}} \frac{3\sqrt{3}}{2\pi^3} \psi_{\mathrm{M}_i;\mathrm{M}_k} (\pi - \psi_{\mathrm{M}_i;\mathrm{M}_k})(\pi + \psi_{\mathrm{M}_i;\mathrm{M}_k}) \times \right. \\ & \times H(r_{\mathrm{cut}} - R_{\mathrm{M}_i;\mathrm{M}_k}) \cdot \frac{r_{\mathrm{cut}} - R_{\mathrm{M}_i;\mathrm{M}_k}}{r_{\mathrm{cut}}} \\ & + \sum_{k=1}^{z_{\mathrm{L}}} \frac{3\sqrt{3}}{2\pi^3} \psi_{\mathrm{M}_i;\mathrm{L}_k} (\pi - \psi_{\mathrm{M}_i;\mathrm{L}_k})(\pi + \psi_{\mathrm{M}_i;\mathrm{L}_k}) \times \\ & \left. \times H(r_{\mathrm{cut}} - R_{\mathrm{M}_i;\mathrm{L}_k}) \cdot \frac{r_{\mathrm{cut}} - R_{\mathrm{M}_i;\mathrm{L}_k}}{r_{\mathrm{cut}}} \right). \end{aligned}$$

Here, the angles $\psi_{\mathrm{M}_i;\mathrm{M}_k}$ and $\psi_{\mathrm{M}_i;\mathrm{L}_k}$ are given by $\psi_{\mathrm{M}_i;\mathrm{M}_k} := \bar{\varphi}_{\mathbf{e}_{\mathrm{M}_i\mathrm{M}_k}} - \bar{\varphi}_{\mathrm{M}_i}$ and $\psi_{\mathrm{M}_i;\mathrm{L}_k} := \bar{\varphi}_{\mathbf{e}_{\mathrm{M}_i\mathrm{L}_k}} - (\bar{\varphi}_{\mathrm{M}_i} + \pi)$, respectively, and $r_{\mathrm{cut}} > 0$ denotes the cut-off radius of the interaction potential. According to Figure 3.3, the angle $\psi_{\mathrm{M}_i;\mathrm{M}_k}$ measures the disorientation of the binding site described by $\bar{\varphi}_{\mathrm{M}_i}$ relative to the mutual position of the particles M_i and M_k, and the angle $\psi_{\mathrm{M}_i;\mathrm{L}_k}$ is the corresponding angle for death receptor ligands L_k. The Heaviside function ensures that only particles lying in vicinity of M_i are taken into account. Here, the size of the neighborhood is given by the cut-off radius r_{cut}. Furthermore, the term $\psi_{\mathrm{M}_i;\mathrm{M}_k}(\pi - \psi_{\mathrm{M}_i;\mathrm{M}_k})(\pi + \psi_{\mathrm{M}_i;\mathrm{M}_k})$ is positive for $\psi_{\mathrm{M}_i;\mathrm{M}_k} \in (0, \pi)$ and negative for $\psi_{\mathrm{M}_i;\mathrm{M}_k} \in (-\pi, 0)$. By this, the direction of the rotation caused by the death receptor monomer M_k and the death receptor ligand L_k agrees with the sign of the angle $\psi_{\mathrm{M}_i;\mathrm{M}_k}$ and $\psi_{\mathrm{M}_i;\mathrm{L}_k}$, respectively. Furthermore, small disorientations $|\psi_{\mathrm{M}_i;\mathrm{M}_k}| \ll 1$ and $|\psi_{\mathrm{M}_i;\mathrm{L}_k}| \ll 1$ cause a small rotation. On the other hand, we assume that "large" disorientations, i.e. $|\psi_{\mathrm{M}_i;\mathrm{M}_k}| \approx \pi, |\psi_{\mathrm{M}_i;\mathrm{L}_k}| \approx \pi$, also cause a small rotation of M_i. Finally, the factor $(r_{\mathrm{cut}} - R_{\mathrm{M}_i;\mathrm{M}_k})/r_{\mathrm{cut}}$ ensures a decreasing influence of a death receptor monomer M_k with an increasing distance to the death receptor monomer M_i. For $R_{\mathrm{M}_i;\mathrm{M}_k} = r_{\mathrm{cut}}$, this factor becomes zero, and for $R_{\mathrm{M}_i;\mathrm{M}_k} = 0$, it is one. The corresponding factor for death receptor ligands

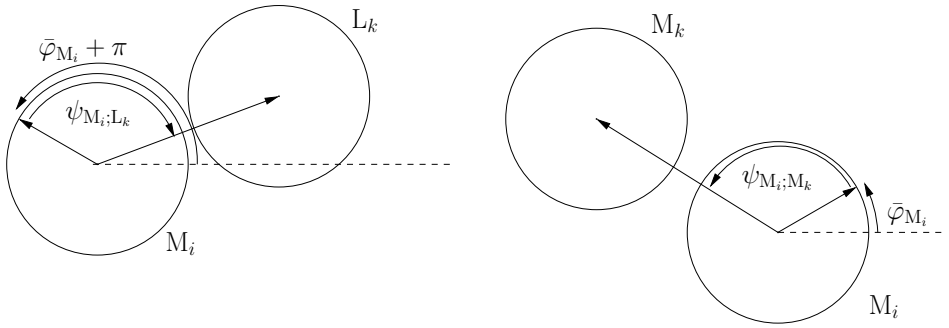

Figure 3.3: The particle L_k causes a rotation of the particle M_i according to the disorientation $\psi_{\mathrm{M}_i;\mathrm{L}_k}$ of the binding site of M_i and the particle M_k causes a rotation according to $\psi_{\mathrm{M}_i;\mathrm{M}_k}$. In summary, the weighted average of both disorientations results in the final rotation of the particle M_i.

is motivated analogously.

2) In case of death receptor dimers, we have two indistinguishable binding sites for the association with death receptor ligands. Thus, the angle $\bar{\varphi}_{\mathrm{D}_i}$ in (3.20) describes one of these binding sites, while the other is given by $\bar{\varphi}_{\mathrm{D}_i} + \pi$. Again, we introduce the vectors $\mathbf{e}_{\mathrm{D}_k\mathrm{D}_i}$, $\mathbf{e}_{\mathrm{M}_k\mathrm{D}_i}$ and $\mathbf{e}_{\mathrm{L}_k\mathrm{D}_i}$ connecting the center of mass of D_k and D_i, M_k and D_i, and L_k and D_i, respectively. Then, we define $\bar{\varphi}_{\mathbf{e}_{\mathrm{L}_k\mathrm{D}_i}}$ denoting the angle between the vector $\mathbf{e}_{\mathrm{L}_k\mathrm{D}_i}$ and the positive real line. In contrast to case 1), the angles $\bar{\varphi}_{\mathbf{e}_{\mathrm{M}_k\mathrm{D}_i}}$ and $\bar{\varphi}_{\mathbf{e}_{\mathrm{L}_k\mathrm{D}_i}}$ are not relevant for the force acting on a death receptor dimer and for the function g due to the angular independence of the interaction between two death receptor dimers and between a death receptor dimer and a monomer. Analogously to the first case, we define $\psi_{\mathrm{L}_k;\mathrm{D}_i} := \bar{\varphi}_{\mathbf{e}_{\mathrm{L}_k\mathrm{D}_i}} - \bar{\varphi}_{\mathrm{L}_k;\mathrm{D}_i}$ with

$$\bar{\varphi}_{\mathrm{L}_k;\mathrm{D}_i} := \underset{\zeta\in\Lambda_{\mathrm{L}_k}}{\operatorname{argmin}}\{|\bar{\varphi}_{\mathbf{e}_{\mathrm{L}_k\mathrm{D}_i}} - \zeta|\}, \text{ where } \Lambda_{\mathrm{L}_k} := \{\bar{\varphi}_{\mathrm{L}_k}, \bar{\varphi}_{\mathrm{L}_k} + \frac{2\pi}{3}, \bar{\varphi}_{\mathrm{L}_k} + \frac{4\pi}{3}\}.$$

With this notation, we define the force acting on death receptor dimers by

$$\begin{aligned}
\bar{\mathbf{F}}_{\mathrm{D}_i}(\bar{\boldsymbol{\xi}}_{\mathrm{M/D/L}}, \bar{\boldsymbol{\varphi}}_{\mathrm{M/D/L}}) = &- \sum_{k=1,k\neq i}^{z_{\mathrm{D}}} \frac{\mathrm{d}}{\mathrm{d}r}\bar{W}^{\mathrm{D}}_{\mathrm{LJ,cut}}(|\bar{\mathbf{x}}_{\mathrm{D}_k} - \bar{\mathbf{x}}_{\mathrm{D}_i}|)\mathbf{e}_{\mathrm{D}_k\mathrm{D}_i} \\
&- \sum_{k=1}^{z_{\mathrm{M}}} \frac{\mathrm{d}}{\mathrm{d}r}\bar{W}^{\mathrm{M}}_{\mathrm{LJ,cut}}(|\bar{\mathbf{x}}_{\mathrm{M}_k} - \bar{\mathbf{x}}_{\mathrm{D}_i}|)\mathbf{e}_{\mathrm{M}_k\mathrm{D}_i} \\
&- \sum_{k=1}^{z_{\mathrm{L}}} \Bigg(\frac{\mathrm{d}}{\mathrm{d}r}\bar{V}^{\mathrm{L}}_{\mathrm{LJ,cut}}(|\bar{\mathbf{x}}_{\mathrm{L}_k} - \bar{\mathbf{x}}_{\mathrm{D}_i}|) \cdot H(\delta - |\psi_{\mathrm{L}_k;\mathrm{D}_i}|) \\
&+ \frac{\mathrm{d}}{\mathrm{d}r}\bar{W}^{\mathrm{L}}_{\mathrm{LJ,cut}}(|\bar{\mathbf{x}}_{\mathrm{L}_k} - \bar{\mathbf{x}}_{\mathrm{D}_i}|) \cdot H(|\psi_{\mathrm{L}_k;\mathrm{D}_i}| - \delta) \Bigg) \mathbf{e}_{\mathrm{L}_k\mathrm{D}_i},
\end{aligned}$$

$i = 1, \ldots, z_{\mathrm{D}}$, where z_{D} denotes the number of death receptor dimers. Thus, the

interaction is both repulsive and attractive between a death receptor dimer D_i and death receptor ligands. Between two death receptor dimers or between a death receptor dimer and a death receptor monomer, there is a sole repulsive interaction. If there only exist death receptor dimers, the number of death receptor monomers is set to zero and the second sum vanishes.

In order to define the function g for death receptor dimers, we introduce the distance $R_{\mathrm{D}_i;\mathrm{L}_k} := |\mathbf{e}_{\mathrm{D}_i\mathrm{L}_k}|$ and the angle $\psi_{\mathrm{D}_i;\mathrm{L}_k} := \bar{\varphi}_{\mathbf{e}_{\mathrm{D}_i\mathrm{L}_k}} - \bar{\varphi}_{\mathrm{D}_i;\mathrm{L}_k}$ with

$$\bar{\varphi}_{\mathrm{D}_i;\mathrm{L}_k} := \underset{\zeta\in\Lambda_{\mathrm{D}_i}}{\operatorname{argmin}}\{|\bar{\varphi}_{\mathbf{e}_{\mathrm{D}_i\mathrm{L}_k}} - \zeta|\} \text{ with } \Lambda_{\mathrm{D}_i} := \{\bar{\varphi}_{\mathrm{D}_i}, \bar{\varphi}_{\mathrm{D}_i} + \pi\},$$

see Figure 3.4. The set Λ_{D_i} contains the orientation of the two indistinguishable binding sites of the death receptor dimer D_i, and the term $\underset{\zeta\in\Lambda_{\mathrm{D}_i}}{\operatorname{argmin}}\{\bar{\varphi}_{\mathbf{e}_{\mathrm{D}_i\mathrm{L}_k}} - \zeta\}$ ensures the choice of the binding site lying closest to the vector $\mathbf{e}_{\mathrm{D}_i\mathrm{L}_k}$. Then, we set

$$\begin{aligned} g_{\mathrm{D}_i}(\bar{\boldsymbol{\xi}}_{\mathrm{D/L}}, \bar{\boldsymbol{\varphi}}_{\mathrm{D/L}}) =& \frac{1}{z_{\mathrm{L}}} \sum_{k=1}^{z_{\mathrm{L}}} \frac{12\sqrt{3}}{\pi^3} \psi_{\mathrm{D}_i;\mathrm{L}_k} \left(\frac{\pi}{2} - \psi_{\mathrm{D}_i;\mathrm{L}_k}\right)\left(\frac{\pi}{2} + \psi_{\mathrm{D}_i;\mathrm{L}_k}\right) \times \\ & \times H(r_{\mathrm{cut}} - R_{\mathrm{D}_i;\mathrm{L}_k}) \cdot \frac{r_{\mathrm{cut}} - R_{\mathrm{D}_i;\mathrm{L}_k}}{r_{\mathrm{cut}}}. \end{aligned}$$

The function g_{D_i} only contains one sum for death receptor ligands since only death

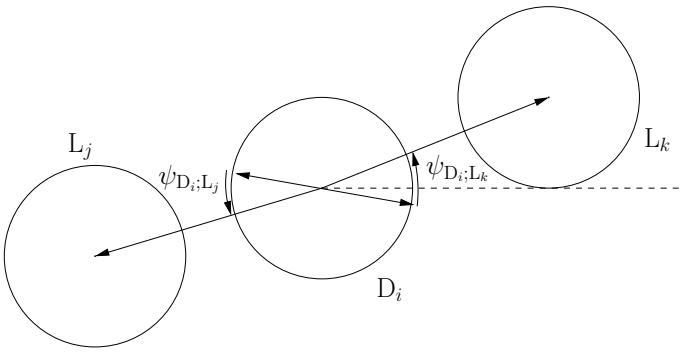

Figure 3.4: The particle L_k causes a rotation of the particle D_i according to the disorientation $\psi_{\mathrm{D}_i;\mathrm{L}_k}$ of the binding site of D_i, and the particle L_j causes a rotation according to $\psi_{\mathrm{D}_i;\mathrm{L}_j}$. In summary, the weighted average of both disorientations results in the final rotation of the particle D_i.

receptor ligands bind to death receptor dimers. The other particles, namely death receptor monomers and the remaining death receptor dimers, do not influence the rotation of the death receptor dimer D_i. The structure of the function g_{D_i} is similar to the structure of the function g_{M_i}. Again, we only take into account death receptor ligands in close vicinity of the death receptor dimer D_i, hence, we use the Heaviside function $H(\,\cdot\,)$. The term $(r_{\mathrm{cut}} - R_{\mathrm{D}_i;\mathrm{L}_k})/r_{\mathrm{cut}}$ diminishes the influence of death

receptor ligands whose distance to the death receptor dimer D_i is large. Last but not least, the term $\psi_{\mathrm{D}_i;\mathrm{L}_k}(\frac{\pi}{2} - \psi_{\mathrm{D}_i;\mathrm{L}_k})(\frac{\pi}{2} + \psi_{\mathrm{D}_i;\mathrm{L}_k})$ ensures a rotation of the death receptor dimer according to the disorientation $\psi_{\mathrm{D}_i;\mathrm{L}_k}$. In contrast to the function g_{M_i}, the support of the function g_{D_i} is restricted to the interval $[-\pi/2, \pi/2]$ since death receptor dimers have two indistinguishable binding sites and the maximal absolute value of the disorientation to one of the binding sites is therefore $\pi/2$. Again, we assume that small disorientations $|\psi_{\mathrm{D}_i;\mathrm{L}_k}| \ll 1$ as well as large disorientations $|\psi_{\mathrm{D}_i;\mathrm{L}_k}| \approx \pi/2$ lead to small rotations of D_i. Finally, averaging the rotation caused by the death receptor ligands in close vicinity of D_i yields the value of g_{D_i}. The factor $12\sqrt{3}/\pi^3$ ensures that the supremum of the function g_{D_i} is given by 1.

3) Next, we state the term for the interaction force for a death receptor trimer. First, we mention that the three binding sites of a death receptor trimer are indistinguishable, and therefore, the angle $\bar{\varphi}_{\mathrm{T}_i}$ in (3.20) describes the orientation of an arbitrary binding site. The other binding sites are given by $\bar{\varphi}_{\mathrm{T}_i} + 2\pi/3$ and $\bar{\varphi}_{\mathrm{T}_i} + 4\pi/3$. We introduce in a first step the vectors $\mathbf{e}_{\mathrm{L}_k\mathrm{T}_i}$ and $\mathbf{e}_{\mathrm{T}_k\mathrm{T}_i}$ connecting the center of mass of L_k and T_i, and T_k and T_i, respectively. Furthermore, $\bar{\varphi}_{\mathbf{e}_{\mathrm{L}_k\mathrm{T}_i}}$ denotes the angle between the vector $\mathbf{e}_{\mathrm{L}_k\mathrm{T}_i}$ and the positive real line. Following the same arguments as in the second case, the angle $\bar{\varphi}_{\mathbf{e}_{\mathrm{T}_k\mathrm{T}_i}}$ is not required. Finally, we obtain for death receptor trimers the interaction force

$$\begin{aligned}\bar{\mathbf{F}}_{\mathrm{T}_i}(\bar{\boldsymbol{\xi}}_{\mathrm{T/L}}, \bar{\boldsymbol{\varphi}}_{\mathrm{T/L}}) = &- \sum_{k=1,k\neq i}^{z_{\mathrm{T}}} \frac{\mathrm{d}}{\mathrm{d}r}\bar{W}^{\mathrm{T}}_{\mathrm{LJ,cut}}(|\bar{\mathbf{x}}_{\mathrm{T}_k} - \bar{\mathbf{x}}_{\mathrm{T}_i}|)\mathbf{e}_{\mathrm{T}_k\mathrm{T}_i} \\ &- \sum_{k=1}^{z_{\mathrm{L}}} \Bigg(\frac{\mathrm{d}}{\mathrm{d}r}\bar{V}^{\mathrm{L}}_{\mathrm{LJ,cut}}(|\bar{\mathbf{x}}_{\mathrm{L}_k} - \bar{\mathbf{x}}_{\mathrm{T}_i}|) \cdot H(\delta - |\psi_{\mathrm{L}_k;\mathrm{T}_i}|) \\ &+ \frac{\mathrm{d}}{\mathrm{d}r}\bar{W}^{\mathrm{L}}_{\mathrm{LJ,cut}}(|\bar{\mathbf{x}}_{\mathrm{L}_k} - \bar{\mathbf{x}}_{\mathrm{T}_i}|) \cdot H(|\psi_{\mathrm{L}_k;\mathrm{T}_i}| - \delta) \Bigg) \mathbf{e}_{\mathrm{L}_k\mathrm{T}_i},\end{aligned}$$

$i = 1, \ldots, z_{\mathrm{T}}$, where z_{T} denotes the number of death receptor trimers. Furthermore, we set $\psi_{\mathrm{L}_k;\mathrm{T}_i} := \bar{\varphi}_{\mathbf{e}_{\mathrm{L}_k\mathrm{T}_i}} - \bar{\varphi}_{\mathrm{L}_k;\mathrm{T}_i}$ with

$$\bar{\varphi}_{\mathrm{L}_k;\mathrm{T}_i} := \underset{\zeta\in\Lambda_{\mathrm{L}_k}}{\operatorname{argmin}}\{|\bar{\varphi}_{\mathbf{e}_{\mathrm{L}_k\mathrm{T}_i}} - \zeta|\} \text{ with } \Lambda_{\mathrm{L}_k} = \{\bar{\varphi}_{\mathrm{L}_k}, \bar{\varphi}_{\mathrm{L}_k} + \frac{2\pi}{3}, \bar{\varphi}_{\mathrm{L}_k} + \frac{4\pi}{3}\},$$

i.e., Λ_{L_k} contains the directions of the three binding sites of the death receptor ligand L_k. Concluding, we mention that the force contains an attractive and a repulsive interaction term between death receptor trimers and death receptor ligands dependent on their mutual orientation and a sole repulsive impact between death receptor trimers.

Next, we define the function g for death receptor trimers. For this purpose, we first

introduce the abbreviations $R_{\mathrm{T}_i;\mathrm{L}_k} := |\mathbf{e}_{\mathrm{T}_i\mathrm{L}_k}|$ and

$$\psi_{\mathrm{T}_i;\mathrm{L}_k} := \bar{\varphi}_{\mathbf{e}_{\mathrm{T}_i\mathrm{L}_k}} - \underset{\zeta\in\Lambda_{\mathrm{T}_i}}{\operatorname{argmin}}\{|\bar{\varphi}_{\mathbf{e}_{\mathrm{T}_i\mathrm{L}_k}} - \zeta|\} \text{ with } \Lambda_{\mathrm{T}_i} = \{\bar{\varphi}_{\mathrm{T}_i}; \bar{\varphi}_{\mathrm{T}_i} + \frac{2\pi}{3}; \bar{\varphi}_{\mathrm{T}_i} + \frac{4\pi}{3}\}.$$

Here, the set Λ_{T_i} contains the orientations of the three binding sites of the death receptor trimer T_i, and the term $\underset{\zeta\in\Lambda_{\mathrm{T}_i}}{\operatorname{argmin}}\{\bar{\varphi}_{\mathbf{e}_{\mathrm{T}_i\mathrm{L}_k}} - \zeta\}$ cares for the 'correct' choice of the binding site of T_i. The angle $\psi_{\mathrm{T}_i;\mathrm{L}_k}$ is illustrated in Figure 3.5 for three death receptor ligands located in close vicinity to the death receptor ligand T_i. We define

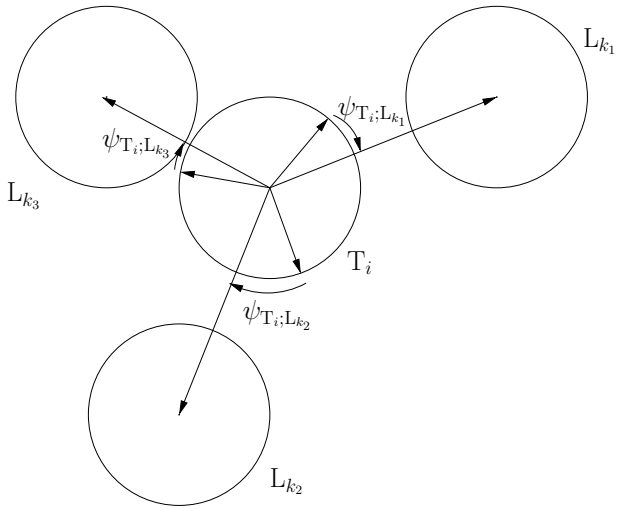

Figure 3.5: The death receptor ligand $\mathrm{L}_{k_j}, j = 1, 2, 3$, causes a rotation of the death receptor trimer T_i according to the disorientation $\psi_{\mathrm{T}_i;\mathrm{L}_{k_j}}$. In summary, the weighted average of the three disorientations yields the final rotation of the death receptor trimer T_i.

the function g for death receptor trimers by

$$\begin{aligned} g_{\mathrm{T}_i}(\bar{\boldsymbol{\xi}}_{\mathrm{T/L}}, \bar{\boldsymbol{\varphi}}_{\mathrm{T/L}}) =& \frac{1}{z_{\mathrm{L}}} \sum_{k=1}^{z_{\mathrm{L}}} \frac{81\sqrt{3}}{2\pi^3} \psi_{\mathrm{T}_i;\mathrm{L}_k} (\frac{\pi}{3} - \psi_{\mathrm{T}_i;\mathrm{L}_k})(\frac{\pi}{3} + \psi_{\mathrm{T}_i;\mathrm{L}_k}) \times \\ & \times H(r_{\mathrm{cut}} - R_{\mathrm{T}_i;\mathrm{L}_k}) \cdot \frac{r_{\mathrm{cut}} - R_{\mathrm{T}_i;\mathrm{L}_k}}{r_{\mathrm{cut}}}. \end{aligned}$$

Again, we see that the structure of the function g_{T_i} is the same as for death receptor monomers and death receptor dimers. The only difference is in the term $\psi_{\mathrm{T}_i;\mathrm{L}_k}(\frac{\pi}{3} - \psi_{\mathrm{T}_i;\mathrm{L}_k})(\frac{\pi}{3} + \psi_{\mathrm{T}_i;\mathrm{L}_k})$ and the constant factor which guarantees that the supremum of g_{T_i} is given by 1. Obviously, according to the structure of a trimer with three binding sites, the largest absolute value for a disorientation of a binding site is $\pi/3$. Thus, the angle $\psi_{\mathrm{T}_i;\mathrm{L}_k}$ only takes values in the interval $[-\pi/3, \pi/3]$. And finally, the cubic structure of the term $\psi_{\mathrm{T}_i;\mathrm{L}_k}(\frac{\pi}{3} - \psi_{\mathrm{T}_i;\mathrm{L}_k})(\frac{\pi}{3} + \psi_{\mathrm{T}_i;\mathrm{L}_k})$ ensures that small disorientations $|\psi_{\mathrm{T}_i;\mathrm{L}_k}| \ll 1$ and disorientations close to the boundary of the interval $[-\pi/3, \pi/3]$

cause small rotations of T_i. Additionally, the sign of $\psi_{\mathrm{T}_i;\mathrm{L}_k}$ agrees with the sign of the rotation due to the cubic structure of the term.

4) The death receptor ligands interact with all particle types except the cluster units, i.e. death receptor monomers, death receptor dimers, death receptor trimers and death receptor ligands. While death receptor monomers and death receptor dimers coexist, the existence of death receptor trimers excludes the existence of death receptor monomers and dimers. Nevertheless, we choose a general formalism for the force acting on a death receptor ligand which contains four sums for the different particle types. However, at most three sums occur simultaneously. But before we define the force $\bar{\mathbf{F}}_{\mathrm{L}_i}$, we introduce the angles required for the description of the angular dependent interaction.

   The death receptor ligand has three binding sites and the angle $\bar{\varphi}_{\mathrm{L}_i}$ in (3.20) describes the orientation of one arbitrary binding site. The other binding sites are obtained by adding $2\pi/3$ or $4\pi/3$. Furthermore, we introduce the vectors $\mathbf{e}_{\mathrm{M}_k\mathrm{L}_i}$, $\mathbf{e}_{\mathrm{D}_k\mathrm{L}_i}$, $\mathbf{e}_{\mathrm{T}_k\mathrm{L}_i}$ and $\mathbf{e}_{\mathrm{L}_k\mathrm{L}_i}$ connecting the center of mass of M_k and L_i, D_k and L_i, T_k and L_i, and L_k and L_i, respectively. We recall the fact that the interaction between two death receptor ligands does not depend on the orientation of the particles, whereas the interaction between death receptor ligands and monomeric, dimeric and trimeric death receptors is both repulsive and attractive dependent on the particle orientation. Thus, we introduce for the latter cases the angle $\bar{\varphi}_{\mathbf{e}_{\mathrm{M}_k\mathrm{L}_i}}$ between the vector $\mathbf{e}_{\mathrm{M}_k\mathrm{L}_i}$ and the positive real line, $\bar{\varphi}_{\mathbf{e}_{\mathrm{D}_k\mathrm{L}_i}}$ between the vector $\mathbf{e}_{\mathrm{D}_k\mathrm{L}_i}$ and the positive real line and $\bar{\varphi}_{\mathbf{e}_{\mathrm{T}_k\mathrm{L}_i}}$ between the vector $\mathbf{e}_{\mathrm{T}_k\mathrm{L}_i}$ and the positive real line. With these angles at hand, we set $\psi_{\mathrm{M}_k;\mathrm{L}_i} := \bar{\varphi}_{\mathbf{e}_{\mathrm{M}_k\mathrm{L}_i}} - (\bar{\varphi}_{\mathrm{M}_k} + \pi)$, $\psi_{\mathrm{D}_k;\mathrm{L}_i} := \bar{\varphi}_{\mathbf{e}_{\mathrm{D}_k\mathrm{L}_i}} - \bar{\varphi}_{\mathrm{D}_k;\mathrm{L}_i}$ and $\psi_{\mathrm{T}_k;\mathrm{L}_i} := \bar{\varphi}_{\mathbf{e}_{\mathrm{T}_k\mathrm{L}_i}} - \bar{\varphi}_{\mathrm{T}_k;\mathrm{L}_i}$, where

$$\bar{\varphi}_{\mathrm{D}_k;\mathrm{L}_i} := \operatorname*{argmin}_{\zeta\in\Lambda_{\mathrm{D}_k}}\{|\bar{\varphi}_{\mathbf{e}_{\mathrm{D}_k\mathrm{L}_i}} - \zeta|\} \text{ with } \Lambda_{\mathrm{D}_k} := \{\bar{\varphi}_{\mathrm{D}_k}, \bar{\varphi}_{\mathrm{D}_k} + \pi\},$$
$$\bar{\varphi}_{\mathrm{T}_k;\mathrm{L}_i} := \operatorname*{argmin}_{\zeta\in\Lambda_{\mathrm{T}_k}}\{|\bar{\varphi}_{\mathbf{e}_{\mathrm{T}_k\mathrm{L}_i}} - \zeta|\} \text{ with } \Lambda_{\mathrm{T}_k} := \{\bar{\varphi}_{\mathrm{T}_k}, \bar{\varphi}_{\mathrm{T}_k} + \frac{2\pi}{3}, \bar{\varphi}_{\mathrm{T}_k} + \frac{4\pi}{3}\}.$$

   Again, Λ_{D_k} and Λ_{T_k} contain the binding sites of the death receptor dimer D_k and the death receptor trimer T_k, respectively. With the introduced notations, the force acting on a death receptor ligand reads

$$\begin{aligned}\bar{\mathbf{F}}_{\mathrm{L}_i}(\bar{\boldsymbol{\xi}}_{\mathrm{M/D/T/L}}, \bar{\boldsymbol{\varphi}}_{\mathrm{M/D/T/L}}) = -\sum_{k=1}^{z_{\mathrm{M}}} \Bigg(&\frac{\mathrm{d}}{\mathrm{d}r}\bar{V}^{\mathrm{M}}_{\mathrm{LJ,cut}}(|\bar{\mathbf{x}}_{\mathrm{M}_k} - \bar{\mathbf{x}}_{\mathrm{L}_i}|)\cdot H(\delta - |\psi_{\mathrm{M}_k;\mathrm{L}_i}|) \\ &+ \frac{\mathrm{d}}{\mathrm{d}r}\bar{W}^{\mathrm{M}}_{\mathrm{LJ,cut}}(|\bar{\mathbf{x}}_{\mathrm{M}_k} - \bar{\mathbf{x}}_{\mathrm{L}_i}|)\cdot H(|\psi_{\mathrm{M}_k;\mathrm{L}_i}| - \delta)\Bigg)\mathbf{e}_{\mathrm{M}_k\mathrm{L}_i}\end{aligned}$$

$$
\begin{aligned}
&- \sum_{k=1}^{z_{\mathrm{D}}} \Bigg(\frac{\mathrm{d}}{\mathrm{d}r} \bar{V}^{\mathrm{D}}_{\mathrm{LJ,cut}}(|\bar{\mathbf{x}}_{\mathrm{D}_k} - \bar{\mathbf{x}}_{\mathrm{L}_i}|) \cdot H(\delta - |\psi_{\mathrm{D}_k;\mathrm{L}_i}|) \\
&+ \frac{\mathrm{d}}{\mathrm{d}r} \bar{W}^{\mathrm{D}}_{\mathrm{LJ,cut}}(|\bar{\mathbf{x}}_{\mathrm{D}_k} - \bar{\mathbf{x}}_{\mathrm{L}_i}|) \cdot H(|\psi_{\mathrm{D}_k;\mathrm{L}_i}| - \delta) \Bigg) \mathbf{e}_{\mathrm{D}_k\mathrm{L}_i} \\
&- \sum_{k=1}^{z_{\mathrm{T}}} \Bigg(\frac{\mathrm{d}}{\mathrm{d}r} \bar{V}^{\mathrm{T}}_{\mathrm{LJ,cut}}(|\bar{\mathbf{x}}_{\mathrm{T}_k} - \bar{\mathbf{x}}_{\mathrm{L}_i}|) \cdot H(\delta - |\psi_{\mathrm{T}_k;\mathrm{L}_i}|) \\
&+ \frac{\mathrm{d}}{\mathrm{d}r} \bar{W}^{\mathrm{T}}_{\mathrm{LJ,cut}}(|\bar{\mathbf{x}}_{\mathrm{T}_k} - \bar{\mathbf{x}}_{\mathrm{L}_i}|) \cdot H(|\psi_{\mathrm{T}_k;\mathrm{L}_i}| - \delta) \Bigg) \mathbf{e}_{\mathrm{T}_k\mathrm{L}_i} \\
&- \sum_{k=1,k\neq i}^{z_{\mathrm{L}}} \frac{\mathrm{d}}{\mathrm{d}r} \bar{W}^{\mathrm{L}}_{\mathrm{LJ,cut}}(|\bar{\mathbf{x}}_{\mathrm{L}_k} - \bar{\mathbf{x}}_{\mathrm{L}_i}|) \mathbf{e}_{\mathrm{L}_k\mathrm{L}_i}, \qquad (3.21)
\end{aligned}
$$

$i = 1, \ldots, z_{\mathrm{L}}$, where z_{L} denotes the number of death receptor ligands. Here, the force acting on a death receptor ligand is given in the most general form. The term is composed of four sums describing the interaction of a death receptor ligand with monomeric, dimeric and trimeric death receptors, and additionally with the remaining death receptor ligands. Since we assume that death receptor trimers do not coexist with death receptor monomers or death receptor dimers, in none of the cases all four sums occur. In case of the existence of monomeric or dimeric death receptors, the third sum in (3.21) vanishes, and in case of trimeric death receptors, the first and second sum in (3.21) are omitted. Furthermore, the interaction between the death receptors and death receptor ligands is both repulsive and attractive dependent on the orientation of the particles, whereas the interaction between two death receptor ligands is only repulsive.

To close the interaction for death receptor ligands, we define the function g for death receptor ligands. For this purpose, we introduce the distances between the particles $R_{\mathrm{L}_i;\mathrm{M}_k} := |\mathbf{e}_{\mathrm{L}_i\mathrm{M}_k}|$, $R_{\mathrm{L}_i;\mathrm{D}_k} := |\mathbf{e}_{\mathrm{L}_i\mathrm{D}_k}|$ and $R_{\mathrm{L}_i;\mathrm{T}_k} := |\mathbf{e}_{\mathrm{L}_i\mathrm{T}_k}|$. Additionally, we define the angles

$$
\begin{aligned}
\psi_{\mathrm{L}_i;\mathrm{M}_k} &:= \bar{\varphi}_{\mathbf{e}_{\mathrm{L}_i\mathrm{M}_k}} - \operatorname*{argmin}_{\zeta \in \Lambda_{\mathrm{L}_i}} \{|\bar{\varphi}_{\mathbf{e}_{\mathrm{L}_i\mathrm{M}_k}} - \zeta|\}, \\
\psi_{\mathrm{L}_i;\mathrm{D}_k} &:= \bar{\varphi}_{\mathbf{e}_{\mathrm{L}_i\mathrm{D}_k}} - \operatorname*{argmin}_{\zeta \in \Lambda_{\mathrm{L}_i}} \{|\bar{\varphi}_{\mathbf{e}_{\mathrm{L}_i\mathrm{D}_k}} - \zeta|\}, \\
\psi_{\mathrm{L}_i;\mathrm{T}_k} &:= \bar{\varphi}_{\mathbf{e}_{\mathrm{L}_i\mathrm{T}_k}} - \operatorname*{argmin}_{\zeta \in \Lambda_{\mathrm{L}_i}} \{|\bar{\varphi}_{\mathbf{e}_{\mathrm{L}_i\mathrm{T}_k}} - \zeta|\},
\end{aligned}
$$

where $\Lambda_{\mathrm{L}_i} := \{\bar{\varphi}_{\mathrm{L}_i}; \bar{\varphi}_{\mathrm{L}_i} + \frac{2\pi}{3}; \bar{\varphi}_{\mathrm{L}_i} + \frac{4\pi}{3}\}$ contains the three binding sites of the death receptor ligands and $\bar{\varphi}_{\mathbf{e}_{\mathrm{L}_i\mathrm{M}_k}}$, $\bar{\varphi}_{\mathbf{e}_{\mathrm{L}_i\mathrm{D}_k}}$, $\bar{\varphi}_{\mathbf{e}_{\mathrm{L}_i\mathrm{T}_k}}$ describe the angles between the vectors $\mathbf{e}_{\mathrm{L}_i\mathrm{M}_k}$, $\mathbf{e}_{\mathrm{L}_i\mathrm{D}_k}$, $\mathbf{e}_{\mathrm{L}_i\mathrm{T}_k}$ and the positive real line, cf. Figure 3.6. Then, we write

$$
g_{\mathrm{L}_i}(\bar{\boldsymbol{\xi}}_{\mathrm{M/D/T/L}}, \bar{\boldsymbol{\varphi}}_{\mathrm{M/D/T/L}}) = \frac{1}{z_{\mathrm{M}} + z_{\mathrm{D}} + z_{\mathrm{T}}} \times \qquad (3.22)
$$

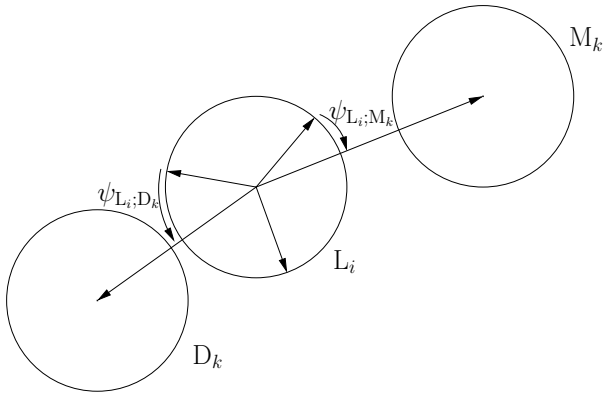

Figure 3.6: The death receptor monomer M_k and dimer D_k cause a rotation according to the angles $\psi_{L_i;M_k}$ and $\psi_{L_i;D_k}$. In summary, the weighted average gives the rotation of the death receptor ligand L_i.

$$\times \left(\sum_{k=1}^{z_M} \frac{81\sqrt{3}}{2\pi^3} \psi_{L_i;M_k} \left(\frac{\pi}{3} - \psi_{L_i;M_k}\right)\left(\frac{\pi}{3} + \psi_{L_i;M_k}\right) \cdot H(r_{cut} - R_{L_i;M_k}) \frac{r_{cut} - R_{L_i;M_k}}{r_{cut}} \right.$$
$$+ \sum_{k=1}^{z_D} \frac{81\sqrt{3}}{2\pi^3} \psi_{L_i;D_k} \left(\frac{\pi}{3} - \psi_{L_i;D_k}\right)\left(\frac{\pi}{3} + \psi_{L_i;D_k}\right) \cdot H(r_{cut} - R_{L_i;D_k}) \frac{r_{cut} - R_{L_i;D_k}}{r_{cut}}$$
$$\left. + \sum_{k=1}^{z_T} \frac{81\sqrt{3}}{2\pi^3} \psi_{L_i;T_k} \left(\frac{\pi}{3} - \psi_{L_i;T_k}\right)\left(\frac{\pi}{3} + \psi_{L_i;T_k}\right) \cdot H(r_{cut} - R_{L_i;T_k}) \frac{r_{cut} - R_{L_i;T_k}}{r_{cut}} \right).$$

Again, in case of the existence of trimeric death receptors, the first and second sum in (3.22) vanish and in case of monomeric or dimeric death receptors, the third sum in (3.22) is zero. The structure of the function g_{L_i} is similar to the structure of the previously introduced functions g of the other particle types. According to the trimeric structure of death receptor ligands and death receptor trimers, the cubic terms in the angle $\psi_{L_i;M_k}, \psi_{L_i;D_k}, \psi_{L_i;T_k}$ agree with the corresponding term in the function g_{T_i}. Again, the factor $81\sqrt{3}/(2\pi^3)$ guarantees that the supremum of each sum is one. Obviously, according to the trimeric structure of death receptor ligands with the three binding sites, the largest absolute value for a disorientation of a binding site is $\pi/3$. Thus, the angles $\psi_{L_i;M_k}, \psi_{L_i;D_k}$ and $\psi_{L_i;T_k}$ only take values in the interval $[-\pi/3, \pi/3]$. Besides, the cubic structure of the term in the angle $\psi_{L_i;M_k}$ in the first sum ensures that small disorientations $|\psi_{L_i;M_k}| \ll 1$ and disorientations close to the boundary of the interval $[-\pi/3, \pi/3]$ cause small rotations of L_i. Analogous arguments explain the structure of the terms dependent on $\psi_{L_i;D_k}$ and $\psi_{L_i;T_k}$ in the second and third sum, respectively. Furthermore, the Heaviside function guarantees that only death receptors in close vicinity to the death receptor ligand L_i influence the rotation of L_i and the last factor in each summand of (3.22) diminishes the influence of death receptors whose distance to the death receptor ligand L_i is large,

more precisely, close to the cut-off radius r_{cut}.

5) Last but not least, we consider the case where death receptor monomers and death receptor ligands form pre-associated cluster units, i.e., one death receptor ligand binds three death receptor monomers. According to the three death receptor monomers bound to one death receptor ligand, we assume that the cluster unit has three binding sites for the association with other cluster units. Here, the binding between two cluster units occurs via the binding of two death receptor monomers according to the structure of the cluster units. Again, the interaction between cluster units is both repulsive and attractive dependent on the orientation of the particles. In order to introduce the interaction force, we first define angles describing the mutual orientation of the particles. The angle $\bar{\varphi}_{\mathrm{U}_i}$ in (3.20) describes the orientation of one binding site of the cluster unit U_i, and the other binding sites are given by $\bar{\varphi}_{\mathrm{U}_i} + 2\pi/3$ and $\bar{\varphi}_{\mathrm{U}_i} + 4\pi/3$. Furthermore, we need the vector $\mathbf{e}_{\mathrm{U}_k\mathrm{U}_i}$ connecting the center of mass of the cluster units U_k and U_i, and the angle $\bar{\varphi}_{\mathbf{e}_{\mathrm{U}_k\mathrm{U}_i}}$ between the vector $\mathbf{e}_{\mathrm{U}_k\mathrm{U}_i}$ and the positive real line. We define the disorientation $\psi_{\mathrm{U}_k;\mathrm{U}_i} := \bar{\varphi}_{\mathbf{e}_{\mathrm{U}_k\mathrm{U}_i}} - \bar{\varphi}_{\mathrm{U}_k;\mathrm{U}_i}$ where

$$\bar{\varphi}_{\mathrm{U}_k;\mathrm{U}_i} := \underset{\zeta\in\Lambda_{\mathrm{U}_k}}{\operatorname{argmin}}\{|\bar{\varphi}_{\mathbf{e}_{\mathrm{U}_k\mathrm{U}_i}} - \zeta|\} \text{ with } \Lambda_{\mathrm{U}_k} := \{\bar{\varphi}_{\mathrm{U}_k}, \bar{\varphi}_{\mathrm{U}_k} + \frac{2\pi}{3}, \bar{\varphi}_{\mathrm{U}_k} + \frac{4\pi}{3}\}.$$

Hence, Λ_{U_k} contains the binding sites of the cluster unit U_k. We define the force acting on a cluster unit by

$$\begin{aligned}\bar{\mathbf{F}}_{\mathrm{U}_i}(\bar{\boldsymbol{\xi}}_{\mathrm{U}}, \bar{\boldsymbol{\varphi}}_{\mathrm{U}}) = -\sum_{k=1,k\neq i}^{z_{\mathrm{U}}} \Bigg(&\frac{\mathrm{d}}{\mathrm{d}r}\bar{V}^{\mathrm{U}}_{\mathrm{LJ,cut}}(|\bar{\mathbf{x}}_{\mathrm{U}_k} - \bar{\mathbf{x}}_{\mathrm{U}_i}|)\cdot H(\delta - |\psi_{\mathrm{U}_k;\mathrm{U}_i}|) \\ &+ \frac{\mathrm{d}}{\mathrm{d}r}\bar{W}^{\mathrm{U}}_{\mathrm{LJ,cut}}(|\bar{\mathbf{x}}_{\mathrm{U}_k} - \bar{\mathbf{x}}_{\mathrm{U}_i}|)\cdot H(|\psi_{\mathrm{U}_k;\mathrm{U}_i}| - \delta)\Bigg)\mathbf{e}_{\mathrm{U}_k\mathrm{U}_i},\end{aligned} \tag{3.23}$$

$i = 1, \ldots, z_{\mathrm{U}}$, with z_{U} the number of cluster units. Since we consider in this case only one particle type, the right-hand side of (3.23) only consists of one sum over all cluster units U_k except U_i. The interaction is both repulsive and attractive dependent on the angle $\psi_{\mathrm{U}_k;\mathrm{U}_i}$.

In the end, we define the function g for cluster units. For this purpose, we define the distance between two cluster units $R_{\mathrm{U}_i;\mathrm{U}_k} := |\mathbf{e}_{\mathrm{U}_i\mathrm{U}_k}|$ and define the disorientation

$$\psi_{\mathrm{U}_i;\mathrm{U}_k} := \bar{\varphi}_{\mathbf{e}_{\mathrm{U}_i\mathrm{U}_k}} - \underset{\zeta\in\Lambda_{\mathrm{U}_i}}{\operatorname{argmin}}\{|\bar{\varphi}_{\mathbf{e}_{\mathrm{U}_i\mathrm{U}_k}} - \zeta|\}$$

with $\Lambda_{\mathrm{U}_i} := \{\bar{\varphi}_{\mathrm{U}_i}; \bar{\varphi}_{\mathrm{U}_i} + \frac{2\pi}{3}; \bar{\varphi}_{\mathrm{U}_i} + \frac{4\pi}{3}\}$. Then, the function g for cluster units is given

by

$$g_{\mathrm{U}_i}(\bar{\boldsymbol{\xi}}_{\mathrm{U}}, \bar{\boldsymbol{\varphi}}_{\mathrm{U}}) = \frac{1}{z_{\mathrm{U}}} \sum_{k=1, k\neq i}^{z_{\mathrm{U}}} \frac{81\sqrt{3}}{2\pi^3} \psi_{\mathrm{U}_i;\mathrm{U}_k} \left(\frac{\pi}{3} - \psi_{\mathrm{U}_i;\mathrm{U}_k}\right)\left(\frac{\pi}{3} + \psi_{\mathrm{U}_i;\mathrm{U}_k}\right) \times$$
$$\times H(r_{\mathrm{cut}} - R_{\mathrm{U}_i;\mathrm{U}_k}) \cdot \frac{r_{\mathrm{cut}} - R_{\mathrm{U}_i;\mathrm{U}_k}}{r_{\mathrm{cut}}}.$$

Again, the set Λ_{U_i} contains the three binding sites of the cluster units, $R_{\mathrm{U}_i;\mathrm{U}_k}$ denotes the distance between the cluster units U_i and U_k and $\psi_{\mathrm{U}_i;\mathrm{U}_k}$ describes the disorientation of the binding site lying closest to the vector $\mathbf{e}_{\mathrm{U}_i\mathrm{U}_k}$, relative to $\mathbf{e}_{\mathrm{U}_i\mathrm{U}_k}$, see Figure 3.7. We mention that the structure of the function g_{U_i} agrees with the structure of the function g_{T_i}, and so, the explanation of the single terms can be transferred.

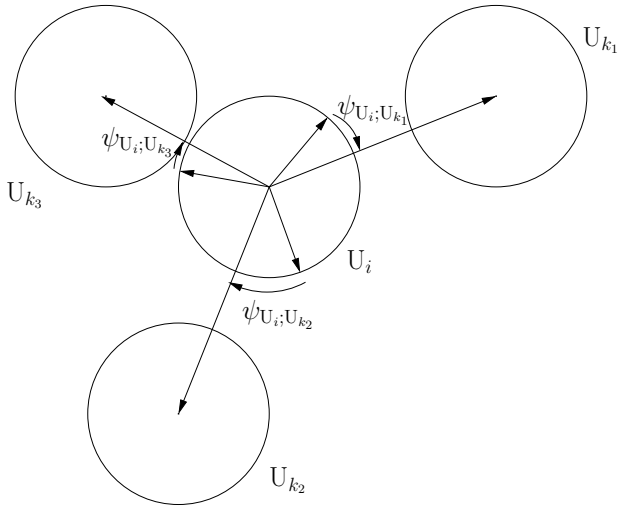

Figure 3.7: The cluster units $\mathrm{U}_{k_j}, j = 1, 2, 3$, cause a rotation of the cluster unit U_i according to the disorientation $\psi_{\mathrm{U}_i;\mathrm{U}_{k_j}}$. Since the distance of the cluster unit U_{k_3} to U_i is smaller than the distance of U_{k_1} to U_i, the influence of the cluster unit U_{k_3} on the rotation of U_i is larger. In summary, the weighted average of the three disorientations yields the final rotation of the cluster unit U_i.

With the forces $\bar{\mathbf{F}}_{\mathrm{interact}}$ and the functions g for the different particle types at hand, the particle translation and the particle rotation is completely described by the stochastic differential equations (3.6) and (3.19).

3.3.5 Particle Model for the Different Particle Configurations

After introducing the stochastic differential equations for the particle translation and particle rotation in Section 3.3.1 and Section 3.3.2 and defining $\bar{\mathbf{F}}_{\mathrm{interact}}$ and g in Section 3.3.4, we assemble the equations to a nonlinearly coupled system of stochastic

differential equations for the different particle configurations introduced in Section 3.3.3. Since we consider in each case a huge amount of particles, we obtain a large system of stochastic differential equations nonlinearly coupled by the interaction forces $\bar{\mathbf{F}}_{\text{interact}}$ and the functions g describing the mutual influence on the particle rotation. For the description of the motion of a single particle, two stochastic differential equations for the particle translation and one stochastic differential equation for the particle rotation are required.

Before we list the systems of stochastic differential equation for each particle configuration, we first specify the parameters in equation (3.6) and equation (3.19) since the values of μ and ζ depend on the particle type, especially their size. Therefore, we distinguish in the following the parameters μ_{M}, μ_{D}, μ_{T}, μ_{L}, μ_{U}, ζ_{M}, ζ_{D}, ζ_{T}, ζ_{L} and ζ_{U} for the different particle types.

a.i) **Death Receptor Monomers and Death Receptor Ligands**
We consider a simulation domain with z_{M} death receptor monomers and z_{L} death receptor ligands. Thus, we obtain a system of $3(z_{\text{M}} + z_{\text{L}})$ stochastic differential equations

$$\begin{aligned}
\mathrm{d}\bar{\mathbf{x}}_{\text{M}_i} &= 6\mu_{\text{M}}^2 \bar{\mathbf{F}}_{\text{M}_i}(\bar{\boldsymbol{\xi}}_{\text{M}}, \bar{\boldsymbol{\xi}}_{\text{D}}, \bar{\boldsymbol{\xi}}_{\text{L}}, \bar{\boldsymbol{\varphi}}_{\text{M}}, \bar{\boldsymbol{\varphi}}_{\text{D}}, \bar{\boldsymbol{\varphi}}_{\text{L}})\mathrm{d}\bar{t} + \sqrt{2}\mu_{\text{M}}\mathrm{d}\widetilde{\mathbf{W}}_{\text{trans,M}_i,\bar{t}},\\
\mathrm{d}\bar{\mathbf{x}}_{\text{L}_j} &= 6\mu_{\text{L}}^2 \bar{\mathbf{F}}_{\text{L}_j}(\bar{\boldsymbol{\xi}}_{\text{M}}, \bar{\boldsymbol{\xi}}_{\text{D}}, \bar{\boldsymbol{\xi}}_{\text{T}}, \bar{\boldsymbol{\xi}}_{\text{L}}, \bar{\boldsymbol{\varphi}}_{\text{M}}, \bar{\boldsymbol{\varphi}}_{\text{D}}, \bar{\boldsymbol{\varphi}}_{\text{T}}, \bar{\boldsymbol{\varphi}}_{\text{L}})\mathrm{d}\bar{t} + \sqrt{2}\mu_{\text{L}}\mathrm{d}\widetilde{\mathbf{W}}_{\text{trans,L}_j,\bar{t}},\\
\mathrm{d}\bar{\varphi}_{\text{M}_i} &= \kappa\mu_{\text{M}}^2\zeta_{\text{M}}^2 g_{\text{M}_i}(\bar{\boldsymbol{\xi}}_{\text{M}}, \bar{\boldsymbol{\xi}}_{\text{L}}, \bar{\boldsymbol{\varphi}}_{\text{M}}, \bar{\boldsymbol{\varphi}}_{\text{L}})\mathrm{d}\bar{t} + \sqrt{2}\mu_{\text{M}}\zeta_{\text{M}}\mathrm{d}\widetilde{W}_{\text{rot,M}_i,\bar{t}},\\
\mathrm{d}\bar{\varphi}_{\text{L}_j} &= \kappa\mu_{\text{L}}^2\zeta_{\text{L}}^2 g_{\text{L}_j}(\bar{\boldsymbol{\xi}}_{\text{M}}, \bar{\boldsymbol{\xi}}_{\text{D}}, \bar{\boldsymbol{\xi}}_{\text{T}}, \bar{\boldsymbol{\xi}}_{\text{L}}, \bar{\boldsymbol{\varphi}}_{\text{M}}, \bar{\boldsymbol{\varphi}}_{\text{D}}, \bar{\boldsymbol{\varphi}}_{\text{T}}, \bar{\boldsymbol{\varphi}}_{\text{L}})\mathrm{d}\bar{t} + \sqrt{2}\mu_{\text{L}}\zeta_{\text{L}}\mathrm{d}\widetilde{W}_{\text{rot,L}_j,\bar{t}},
\end{aligned}$$

$i = 1, \ldots, z_{\text{M}}; j = 1, \ldots, z_{\text{L}}; z_{\text{D}} = 0; z_{\text{T}} = 0$. The system of stochastic differential equations is nonlinearly coupled by the functions $\bar{\mathbf{F}}_{\text{M}_i}, \bar{\mathbf{F}}_{\text{L}_j}, g_{\text{M}_i}$ and g_{L_j}.

a.ii) **Death Receptor Dimers and Death Receptor Ligands**
If all death receptors exist in a dimeric pre-form, we again obtain a system of stochastic differential equations with two equations for the particle translation and one equation for the particle rotation. Since we consider z_{D} death receptors dimers and z_{L} death receptor ligands, we get a system of $3(z_{\text{D}} + z_{\text{L}})$ equations

$$\begin{aligned}
\mathrm{d}\bar{\mathbf{x}}_{\text{D}_k} &= 6\mu_{\text{D}}^2 \bar{\mathbf{F}}_{\text{D}_k}(\bar{\boldsymbol{\xi}}_{\text{M}}, \bar{\boldsymbol{\xi}}_{\text{D}}, \bar{\boldsymbol{\xi}}_{\text{L}}, \bar{\boldsymbol{\varphi}}_{\text{M}}, \bar{\boldsymbol{\varphi}}_{\text{D}}, \bar{\boldsymbol{\varphi}}_{\text{L}})\mathrm{d}\bar{t} + \sqrt{2}\mu_{\text{D}}\mathrm{d}\widetilde{\mathbf{W}}_{\text{trans,D}_k,\bar{t}},\\
\mathrm{d}\bar{\mathbf{x}}_{\text{L}_j} &= 6\mu_{\text{L}}^2 \bar{\mathbf{F}}_{\text{L}_j}(\bar{\boldsymbol{\xi}}_{\text{M}}, \bar{\boldsymbol{\xi}}_{\text{D}}, \bar{\boldsymbol{\xi}}_{\text{T}}, \bar{\boldsymbol{\xi}}_{\text{L}}, \bar{\boldsymbol{\varphi}}_{\text{M}}, \bar{\boldsymbol{\varphi}}_{\text{D}}, \bar{\boldsymbol{\varphi}}_{\text{T}}, \bar{\boldsymbol{\varphi}}_{\text{L}})\mathrm{d}\bar{t} + \sqrt{2}\mu_{\text{L}}\mathrm{d}\widetilde{\mathbf{W}}_{\text{trans,L}_j,\bar{t}},\\
\mathrm{d}\bar{\varphi}_{\text{D}_k} &= \kappa\mu_{\text{D}}^2\zeta_{\text{D}}^2 g_{\text{D}_k}(\bar{\boldsymbol{\xi}}_{\text{D}}, \bar{\boldsymbol{\xi}}_{\text{L}}, \bar{\boldsymbol{\varphi}}_{\text{D}}, \bar{\boldsymbol{\varphi}}_{\text{L}})\mathrm{d}\bar{t} + \sqrt{2}\mu_{\text{D}}\zeta_{\text{D}}\mathrm{d}\widetilde{W}_{\text{rot,D}_k,\bar{t}},\\
\mathrm{d}\bar{\varphi}_{\text{L}_j} &= \kappa\mu_{\text{L}}^2\zeta_{\text{L}}^2 g_{\text{L}_j}(\bar{\boldsymbol{\xi}}_{\text{M}}, \bar{\boldsymbol{\xi}}_{\text{D}}, \bar{\boldsymbol{\xi}}_{\text{T}}, \bar{\boldsymbol{\xi}}_{\text{L}}, \bar{\boldsymbol{\varphi}}_{\text{M}}, \bar{\boldsymbol{\varphi}}_{\text{D}}, \bar{\boldsymbol{\varphi}}_{\text{T}}, \bar{\boldsymbol{\varphi}}_{\text{L}})\mathrm{d}\bar{t} + \sqrt{2}\mu_{\text{L}}\zeta_{\text{L}}\mathrm{d}\widetilde{W}_{\text{rot,L}_j,\bar{t}},
\end{aligned}$$

$k = 1, \ldots, z_{\text{D}}; j = 1, \ldots, z_{\text{L}}; z_{\text{M}} = 0; z_{\text{T}} = 0$. The structure of the system seems the same as for death receptor monomers, but the difference lies in the structure of the functions $\bar{\mathbf{F}}_{\text{D}_k}$ and g_{D_k}.

a.iii) **Death Receptor Monomers, Death Receptor Dimers and Death Receptor Ligands**

Three different particle types are involved in the model where monomeric and dimeric death receptors coexist on the cell membrane. Besides the death receptors, the model also includes death receptor ligands, so that we obtain a system of $3(z_{\mathrm{M}} + z_{\mathrm{D}} + z_{\mathrm{L}})$ stochastic differential equations

$$\begin{aligned}
\mathrm{d}\bar{\mathbf{x}}_{\mathrm{M}_i} &= 6\mu_{\mathrm{M}}^2 \bar{\mathbf{F}}_{\mathrm{M}_i}(\bar{\boldsymbol{\xi}}_{\mathrm{M}}, \bar{\boldsymbol{\xi}}_{\mathrm{D}}, \bar{\boldsymbol{\xi}}_{\mathrm{L}}, \bar{\boldsymbol{\varphi}}_{\mathrm{M}}, \bar{\boldsymbol{\varphi}}_{\mathrm{D}}, \bar{\boldsymbol{\varphi}}_{\mathrm{L}})\mathrm{d}\bar{t} + \sqrt{2}\mu_{\mathrm{M}}\mathrm{d}\widetilde{\mathbf{W}}_{\mathrm{trans},\mathrm{M}_i,\bar{t}}, \\
\mathrm{d}\bar{\mathbf{x}}_{\mathrm{D}_k} &= 6\mu_{\mathrm{D}}^2 \bar{\mathbf{F}}_{\mathrm{D}_k}(\bar{\boldsymbol{\xi}}_{\mathrm{M}}, \bar{\boldsymbol{\xi}}_{\mathrm{D}}, \bar{\boldsymbol{\xi}}_{\mathrm{L}}, \bar{\boldsymbol{\varphi}}_{\mathrm{M}}, \bar{\boldsymbol{\varphi}}_{\mathrm{D}}, \bar{\boldsymbol{\varphi}}_{\mathrm{L}})\mathrm{d}\bar{t} + \sqrt{2}\mu_{\mathrm{D}}\mathrm{d}\widetilde{\mathbf{W}}_{\mathrm{trans},\mathrm{D}_k,\bar{t}}, \\
\mathrm{d}\bar{\mathbf{x}}_{\mathrm{L}_j} &= 6\mu_{\mathrm{L}}^2 \bar{\mathbf{F}}_{\mathrm{L}_j}(\bar{\boldsymbol{\xi}}_{\mathrm{M}}, \bar{\boldsymbol{\xi}}_{\mathrm{D}}, \bar{\boldsymbol{\xi}}_{\mathrm{T}}, \bar{\boldsymbol{\xi}}_{\mathrm{L}}, \bar{\boldsymbol{\varphi}}_{\mathrm{M}}, \bar{\boldsymbol{\varphi}}_{\mathrm{D}}, \bar{\boldsymbol{\varphi}}_{\mathrm{T}}, \bar{\boldsymbol{\varphi}}_{\mathrm{L}})\mathrm{d}\bar{t} + \sqrt{2}\mu_{\mathrm{L}}\mathrm{d}\widetilde{\mathbf{W}}_{\mathrm{trans},\mathrm{L}_j,\bar{t}}, \\
\mathrm{d}\bar{\varphi}_{\mathrm{M}_i} &= \kappa\mu_{\mathrm{M}}^2\zeta_{\mathrm{M}}^2 g_{\mathrm{M}_i}(\bar{\boldsymbol{\xi}}_{\mathrm{M}}, \bar{\boldsymbol{\xi}}_{\mathrm{D}}, \bar{\boldsymbol{\xi}}_{\mathrm{L}}, \bar{\boldsymbol{\varphi}}_{\mathrm{M}}, \bar{\boldsymbol{\varphi}}_{\mathrm{D}}, \bar{\boldsymbol{\varphi}}_{\mathrm{L}})\mathrm{d}\bar{t} + \sqrt{2}\mu_{\mathrm{M}}\zeta_{\mathrm{M}}\mathrm{d}\widetilde{W}_{\mathrm{rot},\mathrm{M}_i,\bar{t}}, \\
\mathrm{d}\bar{\varphi}_{\mathrm{D}_k} &= \kappa\mu_{\mathrm{D}}^2\zeta_{\mathrm{D}}^2 g_{\mathrm{D}_k}(\bar{\boldsymbol{\xi}}_{\mathrm{D}}, \bar{\boldsymbol{\xi}}_{\mathrm{L}}, \bar{\boldsymbol{\varphi}}_{\mathrm{D}}, \bar{\boldsymbol{\varphi}}_{\mathrm{L}})\mathrm{d}\bar{t} + \sqrt{2}\mu_{\mathrm{D}}\zeta_{\mathrm{D}}\mathrm{d}\widetilde{W}_{\mathrm{rot},\mathrm{D}_k,\bar{t}}, \\
\mathrm{d}\bar{\varphi}_{\mathrm{L}_j} &= \kappa\mu_{\mathrm{L}}^2\zeta_{\mathrm{L}}^2 g_{\mathrm{L}_j}(\bar{\boldsymbol{\xi}}_{\mathrm{M}}, \bar{\boldsymbol{\xi}}_{\mathrm{D}}, \bar{\boldsymbol{\xi}}_{\mathrm{T}}, \bar{\boldsymbol{\xi}}_{\mathrm{L}}, \bar{\boldsymbol{\varphi}}_{\mathrm{M}}, \bar{\boldsymbol{\varphi}}_{\mathrm{D}}, \bar{\boldsymbol{\varphi}}_{\mathrm{T}}, \bar{\boldsymbol{\varphi}}_{\mathrm{L}})\mathrm{d}\bar{t} + \sqrt{2}\mu_{\mathrm{L}}\zeta_{\mathrm{L}}\mathrm{d}\widetilde{W}_{\mathrm{rot},\mathrm{L}_j,\bar{t}},
\end{aligned}$$

$i = 1, \ldots, z_{\mathrm{M}}; k = 1, \ldots, z_{\mathrm{D}}; j = 1, \ldots, z_{\mathrm{L}}; z_{\mathrm{T}} = 0$. Again, the interaction between the particles is described by the functions $\bar{\mathbf{F}}_{\mathrm{M}_i}$, $\bar{\mathbf{F}}_{\mathrm{D}_k}$, $\bar{\mathbf{F}}_{\mathrm{L}_j}$, g_{M_i}, g_{D_k} and g_{L_j}.

b) **Death Receptor Trimers and Death Receptor Ligands**

For death receptor trimers we obtain a system of stochastic differential equations with $3(z_{\mathrm{T}} + z_{\mathrm{L}})$ equations

$$\begin{aligned}
\mathrm{d}\bar{\mathbf{x}}_{\mathrm{T}_\iota} &= 6\mu_{\mathrm{T}}^2 \bar{\mathbf{F}}_{\mathrm{T}_\iota}(\bar{\boldsymbol{\xi}}_{\mathrm{T}}, \bar{\boldsymbol{\xi}}_{\mathrm{L}}, \bar{\boldsymbol{\varphi}}_{\mathrm{T}}, \bar{\boldsymbol{\varphi}}_{\mathrm{L}})\mathrm{d}\bar{t} + \sqrt{2}\mu_{\mathrm{T}}\mathrm{d}\widetilde{\mathbf{W}}_{\mathrm{trans},\mathrm{T}_\iota,\bar{t}}, \\
\mathrm{d}\bar{\mathbf{x}}_{\mathrm{L}_j} &= 6\mu_{\mathrm{L}}^2 \bar{\mathbf{F}}_{\mathrm{L}_j}(\bar{\boldsymbol{\xi}}_{\mathrm{M}}, \bar{\boldsymbol{\xi}}_{\mathrm{D}}, \bar{\boldsymbol{\xi}}_{\mathrm{T}}, \bar{\boldsymbol{\xi}}_{\mathrm{L}}, \bar{\boldsymbol{\varphi}}_{\mathrm{M}}, \bar{\boldsymbol{\varphi}}_{\mathrm{D}}, \bar{\boldsymbol{\varphi}}_{\mathrm{T}}, \bar{\boldsymbol{\varphi}}_{\mathrm{L}})\mathrm{d}\bar{t} + \sqrt{2}\mu_{\mathrm{L}}\mathrm{d}\widetilde{\mathbf{W}}_{\mathrm{trans},\mathrm{L}_j,\bar{t}}, \\
\mathrm{d}\bar{\varphi}_{\mathrm{T}_\iota} &= \kappa\mu_{\mathrm{T}}^2\zeta_{\mathrm{T}}^2 g_{\mathrm{T}_\iota}(\bar{\boldsymbol{\xi}}_{\mathrm{T}}, \bar{\boldsymbol{\xi}}_{\mathrm{L}}, \bar{\boldsymbol{\varphi}}_{\mathrm{T}}, \bar{\boldsymbol{\varphi}}_{\mathrm{L}})\mathrm{d}\bar{t} + \sqrt{2}\mu_{\mathrm{T}}\zeta_{\mathrm{T}}\mathrm{d}\widetilde{W}_{\mathrm{rot},\mathrm{T}_\iota,\bar{t}}, \\
\mathrm{d}\bar{\varphi}_{\mathrm{L}_j} &= \kappa\mu_{\mathrm{L}}^2\zeta_{\mathrm{L}}^2 g_{\mathrm{L}_j}(\bar{\boldsymbol{\xi}}_{\mathrm{M}}, \bar{\boldsymbol{\xi}}_{\mathrm{D}}, \bar{\boldsymbol{\xi}}_{\mathrm{T}}, \bar{\boldsymbol{\xi}}_{\mathrm{L}}, \bar{\boldsymbol{\varphi}}_{\mathrm{M}}, \bar{\boldsymbol{\varphi}}_{\mathrm{D}}, \bar{\boldsymbol{\varphi}}_{\mathrm{T}}, \bar{\boldsymbol{\varphi}}_{\mathrm{L}})\mathrm{d}\bar{t} + \sqrt{2}\mu_{\mathrm{L}}\zeta_{\mathrm{L}}\mathrm{d}\widetilde{W}_{\mathrm{rot},\mathrm{L}_j,\bar{t}},
\end{aligned}$$

$\iota = 1, \ldots, z_{\mathrm{T}}; j = 1, \ldots, z_{\mathrm{L}}; z_{\mathrm{D}} = 0; z_{\mathrm{M}} = 0$, where z_{T} denotes the number of death receptor trimers and z_{L} is the number of death receptor ligands.

c) **Cluster Units consisting of Death Receptor Monomers and Death Receptor Ligands**

Last but not least, we state the system of stochastic differential equations in case of cluster units. We obtain a system with $3z_{\mathrm{U}}$ equations

$$\begin{aligned}
\mathrm{d}\bar{\mathbf{x}}_{\mathrm{U}_\nu} &= 6\mu_{\mathrm{U}}^2 \bar{\mathbf{F}}_{\mathrm{U}_\nu}(\bar{\boldsymbol{\xi}}_{\mathrm{U}}, \bar{\boldsymbol{\varphi}}_{\mathrm{U}})\mathrm{d}\bar{t} + \sqrt{2}\mu_{\mathrm{U}}\mathrm{d}\widetilde{\mathbf{W}}_{\mathrm{trans},U_\nu,\bar{t}}, \\
\mathrm{d}\bar{\varphi}_{\mathrm{U}_\nu} &= \kappa\mu_{\mathrm{U}}^2\zeta_{\mathrm{U}}^2 g_{\mathrm{U}_\nu}(\bar{\boldsymbol{\xi}}_{\mathrm{U}}, \bar{\boldsymbol{\varphi}}_{\mathrm{U}})\mathrm{d}\bar{t} + \sqrt{2}\mu_{\mathrm{U}}\zeta_{\mathrm{U}}\mathrm{d}\widetilde{W}_{\mathrm{rot},\mathrm{U}_\nu,\bar{t}},
\end{aligned}$$

$\nu = 1, \ldots, z_{\mathrm{U}}$. The equations are nonlinearly coupled by the functions $\bar{\mathbf{F}}_{\mathrm{U}_\nu}$ and g_{U_ν}. This is the most simple of the five introduced systems since we only consider one particle type. The price for the simplicity of the model is the strong assumption that the structure of the cluster units remains fix all the time and the binding between

death receptor ligands and death receptor monomers does not break.

Given a certain initial condition for the coordinates and the orientations for all particles in each of the scenarios above, the random motion of the particles is determined by the Wiener processes $\widetilde{\mathbf{W}}_{\text{trans}}$ and $\widetilde{W}_{\text{rot}}$.

Since we are interested in the evolution of the signal competent cluster units, we need appropriate binding conditions which enable a decision whether two particles are bound. We propose that two particles are bound if the distance between the centers of mass of the particles is smaller than a certain threshold r_{cut} and if the angle between the vector connecting the centers of mass of the particles and the compatible binding site, lying closest to this vector, is smaller than δ. Here, we demand the corresponding binding site to be unoccupied.

So, in this section we finalized the particle model for the different scenarios concerning the various death receptor structures by assembling the stochastic differential equations derived in Section 3.3.1 and Section 3.3.2 to a nonlinearly coupled system of stochastic differential equations. Due to its complex structure, we solve the system of stochastic differential equations numerically. For this purpose, we introduce in the next section the Euler-Maruyama approximation.

3.4 Euler-Maruyama Approximation of the Equations

In order to solve the nonlinearly coupled system of stochastic differential equations numerically, we introduce a discretization $0 = \bar{t}_0 < \bar{t}_1 < \cdots < \bar{t}_n < \cdots < \bar{t}_N = T$ of the time interval $[0, T]$. Then, the approximation of the solution at the time $\bar{t}_n$ in general is denoted by $\bar{\mathbf{x}}^n$ and $\bar{\varphi}^n$. Furthermore, we assume the discretization in time to be equidistant with a step size $\bar{t}_{n+1} - \bar{t}_n =: \Delta\bar{t}$. In the following, the matrices $\bar{\boldsymbol{\xi}}^n_{\text{M}}$, $\bar{\boldsymbol{\xi}}^n_{\text{D}}$, $\bar{\boldsymbol{\xi}}^n_{\text{T}}$, $\bar{\boldsymbol{\xi}}^n_{\text{L}}$ and $\bar{\boldsymbol{\xi}}^n_{\text{U}}$ contain the approximation of the coordinates of death receptor monomers, death receptor dimers, death receptor trimers, death receptor ligands and cluster units, respectively, at time $\bar{t}_n$. Analogously, the components of the vectors $\bar{\boldsymbol{\varphi}}^n_{\text{M}}$, $\bar{\boldsymbol{\varphi}}^n_{\text{D}}$, $\bar{\boldsymbol{\varphi}}^n_{\text{T}}$, $\bar{\boldsymbol{\varphi}}^n_{\text{L}}$ and $\bar{\boldsymbol{\varphi}}^n_{\text{U}}$ describe the approximation of the direction of the binding sites of death receptor monomers, death receptor dimers, death receptor trimers, death receptor ligands and cluster units, respectively, at time $\bar{t}_n$. With these notations, we obtain the time discrete approximation of the solution, which is often called Euler-Maruyama approximation, for the different scenarios [34].

a.i) **Death Receptor Monomers and Death Receptor Ligands**

$$\begin{aligned}
\Delta\bar{\mathbf{x}}^n_{\mathrm{M}_i} &= 6\mu^2_{\mathrm{M}}\bar{\mathbf{F}}_{\mathrm{M}_i}(\bar{\boldsymbol{\xi}}^n_{\mathrm{M}},\bar{\boldsymbol{\xi}}^n_{\mathrm{D}},\bar{\boldsymbol{\xi}}^n_{\mathrm{L}},\bar{\boldsymbol{\varphi}}^n_{\mathrm{M}},\bar{\boldsymbol{\varphi}}^n_{\mathrm{D}},\bar{\boldsymbol{\varphi}}^n_{\mathrm{L}})\Delta\bar{t}+\sqrt{2}\mu_{\mathrm{M}}\Delta\widetilde{\mathbf{W}}_{\mathrm{trans},\mathrm{M}_i,n},\\
\Delta\bar{\mathbf{x}}^n_{\mathrm{L}_j} &= 6\mu^2_{\mathrm{L}}\bar{\mathbf{F}}_{\mathrm{L}_j}(\bar{\boldsymbol{\xi}}^n_{\mathrm{M}},\bar{\boldsymbol{\xi}}^n_{\mathrm{D}},\bar{\boldsymbol{\xi}}^n_{\mathrm{T}},\bar{\boldsymbol{\xi}}^n_{\mathrm{L}},\bar{\boldsymbol{\varphi}}^n_{\mathrm{M}},\bar{\boldsymbol{\varphi}}^n_{\mathrm{D}},\bar{\boldsymbol{\varphi}}^n_{\mathrm{T}},\bar{\boldsymbol{\varphi}}^n_{\mathrm{L}})\Delta\bar{t}+\sqrt{2}\mu_{\mathrm{L}}\Delta\widetilde{\mathbf{W}}_{\mathrm{trans},\mathrm{L}_j,n},\\
\Delta\bar{\varphi}^n_{\mathrm{M}_i} &= \kappa\mu^2_{\mathrm{M}}\zeta^2_{\mathrm{M}}g_{\mathrm{M}_i}(\bar{\boldsymbol{\xi}}^n_{\mathrm{M}},\bar{\boldsymbol{\xi}}^n_{\mathrm{L}},\bar{\boldsymbol{\varphi}}^n_{\mathrm{M}},\bar{\boldsymbol{\varphi}}^n_{\mathrm{L}})\Delta\bar{t}+\sqrt{2}\mu_{\mathrm{M}}\zeta_{\mathrm{M}}\Delta\widetilde{W}_{\mathrm{rot},\mathrm{M}_i,n},\\
\Delta\bar{\varphi}^n_{\mathrm{L}_j} &= \kappa\mu^2_{\mathrm{L}}\zeta^2_{\mathrm{L}}g_{\mathrm{L}_j}(\bar{\boldsymbol{\xi}}^n_{\mathrm{M}},\bar{\boldsymbol{\xi}}^n_{\mathrm{D}},\bar{\boldsymbol{\xi}}^n_{\mathrm{T}},\bar{\boldsymbol{\xi}}^n_{\mathrm{L}},\bar{\boldsymbol{\varphi}}^n_{\mathrm{M}},\bar{\boldsymbol{\varphi}}^n_{\mathrm{D}},\bar{\boldsymbol{\varphi}}^n_{\mathrm{T}},\bar{\boldsymbol{\varphi}}^n_{\mathrm{L}})\Delta\bar{t}+\sqrt{2}\mu_{\mathrm{L}}\zeta_{\mathrm{L}}\Delta\widetilde{W}_{\mathrm{rot},\mathrm{L}_j,n},
\end{aligned}$$

$i=1,\ldots,z_{\mathrm{M}}; j=1,\ldots,z_{\mathrm{L}}; z_{\mathrm{D}}=0; z_{\mathrm{T}}=0.$

a.ii) **Death Receptor Dimers and Death Receptor Ligands**

$$\begin{aligned}
\Delta\bar{\mathbf{x}}^n_{\mathrm{D}_k} &= 6\mu^2_{\mathrm{D}}\bar{\mathbf{F}}_{\mathrm{D}_k}(\bar{\boldsymbol{\xi}}^n_{\mathrm{M}},\bar{\boldsymbol{\xi}}^n_{\mathrm{D}},\bar{\boldsymbol{\xi}}^n_{\mathrm{L}},\bar{\boldsymbol{\varphi}}^n_{\mathrm{M}},\bar{\boldsymbol{\varphi}}^n_{\mathrm{D}},\bar{\boldsymbol{\varphi}}^n_{\mathrm{L}})\Delta\bar{t}+\sqrt{2}\mu_{\mathrm{D}}\Delta\widetilde{\mathbf{W}}_{\mathrm{trans},\mathrm{D}_k,n},\\
\Delta\bar{\mathbf{x}}^n_{\mathrm{L}_j} &= 6\mu^2_{\mathrm{L}}\bar{\mathbf{F}}_{\mathrm{L}_j}(\bar{\boldsymbol{\xi}}^n_{\mathrm{M}},\bar{\boldsymbol{\xi}}^n_{\mathrm{D}},\bar{\boldsymbol{\xi}}^n_{\mathrm{T}},\bar{\boldsymbol{\xi}}^n_{\mathrm{L}},\bar{\boldsymbol{\varphi}}^n_{\mathrm{M}},\bar{\boldsymbol{\varphi}}^n_{\mathrm{D}},\bar{\boldsymbol{\varphi}}^n_{\mathrm{T}},\bar{\boldsymbol{\varphi}}^n_{\mathrm{L}})\Delta\bar{t}+\sqrt{2}\mu_{\mathrm{L}}\Delta\widetilde{\mathbf{W}}_{\mathrm{trans},\mathrm{L}_j,n},\\
\Delta\bar{\varphi}^n_{\mathrm{D}_k} &= \kappa\mu^2_{\mathrm{D}}\zeta^2_{\mathrm{D}}g_{\mathrm{D}_k}(\bar{\boldsymbol{\xi}}^n_{\mathrm{D}},\bar{\boldsymbol{\xi}}^n_{\mathrm{L}},\bar{\boldsymbol{\varphi}}^n_{\mathrm{D}},\bar{\boldsymbol{\varphi}}^n_{\mathrm{L}})\Delta\bar{t}+\sqrt{2}\mu_{\mathrm{D}}\zeta_{\mathrm{D}}\Delta\widetilde{W}_{\mathrm{rot},\mathrm{D}_k,n},\\
\Delta\bar{\varphi}^n_{\mathrm{L}_j} &= \kappa\mu^2_{\mathrm{L}}\zeta^2_{\mathrm{L}}g_{\mathrm{L}_j}(\bar{\boldsymbol{\xi}}^n_{\mathrm{M}},\bar{\boldsymbol{\xi}}^n_{\mathrm{D}},\bar{\boldsymbol{\xi}}^n_{\mathrm{T}},\bar{\boldsymbol{\xi}}^n_{\mathrm{L}},\bar{\boldsymbol{\varphi}}^n_{\mathrm{M}},\bar{\boldsymbol{\varphi}}^n_{\mathrm{D}},\bar{\boldsymbol{\varphi}}^n_{\mathrm{T}},\bar{\boldsymbol{\varphi}}^n_{\mathrm{L}})\Delta\bar{t}+\sqrt{2}\mu_{\mathrm{L}}\zeta_{\mathrm{L}}\Delta\widetilde{W}_{\mathrm{rot},\mathrm{L}_j,n},
\end{aligned}$$

$k=1,\ldots,z_{\mathrm{D}}, j=1,\ldots,z_{\mathrm{L}}; z_{\mathrm{M}}=0; z_{\mathrm{T}}=0.$

a.iii) **Death Receptor Monomers, Death Receptor Dimers and Death Receptor Ligands**

$$\begin{aligned}
\Delta\bar{\mathbf{x}}^n_{\mathrm{M}_i} &= 6\mu^2_{\mathrm{M}}\bar{\mathbf{F}}_{\mathrm{M}_i}(\bar{\boldsymbol{\xi}}^n_{\mathrm{M}},\bar{\boldsymbol{\xi}}^n_{\mathrm{D}},\bar{\boldsymbol{\xi}}^n_{\mathrm{L}},\bar{\boldsymbol{\varphi}}^n_{\mathrm{M}},\bar{\boldsymbol{\varphi}}^n_{\mathrm{D}},\bar{\boldsymbol{\varphi}}^n_{\mathrm{L}})\Delta\bar{t}+\sqrt{2}\mu_{\mathrm{M}}\Delta\widetilde{\mathbf{W}}_{\mathrm{trans},\mathrm{M}_i,n},\\
\Delta\bar{\mathbf{x}}^n_{\mathrm{D}_k} &= 6\mu^2_{\mathrm{D}}\bar{\mathbf{F}}_{\mathrm{D}_k}(\bar{\boldsymbol{\xi}}^n_{\mathrm{M}},\bar{\boldsymbol{\xi}}^n_{\mathrm{D}},\bar{\boldsymbol{\xi}}^n_{\mathrm{L}},\bar{\boldsymbol{\varphi}}^n_{\mathrm{M}},\bar{\boldsymbol{\varphi}}^n_{\mathrm{D}},\bar{\boldsymbol{\varphi}}^n_{\mathrm{L}})\Delta\bar{t}+\sqrt{2}\mu_{\mathrm{D}}\Delta\widetilde{\mathbf{W}}_{\mathrm{trans},\mathrm{D}_k,n},\\
\Delta\bar{\mathbf{x}}^n_{\mathrm{L}_j} &= 6\mu^2_{\mathrm{L}}\bar{\mathbf{F}}_{\mathrm{L}_j}(\bar{\boldsymbol{\xi}}^n_{\mathrm{M}},\bar{\boldsymbol{\xi}}^n_{\mathrm{D}},\bar{\boldsymbol{\xi}}^n_{\mathrm{T}},\bar{\boldsymbol{\xi}}^n_{\mathrm{L}},\bar{\boldsymbol{\varphi}}^n_{\mathrm{M}},\bar{\boldsymbol{\varphi}}^n_{\mathrm{D}},\bar{\boldsymbol{\varphi}}^n_{\mathrm{T}},\bar{\boldsymbol{\varphi}}^n_{\mathrm{L}})\Delta\bar{t}+\sqrt{2}\mu_{\mathrm{L}}\Delta\widetilde{\mathbf{W}}_{\mathrm{trans},\mathrm{L}_j,n},\\
\Delta\bar{\varphi}^n_{\mathrm{M}_i} &= \kappa\mu^2_{\mathrm{M}}\zeta^2_{\mathrm{M}}g_{\mathrm{M}_i}(\bar{\boldsymbol{\xi}}^n_{\mathrm{M}},\bar{\boldsymbol{\xi}}^n_{\mathrm{L}},\bar{\boldsymbol{\varphi}}^n_{\mathrm{M}},\bar{\boldsymbol{\varphi}}^n_{\mathrm{L}})\Delta\bar{t}+\sqrt{2}\mu_{\mathrm{M}}\zeta_{\mathrm{M}}\Delta\widetilde{W}_{\mathrm{rot},\mathrm{M}_i,n},\\
\Delta\bar{\varphi}^n_{\mathrm{D}_k} &= \kappa\mu^2_{\mathrm{D}}\zeta^2_{\mathrm{D}}g_{\mathrm{D}_k}(\bar{\boldsymbol{\xi}}^n_{\mathrm{D}},\bar{\boldsymbol{\xi}}^n_{\mathrm{L}},\bar{\boldsymbol{\varphi}}^n_{\mathrm{D}},\bar{\boldsymbol{\varphi}}^n_{\mathrm{L}})\Delta\bar{t}+\sqrt{2}\mu_{\mathrm{D}}\zeta_{\mathrm{D}}\Delta\widetilde{W}_{\mathrm{rot},\mathrm{D}_k,n},\\
\Delta\bar{\varphi}^n_{\mathrm{L}_j} &= \kappa\mu^2_{\mathrm{L}}\zeta^2_{\mathrm{L}}g_{\mathrm{L}_j}(\bar{\boldsymbol{\xi}}^n_{\mathrm{M}},\bar{\boldsymbol{\xi}}^n_{\mathrm{D}},\bar{\boldsymbol{\xi}}^n_{\mathrm{T}},\bar{\boldsymbol{\xi}}^n_{\mathrm{L}},\bar{\boldsymbol{\varphi}}^n_{\mathrm{M}},\bar{\boldsymbol{\varphi}}^n_{\mathrm{D}},\bar{\boldsymbol{\varphi}}^n_{\mathrm{T}},\bar{\boldsymbol{\varphi}}^n_{\mathrm{L}})\Delta\bar{t}+\sqrt{2}\mu_{\mathrm{L}}\zeta_{\mathrm{L}}\Delta\widetilde{W}_{\mathrm{rot},\mathrm{L}_j,n},
\end{aligned}$$

$i=1,\ldots,z_{\mathrm{M}}; k=1,\ldots,z_{\mathrm{D}}; j=1,\ldots,z_{\mathrm{L}}; z_{\mathrm{T}}=0.$

b) **Death Receptor Trimers and Death Receptor Ligands**

$$\begin{aligned}
\Delta\bar{\mathbf{x}}^n_{\mathrm{T}_\iota} &= 6\mu^2_{\mathrm{T}}\bar{\mathbf{F}}_{\mathrm{T}_\iota}(\bar{\boldsymbol{\xi}}^n_{\mathrm{T}},\bar{\boldsymbol{\xi}}^n_{\mathrm{L}},\bar{\boldsymbol{\varphi}}^n_{\mathrm{T}},\bar{\boldsymbol{\varphi}}^n_{\mathrm{L}})\Delta\bar{t}+\sqrt{2}\mu_{\mathrm{T}}\Delta\widetilde{\mathbf{W}}_{\mathrm{trans},\mathrm{T}_\iota,n},\\
\Delta\bar{\mathbf{x}}^n_{\mathrm{L}_j} &= 6\mu^2_{\mathrm{L}}\bar{\mathbf{F}}_{\mathrm{L}_j}(\bar{\boldsymbol{\xi}}^n_{\mathrm{M}},\bar{\boldsymbol{\xi}}^n_{\mathrm{D}},\bar{\boldsymbol{\xi}}^n_{\mathrm{T}},\bar{\boldsymbol{\xi}}^n_{\mathrm{L}},\bar{\boldsymbol{\varphi}}^n_{\mathrm{M}},\bar{\boldsymbol{\varphi}}^n_{\mathrm{D}},\bar{\boldsymbol{\varphi}}^n_{\mathrm{T}},\bar{\boldsymbol{\varphi}}^n_{\mathrm{L}})\Delta\bar{t}+\sqrt{2}\mu_{\mathrm{L}}\Delta\widetilde{\mathbf{W}}_{\mathrm{trans},\mathrm{L}_j,n},\\
\Delta\bar{\varphi}^n_{\mathrm{T}_\iota} &= \kappa\mu^2_{\mathrm{T}}\zeta^2_{\mathrm{T}}g_{\mathrm{T}_\iota}(\bar{\boldsymbol{\xi}}^n_{\mathrm{T}},\bar{\boldsymbol{\xi}}^n_{\mathrm{L}},\bar{\boldsymbol{\varphi}}^n_{\mathrm{T}},\bar{\boldsymbol{\varphi}}^n_{\mathrm{L}})\Delta\bar{t}+\sqrt{2}\mu_{\mathrm{T}}\zeta_{\mathrm{T}}\Delta\widetilde{W}_{\mathrm{rot},\mathrm{T}_\iota,n},\\
\Delta\bar{\varphi}^n_{\mathrm{L}_j} &= \kappa\mu^2_{\mathrm{L}}\zeta^2_{\mathrm{L}}g_{\mathrm{L}_j}(\bar{\boldsymbol{\xi}}^n_{\mathrm{M}},\bar{\boldsymbol{\xi}}^n_{\mathrm{D}},\bar{\boldsymbol{\xi}}^n_{\mathrm{T}},\bar{\boldsymbol{\xi}}^n_{\mathrm{L}},\bar{\boldsymbol{\varphi}}^n_{\mathrm{M}},\bar{\boldsymbol{\varphi}}^n_{\mathrm{D}},\bar{\boldsymbol{\varphi}}^n_{\mathrm{T}},\bar{\boldsymbol{\varphi}}^n_{\mathrm{L}})\Delta\bar{t}+\sqrt{2}\mu_{\mathrm{L}}\zeta_{\mathrm{L}}\Delta\widetilde{W}_{\mathrm{rot},\mathrm{L}_j,n},
\end{aligned}$$

$\iota=1,\ldots,z_{\mathrm{T}}; j=1,\ldots,z_{\mathrm{L}},; z_{\mathrm{D}}=0; z_{\mathrm{M}}=0.$

c) **Cluster Units of Death Receptors and Death Receptor Ligands**

$$\begin{aligned}
\Delta\bar{\mathbf{x}}^n_{\mathrm{U}_\nu} &= 6\mu^2_{\mathrm{U}}\bar{\mathbf{F}}_{\mathrm{U}_\nu}(\bar{\boldsymbol{\xi}}^n_{\mathrm{U}},\bar{\boldsymbol{\varphi}}^n_{\mathrm{U}})\Delta\bar{t}+\sqrt{2}\mu_{\mathrm{U}}\Delta\widetilde{\mathbf{W}}_{\mathrm{trans},\mathrm{U}_\nu,n},\\
\Delta\bar{\varphi}^n_{\mathrm{U}_\nu} &= \kappa\mu^2_{\mathrm{U}}\zeta^2_{\mathrm{U}}g_{\mathrm{U}_\nu}(\bar{\boldsymbol{\xi}}^n_{\mathrm{U}},\bar{\boldsymbol{\varphi}}^n_{\mathrm{U}})\Delta\bar{t}+\sqrt{2}\mu_{\mathrm{U}}\zeta_{\mathrm{U}}\Delta\widetilde{W}_{\mathrm{rot},\mathrm{U}_\nu,n},
\end{aligned}$$

$\nu = 1, \ldots, z_{\mathrm{U}}$.

Here, the random variables

$$\begin{aligned}[\Delta\widetilde{\mathbf{W}}_{\mathrm{trans,M}_i/\mathrm{D}_k/\mathrm{T}_\iota/\mathrm{L}_j/\mathrm{U}_\nu,n}]_{l=1,2} :=& [\widetilde{\mathbf{W}}_{\mathrm{trans,M}_i/\mathrm{D}_k/\mathrm{T}_\iota/\mathrm{L}_j/\mathrm{U}_\nu,n+1}]_{l=1,2} \\ & - [\widetilde{\mathbf{W}}_{\mathrm{trans,M}_i/\mathrm{D}_k/\mathrm{T}_\iota/\mathrm{L}_j/\mathrm{U}_\nu,n}]_{l=1,2}, \\ \Delta\widetilde{W}_{\mathrm{rot,M}_i/\mathrm{D}_k/\mathrm{T}_\iota/\mathrm{L}_j/\mathrm{U}_\nu,n} :=& \widetilde{W}_{\mathrm{rot,M}_i/\mathrm{D}_k/\mathrm{T}_\iota/\mathrm{L}_j/\mathrm{U}_\nu,n+1} - \widetilde{W}_{\mathrm{rot,M}_i/\mathrm{D}_k/\mathrm{T}_\iota/\mathrm{L}_j/\mathrm{U}_\nu,n}\end{aligned}$$

are independent and $\mathcal{N}(0, \Delta\bar{t})$ distributed, that means

$$E([\Delta\widetilde{\mathbf{W}}_{\mathrm{trans,M}_i/\mathrm{D}_k/\mathrm{T}_\iota/\mathrm{L}_j/\mathrm{U}_\nu,n}]_{l=1,2}) = E(\Delta\widetilde{W}_{\mathrm{rot,M}_i/\mathrm{D}_k/\mathrm{T}_\iota/\mathrm{L}_j/\mathrm{U}_\nu,n}) = 0$$

and

$$E(([\Delta\widetilde{\mathbf{W}}_{\mathrm{trans,M}_i/\mathrm{D}_k/\mathrm{T}_\iota/\mathrm{L}_j/\mathrm{U}_\nu,n}]_{l=1,2})^2) = E((\Delta\widetilde{W}_{\mathrm{rot,M}_i/\mathrm{D}_k/\mathrm{T}_\iota/\mathrm{L}_j/\mathrm{U}_\nu,n})^2) = \Delta\bar{t}.$$

Since $\mathcal{N}(0, \Delta\bar{t})$ distributed random variables can be written as $\Delta\widetilde{W}_{\cdot,\cdot,n} = Z_n \cdot \sqrt{\Delta\bar{t}}$, where Z_n is a normally distributed random variable with mean zero and variance one, i.e. $Z_n \sim \mathcal{N}(0,1)$, the computation of the random variables is reduced to the computation of $\mathcal{N}(0,1)$ distributed random variables. For this purpose, we apply the central limit theorem, which can be found in [45, Corollary 7.39] for instance.

Theorem 3.1 (Central Limit Theorem).
Let $(X_n)_{n\in\mathbb{N}}$ a sequence of independent and identically distributed (i.i.d.) random variables with $\sigma^2 := \mathbb{V}(X_1) < \infty$. Then, the standardized sum S_n^* converges in distribution to the standardized normal distribution, that means

$$S_n^* = \frac{\sum_{i=1}^n (X_i - \mathbb{E}(X_1))}{\sigma\sqrt{n}} \xrightarrow{d} \chi,$$

with $\chi \sim \mathcal{N}(0,1)$.

For the application of this result, we choose a sequence of i.i.d. random variables on the interval $[0,1]$ with $\mathbb{E}(X_i) = 1/2$ and $\mathbb{V}(X_i) = 1/12$. In order to simplify the calculation of the random variables, we take a set of twelve i.i.d. random variables $X_1, \ldots, X_{12}$, and thereby S_{12}^* gets

$$S_{12}^* = \frac{\sum_{i=1}^{12} (X_i - \mathbb{E}(X_1))}{\sigma\sqrt{n}} = \frac{\sum_{i=1}^{12} (X_i - \frac{1}{2})}{\sqrt{\frac{1}{12}}\sqrt{12}} = \sum_{i=1}^{12} X_i - 6.$$

The standardized sum S_{12}^* takes values in $[-6, 6]$ and describes approximately a $\mathcal{N}(0,1)$ distributed random variable. The code fragment in C notation for their approximation is as follows

Algorithm 3.1.

```
int i=0;
double ZV = 0;
while (i<12) {
  ZV+=rand()/RAND_MAX;
  i++;
}
ZV-=6;
```

An alternative is the Box-Muller method, confer for instance [34, p. 13]. Starting with two i.i.d. random variables $\mathcal{V}_1$ and $\mathcal{V}_2$ on the interval $[0, 1]$, the transformation

$$N_1 = \sqrt{-2\ln(\mathcal{V}_1)} \cdot \cos(2\pi\mathcal{V}_2),$$
$$N_2 = \sqrt{-2\ln(\mathcal{V}_1)} \cdot \sin(2\pi\mathcal{V}_2)$$

yields two independent standard Gaussian random variables N_1 and N_2. Using this method, numerical problems can occur. If the random variable $\mathcal{V}_1$ takes the value 0, then the transformation fails. Considering thousands of particles and a step size in time of one nanosecond that yields billions of time steps, the case $\mathcal{V}_1 = 0$ can not be excluded. So, we choose for the generation of the random numbers the method applying the central limit theorem.
In order to compute the Euler-Maruyama approximation of the solution of the nonlinearly coupled system of stochastic differential equations, we have to evaluate the functions $\bar{\mathbf{F}}_{\mathrm{M}_i/\mathrm{D}_k/\mathrm{T}_\iota/\mathrm{L}_j/\mathrm{U}_\nu}$ and $g_{\mathrm{M}_i/\mathrm{D}_k/\mathrm{T}_\iota/\mathrm{L}_j/\mathrm{U}_\nu}$ besides the generation of normally distributed random variables. According to the short-ranged interaction between the particles, the simulation domain is decomposed into quadratic grid cells of a suitable size so that the interaction only occurs between particles in adjacent grid cells. To utilize this fact, we apply the Linked-Cell Method established in [23] to achieve a more efficient computation of the Euler-Maruyama approximation. The basic idea of the implementation is reflected in the subsequent Section 3.5.

3.5 The Linked-Cell Method

After introducing the particle model described by a system of stochastic differential equations in Section 3.3, we presented in Section 3.4 a discretization of the system, namely the Euler-Maruyama approximation. In order to compute an approximation of the solution, we apply the Linked-Cell Method established in [23] and implement the algorithms in the computer language C in order to achieve a higher efficiency compared to a 'simple' Matlab implementation, for instance. So, we explain in this section the basic idea of the Linked-

Cell Method and highlight the specifics of the model with multiple particle types and the additional particle rotation. Instead of listing the complete code, we state code fragments both in C syntax as well as in pseudo-code notation. For the Linked-Cell Method the simulation domain is decomposed in a first instance in quadratic grid cells. The grid cells are of size $l \times l$, where l is chosen larger or equal to the cut-off radius r_{cut}. Here, the cut-off radius is determined by the range of influence of the truncated interaction potential. For instance, the particle in the center of the circle in Figure 3.8 only interacts with particles within the dark-gray shaded area. Therefore, for the computation of the interaction between the particles, only nine grid cells have to be taken into account, namely the eight adjacent cells and the grid cell that contains the particle under consideration, illustrated by the light-gray shaded area in Figure 3.8. For particles lying close to the boundary, the

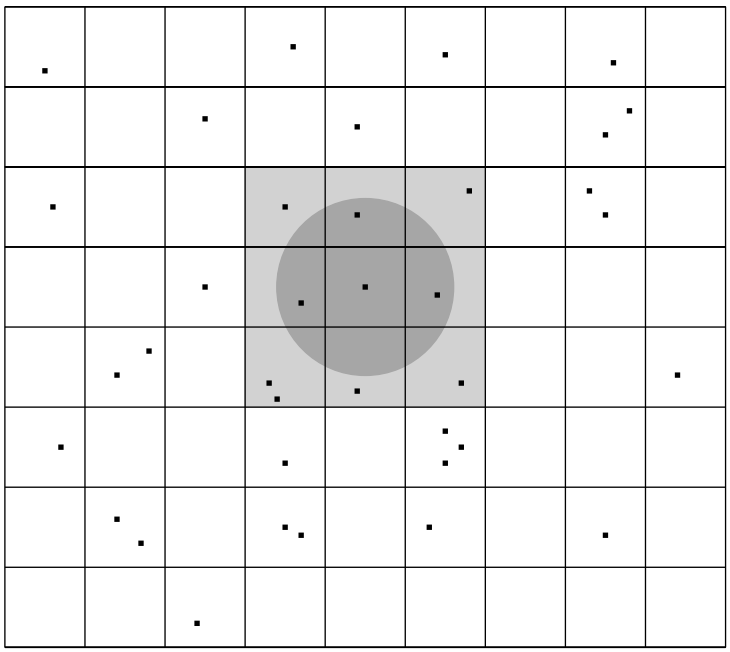

Figure 3.8: The simulation domain is decomposed into quadratic grid cells of size $l \times l$ for the application of the Linked-Cell Method, cf. [23]. The dark-gray and the light-gray shaded area illustrate the domain of influence of a particle and the grid cells containing fragments of this domain, respectively.

periodic boundary conditions play a decisive role. In this case, the particles also interact with particles at the opposite sites of the simulation domain, illustrated by the light-gray shaded area in Figure 3.9. The circle describing the interaction area is now decomposed into several unconnected fragments distributed over the simulation domain, depicted by the dark-gray shaded area in Figure 3.9. With the decomposition at hand, we introduce to each grid cell a list containing all particles of a certain particle type lying in the corresponding cell. For this purpose, we define the structure `ParticleList` composed of the structure `Particle` and a pointer `next` that points to the next element of the list, hence

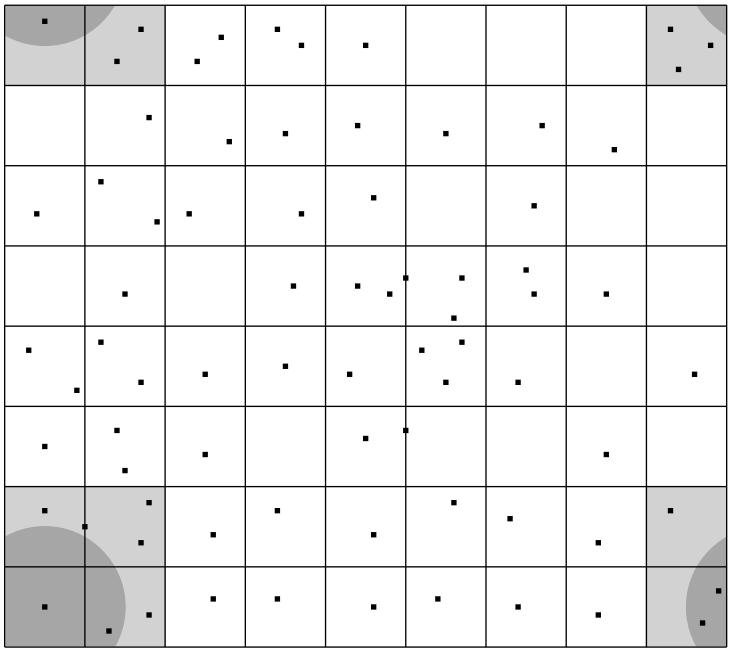

Figure 3.9: The simulation domain with its decomposition and periodic boundary conditions, cf. [23]. The domain of influence of a particle (dark-gray shaded area) is now an unconnected domain and contains parts at the opposite site of the simulation domain. The light-gray shaded area describes the grid cells that contain fragments of the domain of influence.

```
typedef struct ParticleList {
  Particle p;
  struct ParticleList *next;
} ParticleList.
```

Here, the structure `Particle` contains all properties of the particles, namely the coordinates $\mathbf{x}$, the force $\mathbf{F}$, the direction of the binding site $\mathbf{E}$, the occupation state of the binding sites $\mathbf{B}$, the moment of inertia D, the number of particles *count* that influences the rotation of the particle, the index of the particle and its type. We define

```
typedef struct {
  real x[2], F[2], E[2], B[3], D;
  int count, INDEX;
  char Typ;
} Particle.
```

The structure `ParticleList` finally enables the listing of particles located inside a single grid cell, cf. Figure 3.10. In order to set the anchor of such a list of particles, we define

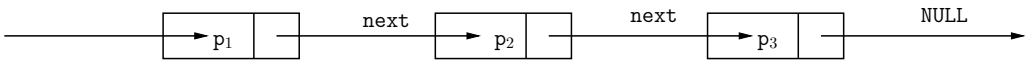

Figure 3.10: A list with particles which are located in a single grid cell. It consists of modules of the structure `ParticleList` which are linked by the pointer `next`. The `next`-pointer of the last particle is the `NULL`-pointer signalizing the end of the list.

the structure

```
typedef ParticleList* Cell.
```

Since we obtain a large amount of grid cells through the decomposition of the simulation domain, we need a particle list to each grid cell of the decomposition. Here, each of the particle lists contains all particles located in the corresponding grid cell. In order to store the list of particles to a certain grid cell, we need the address in the storage of the first particle of the list. We shortly call it anchor. According to the decomposition of the simulation domain, we have a large amount of grid cells and one anchor to each grid cell. These anchors can be efficiently stored by the pointer `grid` on the structure `Cell`. In doing so, we receive a dynamical structure for the storage of all particles under consideration. The advantage of the pointer structure is obvious. On the one hand, the size of a particle list is not known initially, so that the storage for the lists can be allocated dynamically. On the other hand, the length of the particle lists varies from grid cell to grid cell, so that a matrix of a fixed size is unsuitable for the storage of the particles in a list. In order to decide which grid cell is stored at which position in the 'vector' `grid`, we need a mapping of the geometric index of the grid cell to the index of the component of the vector `grid`. Let `nc[0]` be the number of grid cells in x-direction, then the grid cell with the geometric index `(ic[0],ic[1])` is stored at the position

```
#define index(ic,nc) ( (ic)[0] + (nc)[0]*(ic)[1] ).
```

With this notation, we obtain a comfortable opportunity to implement a loop over all particles within a grid cell, namely

```
for (ParticleList *i=grid[index(ic,nc)];NULL!=i;i=i->next)
```

for an arbitrary but fixed index `(ic[0],ic[1])`. Actually, the loop over all particles of one type is written in the form

```
for (ic[0]=0;ic[0]<nc[0];ic[0]++)
  for (ic[1]=0;ic[1]<nc[1];ic[1]++)
    for (ParticleList *i=grid[index(ic,nc)];NULL!=i;i=i->next),
```

where `nc[0]` denotes the number of grid cells in x-direction and `nc[1]` is the number of grid cells in y-direction. With the data structure and the module for a loop at hand, we state the most important implementation steps of the algorithms and start with the central program `main`:

```
int main() {
Setting of Simulation Configuration
pnc = 1;
for (int d=0;d<2;d++)
    pnc *= nc[d];
Cell *gridi = (Cell*)malloc(pnc*sizeof(*gridi));
initData_LC(grid1,grid2,grid3,nc,l);
TimeIntegration_LC(0,dt,T,grid1,grid2,grid3,nc,l);
freeList_LC(gridi,nc);
free(gridi);
return 0;
},
```

where `gridi` is a placeholder for `grid1`, `grid2` and `grid3` since we consider up to three different particle types. In the first step, we configure the simulation by choosing the domain size, the number of grid cells, the step size in time, the number of time steps, the number of particles and the particle type. Obviously, a large part of the routine `main` deals with the allocation and the deallocation of storage. But the main part of the routine `main` is the call of the routine `TimeIntegration_LC` after the initial conditions of the particles are set by the routine `initData_LC`. The routine `TimeIntegration_LC` essentially effects the successive integration of the discrete system of stochastic differential equations:

```
void TimeIntegration_LC(real t,real dt,real T,Cell *grid1,Cell *grid2,
                        Cell *grid3,int *nc,real *l) {
int ic[2];
while (t <= T) {
  for (ic[0]=0;ic[0]<nc[0];ic[0]++)
    for (ic[1]=0;ic[1]<nc[1];ic[1]++) {
      for (ParticleList *i=gridi[index(ic,nc)];NULL!=i;i=i->next) {
        reset_bindingsites(&i->p);
        reset_forces(&i->p);
      }
    }
  compF_LC(gridi, gridj, nc); // all combinations
  compX_LC(gridi, nc, l, dt);
```

```
  clusterDet(grid1,grid2,grid3,nc);
  t += dt;
}
}.
```

First, the binding sites and the forces for all particles are reset to zero. Here, the comfortable structure of the loop module is used. Afterward, the interaction forces between all particles are computed. The notation `compF_LC(gridi, gridj, nc)` means, that the interaction between all particle types is considered. For instance in case of the interaction between death receptor monomers and death receptor ligands, we have `compF_LC(grid1, grid3, nc)` under the assumption that death receptor monomers are listed in the vector `grid1` and death receptor ligands are stored in `grid3`. The routine `compF_LC` will be explained at the end of this section in more detail together with the implementation of the calculation of the forces and moments. The expression `compX_LC(gridi, nc, l, dt)` stands also representative for the enumeration `compX_LC(grid1, nc, l, dt)`, `compX_LC(grid2, nc, l, dt)`, `compX_LC(grid3, nc, l, dt)`. The respective routine simply regulates the update of the particle coordinates and the particle orientation, hence

```
void compX_LC(Cell *grid, int *nc, real *l, real dt) {
int ic[2];
for (ic[0] = 0;ic[0] < nc[0];ic[0]++)
  for (ic[1]=0; ic[1]<nc[1];ic[1]++)
    for (ParticleList *i=grid[index(ic,nc)]; NULL!=i; i=i->next)
      update(&i->p, dt);
moveParticles_LC(grid,nc,l);
}.
```

The essential part of the routine `compX_LC` is the call of the routine `update` for each particle of a certain type. In detail, the routine `update` reads

```
void update(Particle *p, real dt) {
Initialization of the variables
for (int d=0;d<2;d++) {
  for (int k=0;k<12;k++)
    zvx[d]+=( rand() / (real) RAND_MAX );
  zvx[d]-=6;
  p->x[d]+=6.0*GAMMA_N*MU*MU*p->F[d]*dt + sqrt(2)*MU*sqrt(dt)*zvx[d];
}
for (int q=0;q<12;q++)
  zvE += ( rand() / (real) RAND_MAX );
```

```
zvE -= 6;
for (int d=0;d<2;d++)
  dir[d] = p->E[d];
help = (p->count!=0)*p->count+(p->count==0)*1;
angle =  KAPPA*dt*MU*MU*ZETA*ZETA*p->D/help + MU*ZETA*sqrt(dt)*zvE;
p->E[0] = cos(angle)*dir[0]-sin(angle)*dir[1];
p->E[1] = sin(angle)*dir[0]+cos(angle)*dir[1];
}.
```

We recognize in the first half of the routine `update` the generation of the normally distributed random variable through the application of the central limit theorem and the update of the particle coordinates according to the discretized stochastic differential equation for the particle translation. In the second half of the routine, we find the generation of an approximation of a normally distributed random number for the particle rotation and the computation of the angle φ according to the discretized stochastic differential equation for the particle rotation. Finally, with the help of a rotation matrix and a matrix-vector multiplication, we determine the new direction of the binding site. The only task of the routine `moveParticles_LC` in the routine `compX_LC` is the update of the status of the lists. If a particle leaves a grid cell according to the new coordinates computed in `update`, the particle has to be deleted from the old list and inserted into the list of the new grid cell. The deletion from lists and the insertion in lists is done with the routine `moveParticles_LC`:

```
void moveParticles_LC(Cell *grid, int *nc, real *l) {
int ic[2], kc[2];
for (ic[0]=0;ic[0]<nc[0];ic[0]++)
  for (ic[1]=0; ic[1]<nc[1];ic[1]++) {
    ParticleList **q = &grid[index(ic,nc)];
    ParticleList *i = *q;
    while (NULL!=i) {
      for (int d=0;d<2;d++) {
        i->p.x[d] = i->p.x[d] - floor(i->p.x[d]/l[d])*l[d];
        kc[d] = (int)floor(i->p.x[d]*nc[d]/l[d]);
      }
      if ((ic[0]!=kc[0])||(ic[1]!=kc[1])) {
        deleteList(q);
        insertList(&grid[index(kc,nc)],i);
      }
      else q = &i->next;
      i = *q;
```

```
    }
  }
}.
```

Of course, the periodic boundary conditions have to be respected. The rest agrees exactly with the code in [23] and is here stated just for the sake of completeness. The routines `deleteList` and `insertList`, also given in [23], are omitted here.
Up to now, the routines agree or are very close to the code fragments given in [23] except the routine `update` where the concrete structure of the stochastic differential equations is implemented. Additionally, a further extension of the routines in [23] is the consideration of several particle types.
In the following, we present code fragments for the computation of the interaction forces, for the computation of the moments of inertia and the determination of the bindings between the particles. We state the main idea of the implementation in short code fragments since the complete code for all particle configurations would be beyond the scope of this thesis. In the routine `TimeIntegration_LC`, two routines, namely `compF_LC` and `clusterDet`, are called which are not explained in detail until now. However, with the routine `compF_LC` the interaction forces and the moments of inertia are computed:

```
void compF_LC(Cell *gridi, Cell *gridj, int *nc) {
Initialization of the variables
Loop over all particles in grid i
 Loop over all particles in adjacent grids j {
  Index shift according to the periodic boundary conditions
  if (!(i->p.x[0]==j->p.x[0] && i->p.x[1]==j->p.x[1])) {
   r = 0.0;
// coordinate shift according to periodic boundary conditions
   j->p.x[0] = j->p.x[0]-(kc[0]<0)*1+(kc[0]>=nc[0])*1;
   j->p.x[1] = j->p.x[1]-(kc[1]<0)*1+(kc[1]>=nc[1])*1;
   for (int d=0;d<2;d++)
    r += sqr(j->p.x[d]-i->p.x[d]);
   r = sqrt(r);
   if (r<=RCUT) {
    moment(&i->p, &j->p, r);
    force_heavi(&i->p, &j->p, r);
   }
// shift back according to periodic boundary conditions
   j->p.x[0] = j->p.x[0]+(kc[0]<0)*1-(kc[0]>=nc[0])*1;
   j->p.x[1] = j->p.x[1]+(kc[1]<0)*1-(kc[1]>=nc[1])*1;
  }
```

```
 }
}.
```

The essential part of the routine `compF_LC` is the call of the routines `moment` and `force_heavi`. Due to the decomposition of the simulation domain, the second loop only runs over nine grid cells adjacent to the grid cell of the first loop. By this, the costs for the algorithms can be significantly reduced. Besides, the interaction between two particles is only computed by the routines `moment` and `force_heavi` if the distance between the particles is less than the cut-off radius r_{cut} according to the truncated interaction potential. For this purpose, the distance between each two particles has to be computed. At the end, the routines `force_heavi` and `moment` contain the concrete structure of the interaction. In the following, the introduced code fragments show the implementation of the interactions between death receptor monomers and death receptor ligands. The other interactions possess the same structure and are replaced by dots in the given code fragments:

```
void force_heavi(Particle *i, Particle *j, real r) {
real phii = detAngle(i->x[0]-j->x[0],i->x[1]-j->x[1]);
real phi0i, phi0j;
real phij = detAngle(j->x[0]-i->x[0],j->x[1]-i->x[1]);
real kraft = 0.0;
...
phi0i = detAngle(j->E[0],j->E[1]);
phi0j = detAngle(-i->E[0],-i->E[1]);
kraft = pow(SIGMA_L/r,POT);
i->F[0]+=10.0/r*cos(phii)*POT*(2.0*kraft*kraft- ALPHA_N*kraft*
         (heaviside(DELTA-abs(phii-phi0i))+
          heaviside(DELTA-abs(phii-phi0i-2.0*M_PI/3.0))+
          heaviside(DELTA-abs(phii-phi0i-4.0*M_PI/3.0))));
i->F[1]+=10.0/r*sin(phii)*POT*(2.0*kraft*kraft- ALPHA_N*kraft*
         (heaviside(DELTA-abs(phii-phi0i))+
          heaviside(DELTA-abs(phii-phi0i-2.0*M_PI/3.0))+
          heaviside(DELTA-abs(phii-phi0i-4.0*M_PI/3.0))));
kraft = pow(SIGMA_M/r,POT);
j->F[0]+=10.0/r*cos(phij)*POT*(2.0*kraft*kraft -
         ALPHA_N*kraft*heaviside(DELTA-abs(phij-phi0j)));
j->F[1]+=10.0/r*sin(phij)*POT*(2.0*kraft*kraft -
         ALPHA_N*kraft*heaviside(DELTA-abs(phij-phi0j)));
...
}.
```

First, we mention that the factor 10.0 occurs in the formula for the forces due to the by a factor ten larger binding energy between a death receptor monomer and a death receptor ligand. Furthermore, the Heaviside function implemented in the routine `heaviside` provides the directional dependence of the interaction potential. That means the attractive part of the potential is multiplied by the Heaviside function and thereby gets switched-off for negative arguments of the Heaviside function.

According to the three binding sites of the death receptor ligands, for the computation of the force acting on a death receptor monomer, the attractive part of the potential is multiplied with a sum of three Heaviside-functions with disjoint arguments. For the force acting on a death receptor ligand, the attractive part is multiplied with a single Heaviside-function according to the sole binding site of death receptor monomers for the association with death receptor ligands. On the other hand, the repulsive part of the interaction is always active since it does not depend on the mutual orientation of the particles. The parameter `POT` describes the exponent of the Lennard-Jones potential and is specified in the `headerfile` as well as the parameter `ALPHA_N`. Besides, the terms `cos(phii)`, `sin(phii)`, `cos(phij)` and `sin(phij)` care for the direction of the forces, and the angles are determined by the routine `detAngle`, namely

```
real detAngle(real x, real y) {
return atan(y/x) + (x<0.0)*M_PI + (x>0.0)*(y<0.0)*2.0*M_PI;
}.
```

Since the function `atan()` yields values in the interval $[-\pi/2, \pi/2]$, we map the values obtained by the function `atan()` to angles in the interval $[0, 2\pi]$. Last but not least, the implementation of the computation of the moments of inertia effected by adjacent particles is introduced. The code fragment for death receptor monomers and death receptor ligands reads

```
void moment(Particle *i, Particle *j, real r) {
real phi = 0.0, psi = 0.0;
real A = -2.598/(M_PI*M_PI*M_PI);
...
real phi_Ei = detAngle(-i->E[0],-i->E[1]);
real phi_ij = detAngle(j->x[0]-i->x[0],j->x[1]-i->x[1]);
phi = phi_ij - phi_Ei;
Shift phi to the interval (-pi,pi)
real phi_Ej = detAngle(j->E[0],j->E[1]);
real phi_ji = detAngle(i->x[0]-j->x[0],i->x[1]-j->x[1]);
psi = phi_ji - phi_Ej;
Shift psi to the interval (-pi/3,pi/3)
```

```
i->D += A*phi*(phi-M_PI)*(phi+M_PI)*
        *heaviside(RCUT_M-r)*(RCUT_M-r)/(RCUT_M);
i->count += 1;
j->D += A*27*psi*(psi-M_PI/3.0)*(psi+M_PI/3.0)*
        *heaviside(RCUT_L-r)*(RCUT_L-r)/(RCUT_L);
j->count += 1
...
}.
```

Initially, the variables are initialized and a standardization parameter `A` is specified. Then, the angles $\psi_{\mathrm{L}_i;\mathrm{M}_k}$ and $\psi_{\mathrm{M}_i;\mathrm{L}_k}$ are determined. Since the angles `phi_Ei` and `phi_ij` take values in the interval $[0, 2\pi]$, we obtain `phi` $\in [-2\pi, 2\pi]$, so that we shift `phi` to the interval $[-\pi, \pi]$ according to the two binding sites of the death receptor monomers. The same arguments hold for the implementation of the angle `psi` and the shift to the interval $[-\pi/3, \pi/3]$ according to the three binding sites of death receptor ligands. Finally, the function g is implemented in the computation of `i->D` and `j->D`, respectively. Here, the parameter `A` ensures that the supremum for the moment of inertia is one. The last factor in the formula for the computation of the moments of inertia diminishes the influence of particles whose distance to the particle under consideration is relatively large.

These routines enable an efficient simulation of the particle translation and particle rotation on the cellular membrane. Since we are not only interested in the motion of the particles but also in the formation of ligand-receptor clusters, a routine for the determination of the bindings between the particles is required. Again, we only state a code fragment for the association of death receptor monomers with death receptor ligands and of a death receptor monomer with another death receptor monomer. The structure of the code for the other associations is similar and is replaced here by dots. The routine `clusterDet` reads

```
void clusterDet(Cell *grid1, Cell *grid2, Cell *grid3, int *nc) {
...
Loop over all death receptor monomers (i) {
 if (i->p.B[0] == 0) {
  Loop over all death receptor monomers in adjacent cells (j) {
   r = 0.0;
   for (int d=0;d<2;d++)
    r += sqr(i->p.x[d] - j->p.x[d]);
   r = sqrt(r);
   if (r<=RCUT) {
    sp1 = i->p.E[0]*(j->p.x[0]-i->p.x[0]) +
```

```
          i->p.E[1]*(j->p.x[1]-i->p.x[1]);
    sp2 = j->p.E[0]*(i->p.x[0]-j->p.x[0]) +
          j->p.E[1]*(i->p.x[1]-j->p.x[1]);
    bed1 = sp1 / (r * sqrt(sqr(i->p.E[0])+sqr(i->p.E[1])));
    bed2 = sp2 / (r * sqrt(sqr(j->p.E[0])+sqr(j->p.E[1])));
    if ( bed1>=cos(DELTA) && bed2 >= cos(DELTA) )
     if (i->p.B[0] == 0 && j->p.B[0] == 0) {
      i->p.B[0] = j->p.INDEX;
      j->p.B[0] = i->p.INDEX;
     }
    }
   }
 }
 if (i->p.B[1]==0) {
  Loop over all death receptor ligands (j)
   MaximumML = -1.0;
   IndexML = 0;
   r = 0.0;
   for (int d=0;d<2;d++)
    r += sqr(i->p.x[d] - j->p.x[d]);
   r = sqrt(r);
   if (r<=RCUT) {
    sp1 = -i->p.E[0]*(j->p.x[0]-i->p.x[0])
          -i->p.E[1]*(j->p.x[1]-i->p.x[1]);
    bed1 = sp1 / (r * sqrt(sqr(i->p.E[0])+sqr(i->p.E[1])));
    for (int q=0;q<3;q++) {
     phij = q * 2.0 * M_PI / 3.0;
     sp2=(cos(phij)*j->p.E[0]-sin(phij)*j->p.E[1])*(i->p.x[0]-j->p.x[0])+
         (sin(phij)*j->p.E[0]+cos(phij)*j->p.E[1])*(i->p.x[1]- j->p.x[1]);
     bed2=sp2 / (sqrt(sqr(j->p.E[0]) + sqr(j->p.E[1])) * r);
     if (bed2 >= MaximumML) {
      MaximumML = bed2;
      IndexML = q;
     }
    }
    if ( bed1>= cos(DELTA) && MaximumML >= cos(DELTA) )
     if (i->p.B[1] == 0 && j->p.B[IndexML] == 0) {
      i->p.B[1] = j->p.INDEX;
```

```
      j->p.B[IndexML] = i->p.INDEX;
     }
    }
 }
}
...
}.
```

The given code fragment starts with a loop over all death receptor monomers. The subsequent if-condition `if (i->p.B[0] == 0)` cares for the state of the binding site for the association with death receptor monomers whereas the if-condition `if (i->p.B[1] == 0)` looks at the binding site for the association with death receptor ligands. The binding site is unoccupied if the value for the corresponding component of the vector `B` is zero. Two conditions must be fulfilled for the association of two death receptor monomers.

(i) the distance between the death receptor monomers is smaller than r_{cut},

(ii) the angle between the vector `E` defining the first binding site of the death receptor monomer `i` and the vector `j->p.x - i->p.x` connecting the death receptor monomers `i` and `j` is smaller than `DELTA`. Of course, the same condition must be satisfied for the death receptor monomer `j`.

The angle between two vectors is naturally computed via the scalar product of the two vectors divided by the norms of the vectors. Then, instead of computing the arccos, we ask the cosinus of the angle to be larger than the cosinus of `DELTA`. If the two conditions (i) and (ii) are satisfied, we again have to check whether the corresponding binding sites of the involved particles are *still* unoccupied, therefore the final condition `if (i->p.B[0] == 0 && j->p.B[0] == 0)`. In case of the association of death receptor monomers with death receptor ligands, the conditions have to be modified. Since death receptor ligands have three binding sites for death receptor monomers, the binding site lying closest to the vector connecting the corresponding particles has to be found. For this purpose, a loop over the three binding sites is implemented and the smallest angle between the vector `j->p.E` defining the binding site of the death receptor ligand and the vector `i->p.x - j->p.x` is found. Again, we provide the cosinus of the angles to be larger than the cosinus function evaluated at `DELTA`. The final condition `if (i->p.B[1] == 0 && j->p.B[IndexML] == 0)` ensures again that the corresponding binding sites are *still* unoccupied. Of course, the routine `clusterDet` also contains the conditions for the association of other particles. To avoid a section overcrowded with programming code, we restrict the presentation of the main idea to the introduced particle configuration with death receptor ligands and death receptor monomers.

In this section, we replicated the main concept of the Linked-Cell Method and modified the algorithms according to the special structure of the particle model introduced in Section 3.3.4 and Section 3.3.5. In contrast to [23], our particle model contains several distinguishable particle types and thus, we have to consider the particle-specific interactions between the particles. A further extension of the Linked-Cell Method in [23] is the additional consideration of the particle rotation established in the particle model in Section 3.3.5. Additionally, the evaluation of the bindings between the particles is implemented. In the subsequent section, we first give the parameter setting of the particle model. Afterward, we present the results of the numerical simulations. At this juncture, we distinguish the different scenarios established in Section 3.3.3 and analyze the evolution of signal competent cluster units.

3.6 Results of the Numerical Simulations

In this section, we present numerical results of the Euler-Maruyama approximation introduced in Section 3.4. In order to compare the evolution of signal competent cluster units, we perform the simulation for various particle numbers. But before we analyze the results, we first give the values for the parameters in the system of stochastic differential equations and introduce subsequently the notations for the different ligand-receptor complexes.

Parameter Values of the System of Stochastic Differential Equations

For our model, we consider a typical type I cell, namely the rhabdomyosarcoma cell line KYM-1, cf. Chapter 2. For simplicity, we assume that these cells can be modeled as a sphere with radius $10\,\mu\text{m}$. Then, the spherical cell has a surface of approximately $1200\,\mu\text{m}^2$. In Section 3.2, we introduced a two-dimensional simulation domain modeling the cell surface, and for simplicity, we choose in the following a square of size $10\,\mu\text{m} \times 10\,\mu\text{m}$ which can be considered as a section of the cell surface. Taking the length scale $L = 10\,\mu\text{m}$ introduced in Section 3.3.1, we obtain the dimensionless simulation domain $\Omega = [0,1]^2$.

Considering a KYM-1 cell, the number of TNF receptors vary significantly for different cell lines [44, Table 2]. Here, the number of TNF receptors of type 1 on the cell membrane are in the range of about 1200 to 3200. In personal discussions with Peter Scheurich, the number of TNFR1-Fas chimeras were amounted to about 30.000 either in dimeric or monomeric pre-form. Both numbers refer to a cell with a surface of approximately $1200\,\mu\text{m}^2$. Thus, we obtain a death receptor number of about 2500 in case of TNFR1-Fas

and 100 to 250 in case of TNFR1 on a square of size $10\,\mu m \times 10\,\mu m$. Indeed, we do not consider one special choice for the number of death receptors for our simulations since the size of the cell surface significantly influences the density of death receptors. For instance, a radius of $5\,\mu m$ leads to a surface with a size of approximately $300\,\mu m^2$. Thus, a total number of about 30.000 death receptors yields about 10.000 death receptors on a square of size $10\,\mu m \times 10\,\mu m$. Next, we derive typical concentrations for death receptor ligands. In [44], the concentrations for TNF that finally results in the survival of the cell is in the range of $10\,pg/ml$ to $500\,pg/ml$ dependent on the temperature. For other cell lines we obtain different TNF concentrations. For the subsequent thoughts we assume an averaged value of $100\,pg/ml = 10^{-16}\,g/nl$. Since a TNF ligand has a mass of $m_{\text{ligand}} \approx 8.47 \cdot 10^{-23}\,kg$, we obtain a number of about 1200 TNF ligands in a volume of one nanoliter. Again, we allow the number of death receptor ligands to vary in a certain range, say from 500 to 5000 molecules. Actually, higher number of death receptor ligands are also possible especially for other cell lines of KYM-1 [44, Table 1]. Finally, in case of the artificial structure of cluster units, we consider a number of cluster units in the range of about 500 to circa 5000. In summary, we mention that the poor knowledge of exact particle numbers requires a variation of the particle numbers.

Besides the particle number, the system of stochastic differential equations contains even more parameters whose values we did not indicate up to now. First of all, the values for the scaling parameters are given by $L = 10\,\mu m$ due to the size of the cell surface and $\tau = 1\,s$. In order to determine the friction coefficient $\beta = 6\pi\eta R$ for the different particle types, we need the viscosity of the cell membrane and the radius of the particles. For the viscosity, various values are given in [26] dependent on the temperature and the cell type. An averaged value of the viscosity in [26] is $\eta = 100\,cP = 100\,\text{centipoise}$. Since the relationship $1000\,cP = 1\,Ns/m^2$ holds, we have a membrane-viscosity of $\eta = 0.1\,Ns/m^2$. Actually, an increased membrane-viscosity is associated with aging and a variety of diseases [26]. We suggest a value for the membrane-viscosity of $\eta = 10\,Ns/m^2$. For the friction coefficient we further need the radius of the different particle types. We set $R_M = 1\,nm$, $R_{D/L} = 2\,nm$ and $R_{T/U} = 3\,nm$ and obtain for β the values $\beta_M = 1.89 \cdot 10^{-9}\,Ns/m$, $\beta_{D/L} = 3.77 \cdot 10^{-9}\,Ns/m$ and $\beta_{T/U} = 5.66 \cdot 10^{-9}\,Ns/m$. With the friction coefficient at hand, we determine the value for the parameter μ in equation (3.6). With the thermal energy $k_B T = 5 \cdot 10^{-21}\,J$, we obtain $\mu_M \approx 0.0163$, $\mu_{D/L} \approx 0.01115$ and $\mu_{T/U} \approx 0.0094$. Besides the visible parameters in equation (3.6), there are also some hidden parameters concerning the interaction potential. On the one hand, the Lennard-Jones potential contains two parameters, namely $\sigma_{LJ}^P = R_P/L$ and the exponent $n = 6$. On the other hand, we established in Section 3.3.4 the orientation dependent interaction by introducing the angle δ. For our simulations, we choose $\delta = \pi/3$. Furthermore, due to the short range potential, we introduced a dimensionless cut-off radius r_{cut} whose value is

set to $r_{\text{cut}} = 0.001$. Finally, we conclude this section about the parameter values with the remaining parameters for the particle rotation. The friction coefficient for the particle rotation is given by $\gamma_{\text{rot}} = 8\pi\eta R_{\text{P}}^3$ and with the given membrane-viscosity and the given radii of the particles, we obtain $\gamma_{\text{rot}}^{\text{M}} = 2.513 \cdot 10^{-25}\,\text{Nms}$, $\gamma_{\text{rot}}^{\text{D/L}} = 2.011 \cdot 10^{-24}\,\text{Nms}$ and $\gamma_{\text{rot}}^{\text{T/U}} = 6.786 \cdot 10^{-24}\,\text{Nms}$. These values finally determine the value for the parameter ζ_{P}, namely $\zeta_{\text{M}} \approx 8661$, $\zeta_{\text{D/L}} \approx 4330$ and $\zeta_{\text{T/U}} \approx 2887$. In the end, we set $\kappa = 1000$ and the step size for the time discretization is $\Delta\bar{t} = 1\text{e} - 9$. The small step size $\Delta\bar{t}$ is required because of the steep Lennard-Jones potential. Therewith, we finalize the parameter setting of the systems of stochastic differential equation for the different particle types.

In the next step, we introduce notations for the ligand-receptor complexes consisting of up to four particles. These notations will be used for the numerical analysis in the subsequent section.

Notation for the Ligand-Receptor Complexes and Bindings

To obtain a well-arranged overview of the ligand-receptor complexes occurring in the evaluation of the simulation results, we summarize the most important binding structures in the following tables. We start with complexes with at least one death receptor monomer in Table 3.1. Afterward, we list in Table 3.2 the notations for ligand-receptor complexes with at least one death receptor dimer and in Table 3.3, we show the corresponding structures in case of death receptor trimers. For the sake of completeness, we close the introduction of the notations with the binding for the cluster units in Table 3.4. After

Structure	Size	Composition	Properties
'M-M'	2	2 bound monomers	
'M-L'	2	1 monomer bound to 1 ligand	
'L-M-M'	3	1 monomer bound to 1 ligand and 1 monomer opposite	
'L-M-M-L'	4	2 monomers each bound to 1 ligand	contains twice the structure 'L-M-M'.
'M-L-M'	3	2 monomers bound to 1 ligand	the third binding site of the ligand is not occupied by a monomer but possibly by a dimer.
'L-3M'	4	1 ligand associated with 3 monomers	the monomers themselves can also bind another monomer.

Table 3.1: Overview of ligand-receptor complexes consisting of up to four particles with participation of at least one death receptor monomer. Actually, clusters consisting of at least five particles, which contains the indicated structures, are also counted.

Structure	Size	Composition	Properties
'D-L'	2	1 dimer bound to 1 ligand	
'L-D-L'	3	1 dimer bound to 2 ligands	
'D-L-D'	3	2 dimers bound to 1 ligand	the third binding site of the ligand is not occupied by a dimer.

Table 3.2: Overview of ligand-receptor complexes consisting of up to four particles with participation of at least one death receptor dimer. Actually, clusters consisting of at least four particles, which contains the indicated structures, are also counted.

Structure	Size	Composition	Properties
'T-L'	2	1 trimer bound to 1 ligand	
'L-T-L'	3	1 trimer bound to 2 ligands	
'T-L-T'	3	2 trimers bound to 1 ligand	the third binding site of the ligand is not occupied by a trimer.
'L-3T'	4	1 ligand associated with 3 trimers	the trimers themselves can also bind ligands.
'T-3L'	4	1 trimer associated with 3 ligands	the ligands themselves can also bind trimers.

Table 3.3: Overview of ligand-receptor complexes consisting of up to four particles with participation of at least one death receptor trimer. Actually, clusters consisting of at least five particles, which contains the indicated structures, are also counted.

introducing short notations for ligand-receptor complexes for the different particle types, we evaluate the results of the numerical simulations.

Evaluation of the Numerical Results

In the following section, we investigate the formation of signal competent cluster units depending on the particle type. For this purpose, we perform simulations for the particle configurations introduced in Section 3.3.3 and determine the evolution of ligand-receptor complexes. However, we do not consider the scenarios *a.i*), *a.ii*) and *a.iii*) separately, but we study particle configurations with death receptor monomers or death receptor dimers. For the evaluation of the number of a certain complex at time $\bar{t}_n$, we average its number at 100 proximate times $\bar{t}_{n-50}, \ldots, \bar{t}_{n+50}$ if $n > 50$ and at $2k, k < n$, proximate times $\bar{t}_{n-k}, \ldots, \bar{t}_{n+k}$ if $n \leq 50$. Instead of performing several realizations of the stochastic process for each particle configuration and average the number of ligand-receptor complexes over the different realizations, we only compute a single realization and

Structure	Size	Composition	Properties
'U-U'	2	2 bound cluster units	large clusters of cluster units are also counted. The number of 'U-U' bindings is counted according to their multiplicity within a cluster.

Table 3.4: Notation for the binding between two cluster units. Actually, clusters of size larger than two are also counted.

average the number of complexes in time.

But before we compare the results for the various particle types, we first give a justification for the chosen time scale. For this purpose, we perform simulations on a time scale of 1 s for two different particle configurations. Here, we arbitrarily choose the configurations with on the one hand 576 death receptor monomers, 2496 death receptor dimers and 2496 death receptor ligands and on the other hand 2496 death receptor monomers, 2496 death receptor dimers and 960 death receptor ligands. The evolution of 'L-D-L' complexes is illustrated in Figure 3.11. Actually, we observe in Figure 3.11 that the num-

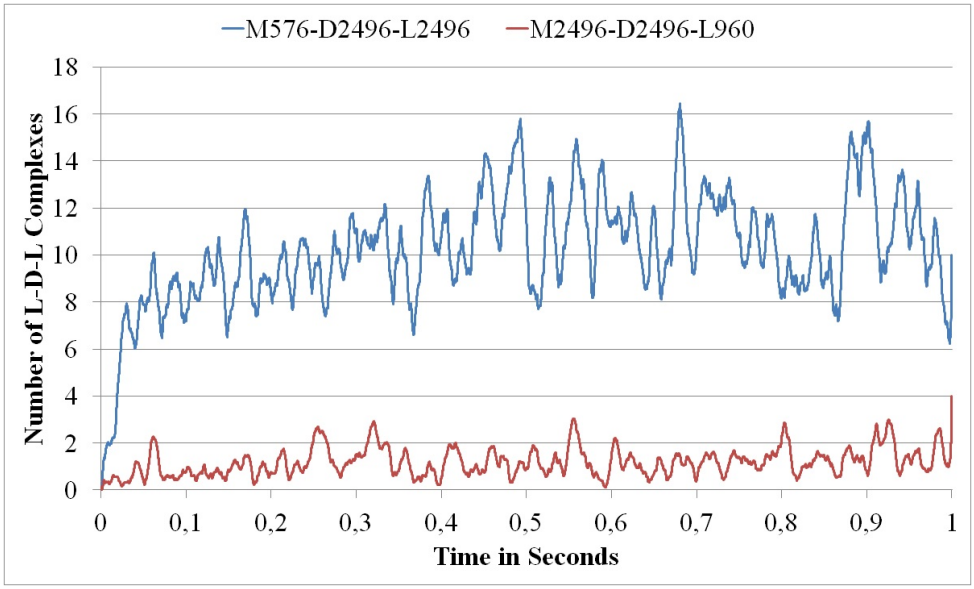

Figure 3.11: The evolution of 'L-D-L' complexes on a time scale of 1 s for 576 death receptor monomers, 2496 dimers and 2496 ligands (blue graph) and 2496 monomers, 2496 dimers and 960 ligands (red graph).

ber of 'L-D-L' complexes essentially fluctuates around a mean value of about eleven in case of the blue graph and one in case of the red graph. In fact, these mean values are reached the first time on a very short time scale of about 0.1 s. Therefore, we perform the following investigations on a time scale of 0.1 s.

Death Receptor Dimers versus Death Receptor Monomers

In a first study, we investigate the suggestion of Boschert et al. [6] that the majority of death receptors exist in a dimeric pre-form. For this purpose, we vary the number of death receptor dimers and monomers under the assumption that the total amount of death receptors adds up to 4992, thus $\#D + \#M = 4992$. Besides, the number of death receptor ligands is arbitrarily chosen to be $\#L = 4992$. According to [6], the signal competent cluster unit is supposed to be the complex 'L-D-L' or the complex 'L-M-M-L' in case of death receptor monomers. Therefore, we illustrate the evolution of 'L-D-L' and 'L-M-M-L' complexes, see Figure 3.12 and Figure 3.13. Obviously, the number of 'L-D-L'

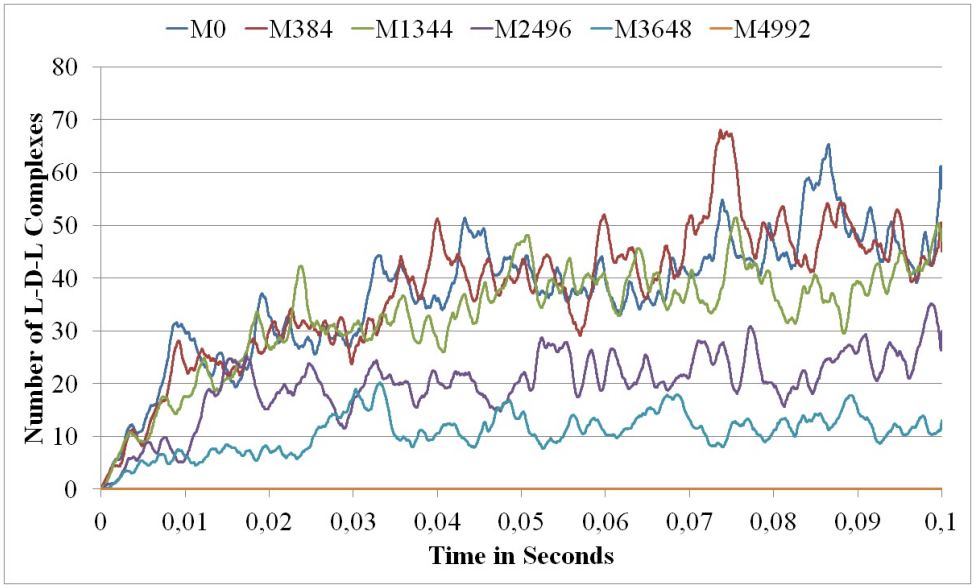

Figure 3.12: The evolution of 'L-D-L' complexes for $\#L = 4992$. The number of death receptor monomers and death receptor dimers adds up to 4992. Hence, the number of death receptor monomers given in the legend of the plot directly implies the number of death receptor dimers.

complexes increases with a decreasing number of death receptor monomers. On the other hand, a decreasing number of death receptor monomers corresponds to an increasing number of dimers, and vice versa, due to the fixed total amount of death receptors. Thus, it is not astonishing that the number of 'L-D-L' complexes increases for decreasing numbers of death receptor monomers. However, we expect that the number of 'L-M-M-L' complexes also increases with an increasing number of death receptor monomers, but Figure 3.13 shows that the number of 'L-M-M-L' complexes is tiny compared to the number of 'L-D-L' complexes. Hence, concerning the total amount of signal competent cluster units, i.e. $\#L - D - L + \#L - M - M - L$, we see that the contribution of 'L-M-M-L' complexes to the total amount of signal competent cluster units is negligible. Thus, in order to observe high numbers of signal competent cluster units, the majority of the death receptors have to exist in a dimeric pre-form.

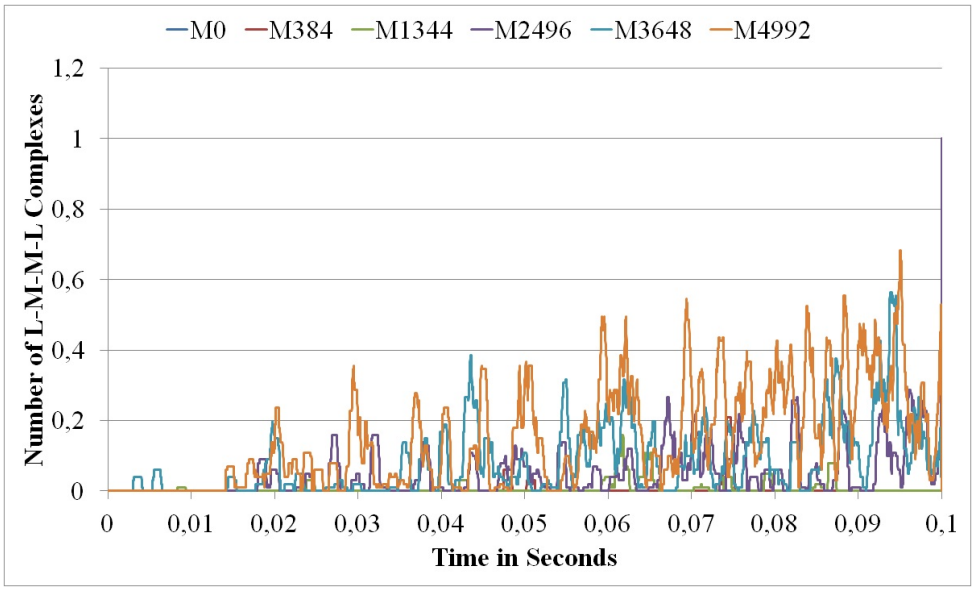

Figure 3.13: The evolution of 'L-M-M-L' complexes for #L = 4992. The number of death receptor monomers and dimers adds up to 4992. Hence, the number of death receptor monomers given in the legend of the plot directly implies the number of death receptor dimers.

In order to understand this behavior, we consider the evolution of simple bindings between death receptor ligands and death receptor monomers and between death receptor ligands and death receptor dimers. For this purpose, we compare the scenarios where death receptors exist either in a dimeric or monomeric pre-form, namely $\#\mathrm{M} = 4992, \#\mathrm{D} = 0, \#\mathrm{L} = 4992$ and $\#\mathrm{M} = 0, \#\mathrm{D} = 4992, \#\mathrm{L} = 4992$. The evolutions of the 'M-L' and 'D-L' bindings agree very well on a short time scale and diverges for larger times, see Figure 3.14. The agreement of the blue and the red graph in Figure 3.14 can not be expected since death receptor monomers and death receptor dimers have different sizes, namely $R_{\mathrm{M}} = 1\,\mathrm{nm}$ and $R_{\mathrm{D}} = 2\,\mathrm{nm}$, and the parameter values in the system of stochastic differential equations, especially μ_{M} and μ_{D}, depend significantly on the particle size. Moreover, the parameter values of μ_{M} and μ_{D} influence the particle translation and rotation and thereby the binding behavior of the particles. Furthermore, we oppose the evolution of 'M-L' and 'M-M' bindings, cf. Figure 3.14. First, we observe that the number of 'M-M' bindings is significantly smaller than the number of 'M-L' bindings. In order to explain this behavior, we look at the binding sites of death receptor monomers and death receptor ligands. On the one hand, a death receptor monomer is involved in both bindings, namely 'M-L' and 'M-M', with the size of a binding site that is proportional to δ. On the other hand, the binding site of the death receptor ligand has a size that is proportional to 3δ. So, the likelihood for the association of a death receptor monomer and a death receptor ligand goes with $\delta \cdot 3\delta$ and the corresponding likelihood for the self-association of two death receptor monomers is proportional to $\delta \cdot \delta$. Thus, the

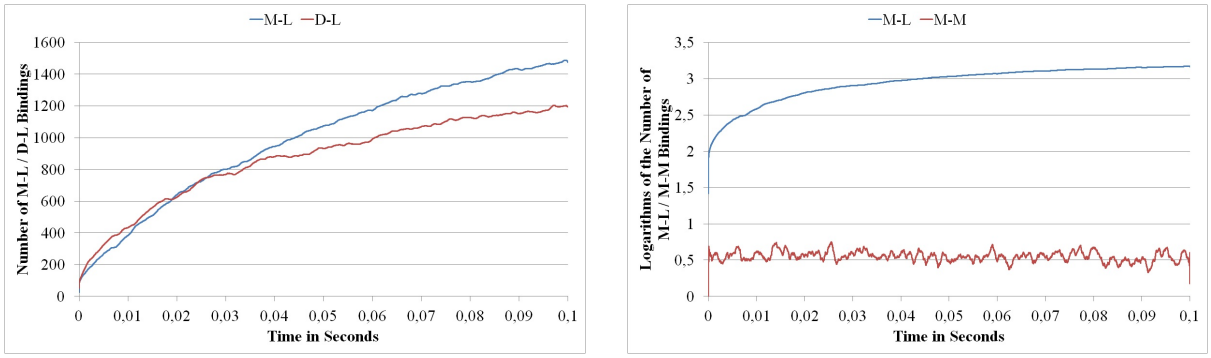

Figure 3.14: The evolution of 'M-L' / 'D-L' (left panel) and 'M-L' / 'M-M' (right panel) bindings for $\#\mathrm{L} = 4992$. In the left picture, the two graphs are obtained for different particle configurations: the blue graph for $\#\mathrm{M} = 4992, \#\mathrm{D} = 0$ and the red graph for $\#\mathrm{M} = 0, \#\mathrm{D} = 4992$. In the right picture, the logarithmic numbers of the 'M-L' and 'M-M' bindings are illustrated. Here, we performed the simulation for $\#\mathrm{M} = 4992$ and $\#\mathrm{D} = 0$.

likelihood for the binding of a death receptor ligand and a death receptor monomer is by a factor three larger than the self-association of two monomers. In fact, there are two additional factors which negatively influence the formation of 'M-M' bindings compared to the 'M-L' bindings. On the one hand, the binding energy and thereby the attractive part of the interaction potential between a death receptor ligand and a death receptor monomer is by a factor ten larger than between two death receptor monomers. On the other hand, due to the difference in the particle sizes, namely $R_{\mathrm{M}} = 1\,\mathrm{nm}$ and $R_{\mathrm{L}} = 2\,\mathrm{nm}$, the parameter values $\sigma_{\mathrm{LJ}}^{\mathrm{M}}$ and $\sigma_{\mathrm{LJ}}^{\mathrm{L}}$ in the Lennard-Jones potential differ by a factor two. In summary, we have three meaningful reasons for the large difference in the number of 'M-L' and 'M-M' bindings.

After considering the bindings between two particles, we proceed with complexes of size three. Starting with a 'D-L' binding, there are two possibilities to obtain a complex of size three, namely a 'L-D-L' or a 'D-L-D' complex. We observe that the number of 'L-D-L' complexes is significantly higher than the number of 'D-L-D' complexes, cf. Figure 3.15. Starting with a 'D-L' binding, a 'L-D-L' complex is formed through the association of a death receptor ligand. Assuming an apex angle of δ for a binding site of death receptor ligands, the size of the area allowing an association with a death receptor dimer is proportional to 3δ if all binding sites of the death receptor ligand are unoccupied. On the other hand, the size of the corresponding area of the death receptor dimer which is already bound with a death receptor ligand is proportional to δ. Therefore, the likelihood for the binding of a death receptor ligand to a 'D-L' binding is proportional to $3\delta \cdot \delta$. On the other hand, starting again with a 'D-L' binding, we have two unoccupied binding sites of the death receptor ligand for the association with a death receptor dimer. Thus, the size of the area that allows for the association with a death receptor dimer is proportional to 2δ the same as the corresponding area of a death

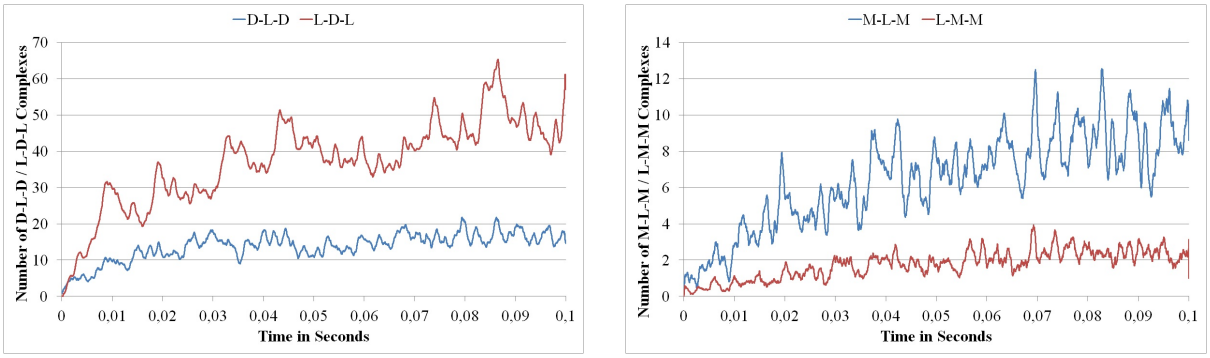

Figure 3.15: The evolution of 'L-D-L' / 'D-L-D' (left panel) and 'M-L-M' / 'L-M-M' (right panel) complexes for #L = 4992. In the left picture, we take the configuration with #D = 4992, #M = 0 and in the right picture, we have #D = 0, #M = 4992.

receptor dimer. In summary, we obtain a likelihood which is proportional to $2\delta \cdot 2\delta$ and thereby larger than for 'L-D-L' complexes. This result seems surprising on the first sight: although the likelihood for the formation of 'D-L-D' complexes is larger than for 'L-D-L' complexes, the number of 'L-D-L' complexes is even larger, see Figure 3.15. Actually, we assumed for the arguments above that the death receptor dimer and the ligand are free. However, if two 'D-L' bindings self-associate, we obtain the structure 'L-D-L-D' which includes both a 'L-D-L' and a 'D-L-D' complex. Here, it does not matter, at which binding site the self-association of the two 'D-L' bindings occurs. Furthermore, it is easy to see, that both possibilities have the same likelihood, namely $2\delta \cdot \delta$. However, we notice that the self-association of two 'D-L' complexes and the binding of a single death receptor ligand to a 'D-L' complex explains that the number of 'L-D-L' complexes is higher than the number of 'D-L-D' complexes.

In order to understand the formation of 'L-M-M-L' complexes, we restrict ourselves to the scenario where only death receptor monomers exist. Thereby, we fade out effects through the presence of death receptor dimers. We first oppose the complexes of size three, namely 'M-L-M' and 'L-M-M', whose evolution is illustrated in the right panel in Figure 3.15. A comparison of the blue and the red curve shows that the number of 'M-L-M' complexes is higher than the number of 'L-M-M' complexes. This can be seen as follows: 'M-L-M' complexes are formed through the association of a death receptor monomer to a 'M-L' binding at one of the two unoccupied binding sites of the death receptor ligand. Since two binding sites of the death receptor ligand in the 'M-L' binding are free, the size of the area for the association of a death receptor monomer is proportional to 2δ and the corresponding area of the death receptor monomer is δ. Finally, the likelihood for the binding of a death receptor monomer to the death receptor ligand of the 'M-L'

binding is proportional to $2\delta \cdot \delta$. On the other hand, there are two possibilities to obtain a 'L-M-M' complex: (i) starting with a 'M-M' binding and the subsequent association with a death receptor ligand and (ii) starting with a 'M-L' binding and the binding of a death receptor monomer to the death receptor monomer of the 'M-L' binding. In case (i) the likelihood for the association of a death receptor ligand to a 'M-M' binding is proportional to $2\delta \cdot 3\delta$. Here, the factor two occurs due to the symmetry of the 'M-M' binding. In (ii), the corresponding term reads $\delta \cdot \delta$. In summary, the formation of 'L-M-M' complexes starting with a 'M-M' binding possesses the largest likelihood but since the number of 'M-M' bindings is small, cf. the right panel in Figure 3.14, the effects for the 'L-M-M' complexes are rather negligible. On the other hand, starting with a 'M-L' binding, the likelihood for the binding of a death receptor monomer to the death receptor monomer of a 'M-L' binding is proportional to $\delta \cdot \delta$, and thereby by a factor two smaller than the association of a death receptor monomer with the death receptor ligand of the 'M-L' binding. Besides the likelihood, the difference in the binding energies in the 'M-L' and 'M-M' binding and the different particle sizes play an important role again. Therefore, the number of 'M-L-M' complexes is higher than the number of 'L-M-M' complexes.

Now, we can draw conclusions from the evolution of 'L-M-M' complexes and 'M-L' bindings to the evolution of 'L-M-M-L' complexes in Figure 3.13. There are two possibilities to form a 'L-M-M-L' complex: through the binding of a death receptor ligand to a 'L-M-M' complex or through the self-association of two 'M-L' bindings at the free binding site of the death receptor monomers. Although the likelihood for the binding of a death receptor ligand to the 'L-M-M' complex is proportional to $\delta \cdot 3\delta$ and therefore larger than the likelihood for the association of two 'M-L' bindings, which is proportional to $\delta \cdot \delta$, the contribution of the former binding to the number of 'L-M-M-L' complexes is smaller. Here, we take notice of the fact that the number of 'M-L' bindings is significantly higher than the number of 'L-M-M' bindings.

In contrast to the suggestion of Boschert et al. [6] where 'L-M-M-L' complexes are signal competent, Banner et al. [3] suggests a 'L-3M' complex to be signal competent. To make the results comparable, we restrict ourselves to the case where all death receptors exist as monomers and consider the scenario with 4992 monomers and 4992 ligands. The time evolution of 'L-M-M-L' and 'L-3M' complexes is illustrated in Figure 3.16. As mentioned above, the formation of 'L-M-M-L' complexes occurs either by the association of a death receptor ligand with a 'L-M-M' complex or through the self-association of two 'M-L' bindings. The likelihood for the former association is proportional to $\delta \cdot 3\delta$ and the likelihood for the latter is proportional to $\delta \cdot \delta$. However, the number of 'M-L' bindings is significantly higher than the number of 'L-M-M' complexes. Thus, the contribution of the self-association of two 'M-L' bindings to the number of 'L-M-M-L' complexes is

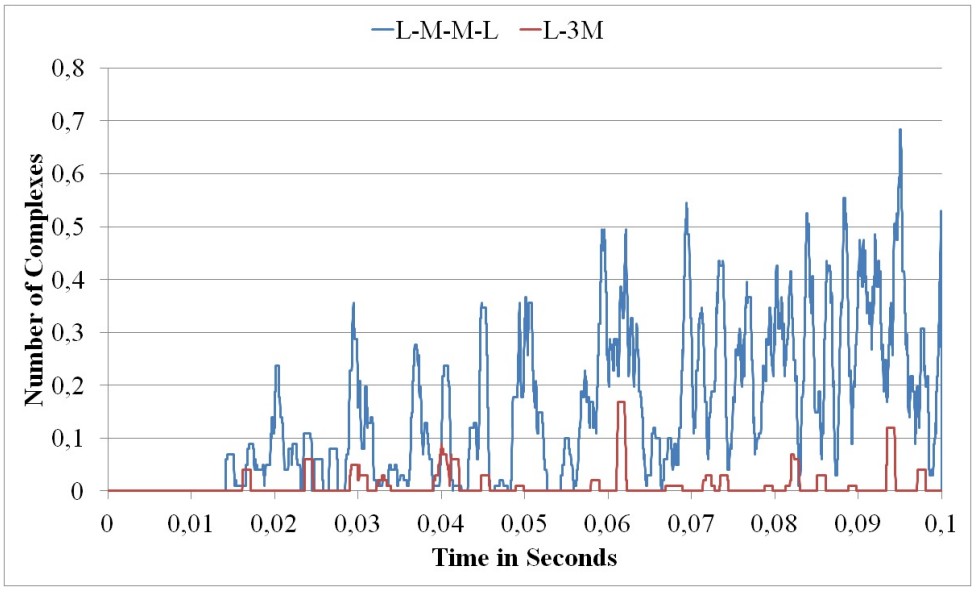

Figure 3.16: The evolution of 'L-M-M-L' / 'L-3M' complexes for #L = 4992 and #M = 4992 in the absence of death receptor dimers.

more meaningful than the binding of a death receptor ligand to a 'L-M-M' complex. On the other hand, a 'L-3M' complex arises from a 'M-L-M' complex through the binding of a death receptor monomer to the free binding site of the death receptor ligand. The likelihood for this binding is proportional to $\delta \cdot \delta$, and thereby the same as for the self-association of two 'M-L' bindings. However, the number of 'M-L-M' complexes is significantly smaller than the number of 'M-L' bindings, and therefore, the formation of 'L-M-M-L' complexes is more likely than the formation of 'L-3M' complexes.

In summary, we find out that the formation of signal competent cluster units is more likely if the majority of death receptors exist in dimeric pre-form. We further observe that the formation of signal competent cluster units in case of death receptor monomers is rather complicated. Additionally, comparing the suggestions in [3] and [6] concerning the structure of signal competent cluster units, the results indicate that the formation of 'L-M-M-L' complexes is more likely than the formation of 'L-3M' complexes.

Inhibitory Effects of Death Receptor Monomers on the Formation of 'L-D-L' Complexes

Next, we study the influence of death receptor monomers on the formation of signal competent cluster units. For this purpose, we consider a scenario with a fixed number of death receptor dimers, namely #D = 2496, and two values for the number of death receptor monomers, namely #M = 0 and #M = 2496. Moreover, the number of death receptor ligands varies. First, we note that the number of 'L-D-L' complexes

increases with an increasing number of death receptor ligands for both values of #M, see Figure 3.17 and Figure 3.18. Furthermore, a comparison of the evolution of 'L-D-L'

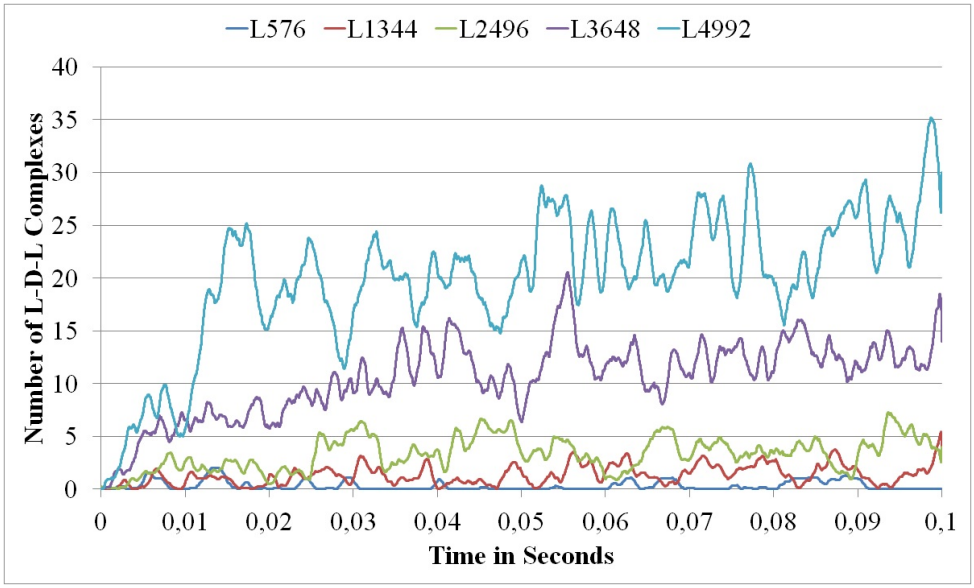

Figure 3.17: The evolution of 'L-D-L' complexes for #M = 2496, #D = 2496 and various numbers of ligands.

complexes shows that the number of 'L-D-L' complexes is smaller if death receptor monomers are added to the system. Small numbers of death receptor ligands lead to small differences in the number of 'L-D-L' complexes for #M = 0 and #M = 2496, whereas large numbers of death receptor ligands, i.e. #L = 3648 or #L = 4992, indicate significant differences in the number of 'L-D-L' complexes. More precisely, the number of 'L-D-L' complexes reaches values of almost 45 for #L = 4992 if #M = 0 compared to less than 35 'L-D-L' complexes if 2496 death receptor monomers are added to the system. For a detailed analysis of this behavior, we restrict ourselves to the scenario with 4992 death receptor ligands. Besides, the number of death receptor dimers is #D = 2496 and the number of death receptor monomers is either #M = 0 or #M = 2496. First, we oppose on the one hand the evolution of 'M-L' and 'D-L' bindings for the configuration with 2496 death receptor monomers and on the other hand the evolution of 'D-L' bindings for #M = 0 and #M = 2496, see Figure 3.19. Comparing the evolution of 'M-L' and 'D-L' bindings, we notice that the number of both bindings is of the same order. In fact, the number of 'M-L' bindings is even larger than the number of 'D-L' bindings. Through the binding of a death receptor monomer to a death receptor ligand, the death receptor ligand loses one binding site for the association with a death receptor dimer. Thus, the likelihood for the binding of a death receptor ligand to a 'D-L' binding is reduced from $\delta \cdot 3\delta$ to $\delta \cdot 2\delta$. In fact, this reduction of the likelihood holds for up to 700 death receptor ligands, cf. the left panel in Figure 3.19.

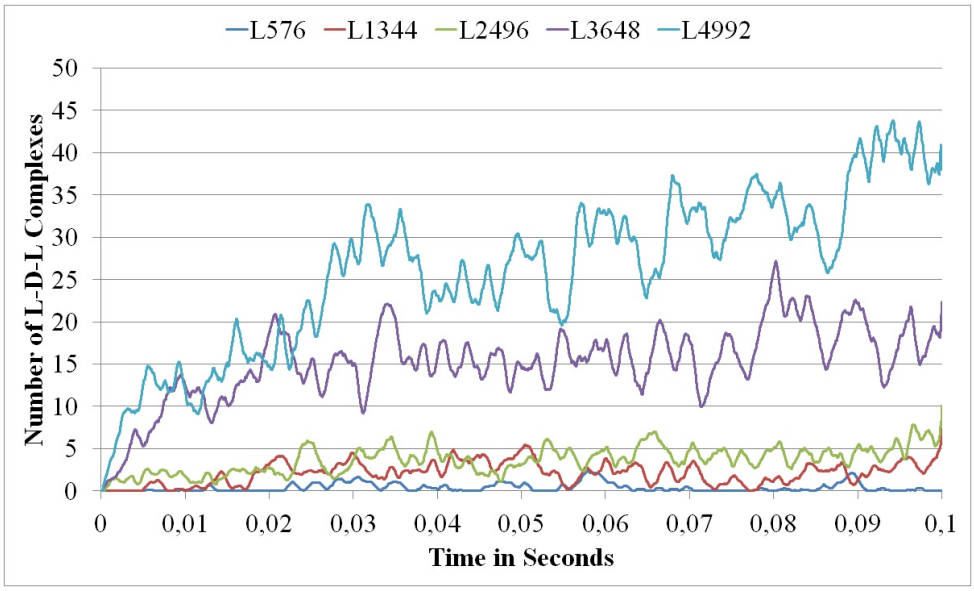

Figure 3.18: The evolution of 'L-D-L' complexes for #M = 0 and #D = 2496 and various numbers of ligands.

Moreover, we observe that the number of 'D-L' bindings is larger for #M = 0 than for #M = 2496, see the right panel in Figure 3.19. However, this is only an indication that the number of 'L-D-L' complexes is larger for #M = 0 than for #M = 2496, since a 'D-L' binding can also associate with a death receptor dimer and form a 'D-L-D' complex. Therefore, we oppose the evolution of 'L-D-L' and 'D-L-D' complexes, cf. the left panel in Figure 3.20. We see that the presence of death receptor monomers is almost irrelevant for the evolution of 'D-L-D' complexes whereas the number of 'L-D-L' complexes is larger for #M = 0 than for #M = 2496. Hence, the excess of 'D-L' bindings for #M = 0 relative to #M = 2496, cf. the right panel in Figure 3.19, rather associates with a death receptor ligand than with a death receptor dimer. We already discussed above that the occurrence of 'L-D-L' complexes is more likely than the occurrence of 'D-L-D' complexes.

In summary, we notice that the number of 'L-D-L' complexes is significantly higher in case of a low number of death receptor monomers. Thus, roughly speaking, death receptor monomers can be regarded as inhibitors for the formation of 'L-D-L' complexes.

The Role of Death Receptor Ligands in Signaling

Looking at the signal competent cluster units 'L-D-L' and 'L-M-M-L', one may ask, why these structures need the death receptor ligands to be signal competent since the death receptor ligands are only present in the extracellular space and the signal transduction occurs via the intracellular part of the death receptors, cf. Figure 2.1. In the following, we argue that the 'M-M' bindings can not be a sufficient structure for signaling. We use

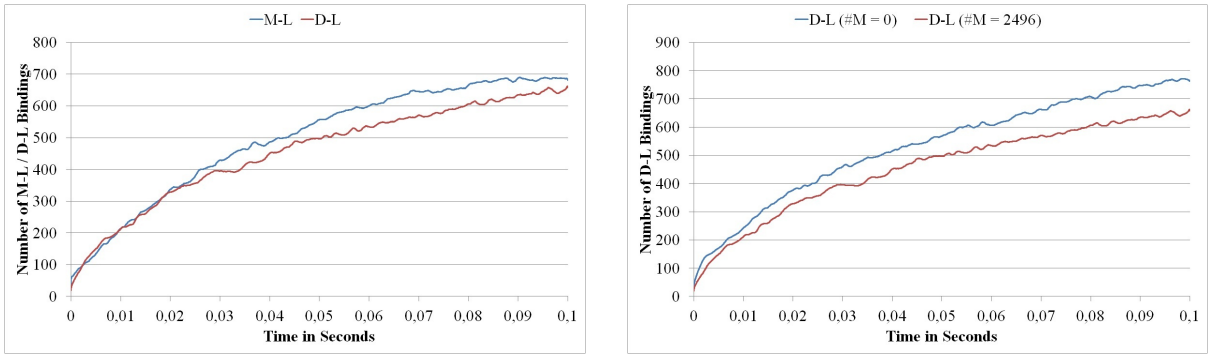

Figure 3.19: The evolution of 'M-L' and 'D-L' bindings for #M = 2496 (left panel) and 'D-L' bindings for #M = 2496 and #M = 0 (right panel). For both figures, we consider a scenario with 2496 death receptor dimers and 4992 death receptor ligands.

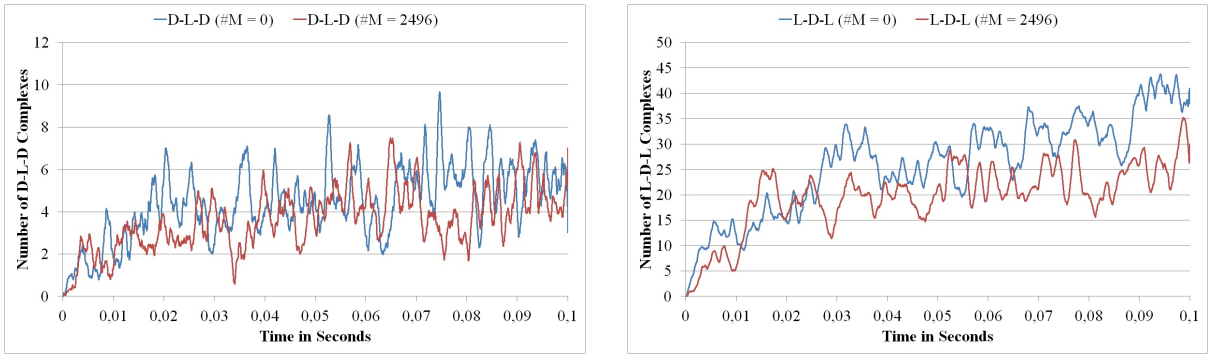

Figure 3.20: The evolution of 'D-L-D' (left panel) and 'L-D-L' (right panel) complexes for #M = 2496 and #M = 0.

the particle configuration with #M = 4992 and #D = 0 and various numbers of death receptor ligands in the range of 576 to 4992. To investigate whether the death receptor ligands are needed for signaling, we cut the death receptor ligands off from the 'L-M-M-L' complex and study instead of that the evolution of 'M-M' bindings. The evolution of the 'M-M' bindings shows that their number does not depend on the number of death receptor ligands, see Figure 3.21. Thus, assumed that a 'M-M' binding is signal competent, this behavior means that the strength of the signal is independent of the ligand concentration. However, from a biological point of view, the death receptor ligands control the signal transmission. So, low numbers of death receptor ligands do not cause the death of the cell while concentrations of death receptor ligands above a certain threshold lead to the death of the cell, cf. [44]. Therefore, a single 'M-M' binding can not be a sufficient structure for a signal competent cluster unit. Furthermore, the number of 'M-M' bindings does not increase in time, but fluctuates around a mean value of about four, see Figure 3.21. Actually, this small number of 'M-M' bindings is expected to be insufficient for signaling. Moreover, considering a fixed number of death receptor ligands, namely

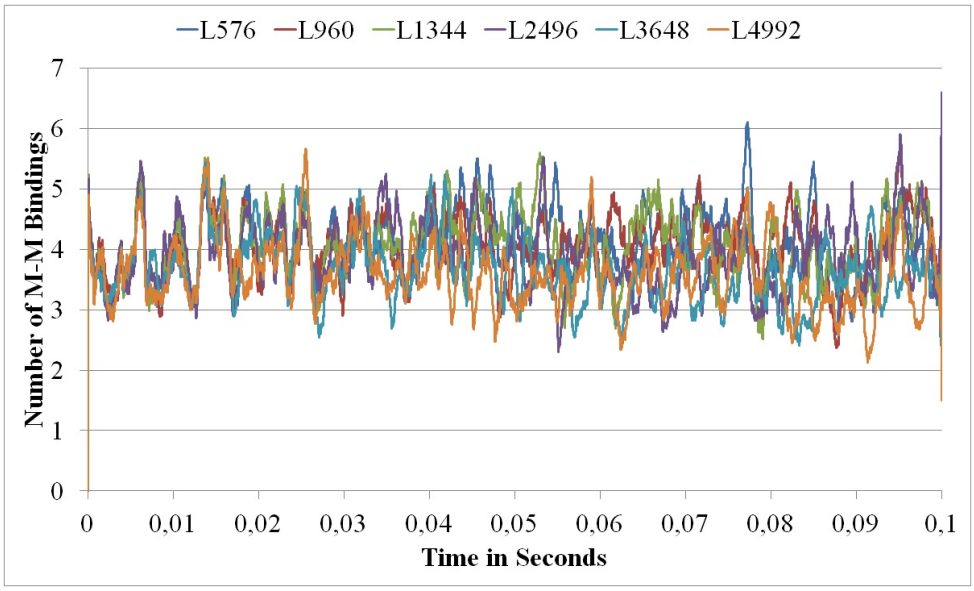

Figure 3.21: The evolution of 'M-M' bindings for various numbers of death receptor ligands. The number of death receptor monomers is #M = 4992.

#L = 4992, and a fixed number of death receptor dimers, say #D = 2496, we take a look at the evolution of 'M-M' bindings for various numbers of death receptor monomers, cf. Figure 3.22. Obviously, the number of 'M-M' bindings increases with an increasing number of death receptor monomers. Furthermore, we observe that the number of 'M-M' bindings is neither influenced by the death receptor ligands nor by the death receptor dimers. To see this, we compare the evolution of 'M-M' bindings for the configuration with #M = 4992, #D = 0 and #L = 4992 depicted by the orange graph in Figure 3.21 and the configuration with #M = 4992, #D = 2496 and #L = 4992 depicted in the light blue graph in Figure 3.22. The mean value for 'M-M' bindings is in both cases about four.

Concluding, we note that the number of 'M-M' bindings is very low even for large numbers of death receptor monomers. Here, we refer in particular to the particle configuration with 4992 death receptor monomers where only an average of eight death receptor monomers are involved in 'M-M' bindings.

The Formation of Ligand-Receptor Complexes in case of Death Receptor Trimers

After analyzing the simulations for death receptors monomers and dimers, we now regard the scenario with death receptor trimers according to [10]. Due to the low number of death receptor trimers on the cell membrane, we consider particle configurations with 192 and 576 death receptor trimers. These numbers are of a realistic biological order. Again, the number of death receptor ligands varies in the range of 576 to 4992. Since

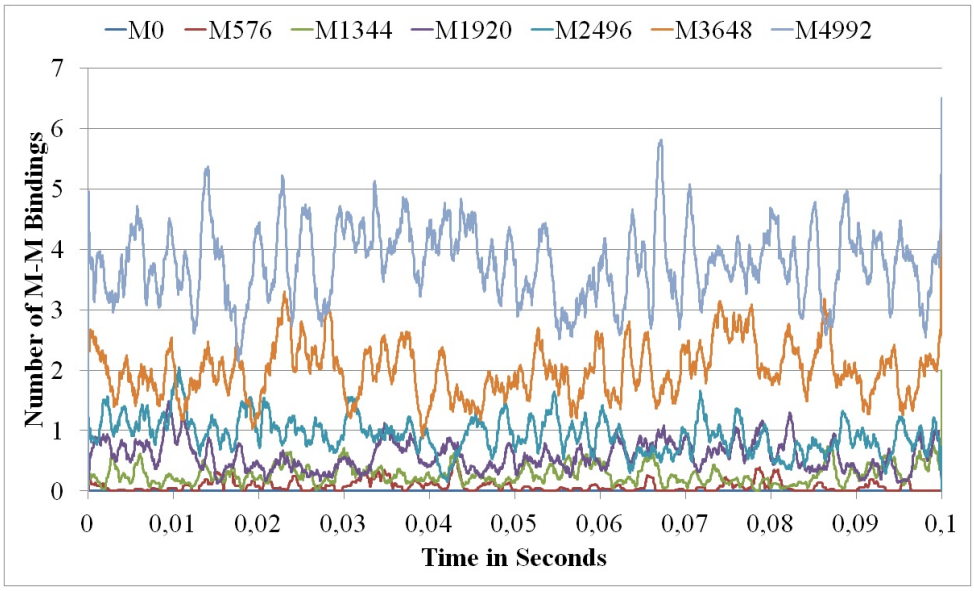

Figure 3.22: The evolution of 'M-M' bindings for various numbers of death receptor monomers. The number of death receptor ligands is #L = 4992 and the number of death receptor dimers is #D = 2496.

the structure of the signal competent cluster units is rather unclear in case of death receptor trimers, we study the evolution of 'T-3L' and 'L-3T' complexes as already introduced in Section 3.3.3. Former corresponds to the 'L-D-L' complex in case of dimeric death receptors, while latter is the analogon to the 'L-3M' complex in case of death receptor monomers. However, the results of the numerical simulations indicate that there are no 'T-3L' and 'L-3T' complexes for all numbers of death receptor ligands and death receptor trimers under consideration. We do not show these data, since the graphs only agree with the horizontal axis. Therefore, the 'L-3T' and 'T-3L' complexes are unlikely to describe the signal competent cluster unit in case of death receptor trimers.

In order to understand this phenomenon, we analyze this result in more detail. First, we look at the evolution of 'T-L' bindings for 192 and 576 death receptor trimers and various numbers of death receptor ligands. It is not astonishing that the number of 'T-L' bindings increases with an increasing number of death receptor ligands, cf. Figure 3.23 and Figure 3.24. Despite the low number of death receptor trimers, we observe that approximately 20 and 50 death receptor trimers, respectively, are involved in 'T-L' bindings. That corresponds to approximately 10% of the death receptor trimers under consideration. Moreover, the number of 'T-L' bindings is significantly higher for 576 than for 192 death receptor trimers.

To understand the nonoccurrence of 'L-3T' and 'T-3L' complexes, we analyze in the next step the evolution of complexes of size three. Starting with a 'T-L' binding there

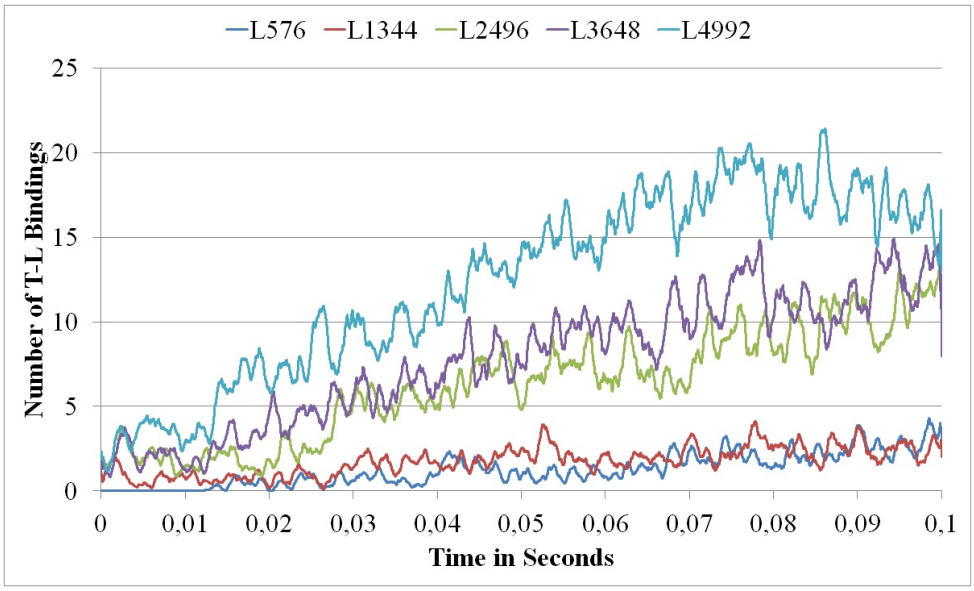

Figure 3.23: The evolution of 'T-L' bindings for various numbers of death receptor ligands and 192 death receptor trimers.

are two possibilities to form a complex of size three: the binding of a death receptor ligand to the death receptor trimer of the 'T-L' binding that yields a 'L-T-L' complex, or the association of a death receptor trimer with the death receptor ligand of the 'T-L' binding that results in a 'T-L-T' complex. First, we oppose the evolution of 'T-L-T' and 'L-T-L' complexes for 192 death receptor trimers, cf. Figure 3.25. A comparison of the 'T-L-T' and 'L-T-L' complexes in case of #T = 192 shows that 'L-T-L' complexes are more likely than 'T-L-T' complexes. The reason for this is obvious. Although the likelihoods for the formation of 'L-T-L' and 'T-L-T' complexes are both proportional to $2\delta \cdot 3\delta$, the number of death receptor trimers being available for an association with a 'T-L' binding is significantly smaller than the number of death receptor ligands. Additionally, we notice that the number of 'T-L-T' and 'L-T-L' complexes is rather negligible. Of course, the small numbers of 'T-L-T' and 'L-T-L' complexes finally explain the nonoccurrence of 'T-3L' and 'L-3T' complexes. Beyond that, the reason for the small numbers of 'T-L-T' and 'L-T-L' complexes lies in the relatively low number of 'T-L' bindings. For the sake of completeness, we present the evolution of 'T-L-T' and 'L-T-L' complexes for #T = 576, see Figure 3.26. Here, we observe that the behavior is almost the same as for #T = 192, whereas 'T-L-T' complexes already occur for smaller numbers of death receptor ligands in case of #T = 576. Additionally, the number of 'L-T-L' complexes is inappreciably higher for #T = 576 than for #T = 192.

In summary, we notice that the nonoccurrence of 'T-3L' and 'L-3T' complexes is primarily caused by the low number of death receptor trimers. If we compare the results

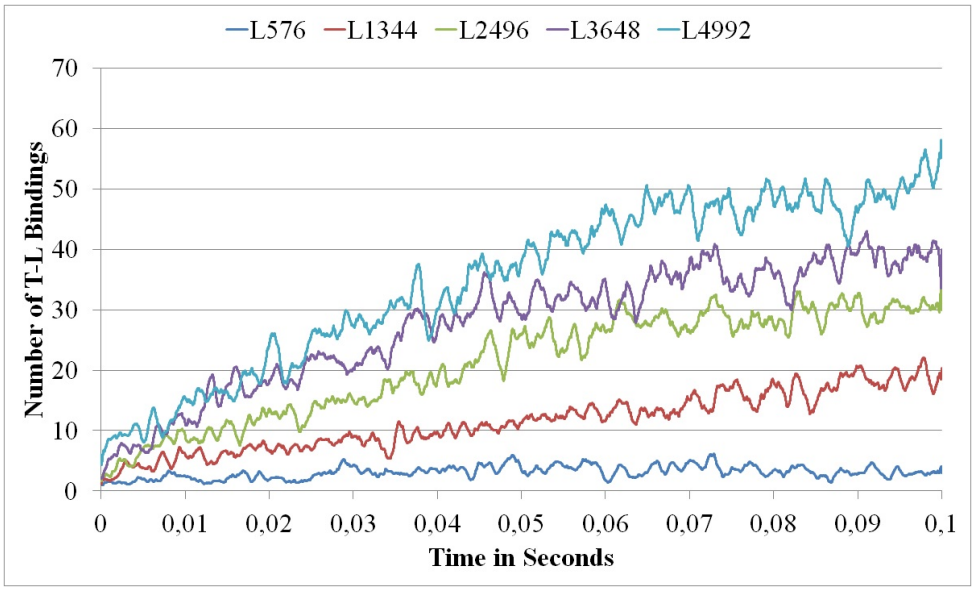

Figure 3.24: The evolution of 'T-L' bindings for various numbers of death receptor ligands and 576 death receptor trimers.

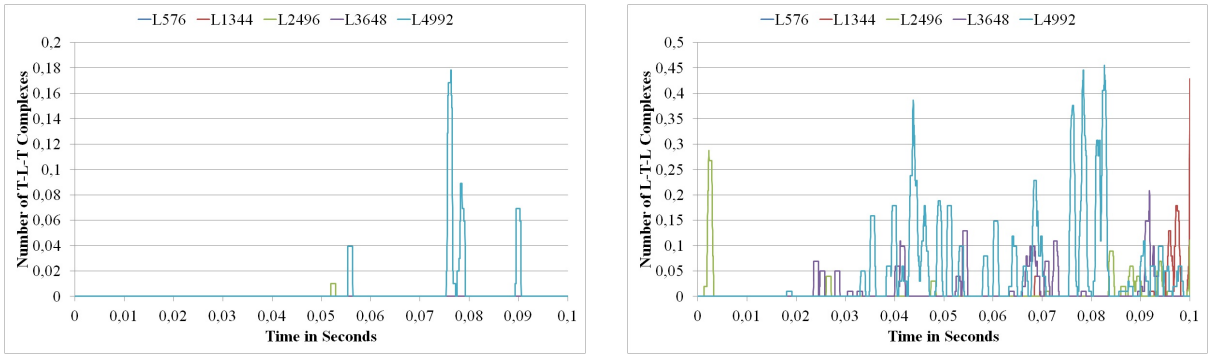

Figure 3.25: The evolution of 'T-L-T' and 'L-T-L' complexes in case of #T = 192 for various numbers of ligands.

of the simulations with death receptor trimers to those with death receptor dimers, we observe that the number of 'L-D-L' complexes is significantly higher than the number of 'L-T-L' complexes and the number of 'D-L-D' complexes is higher than the number of 'T-L-T' complexes. However, the likelihood for the formation of 'L-T-L' and 'T-L-T' complexes is larger than for the formation of the corresponding complexes in case of death receptor dimers, namely 'L-D-L' and 'D-L-D', due to the different number of binding sites for the two particle types. On the other hand, we note that the size of death receptor dimers and death receptor trimers differ significantly. Again, this fact results in different parameter values of the system of stochastic differential equations and thereby a different particle motion on the simulation domain.

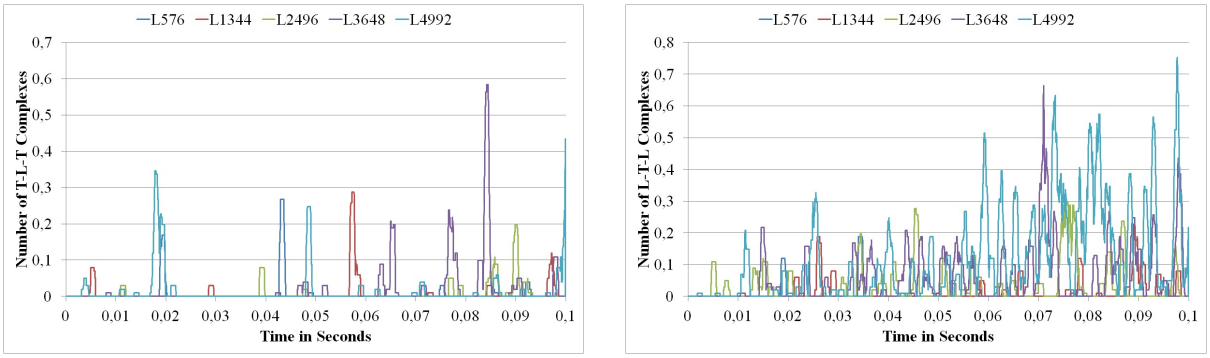

Figure 3.26: The evolution of 'T-L-T' and 'L-T-L' complexes in case of #T = 576 for various numbers of ligands.

Advantages of Fixed Cluster Units for Signaling?

Last but not least, we consider the scenario with the cluster units. This structure is chosen artificially due to the fact that the binding energy between a death receptor monomer and a death receptor ligand is by factor ten larger than between two death receptor monomers. For an investigation of the evolution of 'U-U' bindings, we choose various numbers of cluster units in the range of 576 to 4992. Actually, considering a set of 4992 cluster units, the amount of involved death receptors adds up to almost 15000 whereas the number of death receptor ligands is 4992. Thus, in comparison to the number of death receptors given in [44], this scenario corresponds to an over-expression of death receptor monomers.
The evolution of 'U-U' bindings for various numbers of cluster units is depicted in Figure 3.27. First, we mention that the number of 'U-U' bindings obviously increases

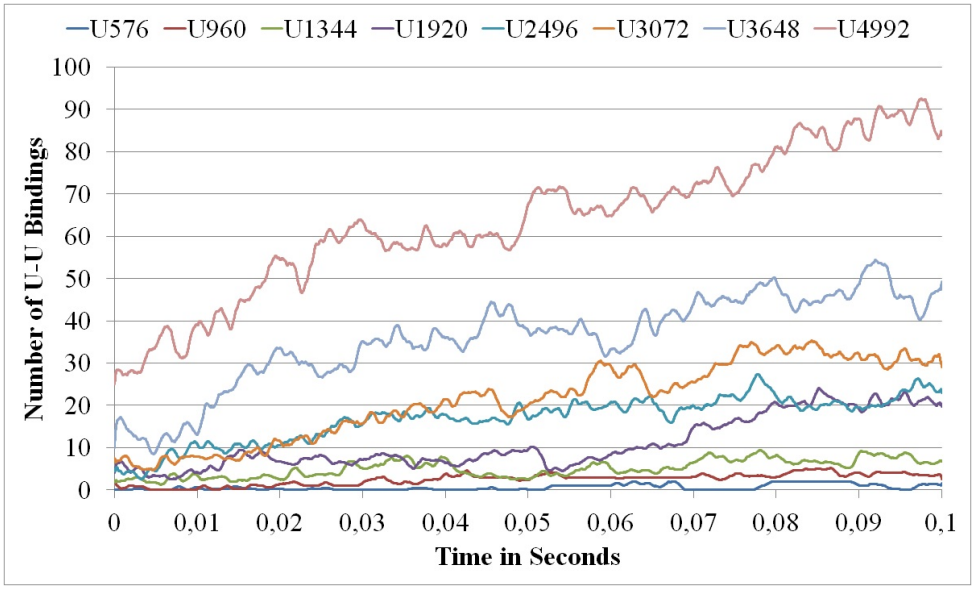

Figure 3.27: The evolution of 'U-U' bindings for various numbers of cluster units. The 'U-U' bindings in large clusters are counted according to their multiplicity.

with the number of cluster units. More precisely, for small numbers of cluster units, i.e. #U $<$ 1500, the number of 'U-U' bindings is smaller than ten. On the other hand, for large numbers of cluster units, for instance #U = 4992, the number of 'U-U' bindings reaches values of up to 90. Thus, the increase in the number of 'U-U' bindings is rapid. More precisely, looking at the data after 0.1 s for instance, the number of 'U-U' bindings increases even faster than linearly in the number of cluster units U.

Actually, the results for the cluster units have to be compared to the results of the other particle types in particular to those of the scenario with death receptor dimers. Indeed, a number of almost 90 signal competent cluster units could be observed in none of the configurations with death receptor dimers.

On the other hand, we have to mention that a cluster unit consists of three death receptor monomers bound to one death receptor ligand. Thus, a number of 4992 cluster units actually contains almost 15000 death receptor monomers. This represents an enormous over-expression of death receptors. For normal expressions, i.e. less than 3000 cluster units, we observe less than 30 'U-U' bindings. However, due to the fast increase of the number of 'U-U' bindings for increasing numbers of cluster units, we compare the results for 4992 cluster units to those particle configurations where death receptor dimers are also over-expressed. For this purpose, we perform simulations with on the one hand 9984 death receptor dimers and 4992 death receptor ligands and on the other hand 2496 death receptor monomers, 7488 death receptor dimers and 4992 death receptor ligands. The evolution of the 'L-D-L' complexes is depicted in Figure 3.28. Since the number of

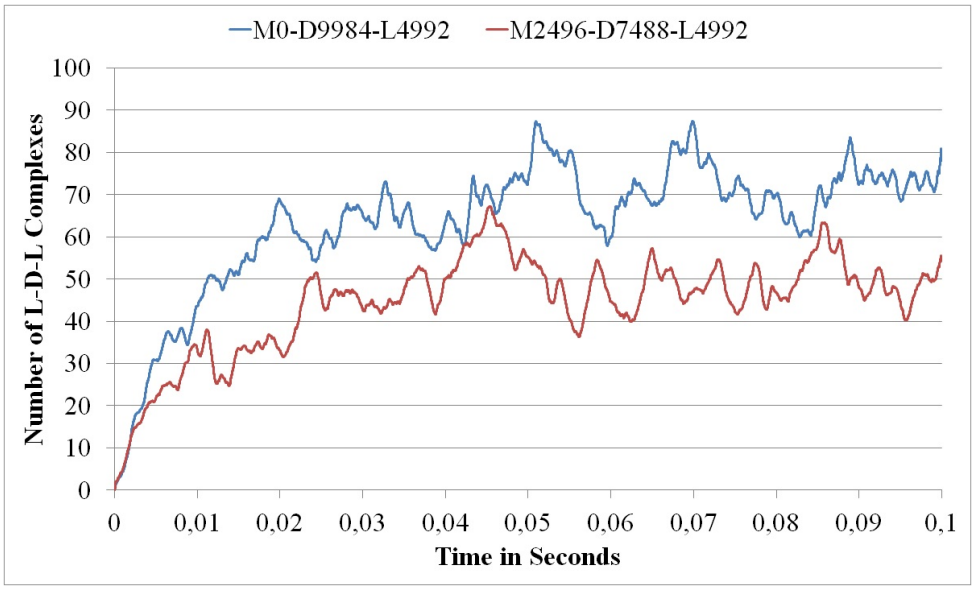

Figure 3.28: The evolution of 'L-D-L' complexes for an over-expression of death receptor dimers.

'L-D-L' complexes is larger for low numbers of death receptor monomers, we restrict the

comparison of 'L-D-L' complexes and 'U-U' bindings to the former particle configuration. We see that the number of 'U-U' bindings for #U = 4992 excesses the barrier of 80 and approaches a value of 100 while the number of 'L-D-L' complexes for 9984 death receptor dimers and 4992 death receptor ligands do not cross the barrier of 80 'L-D-L' complexes significantly, but fluctuates around a mean value of about 70. Hence, the number of 'U-U' bindings is significantly larger than the number of 'L-D-L' complexes in case of over-expressed death receptors.
In summary, we notice that the 'U-U' bindings are more powerful for signaling than the 'L-D-L' complexes in particular for large particle numbers. We note that the fixed cluster units describe an artificial structure which does not really exist on the cellular membrane as a fixed structure.

Visualization of Ligand-Receptor Clusters

Up to now, we evaluated the numerical results of the Euler-Maruyama approximation concerning the number of signal competent cluster units. However, we are also interested in the structure of ligand-receptor clusters of a size larger than three or four. To determine the structure of these clusters, the powerful visualization tool *cellVis* developed by Martin Falk is used.
In the following, we present the visualization of ligand-receptor clusters which are formed for a particle configuration with 9984 death receptor dimers and 4992 death receptor ligands. On a time scale of 0.1 s we find several ligand-receptor clusters with a size of up to seven. We depict two of them in Figure 3.29. The two illustrated ligand-receptor

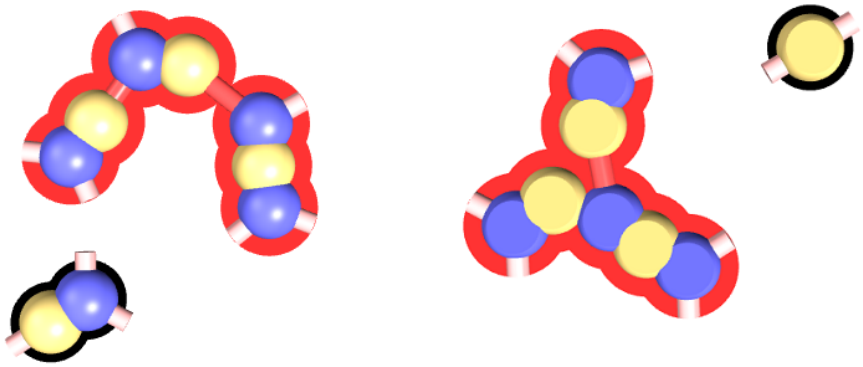

Figure 3.29: Visualization of ligand-receptor clusters of size seven after 0.01365 s (left cluster) and after 0.06576 s (right cluster) for a particle configuration with 9984 death receptor dimers and 4992 death receptor ligands. The ligand-receptor clusters are outlined in red. Besides the ligand-receptor clusters of size seven, the figure also shows a 'D-L' binding and a single death receptor dimer. The visualization of the ligand-receptor clusters is done with the visualization tool *cellVis* implemented by Martin Falk.

clusters occur at different time points, namely after 0.01365 s (left cluster in Figure 3.29) and after 0.06576 s (right cluster in Figure 3.29) and show totally different structures. The ligand-receptor cluster on the left in Figure 3.29 consists of three signal competent cluster units and has the structure of a half hexagon. In fact, according to [42, Figure 1], the preferred structure for ligand-receptor clusters is a hexagon. On the other hand, the ligand-receptor cluster presented on the right in Figure 3.29 consists of three 'L-D-L' complexes as well, but it is star-shaped. Thus, we observe two totally different structures of ligand-receptor clusters of which one fits very well to the theoretically expected structure. In fact, we only considered a very short simulation time of 0.1 s so that the formation of "large" ligand-receptor clusters is not evident.

In this section, we presented the results of the numerical simulations of the receptor clustering. First, we saw that the formation of signal competent cluster units is more likely if the majority of death receptors exist as pre-associated dimers. Furthermore, we observed that death receptor monomers have an inhibitory effect on the formation of signal competent cluster units. We further conclude through the evaluation of the numerical results that the structure 'M-M', i.e. two bound death receptor monomers, is unsuitable for the signal competent cluster unit. In case of death receptor trimers, we found that low numbers of death receptor trimers do not allow the formation of 'L-3T' and 'T-3L' complexes which are suggested to be the signal competent unit in case of death receptor trimers. Finally, with the help of the visualization tool *cellVis*, we even observe ligand-receptor clusters of size up to seven on a time scale of 0.1 s. The clusters have the structure of a half-hexagon and a star, respectively.

Since the simulation for a single particle configuration is extremely expensive even though the Linked-Cell Method is applied, cf. Section 3.5, a more efficient implementation of the algorithms is required. For this purpose, the algorithms are implemented by Claus Braun and Alexander Schöll for GPGPU many-core architectures. We do not respond to the details of the implementation and the ideas for an efficient implementation, but we mention here that the numerical results are obtained through the execution of the corresponding GPU program *parsim*. In the next section, we demonstrate the necessity of the application of GPU computing by indicating the achieved speed-up.

3.7 Mapping of the Algorithms on GPGPU Architectures

Due to the long computation time for the Euler-Maruyama approximation and due to the requirement of a large amount of simulations for various particle configurations, a more efficient implementation of the algorithms is needed. In recent years, several opportunities for parallel programming have been established and multi-core architectures and clusters of CPU have been developed. However, such machines are expensive to purchase, and besides, they need a lot of space. A cheaper variant for high-performance computing is the use of GPUs that enable the parallelization of the simulation on a desktop computer. For the particle model introduced in Section 3.3.5 an efficient algorithmic mapping to a many-core GPGPU architecture is implemented by Claus Braun and his student assistant Alexander Schöll. For a detailed description of the GPGPU architecture and the implementation of the algorithms, we refer the interested reader to the joint article [8]. In the following section, we focus on the acceleration of the algorithms through the parallelization for the different particle configurations and for different numbers of particles by determining the speed-up.

For this purpose, we simulate short time scales and measure the computation time for the code implemented in the computer language C and the GPU code. Since the computation time depends on the hardware, we first state the main facts of the used computer. The platform consists of an Intel Core i7 CPU with 3.07 GHz and 8 GB RAM. Moreover, the system hosts a Nvidia GeForce GTX 480 with 480 CUDA cores at 700 Hz and a memory of 1536 MB.

First, we consider the case with three different particle types, i.e. death receptor monomers, death receptor dimers and death receptor ligands. For simplicity, we take the same number of particles for each particle type and use the same parameter values as in Section 3.6, namely

$$
\begin{array}{llll}
R_{\mathrm{M}} = 1\mathrm{e}-9, & R_{\mathrm{D/L}} = 2\mathrm{e}-9, & \Delta\bar{t} = 1\mathrm{e}-9, & L = 1\mathrm{e}-5, \\
\kappa = 1000, & \tau = 1\,\mathrm{s}, & \sigma_{\mathrm{LJ}}^{\mathrm{M/D/L}} = R_{\mathrm{M/D/L}}/L, & \gamma_{\mathrm{rot,M/D/L}} = 8\pi\eta R_{\mathrm{M/D/L}}^3, \\
\delta = \pi/3, & k_B T = 5\mathrm{e}-21, & \eta = 10, & \beta_{\mathrm{M/D/L}} = 6\pi\eta R_{\mathrm{M/D/L}},
\end{array}
$$

and a fixed number of simulation steps, say 100.000. Then, we obtain the simulation times given in Table 3.5. Thus, we achieve a speed-up of up to 42x for a particle configuration with large particle numbers. First, we mention that the computation time of the C code does not increase quadratically with the number of particles as expected. An obvious reason for this is the fact that only interactions between particles in close vicinity are computed. Otherwise, we would compute $z_{\mathrm{P}} \times z_{\mathrm{P}}$ interactions, with z_{P} the number of

	384	768	1536	3072	6144
CPU time (s)	122	281	795	2400	8324
GPU time (s)	46	53	66	102	197
Speed-Up	2.65x	5.30x	12.05x	23.53x	42,25x

Table 3.5: Computation times for various numbers of death receptor monomers, death receptor dimers and death receptor ligands. The speed-up of the GPU code is given by the quotient of the CPU time divided by the GPU time.

particles, and the increase would be quadratic. For the GPU implementation, the computation time increases even slower than linearly for 'small' particle numbers. Besides the parallelization of the computation of the interactions, several optimizations concerning the storage management and a reduction in the number of interactions are implemented in the GPU algorithms, cf. [8]. For our computer experiments we choose a total amount of particles of a realistic biological order. For large particle numbers, the computation time on a CPU is in the order of days even for a small number of simulation steps, say 100.000. For the corresponding results we refer to the experimental results in [8].

If we consider a particle configuration with only two particle types, i.e. either death receptor monomers and death receptor ligands or death receptor dimers and death receptor ligands, then the speed-up is even larger. The computation times and the speed-up are given in Table 3.6. We see that the computation time on a CPU is larger now, while

	576	1152	2304	4608	9216
CPU time (s)	132	288	817	2631	9518
GPU time (s)	30	34	43	70	157
Speed-Up	4.40x	8.47x	19.00x	37.59x	60.62x

Table 3.6: Computation times for various numbers of death receptor dimers and death receptor ligands. The speed-up of the GPU code is given by the quotient of the CPU time divided by the GPU time.

the GPU implementation is significantly faster in case of two particle types towards the simulation with three particle types. To show that the speed-up does not depend on the chosen particle type, we replace the death receptor dimers by death receptor monomers and repeat the simulation with the same particle numbers. Obviously, the computation times on the GPU and the CPU do not differ significantly, cf. Table 3.7.

In summary, we see that the mapping of the algorithms on GPGPU architectures results in a peak speed-up of 60.62x for particle configurations on a realistic biological order. For larger particle numbers, the speed-up is even larger, cf. [8]. Due to the different platforms and a different parameter setting used for the numerical experiments in [8] and in this section, the results are not expected to be identical, confer for instance

	576	1152	2304	4608	9216
CPU time (s)	115	283	802	2587	9332
GPU time (s)	31	35	46	74	165
Speed-Up	3.71x	8.09x	17.43x	34.96x	56.56x

Table 3.7: Computation times for various numbers of death receptor monomers and death receptor ligands. The speed-up of the GPU code is given by the quotient of the CPU time divided by the GPU time.

the computation times for the particle configuration with a total number of 9216 or 18432 particles. Although the speed-up reaches values of up to 60.62x, the application of GPU computing does not enable the simulation of receptor clustering on time scales of biological interest, namely at least 15 minutes. Simulating 15 minutes requires approximately one trillion time steps if $\Delta\bar{t} = 1\mathrm{e}-9$. That results in a computation time of about one billion seconds or more than 30 years.

3.8 Discussion

In this chapter, we introduced a particle model for the clustering of death receptors on the cell membrane. Due to the flexible structure of the model, the Euler-Maruyama approximation of the underlying system of stochastic differential equations was computed for different particle types and various particles configurations. In particular, the particle model enables the comparison of different biological hypothesis concerning the binding behavior of the different death receptor structures. For this purpose, we considered death receptors in a monomeric, dimeric [6] and trimeric [10] pre-form and compared the results concerning the formation of signal competent cluster units. In a first approach, the numerical results confirmed the suggestion of Boschert et al. [6] that the majority of the TNFR1-Fas chimeras exist in a dimeric pre-form. To show this, we varied the ratios between the number of death receptor dimers and death receptor monomers and found that the highest number of signal competent cluster units was reached for a low number of death receptor monomers. Moreover, we checked that death receptor monomers even constrained the formation of signal competent cluster units. This was done by studying the formation of signal competent cluster units for a fixed number of death receptor dimers and death receptor ligands and for two values of #M, namely $\#\mathrm{M} = 0$ and $\#\mathrm{M} = 2496$. We further showed that death receptor ligands represent an essential ingredient for the signal competent cluster unit with a participation of death receptor monomers. We found that two bound death receptor monomers can not represent the smallest signal competent unit. Since the structure of signal competent cluster units is rather unclear for death receptor trimers, we investigated various structures of ligand-trimer complexes.

The results indicated that a death receptor trimer associated with a death receptor ligand is the only structure which occurs in a sufficient frequency. And the number of ligand-trimer bindings is in the same order as the number of signal competent cluster units in case of dimeric death receptors. Larger complexes of death receptor trimers and death receptor ligands were not observable or rare. In fact, according to [44], the number of death receptor trimers is significantly lower than the number of death receptor monomers and death receptor dimers, respectively. On the other hand, the particle model introduced in Section 3.3.5 do not take into account the structure of so-called lipid rafts which are crucial for the TNF activated signaling pathways [40]. Lipid rafts denote parts of the cell membrane with a higher density of death receptors. However, we assumed in our model a homogeneous distribution of death receptors on the cell membrane.

Moreover, we only considered for our simulations a very short time scale, namely 0.1 s, due to the high costs of the simulations. For instance, the simulation for the particle configuration with 576 death receptor monomers, 2496 death receptor dimers and 2496 death receptor ligands on a time scale of 1 s took more than 13 days for the hardware configuration described in Section 3.7. Thus, the simulation time is significantly limited by the computation time. But even on a small time scale of 0.1 s, the computation time for particle configurations with large particle numbers exceeds one day. For instance, the simulation of the particle configuration with 4992 death receptor dimers and 4992 death receptor ligands took about 28 hours for a simulation time of 0.1 s. On the one hand, these conditions limit the number of investigations of various particle configurations and on the other hand, a variation of the parameter values of the system is not possible. Thus, we restricted the analysis of the particle model to one parameter setting.

However, the detailed analysis in Section 3.6 was only possible due to the mapping of the algorithms on GPGPU architectures by Claus Braun. The speed-up of about 60x decreased the computation time from months to days. Furthermore, with the powerful visualization tool *cellVis* developed by Martin Falk, a cluster analysis could be executed. For our simulations, we even found ligand-receptor clusters of size seven which consist of three signal competent cluster units and exhibits the structures of a half-hexagon and a star, respectively. Unfortunately, a comparison of the numerical results with experimental data was not possible due to the short simulation time.

Concluding, we notice that the established particle model provides new insights into the formation of signal competent cluster units and large ligand-receptor clusters concerning their structure. On the other hand, many open questions remain unanswered due to the high computation effort despite the application of high-performance computing. In fact, the formation of ligand-receptor clusters is a current biological research area with many open biological questions.

4. Outlook

In Chapter 2, we studied a spatially extended reaction-diffusion model for the description of the caspase concentration within a single cell. For simplicity, we neglected the activation of pro-caspase 8 by death receptors at the cellular membrane and chose homogeneous Neumann boundary conditions for all involved caspase types. According to the activation of pro-caspase 8 by death receptors at the cell membrane, more realistic boundary conditions depending on parameters should be introduced. Therefore, we consider again the original reaction-diffusion system (2.14) in two dimensions

$$\begin{array}{rcl} \frac{\partial X_a}{\partial t} & = & \tilde{k}_{c1} X_i Y_a - \tilde{k}_{d1} X_a + \tilde{D}_1 \Delta_{\mathbf{x}} X_a, \\ \frac{\partial Y_a}{\partial t} & = & \tilde{k}_{c2} Y_i X_a^n - \tilde{k}_{d2} Y_a + \tilde{D}_2 \Delta_{\mathbf{x}} Y_a, \\ \frac{\partial X_i}{\partial t} & = & -\tilde{k}_{c1} X_i Y_a - \tilde{k}_{d3} X_i + \tilde{k}_{p1} + \tilde{D}_3 \Delta_{\mathbf{x}} X_i, \\ \frac{\partial Y_i}{\partial t} & = & -\tilde{k}_{c2} Y_i X_a^n - \tilde{k}_{d4} Y_i + \tilde{k}_{p2} + \tilde{D}_4 \Delta_{\mathbf{x}} Y_i, \end{array} \tag{4.1}$$

in $\Omega := \{\mathbf{x} \in \mathbb{R}^2, \|\mathbf{x}\|_\infty \leq 1\}$, where the components of $\mathbf{x}$ are denoted by x and y. The parameter dependent boundary conditions are given by

$$\begin{array}{lll} \frac{\partial X_a}{\partial n}\big|_{\partial\Omega} & = -\frac{\partial X_i}{\partial n}\big|_{\partial\Omega} & = \mu \cdot U(x_{\partial\Omega}, t) \cdot \ X_i|_{\partial\Omega} \\ \frac{\partial Y_a}{\partial n}\big|_{\partial\Omega} & = +\frac{\partial Y_i}{\partial n}\big|_{\partial\Omega} & = 0, \end{array} \tag{4.2}$$

where μ denotes the reaction rate for the activation of pro-caspase 8 by death receptors at the cell membrane, $\partial\Omega$ denotes the boundary of Ω, and the function $U(x_{\partial\Omega}, t)$ describes the concentration of receptor clusters at the cellular membrane. Here, $x_{\partial\Omega}$ denotes the variable that describes the boundary of Ω. Obviously, we keep the homogeneous Neumann boundary conditions for caspase 3 and pro-caspase 3, since the activation of pro-caspase 3 only occurs inside the cell and not at the boundary. We point out the time dependency of the function U. Thereby, we include in our model the situation that the death receptors lose their activity, e.g. by internalization and turnover. The problems that occur in this model are obvious. On the one hand, the parameter value of μ is unknown to the best of our current knowledge, and the concentration distribution of receptor clusters at the cellular membrane is difficult to measure, especially the continuous time dependency. The latter problem can be solved for instance by in silico experiments that yield the distri-

bution of receptor clusters on the cell membrane. Hence, the particle model introduced in Chapter 3 can be used for the determination of the cluster distribution. Since the determination of the parameter μ is more complicated, we can make use of model reduction methods. Thereby, the parametric boundary value problem can be solved efficiently for a large range for the values of μ and the output 'survival' versus 'death' of the cell can be studied under the assumption of an appropriate definition of cell death. In a first preliminary step, we implement for the reaction-diffusion system (4.1) an implicit Euler method in combination with a centered first order Finite Difference method for the spatial discretization in two dimensions, see Appendix A.5. We run the simulation with

$$\Delta x = \Delta y = 0.05, \Delta t = 0.5 \cdot (\min\{\Delta x, \Delta y\})^2,$$

and we arbitrarily choose $\mu = 0.5$. For the function $U(x_{\partial\Omega}, t)$ we define

$$U(x_{\partial\Omega}, t) = H(x_{\partial\Omega} - 0.25) \cdot H(0.75 - x_{\partial\Omega}) \cdot H(T_s - t),$$

where $H(\,\cdot\,)$ again denotes the Heaviside function and T_s is the time where the activity of a death receptor ends, in our case $T_s = T/2$ with the simulation time $T = 10$ corresponding to about one minute on the biological scale. The remaining parameters are set to

$$\tilde{k}_{ci} = 0.444, \quad \tilde{k}_{pi} = 5.556 \cdot 10^{-4}, \quad \tilde{k}_{dj} = 0.0028, \quad i = 1, 2; j = 1, \ldots, 4,$$

and the exponent of the reaction kinetics is $n = 2.5$. The dynamical behavior of the concentrations is illustrated in Figure 4.1–Figure 4.3.

We assume that the active caspase exists in cells in low concentrations whereas the concentration of inactive caspase is high. We further consider inhomogeneous caspase concentrations and choose as initial conditions smooth functions, namely

$$\begin{aligned} X_a(\mathbf{x}, t) &= 1000 \cdot (0.001 \cdot \sin(5\pi x) + 0.001) \cdot (0.001 \cdot \sin(5\pi y) + 0.001), \\ Y_a(\mathbf{x}, t) &= 1000 \cdot (0.001 \cdot \sin(5\pi x) + 0.001) \cdot (0.001 \cdot \sin(5\pi y) + 0.001), \\ X_i(\mathbf{x}, t) &= 10 \cdot (0.1 \cdot \sin(5\pi x) + 0.1) \cdot (0.1 \cdot \sin(5\pi y) + 0.1), \\ Y_i(\mathbf{x}, t) &= 10 \cdot (0.1 \cdot \sin(5\pi x) + 0.1) \cdot (0.1 \cdot \sin(5\pi y) + 0.1), \end{aligned} \tag{4.3}$$

see Figure 4.1. After 10 time steps, most of the oscillations of the initial conditions are balanced, cf. Figure 4.2, and the maximum of the concentrations is significantly decreased due to the fast diffusion. After 50 time steps, the concentrations of active and inactive caspase 8 shows the influence of the boundary conditions, i.e. the concentration of active caspase 8 in the middle of the four edges, where the activation by death receptors takes place, is higher than in the rest of the cell, see Figure 4.2. For the other caspase types, the concentrations take the maximum in the four vertices of the domain.

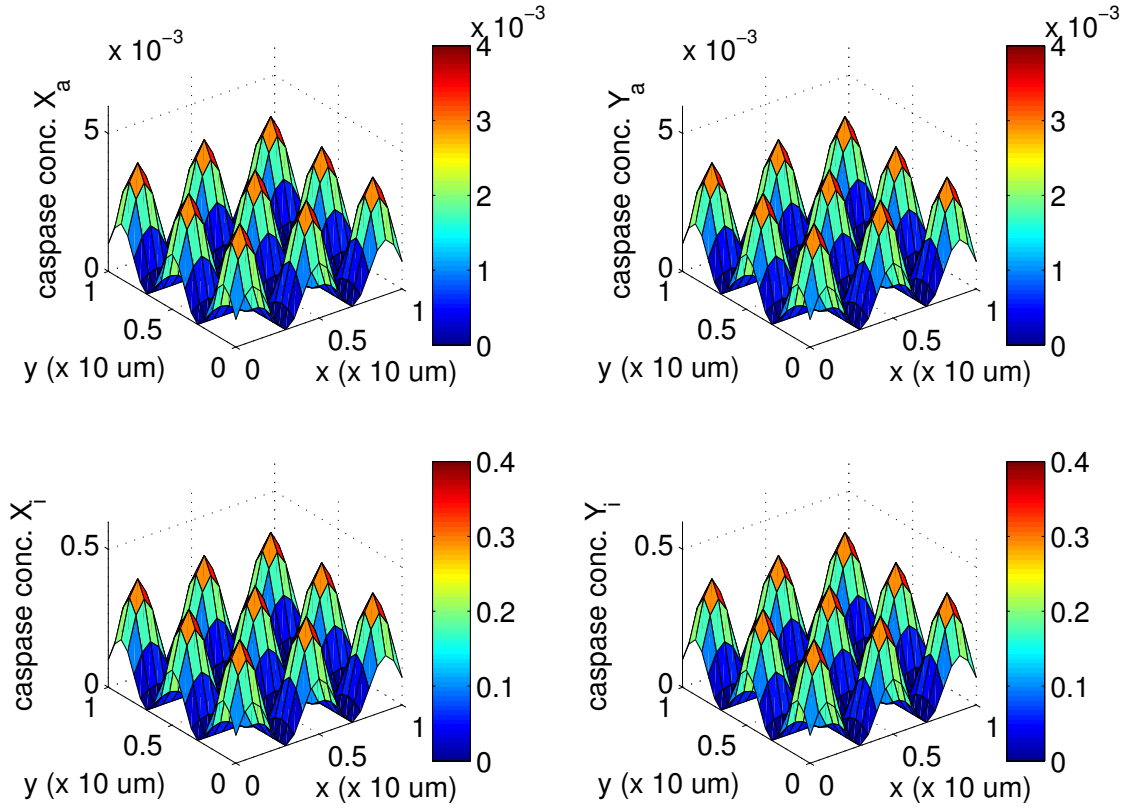

Figure 4.1: The initial condition (4.3) of the reaction-diffusion system (4.1).

Moreover, the concentrations of active and inactive caspase 3 show a similar structure after 50 time steps but on different scales, see Figure 4.3. After the deactivation of the external stimulus, the fast diffusion immediately balances the gradients in the caspase concentrations and subsequently, the dynamics of the system is again determined by the reaction kinetics. Again, the averaged caspase concentrations decide which of the two asymptotically stable stationary solutions is approached. In fact, the concentrations of active caspases significantly depend on the activation time T_s, the strength of the activation μ and the size of the activation domain. For a more detailed analysis of the reaction-diffusion system (4.1) with the parameter dependent boundary conditions (4.2), model reduction methods will be applied in order to admit variations in the parameter values.

The extended reaction-diffusion model introduced above includes the function U describing the distribution of receptor clusters at the cell membrane. Here, the particle model for the clustering of death receptors on the cell membrane introduced in Section 3.3.5 could be used for the determination of the distribution of signal competent ligand-receptor clusters on the cell membrane. However, the disadvantage of the in-

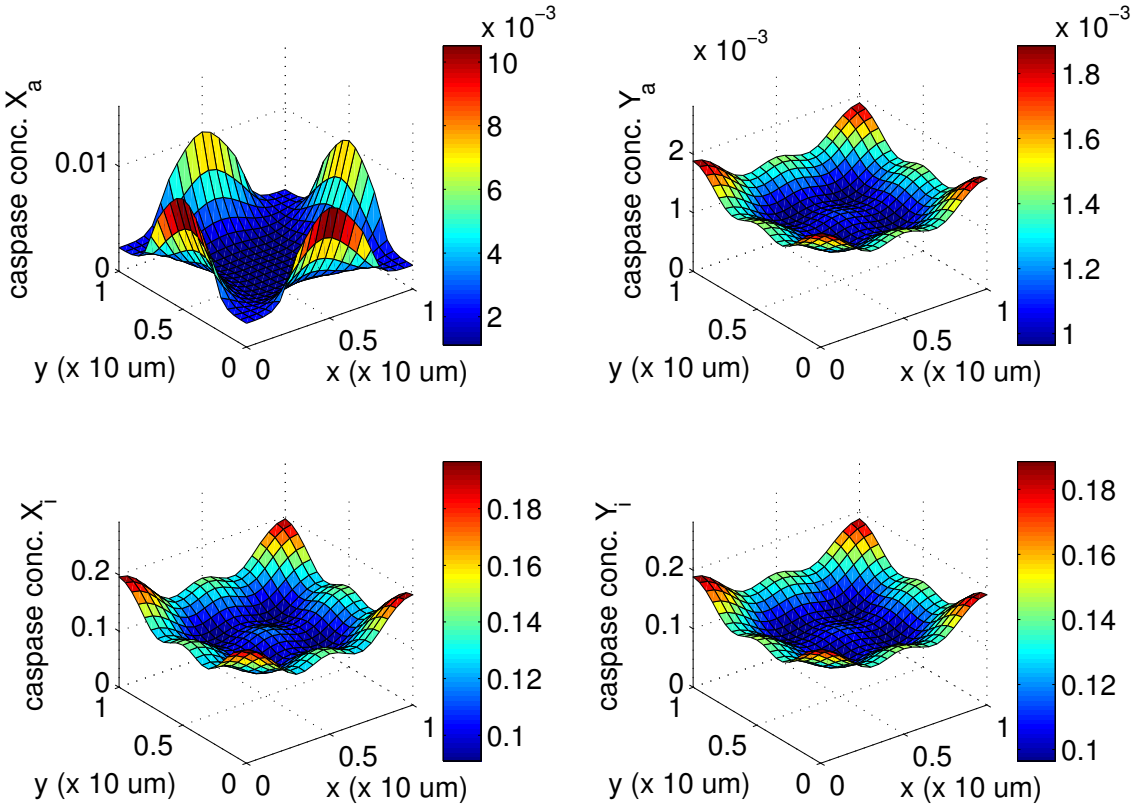

Figure 4.2: The solution of the reaction-diffusion system (4.1) with parametric boundary conditions (4.2) after 10 time steps.

troduced detailed particle model is the high complexity of the simulation. Despite the application of high-performance computing, the cluster evolution could not be determined on a realistic biological time scale, but the GPU implementation enables at least the simulation with different particle configurations. However, the development of analyzable models is desirable. One possibility to model the receptor clustering is the introduction of a phase separation model by considering the concentrations of receptors and lipids on the cell membrane and derive balance equations for both concentrations. Here, the mobility of the receptors would depend on the ligand concentration. Finally, we end with a Cahn-Hilliard equation describing the evolution of the concentrations. However, the incorporation of the cluster structure is the main challenge for this model. The clustering of death receptors can also be modeled by a Smoluchowski equation of the form

$$\frac{\mathrm{d}\tilde{N}(m,t)}{\mathrm{d}t} = \frac{1}{2}\int_0^m K(n,m-n)\tilde{N}(n,t)\tilde{N}(m-n,t)\mathrm{d}n - \int_0^\infty \tilde{K}(m,n)\tilde{N}(m,t)\tilde{N}(n,t)\mathrm{d}n.$$

Here, the function $\tilde{N}(m,t)$ describes the concentration of ligand-receptor clusters of size m at time t. The functions $K(n,m-n)$ and $\tilde{K}(m,n)$ describe the probabilities for the

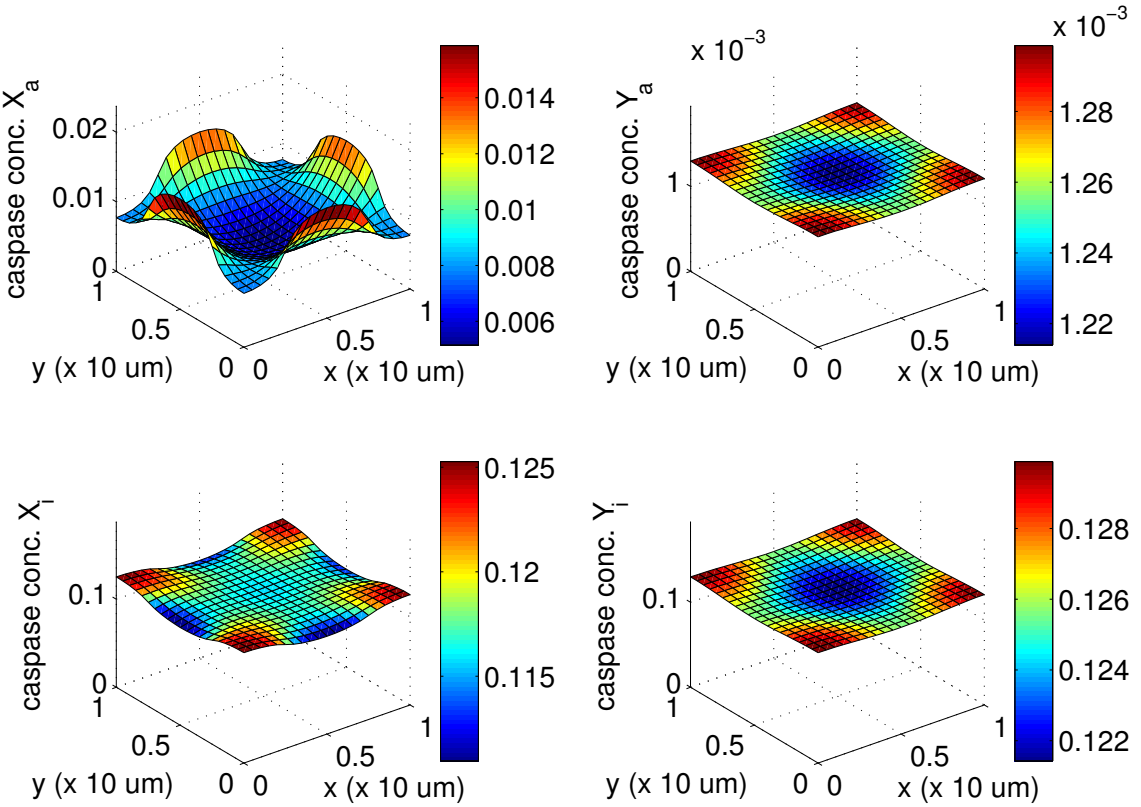

Figure 4.3: The solution of the reaction-diffusion system (4.1) with parametric boundary conditions (4.2) after 50 time steps.

aggregation of the clusters. If we further take into account the diffusion of the clusters, we obtain the equation

$$\begin{aligned}\frac{\partial \tilde{N}(m,x,t)}{\partial t} =& \frac{1}{2}\int_0^m K(n,m-n)\tilde{N}(n,x,t)\tilde{N}(m-n,x,t)\mathrm{d}n \\ &- \int_0^\infty \tilde{K}(m,n)\tilde{N}(m,x,t)\tilde{N}(n,x,t)\mathrm{d}n + D(m)\Delta_x\tilde{N}(m,x,t),\end{aligned} \tag{4.4}$$

where the diffusion coefficient $D(m)$ is a function of the cluster size. The parameters can be determined through the particle simulations: starting with a certain initial condition for the particle simulation, the time until two clusters aggregate and the quadratic displacement of the particles can be measured. Additionally, the size of the clusters is determined. These magnitudes lead to the kernel functions $K(\,\cdot\,)$ and $\tilde{K}(\,\cdot\,)$ and the diffusion coefficient $D(m)$.

On the one hand, the extended Smoluchowski equation contains diffusion and aggregation terms. But on the other hand, effects like the fragmentation of ligand-receptor clusters are not taken into account. However, solving equation (4.4) will give the concentrations of ligand-receptor clusters on a large, biologically relevant time scale.

A. Appendix

A.1 Computation of Biological Quantities

A.1.1 Determination of the Typical Caspase Concentration

We assume that the typical number of caspase molecules in a single cell is in the order of $N_{\text{mol}} = 100.000$. Furthermore, we consider a cell modeled as a sphere with radius $R = 10\,\mu\text{m}$. The relationship between the number of caspase molecules N_{mol} and the caspase concentration is given by

$$N_{\text{mol}} = c \cdot V \cdot N_A \quad \Leftrightarrow \quad c = \frac{N_{\text{mol}}}{V \cdot N_A}, \tag{A.1}$$

where V is the volume of the sphere, N_A is Avogrado's constant, c is the caspase concentration and N_{mol} is the number of caspase molecules. With the given values for the number of molecules and the radius of the sphere, we obtain from (A.1)

$$c = \frac{100.000}{\frac{4}{3}\pi 10^{-12}\,\text{l} \cdot 6.022 \cdot 10^{23}\,\frac{1}{\text{mol}}} \approx 4 \cdot 10^{-8}\,\frac{\text{mol}}{\text{l}} = 4 \cdot 10^{-8}\,\text{M}.$$

For simplicity, we choose for the typical scale of caspase concentrations $10^{-7}\,\text{M} = 100\,\text{nM}$.

A.1.2 Determination of Diffusion Coefficients

In the following, we determine the diffusion coefficients D_n for the different caspase types. According to [31], the diffusion coefficient for a protein is given by

$$D_n = D_{\text{GFP}} \cdot \left(\frac{\text{m}_{\text{GFP}}}{\text{m}_{\text{n}}}\right)^{\frac{1}{3}}, \tag{A.2}$$

where the diffusion coefficient D_{GFP} is $24\,\mu\text{m}^2\text{s}^{-1}$ and the mass of a GFP protein is $\text{m}_{\text{GFP}} = 27\,\text{kDa}$, cf. [31]. Here, the unit kDa is the abbreviation for kilodalton, where Dalton is the American notation for the atomic mass unit, i.e. $1\,\text{Da} = 1\,\text{u} \approx 1.6605 \cdot 10^{-27}\,\text{kg}$. Thus, $1\,\text{kDa} \approx 1.6605 \cdot 10^{-24}\,\text{kg}$. In order to compute the diffusion coefficients with equa-

Protein	Mass	Diffusion coefficient
pro-caspase 8	55 kDa	$18.9\,\mu m^2 s^{-1}$
caspase 8	64 kDa	$18\,\mu m^2 s^{-1}$
pro-caspase 3	32 kDa	$22.7\,\mu m^2 s^{-1}$
caspase 3	58 kDa	$18.6\,\mu m^2 s^{-1}$

Table A.1: The masses and the values for the diffusion coefficients of the different caspases.

tion (A.2), we need the masses of the caspase proteins. From [11], we know that the mass of pro-caspase 3 is $m_{C3} = 32\,\text{kDa}$. Furthermore, when activated, pro-caspase 3 is cleaved into large and small subunits. The small subunit has a mass of 12 kDa and the mass of the large subunit is 17 kDa. Since the active enzyme is composed of two large and two small subunits and exhibits a heterotetrameric structure, the mass of the active caspase 3 is $m_{C3^*} = 58\,\text{kDa}$. Again, the asterisk denotes the active form of caspase 3 and later caspase 8, respectively. In [37], we find the mass of pro-caspase 8 $m_{C8} = 55\,\text{kDa}$. In addition, we know that pro-caspase 8 is cleaved into a large subunit with a mass of 20 kDa and a small subunit with a mass of 12 kDa. The heterotetrameric structure of the active caspase 8 then has a mass of $m_{C8^*} = 64\,\text{kDa}$. In summary, we state in Table A.1 the diffusion rates obtained with (A.2), besides the masses of the different caspase proteins.

A.2 Derivation of the Bessel Differential Equation for the 2D Laplace Operator

In order to compute the eigenvalues of the Laplace operator in two spatial dimensions, we transform the Laplace operator in polar coordinates. Then, the eigenvalue problem can be written as

$$-\frac{1}{r}\frac{\partial}{\partial r}(r\frac{\partial \varphi_k}{\partial r}) - \frac{1}{r^2}\frac{\partial^2 \varphi_k}{\partial \vartheta^2} = \lambda_k \varphi_k, \tag{A.3}$$

with the boundary condition $\frac{\partial \varphi_k}{\partial r}\big|_{r=1} = 0$. We make the ansatz $\varphi_k(r,\vartheta) = \Gamma(r)\cdot\Theta(\vartheta)$ and obtain

$$-\frac{1}{r}\frac{\mathrm{d}}{\mathrm{d}r}\left(r\frac{\mathrm{d}\Gamma(r)}{\mathrm{d}r}\right)\Theta(\vartheta) - \frac{1}{r^2}\Gamma(r)\frac{\mathrm{d}^2\Theta(\vartheta)}{\mathrm{d}\vartheta^2} = \lambda_k \Gamma(r)\Theta(\vartheta) \tag{A.4}$$

with the boundary condition $\Gamma'(1) = 0$ and the periodicity condition $\Theta(\vartheta + 2\pi) = \Theta(\vartheta)$. Multiplying equation (A.4) by r^2 and dividing it by $\Gamma(r)\Theta(\vartheta)$ yields

$$-\frac{r}{\Gamma(r)}\frac{\mathrm{d}}{\mathrm{d}r}\left(r\frac{\mathrm{d}\Gamma(r)}{\mathrm{d}r}\right) - \lambda_k r^2 = \frac{1}{\Theta(\vartheta)}\frac{\mathrm{d}^2\Theta(\vartheta)}{\mathrm{d}\vartheta^2} = const =: -\omega_*^2$$

leading to the two ordinary differential equations

$$\frac{\mathrm{d}^2\Theta(\vartheta)}{\mathrm{d}\vartheta^2} = -\omega_*^2\Theta(\vartheta), \quad \Theta(\vartheta + 2\pi) = \Theta(\vartheta) \tag{A.5}$$

and

$$r\frac{\mathrm{d}}{\mathrm{d}r}\left(r\frac{\mathrm{d}\Gamma(r)}{\mathrm{d}r}\right) + \lambda_k r^2\Gamma(r) = \omega_*^2\Gamma(r). \tag{A.6}$$

The solution of equation (A.5) is

$$\Theta(\vartheta) = a_n\cos(\omega_*\vartheta) + b_n\sin(\omega_*\vartheta), \quad \omega_* \in \mathbb{N}_0.$$

Finally, equation (A.6) reads

$$r\frac{\mathrm{d}}{\mathrm{d}r}\left(r\frac{\mathrm{d}\Gamma(r)}{\mathrm{d}r}\right) + \lambda_k r^2\Gamma(r) - \omega_*^2\Gamma(r) = 0, \quad \Gamma'(1) = 0.$$

Then, the coordinate transformation $\rho = \sqrt{\lambda_k}r$, with $r\frac{\mathrm{d}}{\mathrm{d}r} = \rho\frac{\mathrm{d}}{\mathrm{d}\rho}$, yields

$$\rho\frac{\mathrm{d}}{\mathrm{d}\rho}\left(\rho\frac{\mathrm{d}\tilde{\Gamma}(\rho)}{\mathrm{d}\rho}\right) + (\rho^2 - \omega_*^2)\tilde{\Gamma}(\rho) = 0, \quad \tilde{\Gamma}'(\sqrt{\lambda_k}) = 0. \tag{A.7}$$

A simplification of the derivatives and the division of (A.7) by ρ^2 leads to the Bessel differential equation in the form of [61]

$$\tilde{\Gamma}''(\rho) + \frac{1}{\rho}\tilde{\Gamma}'(\rho) + \left(1 - \frac{\omega_*^2}{\rho^2}\right)\tilde{\Gamma}(\rho) = 0, \quad \tilde{\Gamma}'(\sqrt{\lambda_k}) = 0.$$

Thus, the eigenvalues of the Laplace operator in two dimensions are the squared zeros of the first derivative of the solutions to the Bessel differential equation, also called Bessel functions.

A.3 Unsuitable Invariant Region

As mentioned in Section 2.7, a rectangular domain

$$\Sigma_R = \{(X_a, Y_a, X_i, Y_i) \in \mathbb{R}^4, 0 \le X_a \le a, 0 \le Y_a \le b, 0 \le X_i \le c, 0 \le Y_i \le d\} \tag{A.8}$$

is unsuitable as invariant region for the reaction-diffusion system (2.45). In the following, we show that the parameters a, b, c and d can not be chosen compatibly to the situation

with the two stable stationary solutions. Again, we write the region Σ_R in the form

$$\Sigma_R = \{(X_a, Y_a, X_i, Y_i) \in \mathbb{R}^4, G_i(X_a, Y_a, X_i, Y_i) \leq 0\},$$

where the functions $G_i, i = 1, \ldots, 8$, are given by

$$\begin{aligned}
G_1(X_a, Y_a, X_i, Y_i) &= -X_i, \\
G_2(X_a, Y_a, X_i, Y_i) &= X_i - c, \\
G_3(X_a, Y_a, X_i, Y_i) &= -Y_i, \\
G_4(X_a, Y_a, X_i, Y_i) &= Y_i - d, \\
G_5(X_a, Y_a, X_i, Y_i) &= -X_a, \\
G_6(X_a, Y_a, X_i, Y_i) &= X_a - a, \\
G_7(X_a, Y_a, X_i, Y_i) &= -Y_a, \\
G_8(X_a, Y_a, X_i, Y_i) &= Y_a - b.
\end{aligned} \tag{A.9}$$

In order to check if Σ_R describes an invariant region for the reaction-diffusion system (2.45), we look at the conditions $i) - iii)$ in Theorem 2.9. But first of all, we mention that the diffusion matrix $\tilde{D}$ is positive definite and the reaction-diffusion system (2.45) is f-stable. Furthermore, the functions $G_i, i = 1, \ldots, 8$, are quasi-convex since their second derivative vanishes, and the gradient of the functions $G_i, i = 1, \ldots, 8$, is a multiple of the standard basis vector $e_1, \ldots, e_4$ of $\mathbb{R}^4$ and, hence, a left eigenvector of the diffusion matrix $\tilde{D}$. Therefore, the conditions $i)$ and $ii)$ of Theorem 2.9 are satisfied.

Moreover, we have to check if the function f points into Σ_R from $\partial\Sigma_R$, i.e. $\nabla G_i \cdot f|_{\partial\Sigma_R} \leq 0$. The functions G_1, G_3, G_5 and G_7 are the same as for the invariant region Σ in Section 2.7 and, hence, we obtain the same estimates $X_a \geq 0$, $Y_a \geq 0$, $X_i \geq 0$ and $Y_i \geq 0$. Furthermore, for $G_2 = X_i - c$ with $\nabla G_2 = (0, 0, 1, 0)^\top$, we have the estimate

$$\begin{aligned}
\nabla G_2 \cdot f|_{X_i = c} &= -\tilde{k}_{c1} X_i Y_a - \tilde{k}_{d3} X_i + \tilde{k}_{p1}\Big|_{X_i = c} \\
&\leq -\tilde{k}_{d3} c + \tilde{k}_{p1} \leq 0 \text{ for } c \geq \frac{\tilde{k}_{p1}}{\tilde{k}_{d3}}.
\end{aligned}$$

Thus, we have $X_i \leq c$ if $c \geq \tilde{k}_{p1}/\tilde{k}_{d3}$. For $G_4 = Y_i - d$, the gradient is given by $\nabla G_4 = (0, 0, 0, 1)^\top$, thus

$$\begin{aligned}
\nabla G_4 \cdot f|_{Y_i = d} &= -\tilde{k}_{c2} Y_i X_a^n - \tilde{k}_{d4} Y_i + \tilde{k}_{p2}\Big|_{Y_i = d} \\
&\leq -\tilde{k}_{d4} d + \tilde{k}_{p2} \leq 0 \text{ for } d \geq \frac{\tilde{k}_{p2}}{\tilde{k}_{d4}},
\end{aligned}$$

that implies $Y_i \leq d$ if $d \geq \tilde{k}_{p2}/\tilde{k}_{d4}$. In summary, we obtain for each of the two parameters c and d one condition. This condition fits well to the reaction-diffusion system and the concentrations of the spatially homogeneous, stationary solutions, since these conditions just provides for the parameters c and d to be larger than the concentration of the life state. Finally, we consider the functions $G_6 = X_a - a$ and $G_8 = Y_a - b$. For $G_6 = X_a - a$, we obtain with the gradient $\nabla G_6 = (1,0,0,0)^\top$

$$\nabla G_6 \cdot \ f|_{X_a=a} = \tilde{k}_{c1} X_i Y_a - \tilde{k}_{d1} a \leq \tilde{k}_{c1} cb - \tilde{k}_{d1} a,$$

and for $G_8 = Y_a - b$, the gradient is given by $\nabla G_8 = (0,1,0,0)^\top$, thus

$$\nabla G_8 \cdot \ f|_{Y_a=b} = \tilde{k}_{c2} Y_i X_a^n - \tilde{k}_{d2} b \leq \tilde{k}_{c2} d a^n - \tilde{k}_{d2} b.$$

Hence, we ask for the estimates

$$\tilde{k}_{c1} cb - \tilde{k}_{d1} a \leq 0, \tag{A.10}$$

$$\tilde{k}_{c2} d a^n - \tilde{k}_{d2} b \leq 0. \tag{A.11}$$

Obviously, (A.11) is equivalent to $b \geq \tilde{k}_{c2} d a^n / \tilde{k}_{d2}$. Then, we obtain from (A.10)

$$a \geq \frac{\tilde{k}_{c1} cb}{\tilde{k}_{d1}} \geq \frac{\tilde{k}_{c1}\tilde{k}_{c2} c d a^n}{\tilde{k}_{d1}\tilde{k}_{d2}} \geq \frac{\tilde{k}_{c1}\tilde{k}_{c2}\tilde{k}_{p1}\tilde{k}_{p2} a^n}{\tilde{k}_{d1}\tilde{k}_{d2}\tilde{k}_{d3}\tilde{k}_{d4}}, \tag{A.12}$$

and inequality (A.12) is equivalent to

$$-\tilde{k}_{c1}\tilde{k}_{c2}\tilde{k}_{p1}\tilde{k}_{p2} a^n + \tilde{k}_{d1}\tilde{k}_{d2}\tilde{k}_{d3}\tilde{k}_{d4} a \geq 0. \tag{A.13}$$

We make the assumption $a \geq X_a^{(d)}$ since the death state should be located in the invariant region. We further know

$$\begin{aligned}(\tilde{k}_{c1}\tilde{k}_{c2}\tilde{k}_{d1}\tilde{k}_{p2} + \tilde{k}_{c2}\tilde{k}_{d1}\tilde{k}_{d2}\tilde{k}_{d3})(X_a^{(d)})^{n+1} - \tilde{k}_{c1}\tilde{k}_{c2}\tilde{k}_{p1}\tilde{k}_{p2}(X_a^{(d)})^n \\ + \tilde{k}_{d1}\tilde{k}_{d2}\tilde{k}_{d3}\tilde{k}_{d4} X_a^{(d)} = 0\end{aligned} \tag{A.14}$$

since the death state is a solution of equation (2.26). Obviously, the first summand in (A.14) is strictly positive and therefore the remainder on the left-hand side is strictly negative. We define the function

$$f(x) = -\tilde{k}_{c1}\tilde{k}_{c2}\tilde{k}_{p1}\tilde{k}_{p2} x^n + \tilde{k}_{d1}\tilde{k}_{d2}\tilde{k}_{d3}\tilde{k}_{d4} x$$

describing the last two summands of (A.14) whose zeros are

$$x_1 = 0 \quad \text{and} \quad x_2 = \left(\frac{\tilde{k}_{d1}\tilde{k}_{d2}\tilde{k}_{d3}\tilde{k}_{d4}}{\tilde{k}_{c1}\tilde{k}_{c2}\tilde{k}_{p1}\tilde{k}_{p2}} \right)^{\frac{1}{n-1}}.$$

Further, $f(x)$ is strictly monotone decreasing for

$$x > (1/n)^{1/(n-1)} \cdot (\tilde{k}_{d1}\tilde{k}_{d2}\tilde{k}_{d3}\tilde{k}_{d4}/\tilde{k}_{c1}\tilde{k}_{c2}\tilde{k}_{p1}\tilde{k}_{p2})^{1/(n-1)} = (1/n)^{1/(n-1)}x_2.$$

and strictly monotone increasing for $x < (1/n)^{1/(n-1)}x_2$. Thus, the function $f(x)$ is positive for $x_1 < x < x_2$ and negative for $x > x_2$. From (A.14) we have $f(X_a^{(d)}) < 0$ which implies $X_a^{(d)} > x_2$ and the monotony of $f(x)$ together with the assumption $a \geq X_a^{(d)}$ yields $f(a) < 0$. Thus, we find

$$-\tilde{k}_{c1}\tilde{k}_{c2}\tilde{k}_{p1}\tilde{k}_{p2}a^n + \tilde{k}_{d1}\tilde{k}_{d2}\tilde{k}_{d3}\tilde{k}_{d4}a < 0,$$

the negation of (A.13). Therefore, we do not find values for $a \geq X_a^{(d)}$ and $b \geq Y_a^{(d)}$ such that (A.10) and (A.11) are satisfied. Therefore, the rectangular domain Σ_R is unsuitable as an invariant region for the reaction-diffusion system (2.45).

Remark A.1. If we omit the assumptions $a \geq X_a^{(d)}$ and $b \geq Y_a^{(d)}$, i.e., the rectangular domain do not contain the death state, then, the domain Σ_R is an invariant region for the reaction-diffusion system (2.45) if the parameter a satisfies condition (A.13).

A.4 Finite Difference Method for the Radially Symmetric Reaction-Diffusion System

We introduce an implicit Euler scheme used for the numerical simulation in Section 2.8 in order to solve the radially symmetric reaction-diffusion system numerically. The reaction-diffusion system in short form is given by

$$\frac{\partial u}{\partial t} = \tilde{D}\Delta_x u + f(u), \; u = (X_a, Y_a, X_i, Y_i), \tag{A.15}$$

cf. equation (2.14), where $\tilde{D} = \text{diag}\{\tilde{D}_1, \tilde{D}_2, \tilde{D}_3, \tilde{D}_4\}$ is the diffusion matrix and the function $f(u)$ includes the reaction kinetics. Again, the variables x and t are in dimensionless form. The domain under consideration in the dimensionless case is $\Omega = \{x \in \mathbb{R}^d, \|x\|_2 \leq 1\}$, $d = 1, 2, 3$. Furthermore, we complete the system with homogeneous Neumann boundary conditions and initial conditions $u(x, 0) = u_0(x)$.

With the Laplace operator in polar coordinates, system (A.15) gets

$$\frac{\partial u}{\partial t} = \tilde{D}(\frac{1}{r^{d-1}}\frac{\partial}{\partial r}(r^{d-1}\frac{\partial u}{\partial r}) + T^{\dagger}(\frac{\partial u}{\partial \vartheta}, \frac{\partial^2 u}{\partial \vartheta^2}, \frac{\partial u}{\partial \psi}, \frac{\partial^2 u}{\partial \psi^2})) + f(u), \tag{A.16}$$

where $T^{\dagger}(\,\cdot\,)$ denotes the function which includes the angular dependent terms of the Laplace operator in polar coordinates.
In case of radial symmetric caspase concentrations, the function $T^{\dagger}(\,\cdot\,)$ vanishes and equation (A.16) is simplified to

$$\frac{\partial u}{\partial t} = \tilde{D}\frac{1}{r^{d-1}}\frac{\partial}{\partial r}(r^{d-1}\frac{\partial u}{\partial r}) + f(u) = \tilde{D}\left(\frac{\partial^2 u}{\partial r^2} + (d-1)\cdot\frac{1}{r}\frac{\partial u}{\partial r}\right) + f(u).$$

In order to discretize the spatial derivative, we apply the centered Finite Difference method. Let $0 = r_0 < r_1 < \cdots < r_M = 1$ be an equidistant discretization of the interval $[0,1]$ with the step size Δr and let $\tilde{u}(r,t)$ denote the approximation of the solution $u(r,t)$. We set $u_m := \tilde{u}(r_m, t)$ and then, the approximation of the second derivative of the approximating function $\tilde{u}(r,t)$ is given by

$$\frac{\partial^2 u}{\partial r^2} + (d-1)\frac{1}{r}\frac{\partial u}{\partial r} \approx \frac{u_{m+1} - 2u_m + u_{m-1}}{\Delta r^2} + \frac{d-1}{r_m}\cdot\frac{u_{m+1} - u_{m-1}}{2\Delta r},$$

$m = 1, \ldots, M-1$. In order to compute an approximation of the time dependent problem, we need a discretization of the time interval $[0,T]$, say $0 = t_0 < t_1 < \cdots < t_N = T$. Then, the approximation of the solution at the point r_m at time t_n is denoted with $u_m^n := \tilde{u}(r_m, t_n)$ and the time derivative is approximated by the difference quotient $(u_m^{n+1} - u_m^n)/\Delta t$, where Δt is the step size in time.
Finally, using an implicit Euler method, we obtain a Finite Difference scheme for the approximation $\tilde{u}(r,t)$ at the inner node m, $m = 1, \ldots, M-1$,

$$\frac{u_m^{n+1} - u_m^n}{\Delta t} = \tilde{D}(\frac{1}{\Delta r^2}(u_{m+1}^{n+1} - 2u_m^{n+1} + u_{m-1}^{n+1}) + \frac{d-1}{r_m}\frac{1}{2\Delta r}(u_{m+1}^{n+1} - u_{m-1}^{n+1})) + f(u_m^n).$$

The approximation of the solution at the boundaries is given by

$$\frac{u_0^{n+1} - u_0^n}{\Delta t} = \frac{2\tilde{D}}{\Delta r^2}(u_1^{n+1} - u_0^{n+1}) + f(u_0^n)$$

and

$$\frac{u_M^{n+1} - u_M^n}{\Delta t} = \frac{2\tilde{D}}{\Delta r^2}(u_{M-1}^{n+1} - u_M^{n+1}) + f(u_M^n)$$

due to the homogeneous Neumann boundary conditions. We finally obtain

$$
\begin{aligned}
&u_m^{n+1} - \tilde{D}\cdot\Delta t\cdot\Big(\frac{u_{m+1}^{n+1} - 2u_m^{n+1} + u_{m-1}^{n+1}}{\Delta r^2} + \frac{d-1}{r_m}\cdot\frac{u_{m+1}^{n+1} - u_{m-1}^{n+1}}{2\Delta r}\Big) = u_m^n + f(u_m^n)\cdot\Delta t\\
&u_M^{n+1} - 2\tilde{D}\cdot\frac{\Delta t}{\Delta r^2}\cdot(u_{M-1}^{n+1} - u_M^{n+1}) = u_M^n + f(u_M^n)\cdot\Delta t\\
&u_0^{n+1} - 2\tilde{D}\cdot\frac{\Delta t}{\Delta r^2}\cdot(u_1^{n+1} - u_0^{n+1}) = u_0^n + f(u_0^n)\cdot\Delta t.
\end{aligned}
$$

Introducing $\bar{u}^n := (u_0^n, u_1^n, \ldots, u_M^n)^\top$, this system can shortly be written in matrix form

$$
(\mathrm{Id} - \tilde{D}(A_h + B_h))\bar{u}^{n+1} = \bar{u}^n + \Delta t\cdot f(\bar{u}^n) \tag{A.17}
$$

with

$$
A_h = \frac{\Delta t}{\Delta r^2}\begin{pmatrix}
-2 & 2 & 0 & 0 & \ldots & 0\\
1 & -2 & 1 & 0 & \ldots & 0\\
0 & 1 & -2 & 1 & 0 & 0\\
\vdots & \ddots & \ddots & \ddots & \ddots & 0\\
0 & \ldots & 0 & 1 & -2 & 1\\
0 & \ldots & 0 & 0 & 2 & -2
\end{pmatrix}
$$

and

$$
B_h = (d-1)\cdot\frac{\Delta t}{2\Delta r}\begin{pmatrix}
0 & 0 & 0 & 0 & \ldots & 0\\
-\frac{1}{r_1} & 0 & \frac{1}{r_1} & 0 & \ldots & 0\\
0 & -\frac{1}{r_2} & 0 & \frac{1}{r_2} & 0 & 0\\
\vdots & \ddots & \ddots & \ddots & \ddots & 0\\
0 & \ldots & 0 & -\frac{1}{r_{M-1}} & 0 & \frac{1}{r_{M-1}}\\
0 & \ldots & 0 & 0 & 0 & 0
\end{pmatrix}.
$$

The approximation of the solution $\tilde{u}(r_m, t_n)$ is successively computed by solving the linear system (A.17). Since the matrices A_h and B_h are tridiagonal and thereby sparse, the storage of the matrix entries is cheap and the inverse of the matrix $(\mathrm{Id} - \tilde{D}(A_h + B_h))$ is computed efficiently. The code is implemented in Matlab.

A.5 Finite Difference Method for the Extended Reaction-Diffusion System

To solve the reaction-diffusion system (4.1) with boundary condition (4.2) numerically, we implement an implicit Euler scheme with a Finite Difference method for the spatial discretization, cf. [35]. Analogous to the derivation of the Euler scheme in Appendix A.4, we use the short form of the reaction-diffusion system

$$\frac{\partial u}{\partial t} = \tilde{D}\Delta_{\mathbf{x}} u + f(u),\ u = (X_a, Y_a, X_i, Y_i), \tag{A.18}$$

on the domain $\Omega = [0,1]^2$ and the boundary conditions read

$$\left.\frac{\partial u}{\partial n}\right|_{\partial\Omega} = \mu U(x_{\partial\Omega}, t) \cdot h(u) \tag{A.19}$$

with $h(u) = (u_3, 0, -u_3, 0)$. The function U describes the concentration of receptor clusters at the cell membrane and μ denotes the reaction rate for the activation of pro-caspase 8 by death receptors. In order to introduce a Finite Difference scheme for the Laplace operator in two dimensions, we first give a discretization of the domain Ω. The equidistant discretization in the x-direction is given by $0 = x_1 < x_2 < \cdots < x_N = 1$ and in the y-direction it is $0 = y_1 < y_2 < \cdots < y_M = 1$ with the step sizes Δx and Δy, see Figure A.1. Thus, the coordinates of a grid node are $(x_n, y_m), n = 1, \ldots, N, m = 1, \ldots, M$. Let $\tilde{u}((x,y),t)$ denote the approximation of the solution $u((x,y),t)$ and, by this, we set $u_{n,m} := \tilde{u}((x_n, y_m), t)$. Afterward, we define an equidistant discretization of the time interval $[0,T]$, i.e. $0 = t_1 < t_2 < \cdots < t_K = T$, with a step size Δt and the approximation at a grid node (x_n, y_m) at time t_k is written as $u^k_{n,m}$. With this notification, we obtain for the approximation of the Laplace operator with the help of a five-point stencil, cf. Figure A.1,

$$\begin{aligned}\Delta u((x_n, y_m), t_k) &= \frac{\partial^2}{\partial x^2} u((x_n, y_m), t_k) + \frac{\partial^2}{\partial y^2} u((x_n, y_m), t_k) \\ &\approx \frac{u^k_{n+1,m} - 2u^k_{n,m} + u^k_{n-1,m}}{\Delta x^2} + \frac{u^k_{n,m+1} - 2u^k_{n,m} + u^k_{n,m-1}}{\Delta y^2}.\end{aligned}$$

Using an implicit Euler method, we obtain a scheme for the computation of the approximation $\tilde{u}((x_n, y_m), t_k) = u^k_{n,m}$ at an inner node $(x_n, y_m), n = 2, \ldots, N-1, m = 2, \ldots, M-1$, namely

$$\frac{u^{k+1}_{n,m} - u^k_{n,m}}{\Delta t} = f(u^k_{n,m}) + \tilde{D}\left(\frac{u^{k+1}_{n+1,m} - 2u^{k+1}_{n,m} + u^{k+1}_{n-1,m}}{\Delta x^2} + \frac{u^{k+1}_{n,m+1} - 2u^{k+1}_{n,m} + u^{k+1}_{n,m-1}}{\Delta y^2}\right),$$

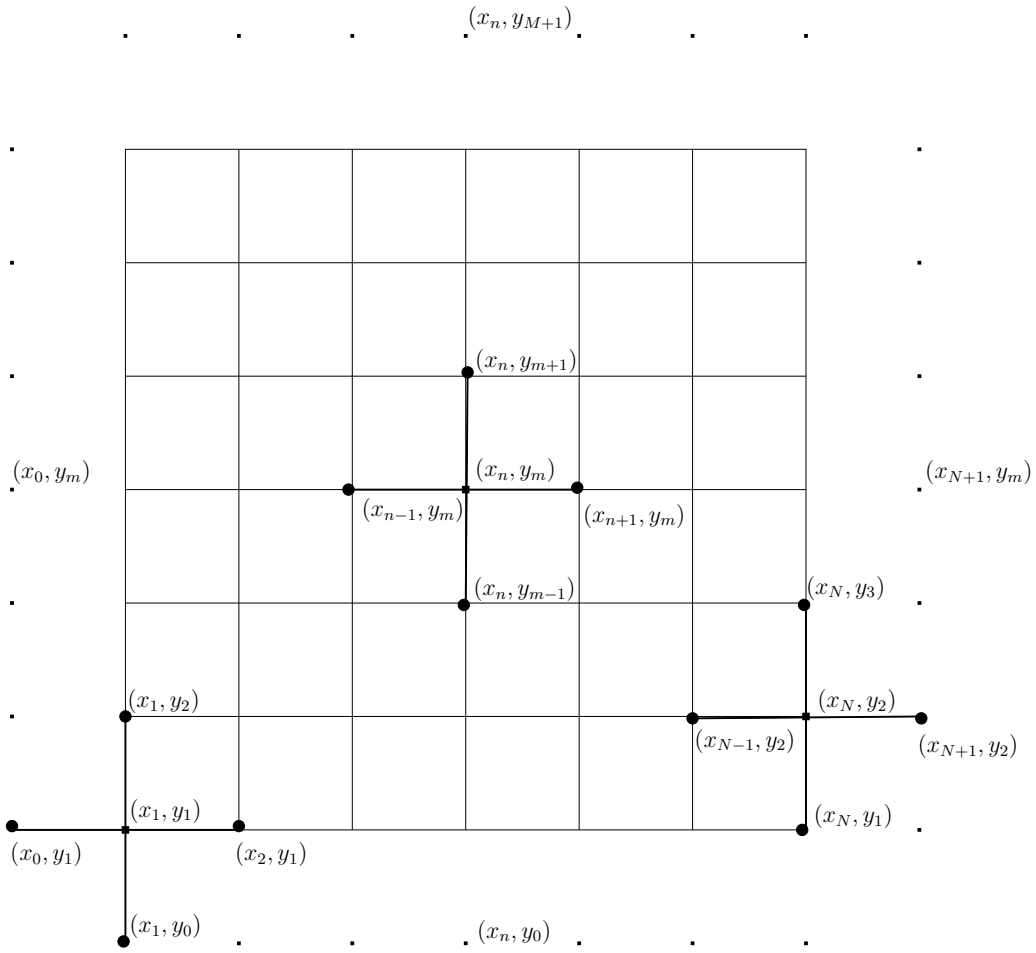

Figure A.1: Discretization of the domain $\Omega = [0,1]^2$ with the inner nodes (x_n, y_m), $n = 1, \ldots, N$, $m = 1, \ldots, M$, and the ghost nodes (x_0, y_m), (x_{N+1}, y_m), (x_n, y_0), (x_n, y_{M+1}), $n = 1, \ldots, N$, $m = 1, \ldots, M$. For the approximation of the Laplace operator, a five-point stencil is used, cf. [35].

$2 \leq n \leq N-1; 2 \leq m \leq M-1, 1 \leq k \leq K$. Sorting the equation leads to

$$u_{n,m}^{k+1} - \tilde{D}\frac{\Delta t}{\Delta x^2}(u_{n+1,m}^{k+1} - 2u_{n,m}^{k+1} + u_{n-1,m}^{k+1}) - \tilde{D}\frac{\Delta t}{\Delta y^2}(u_{n,m+1}^{k+1} - 2u_{n,m}^{k+1} + u_{n,m-1}^{k+1}) = u_{n,m}^{k} + \Delta t \cdot f(u_{n,m}^{k}). \tag{A.20}$$

To derive equations for the approximation at the boundary nodes, we introduce so-called ghost nodes $(x_0, y_m), (x_{N+1}, y_m), m = 1, \ldots, M$, and $(x_n, y_0), (x_n, y_{M+1}), n = 1, \ldots, N$, see Figure A.1. These nodes are located outside of the domain Ω and are required for the approximation of the boundary conditions. The function $U(x_{\partial\Omega}, t)$ evaluated at a grid node (x_n, y_m) is denoted as $\mathcal{U}_{n,m}^k := U((x_n, y_m), t_k)$. Using the ghost nodes we obtain at

the four edges of the domain Ω,

$$\begin{aligned}
\frac{u_{0,m}^{k+1} - u_{2,m}^{k+1}}{2\Delta x} &= \mu \cdot \mathcal{U}_{1,m}^{k} \cdot h(u_{1,m}^{k}),\\
\frac{u_{N+1,m}^{k+1} - u_{N-1,m}^{k+1}}{2\Delta x} &= \mu \cdot \mathcal{U}_{N,m}^{k} \cdot h(u_{N,m}^{k}),\\
\frac{u_{n,0}^{k+1} - u_{n,2}^{k+1}}{2\Delta y} &= \mu \cdot \mathcal{U}_{n,1}^{k} \cdot h(u_{n,1}^{k}),\\
\frac{u_{n,M+1}^{k+1} - u_{n,M-1}^{k+1}}{2\Delta y} &= \mu \cdot \mathcal{U}_{n,M}^{k} \cdot h(u_{n,M}^{k}),
\end{aligned}$$

$n = 1, \ldots, N; m = 1, \ldots, M$. Then, we express the approximation of the solution at the ghost nodes through the approximation of the solution at an inner node

$$\begin{aligned}
u_{0,m}^{k+1} &= u_{2,m}^{k+1} + 2\Delta x \cdot \mu \cdot \mathcal{U}_{1,m}^{k} \cdot h(u_{1,m}^{k}),\\
u_{N+1,m}^{k+1} &= u_{N-1,m}^{k+1} + 2\Delta x \cdot \mu \cdot \mathcal{U}_{N,m}^{k} \cdot h(u_{N,m}^{k}),\\
u_{n,0}^{k+1} &= u_{n,2}^{k+1} + 2\Delta y \cdot \mu \cdot \mathcal{U}_{n,1}^{k} \cdot h(u_{n,1}^{k}),\\
u_{n,M+1}^{k+1} &= u_{n,M-1}^{k+1} + 2\Delta y \cdot \mu \cdot \mathcal{U}_{n,M}^{k} \cdot h(u_{n,M}^{k}),
\end{aligned} \tag{A.21}$$

$n = 1, \ldots, N; m = 1, \ldots, M$. We put the conditions for the ghost nodes into the approximation of the Laplace operator at the edges and present the derivation for the edge $\{(0, y), y \in [0, 1]\}$ in detail and transfer the result to the other edges and vertexes. We have

$$\begin{aligned}
&u_{1,m}^{k+1} - \tilde{D}\frac{\Delta t}{\Delta x^2}(u_{2,m}^{k+1} - 2u_{1,m}^{k+1} + u_{0,m}^{k+1})\\
&\quad - \tilde{D}\frac{\Delta t}{\Delta y^2}(u_{1,m+1}^{k+1} - 2u_{1,m}^{k+1} + u_{1,m-1}^{k+1}) = u_{1,m}^{k} + \Delta t \cdot f(u_{1,m}^{k}),
\end{aligned}$$

and with (A.21) we obtain

$$\begin{aligned}
&u_{1,m}^{k+1} - \tilde{D}\frac{\Delta t}{\Delta x^2}(u_{2,m}^{k+1} - 2u_{1,m}^{k+1} + u_{2,m}^{k+1} + 2\Delta x \cdot \mu \cdot \mathcal{U}_{1,m}^{k} \cdot h(u_{1,m}^{k}))\\
&\quad - \tilde{D}\frac{\Delta t}{\Delta y^2}(u_{1,m+1}^{k+1} - 2u_{1,m}^{k+1} + u_{1,m-1}^{k+1}) = u_{1,m}^{k} + \Delta t \cdot f(u_{1,m}^{k}).
\end{aligned}$$

Sorting the equation with respect to time yields

$$\begin{aligned}
&u_{1,m}^{k+1} - \tilde{D}\frac{\Delta t}{\Delta x^2}(2u_{2,m}^{k+1} - 2u_{1,m}^{k+1}) - \tilde{D}\frac{\Delta t}{\Delta y^2}(u_{1,m+1}^{k+1} - 2u_{1,m}^{k+1} + u_{1,m-1}^{k+1})\\
&\quad = u_{1,m}^{k} + \Delta t \cdot f(u_{1,m}^{k}) + \tilde{D}\frac{2\Delta t}{\Delta x} \cdot \mu \cdot \mathcal{U}_{1,m}^{k} \cdot h(u_{1,m}^{k}),
\end{aligned} \tag{A.22}$$

$m = 2, \ldots, M-1$. At the other edges we obtain

$$u_{N,m}^{k+1} - \tilde{D}\frac{\Delta t}{\Delta x^2}(2u_{N-1,m}^{k+1} - 2u_{N,m}^{k+1}) - \tilde{D}\frac{\Delta t}{\Delta y^2}(u_{N,m+1}^{k+1} - 2u_{N,m}^{k+1} + u_{N,m-1}^{k+1}) = u_{N,m}^{k} + \Delta t \cdot f(u_{N,m}^{k}) + \tilde{D}\frac{2\Delta t}{\Delta x} \cdot \mu \cdot \mathcal{U}_{N,m}^{k} \cdot h(u_{N,m}^{k}), \tag{A.23}$$

$$u_{n,1}^{k+1} - \tilde{D}\frac{\Delta t}{\Delta x^2}(u_{n+1,1}^{k+1} - 2u_{n,1}^{k+1} + u_{n-1,1}^{k+1}) - \tilde{D}\frac{\Delta t}{\Delta y^2}(2u_{n,2}^{k+1} - 2u_{n,1}^{k+1}) = u_{n,1}^{k} + \Delta t \cdot f(u_{n,1}^{k}) + \tilde{D}\frac{2\Delta t}{\Delta y} \cdot \mu \cdot \mathcal{U}_{n,1}^{k} \cdot h(u_{n,1}^{k}), \tag{A.24}$$

$$u_{n,M}^{k+1} - \tilde{D}\frac{\Delta t}{\Delta x^2}(u_{n+1,M}^{k+1} - 2u_{n,M}^{k+1} + u_{n-1,M}^{k+1}) - \tilde{D}\frac{\Delta t}{\Delta y^2}(2u_{n,M-1}^{k+1} - 2u_{n,M}^{k+1}) = u_{n,M}^{k} + \Delta t \cdot f(u_{n,M}^{k}) + \tilde{D}\frac{2\Delta t}{\Delta y} \cdot \mu \cdot \mathcal{U}_{n,M}^{k} \cdot h(u_{n,M}^{k}), \tag{A.25}$$

$n = 2, \ldots, N-1; m = 2, \ldots, M-1$. In the vertexes, the five-point stencil contains two ghost nodes. The substitution of both ghost nodes at each vertex leads to

$$u_{1,1}^{k+1} - \tilde{D}\frac{\Delta t}{\Delta x^2}(2u_{2,1}^{k+1} - 2u_{1,1}^{k+1}) - \tilde{D}\frac{\Delta t}{\Delta y^2}(2u_{1,2}^{k+1} - 2u_{1,1}^{k+1}) = u_{1,1}^{k} + \Delta t \cdot f(u_{1,1}^{k}) + \tilde{D}(\frac{2\Delta t}{\Delta x} + \frac{2\Delta t}{\Delta y}) \cdot \mu \cdot \mathcal{U}_{1,1}^{k} \cdot h(u_{1,1}^{k}), \tag{A.26}$$

$$u_{N,1}^{k+1} - \tilde{D}\frac{\Delta t}{\Delta x^2}(2u_{N-1,1}^{k+1} - 2u_{N,1}^{k+1}) - \tilde{D}\frac{\Delta t}{\Delta y^2}(2u_{N,2}^{k+1} - 2u_{N,1}^{k+1}) = u_{N,1}^{k} + \Delta t \cdot f(u_{N,1}^{k}) + \tilde{D}(\frac{2\Delta t}{\Delta x} + \frac{2\Delta t}{\Delta y}) \cdot \mu \cdot \mathcal{U}_{N,1}^{k} \cdot h(u_{N,1}^{k}), \tag{A.27}$$

$$u_{1,M}^{k+1} - \tilde{D}\frac{\Delta t}{\Delta x^2}(2u_{2,M}^{k+1} - 2u_{1,M}^{k+1}) - \tilde{D}\frac{\Delta t}{\Delta y^2}(2u_{1,M-1}^{k+1} - 2u_{1,M}^{k+1}) = u_{1,M}^{k} + \Delta t \cdot f(u_{1,M}^{k}) + \tilde{D}(\frac{2\Delta t}{\Delta x} + \frac{2\Delta t}{\Delta y}) \cdot \mu \cdot \mathcal{U}_{1,M}^{k} \cdot h(u_{1,M}^{k}), \tag{A.28}$$

$$u_{N,M}^{k+1} - \tilde{D}\frac{\Delta t}{\Delta x^2}(2u_{N-1,M}^{k+1} - 2u_{N,M}^{k+1}) - \tilde{D}\frac{\Delta t}{\Delta y^2}(2u_{N,M-1}^{k+1} - 2u_{N,M}^{k+1}) = u_{N,M}^{k} + \Delta t \cdot f(u_{N,M}^{k}) + \tilde{D}(\frac{2\Delta t}{\Delta x} + \frac{2\Delta t}{\Delta y}) \cdot \mu \cdot \mathcal{U}_{N,M}^{k} \cdot h(u_{N,M}^{k}). \tag{A.29}$$

We introduce the vector

$$\bar{u}^k = (u_{1,1}^k, u_{2,1}^k, \ldots, u_{N,1}^k, u_{1,2}^k, \ldots, u_{N,2}^k, \ldots, u_{1,M}^k, \ldots, u_{N,M}^k)^\top$$

and obtain a linear algebraic system for $\bar{u}^{k+1}$, namely

$$\tilde{A}_h \bar{u}^{k+1} = \bar{u}^k + F(\bar{u}^k) \cdot \Delta t + \bar{h}(\bar{u}^k) \cdot \Delta t, \tag{A.30}$$

where the matrix $\tilde{A}_h$ is assembled according to the equations (A.20)-(A.29), the function $\bar{h}$ contains the boundary conditions at the edges and the vertices and the components of the vector F are given by the function f evaluated at the grid nodes.

Thus, given a certain initial condition, the linear system (A.30) is solved for each time step $t_k, k = 1, \ldots, K$, that yields the time evolution of the caspase concentrations in the cell.

Symbols for the Reaction-Diffusion System

A_h	matrix for a discretization of the radially symmetric Laplace operator	146
B_h	matrix for a discretization of the radially symmetric Laplace operator	146
D_{GFP}	diffusion coefficient of the molecule GFP	139
D_n	diffusion coefficient of an arbitrary molecule	139
D	diffusion matrix for the reaction-diffusion system	15
G_i	functions describing the boundary of Σ	33
$J\|_{X^*}$	Jacobian matrix of the reaction system evaluated at X^*	18
L	length scale	14
$M(\lambda_k)$	matrix defined by $\tilde{A} - \lambda_k \tilde{D}$	22
N_A	Avogadro's constant	19
N_{C3^*}	number of molecules of active caspase 3	46
N_{C8^*}	number of molecules of active caspase 8	46
N_{mol}	number of molecules	19
R_0	radius of the domain $\bar{\Omega}_{\mathrm{in}}$	15
R_c^{1d}	value of R_c in case $d = 1$	46
R_c^{2d}	value of R_c in case $d = 2$	46
R_c^{3d}	value of R_c in case $d = 3$	46
R_c	critical value for the size of the initial death region	46
R	radius of the cell in case of a large spatial scale	50
U	function describing the concentration of receptor clusters on the cell membrane	147
V	notation of a volume of a domain	19
$X^{(d)}$	death state of the reaction system	18
$X^{(l)}$	life state of the reaction system	18
$X^{(u)}$	transition state of the reaction system	18

X^*	steady state of the reaction system	16
X_a	caspase 8 concentration	12
X_i	pro-caspase 8 concentration	12
Y_a	caspase 3 concentration	12
Y_i	pro-caspase 3 concentration	12
Δr	step size of the spatial discretization for the radially symmetric RDS	145
Δt	step size of the time discretization	145
Δx	step size of the discretization in x-direction for two-dimensional RDS	147
Δy	step size of the discretization in y-direction for two-dimensional RDS	147
Ω	domain modeling the cell	14
Σ_R	unsuitable invariant region for the reaction-diffusion system	32
Σ	invariant region for the reaction-diffusion system	33
α	unstable steady state for the Fitzhugh-Nagumo equation	52
$\bar{\Omega}_{\text{in}}$	part of $\bar{\Omega}$ initally filled with the "life state"	15
$\bar{\Omega}_{\text{ext}}$	part of $\bar{\Omega}$ initally filled with the "death state"	15
$\bar{\Omega}$	dimensionless domain	14
$\bar{c}$	dimensionless velocity of the traveling wave solution	52
$\bar{t}$	dimensionless time coordinate for the reaction-diffusion system	14
$\bar{u}^k$	vector with the approximation of the solution at all nodes ($d = 2$)	150
$\bar{u}^n$	vector with the approximation of the solution at all nodes ($d = 1$)	146
$\bar{x}$	dimensionless spatial coordinate for the reaction-diffusion system	14
λ_k	eigenvalues of the Laplace operator in case $d = 1$	22
$\lambda_{\nu,\iota}$	eigenvalues of the Laplace operator in case $d = 2$	26
$\lambda_i^{(d)}$	eigenvalues of the Jacobian matrix for the death state	19
$\lambda_i^{(l)}$	eigenvalues of the Jacobian matrix for the life state	19
$\lambda_i^{(u)}$	eigenvalues of the Jacobian matrix for the transition state	19
$\mathcal{A}$	general elliptic differential operator	30
$\mathcal{B}$	general boundary value operator	30
$\mathcal{G}$	open subset of $\mathbb{R}^N$	30
$\mathcal{M}$	maximum of the maximum norm of the Jacobian matrix	43
$\mathcal{R}$	function describing the switch-like behavior on a large spatial scale	59
$\mathcal{U}_{n,m}^k$	function U evaluated at a grid node (x_n, y_m) at time t_k	148
$\mathcal{V}$	$\{v \in H^{1,p}(\Omega, \mathbb{R}^N), v(\Omega) \subset \mathcal{G}\}$	30
m_{C3^*}	mass of caspase 3	140
m_{C3}	mass of pro-caspase 3	140

m_{C8^*}	mass of caspase 8	140
m_{C8}	mass of pro-caspase 8	140
$\mathrm{m}_{\mathrm{GFP}}$	mass of the molecule GFP	139
$\mu_i(\lambda_k)$	eigenvalues of the matrix $M(\lambda_k)$	22
$\mu_i^{(d)}(\lambda_k)$	eigenvalues of the matrix $M(\lambda_k)$ for the death state ($d = 1$)	24
$\mu_i^{(d)}(\lambda_{\nu,\iota})$	eigenvalues of the matrix $M(\lambda_{\nu,\iota})$ for the death state ($d = 2$)	28
$\mu_i^{(l)}(\lambda_k)$	eigenvalues of the matrix $M(\lambda_k)$ for the life state ($d = 1$)	23
$\mu_i^{(l)}(\lambda_{\nu,\iota})$	eigenvalues of the matrix $M(\lambda_{\nu,\iota})$ for the life state ($d = 2$)	27
$\mu_i^{(u)}(\lambda_k)$	eigenvalues of the matrix $M(\lambda_k)$ for the transition state ($d = 1$)	24
$\mu_i^{(u)}(\lambda_{\nu,\iota})$	eigenvalues of the matrix $M(\lambda_{\nu,\iota})$ for the transition state ($d = 2$)	27
μ	reaction rate for the activation of pro-caspase 8 by death receptors	147
σ	rate for the exponential decay of the gradient in the concentrations	43
τ	time scale	14
$\tilde{A}_h$	matrix for a five-point stencil discretization of the Laplace operator	151
$\tilde{A}$	Jacobian matrix of $\tilde{f}$	21
$\tilde{D}$	modified diffusion matrix for the reaction-diffusion system	16
$\tilde{d}$	smallest eigenvalue of the diffusion matrix $\tilde{D}$	43
$\tilde{f}$	transformation of the function f	21
$\tilde{g}$	function containing the h.o.t. of the linearization of the function $\tilde{f}$	21
$\tilde{k}_{c1}$	dimensionless reaction rate for activation of pro-caspase 8	14
$\tilde{k}_{c2}$	dimensionless reaction rate for activation of pro-caspase 3	14
$\tilde{k}_{dj}$	dimensionless degradation rates for (pro-) caspase 3/8	14
$\tilde{k}_{pi}$	dimensionless production rates for (pro-) caspase 3/8	14
$\tilde{u}((x, y), t)$	approximation of the solution $u((x, y), t)$ of the RDS ($d = 2$)	147
φ_k	eigenfunctions of the Laplace operator in case $d = 1$	22
ζ	first nonzero eigenvalue of the Laplace operator	43
c_{phys}	physical velocity of the traveling wave solution	52
c	general notation for caspase concentrations	19
d_1	diffusion coefficient for caspase 8	14
d_2	diffusion coefficient for caspase 3	14
d_3	diffusion coefficient for pro-caspase 8	14
d_4	diffusion coefficient for pro-caspase 3	14
d	dimension of the domain	13
f	short notation of the reaction kinetics in the reaction system	13
$j_{\nu,\iota}$	ιth zero of the first derivative of the νth Bessel function	26

k_{c1}	reaction rate for activation of pro-caspase 8	12
k_{c2}	reaction rate for activation of pro-caspase 3	12
k_{d1}	degradation rate for caspase 8	12
k_{d2}	degradation rate for caspase 3	12
k_{d3}	degradation rate for pro-caspase 8	12
k_{d4}	degradation rate for pro-caspase 3	12
k_{p1}	production rate for pro-caspase 8	12
k_{p2}	production rate for pro-caspase 3	12
n	exponent describing cooperativity effects in the reaction kinetics	12
r^*	radius of the domain initially filled with death state	57
$r_{d,\cdot}$	value of r^* for which the formation of a traveling wave succeeds	57
$r_{l,\cdot}$	value of r^* for which the formation of a traveling wave fails	57
t^*	stopping time for the simulation of the reaction system	45
t^d	"death time"	45
t^l	"life time"	45
u_0	initial condition for reaction-diffusion system	16
u_m^n	approximation of the solution at the node r_m at time t_n	145
$u_{n,m}^k$	approximation of the solution at a grid point (x_n, y_m) at time t_k	147
u	function with components $X_a(x,t), Y_a(x,t), X_i(x,t), Y_i(x,t)$	15
v	vector valued function with components $X_a(t), Y_a(t), X_i(t), Y_i(t)$	13
x	spatial coordinate for the reaction-diffusion system	13
$z(x,t)$	linear substitution of the vector-valued function $u(x,t)$	21

Symbols for the Receptorclustering

D_r	proportionality constant	72
D_{drill}	external torsional moment of a particle	71
D_{fric}	friction torsional moment of a particle	71
D	torsional moment of a particle	71
$H(\cdot)$	Heaviside function	78
I	moment of inertia of a particle	71
L	length scale of the cell	68
N_1	standard Gaussian random variable	93
N_2	standard Gaussian random variable	93
$R_{\mathrm{D}_i;\mathrm{L}_k}$	distance between the centers of mass of D_i and L_k	80
$R_{\mathrm{L}_i;\mathrm{D}_k}$	distance between the centers of mass of L_i and D_k	84
$R_{\mathrm{L}_i;\mathrm{M}_k}$	distance between the centers of mass of L_i and M_k	84
$R_{\mathrm{L}_i;\mathrm{T}_k}$	distance between the centers of mass of L_i and T_k	84
$R_{\mathrm{M}_i;\mathrm{L}_k}$	distance between the centers of mass of M_i and L_k	78
$R_{\mathrm{M}_i;\mathrm{M}_k}$	distance between the centers of mass of M_i and M_k	78
$R_{\mathrm{T}_i;\mathrm{L}_k}$	distance between the centers of mass of T_i and L_k	82
$R_{\mathrm{U}_i;\mathrm{U}_k}$	distance between the centers of mass of U_i and U_k	86
R	radius of a particle	68
T	temperature	68
$V_{\mathrm{LJ}}^{\mathrm{P}}$	Lennard-Jones potential	70
Z_n	$\mathcal{N}(0,1)$ distributed random variable	92
D	notation for a death receptor dimer	76
L	notation for a death receptor ligand	76
Λ_{D_i}	set containing the directions of the binding sites of D_i	80
Λ_{L_k}	set containing the directions of the binding sites of L_k	77
Λ_{T_i}	set containing the directions of the binding sites of T_i	82
Λ_{U_k}	set containing the directions of the binding sites of U_k	86

M	notation for a death receptor monomer	76
T	notation for a death receptor trimer	76
U	notation for a cluster unit	76
$\bar{V}_{\mathrm{LJ}}^{\mathrm{P}}$	dimensionless Lennard-Jones potential	70
$\bar{W}_{\mathrm{LJ}}^{\mathrm{P}}$	repulsive part of the dimensionless Lennard-Jones potential	71
$\bar{\mathbf{F}}_{\mathrm{D}_i}$	dimensionless force acting on a death receptor dimer D_i	79
$\bar{\mathbf{F}}_{\mathrm{L}_i}$	dimensionless force acting on a death receptor ligand L_i	83
$\bar{\mathbf{F}}_{\mathrm{M}_i}$	dimensionless force acting on a death receptor monomer M_i	77
$\bar{\mathbf{F}}_{\mathrm{T}_i}$	dimensionless force acting on a death receptor trimer T_i	81
$\bar{\mathbf{F}}_{\mathrm{U}_i}$	dimensionless force acting on a cluster unit U_i	86
$\bar{\mathbf{F}}_{\mathrm{interact}}$	dimensionless interaction force	68
$\bar{\mathbf{v}}$	dimensionless particle velocity	68
$\bar{\mathbf{x}}$	dimensionless particle coordinates	68
$\bar{\omega}$	angular velocity of a particle in dimensionless form	72
$\bar{\sigma}_{\mathrm{LJ}}^{\mathrm{P}}$	dimensionless parameter in Lennard-Jones potential for particle size	70
$\bar{\varphi}$	dimensionless angle of rotation of a particle	72
$\bar{r}$	dimensionless distance between two particles	70
$\bar{t}$	dimensionless time coordinate	68
β	friction coefficient for particle translation	68
$\bar{\boldsymbol{\varphi}}_{\mathrm{D}}$	vector with angles of death receptor dimers	76
$\bar{\boldsymbol{\varphi}}_{\mathrm{L}}$	vector with angles of death receptor ligands	76
$\bar{\boldsymbol{\varphi}}_{\mathrm{M}}$	vector with angles of death receptor monomers	76
$\bar{\boldsymbol{\varphi}}_{\mathrm{T}}$	vector with angles of death receptor trimers	76
$\bar{\boldsymbol{\varphi}}_{\mathrm{U}}$	vector with angles of cluster units	76
$\bar{\varphi}_{\mathrm{D}_i;\mathrm{L}_k}$	angle of the binding site of D_i minimizing the distance to $\mathbf{e}_{\mathrm{D}_i\mathrm{L}_k}$	80
$\bar{\varphi}_{\mathrm{D}_k;\mathrm{L}_i}$	angle of the binding site of D_k minimizing the distance to $\mathbf{e}_{\mathrm{D}_k\mathrm{L}_i}$	83
$\bar{\varphi}_{\mathrm{L}_k;\mathrm{D}_i}$	angle of the binding site of L_k minimizing the distance to $\mathbf{e}_{\mathrm{L}_k\mathrm{D}_i}$	79
$\bar{\varphi}_{\mathrm{L}_k;\mathrm{M}_i}$	angle of the binding site of L_k minimizing the distance to $\mathbf{e}_{\mathrm{L}_k\mathrm{M}_i}$	77
$\bar{\varphi}_{\mathrm{L}_k;\mathrm{T}_i}$	angle of the binding site of L_k minimizing the distance to $\mathbf{e}_{\mathrm{L}_k\mathrm{T}_i}$	81
$\bar{\varphi}_{\mathrm{T}_k;\mathrm{L}_i}$	angle of the binding site of T_k minimizing the distance to $\mathbf{e}_{\mathrm{T}_k\mathrm{L}_i}$	83
$\bar{\varphi}_{\mathrm{U}_k;\mathrm{U}_i}$	angle of the binding site of U_k minimizing the distance to $\mathbf{e}_{\mathrm{U}_k\mathrm{U}_i}$	86
$\bar{\varphi}_{\mathbf{e}_{\mathrm{D}_k\mathrm{L}_i}}$	angle between $\mathbf{e}_{\mathrm{D}_k\mathrm{L}_i}$ and the positive real line	83
$\bar{\varphi}_{\mathbf{e}_{\mathrm{L}_k\mathrm{D}_i}}$	angle between $\mathbf{e}_{\mathrm{L}_k\mathrm{D}_i}$ and the positive real line	79
$\bar{\varphi}_{\mathbf{e}_{\mathrm{L}_k\mathrm{M}_i}}$	angle between $\mathbf{e}_{\mathrm{L}_k\mathrm{M}_i}$ and the positive real line	77
$\bar{\varphi}_{\mathbf{e}_{\mathrm{L}_k\mathrm{T}_i}}$	angle between $\mathbf{e}_{\mathrm{L}_k\mathrm{T}_i}$ and the positive real line	81

$\bar{\varphi}_{\mathbf{e}_{\mathrm{M}_k\mathrm{L}_i}}$	angle between $\mathbf{e}_{\mathrm{M}_k\mathrm{L}_i}$ and the positive real line	83
$\bar{\varphi}_{\mathbf{e}_{\mathrm{M}_k\mathrm{M}_i}}$	angle between $\mathbf{e}_{\mathrm{M}_k\mathrm{M}_i}$ and the positive real line	77
$\bar{\varphi}_{\mathbf{e}_{\mathrm{T}_k\mathrm{L}_i}}$	angle between $\mathbf{e}_{\mathrm{T}_k\mathrm{L}_i}$ and the positive real line	83
$\bar{\varphi}_{\mathbf{e}_{\mathrm{U}_k\mathrm{U}_i}}$	angle between $\mathbf{e}_{\mathrm{U}_k\mathrm{U}_i}$ and the positive real line	86
δ	apex angle of the binding sites	78
η	viscosity of the cell membrane	68
γ_{rot}	friction coefficient for the particle rotation	71
κ	proportionality constant	72
$\mathbf{F}_{\mathrm{fric}}$	friction force	68
$\mathbf{F}_{\mathrm{interact}}$	interaction force	68
$\mathbf{F}$	general notation for a force	68
$\mathbf{e}_{\mathrm{D}_k\mathrm{D}_i}$	vector connecting the centers of mass of D_k and D_i	79
$\mathbf{e}_{\mathrm{D}_k\mathrm{L}_i}$	vector connecting the centers of mass of D_k and L_i	83
$\mathbf{e}_{\mathrm{D}_k\mathrm{M}_i}$	vector connecting the centers of mass of D_k and M_i	77
$\mathbf{e}_{\mathrm{L}_k\mathrm{D}_i}$	vector connecting the centers of mass of L_k and D_i	79
$\mathbf{e}_{\mathrm{L}_k\mathrm{L}_i}$	vector connecting the centers of mass of L_k and L_i	83
$\mathbf{e}_{\mathrm{L}_k\mathrm{M}_i}$	vector connecting the centers of mass of L_k and M_i	77
$\mathbf{e}_{\mathrm{L}_k\mathrm{T}_i}$	vector connecting the centers of mass of L_k and T_i	81
$\mathbf{e}_{\mathrm{M}_i\mathrm{L}_k}$	vector connecting the centers of mass of M_i and L_k	78
$\mathbf{e}_{\mathrm{M}_i\mathrm{M}_k}$	vector connecting the centers of mass of M_i and M_k	78
$\mathbf{e}_{\mathrm{M}_k\mathrm{D}_i}$	vector connecting the centers of mass of M_k and D_i	79
$\mathbf{e}_{\mathrm{M}_k\mathrm{L}_i}$	vector connecting the centers of mass of M_k and L_i	83
$\mathbf{e}_{\mathrm{M}_k\mathrm{M}_i}$	vector connecting the centers of mass of M_k and M_i	77
$\mathbf{e}_{\mathrm{T}_k\mathrm{L}_i}$	vector connecting the centers of mass of T_k and L_i	83
$\mathbf{e}_{\mathrm{T}_k\mathrm{T}_i}$	vector connecting the centers of mass of T_k and T_i	81
$\mathbf{e}_{\mathrm{U}_k\mathrm{U}_i}$	vector connecting the centers of mass of U_k and U_i	86
$\mathbf{p}$	momentum of a particle	68
$\mathbf{v}$	particle velocity	68
$\mathbf{x}$	particle coordinates	68
$\mathcal{L}$	angular momentum of a particle	71
$\mathcal{V}_1$	i.i.d. random variable on $[0,1]$	93
$\mathcal{V}_2$	i.i.d. random variable on $[0,1]$	93
$\mathrm{d}\widetilde{W}_{\mathrm{rot},\bar{t}}$	increment of the Wiener process for the particle rotation	73
$\mathrm{d}\widetilde{\mathbf{W}}_{\mathrm{trans},\bar{t}}$	increment of the Wiener process for the particle translation	69
μ	parameter which summarizes other parameters	69

ω	angular velocity of a particle	71
$\psi_{\mathrm{D}_i;\mathrm{L}_k}$	angle between $\mathbf{e}_{\mathrm{D}_i\mathrm{L}_k}$ and the nearest binding site of D_i	80
$\psi_{\mathrm{D}_k;\mathrm{L}_i}$	$\bar{\varphi}_{\mathbf{e}_{\mathrm{D}_k\mathrm{L}_i}} - \bar{\varphi}_{\mathrm{D}_k;\mathrm{L}_i}$	83
$\psi_{\mathrm{L}_i;\mathrm{D}_k}$	angle between $\mathbf{e}_{\mathrm{L}_i\mathrm{D}_k}$ and the nearest binding site of L_i	84
$\psi_{\mathrm{L}_i;\mathrm{M}_k}$	angle between $\mathbf{e}_{\mathrm{L}_i\mathrm{M}_k}$ and the nearest binding site of L_i	84
$\psi_{\mathrm{L}_i;\mathrm{T}_k}$	angle between $\mathbf{e}_{\mathrm{L}_i\mathrm{T}_k}$ and the nearest binding site of L_i	84
$\psi_{\mathrm{L}_k;\mathrm{D}_i}$	$\bar{\varphi}_{\mathbf{e}_{\mathrm{L}_k\mathrm{D}_i}} - \bar{\varphi}_{\mathrm{L}_k;\mathrm{D}_i}$	79
$\psi_{\mathrm{L}_k;\mathrm{M}_i}$	$\bar{\varphi}_{\mathbf{e}_{\mathrm{L}_k\mathrm{M}_i}} - \bar{\varphi}_{\mathrm{L}_k;\mathrm{M}_i}$	77
$\psi_{\mathrm{L}_k;\mathrm{T}_i}$	$\bar{\varphi}_{\mathbf{e}_{\mathrm{L}_k\mathrm{T}_i}} - \bar{\varphi}_{\mathrm{L}_k;\mathrm{T}_i}$	81
$\psi_{\mathrm{M}_i;\mathrm{L}_k}$	angle between $\mathbf{e}_{\mathrm{M}_i\mathrm{L}_k}$ and the binding site of M_i for ligands	78
$\psi_{\mathrm{M}_i;\mathrm{M}_k}$	angle between $\mathbf{e}_{\mathrm{M}_i\mathrm{M}_k}$ and the binding site of M_i for monomers	78
$\psi_{\mathrm{M}_k;\mathrm{L}_i}$	angle between $\mathbf{e}_{\mathrm{M}_k\mathrm{L}_i}$ and the binding site of M_k for ligands	83
$\psi_{\mathrm{M}_k;\mathrm{M}_i}$	angle between $\mathbf{e}_{\mathrm{M}_k\mathrm{M}_i}$ and the binding site of M_k for monomers	77
$\psi_{\mathrm{T}_i;\mathrm{L}_k}$	angle between $\mathbf{e}_{\mathrm{T}_i\mathrm{L}_k}$ and the nearest binding site of T_i	82
$\psi_{\mathrm{T}_k;\mathrm{L}_i}$	$\bar{\varphi}_{\mathbf{e}_{\mathrm{T}_k\mathrm{L}_i}} - \bar{\varphi}_{\mathrm{T}_k;\mathrm{L}_i}$	83
$\psi_{\mathrm{U}_i;\mathrm{U}_k}$	angle between $\mathbf{e}_{\mathrm{U}_i\mathrm{U}_k}$ and the nearest binding site of U_i	86
$\psi_{\mathrm{U}_k;\mathrm{U}_i}$	$\bar{\varphi}_{\mathbf{e}_{\mathrm{U}_k\mathrm{U}_i}} - \bar{\varphi}_{\mathrm{U}_k;\mathrm{U}_i}$	86
$\sigma_{\mathrm{LJ}}^{\mathrm{P}}$	parameter in the Lennard-Jones potential describing the particle size	70
σ_{trans}	fluctuation of the random force $\tilde{\mathbf{X}}_t$	68
τ	time scale	68
$\tilde{D}_t$	random torsional moment	71
$\tilde{\mathbf{X}}_t$	random force	68
$\varepsilon_{\mathrm{RL}}$	binding energy of a death receptor and a death receptor ligand	69
$\varepsilon_{\mathrm{RR}}$	binding energy of two death receptors	69
ε	binding energy of two particles	68
φ	angle of rotation of a particle	71
$\widetilde{W}_{\mathrm{rot}}$	Wiener process for the particle rotation	73
$\widetilde{\mathbf{W}}_{\mathrm{trans}}$	Wiener process for the particle translation	69
$\bar{\boldsymbol{\xi}}_{\mathrm{D}}$	array with coordinates of death receptor dimers	76
$\bar{\boldsymbol{\xi}}_{\mathrm{L}}$	array with coordinates of death receptor ligands	76
$\bar{\boldsymbol{\xi}}_{\mathrm{M}}$	array with coordinates of death receptor monomers	76
$\bar{\boldsymbol{\xi}}_{\mathrm{T}}$	array with coordinates of death receptor trimers	76
$\bar{\boldsymbol{\xi}}_{\mathrm{U}}$	array with coordinates of cluster units	76
ζ	parameter which summarizes other parameters	73
$g(\bar{\mathbf{x}}, \bar{\varphi})$	function for averaging the mutual disorientation of nearby particles	72

g_{D_i}	function $g(\bar{\mathbf{x}}, \bar{\varphi})$ for a death receptor dimer D_i	80
g_{L_i}	function $g(\bar{\mathbf{x}}, \bar{\varphi})$ for a death receptor ligand L_i	84
g_{M_i}	function $g(\bar{\mathbf{x}}, \bar{\varphi})$ for a death receptor monomer M_i	78
g_{T_i}	function $g(\bar{\mathbf{x}}, \bar{\varphi})$ for a death receptor trimer T_i	82
g_{U_i}	function $g(\bar{\mathbf{x}}, \bar{\varphi})$ for a cluster unit U_i	87
k_B	Boltzmann constant	68
l	length of a grid cell of the domain decomposition	94
m_{ligand}	mass of death receptor ligands	68
m_{receptor}	mass of death receptors	68
m	particle mass	68
r_{cut}	cut-off radius of the interaction potential	71
r	distance of two particles	70
t	time coordinate	68
z_{D}	number of death receptor dimers	77
z_{L}	number of death receptor ligands	77
z_{M}	number of death receptor monomers	77
z_{T}	number of death receptor trimers	77
z_{U}	number of cluster units	77

List of Figures

2.1 Sketch of the Extrinsic Pro-Apoptotic Signaling Pathway 9
2.2 Eigenvalues of Matrix M in Stability Analysis for Life State; $d = 1$ 23
2.3 Eigenvalues of Matrix M in Stability Analysis for Transition State; $d = 1$. 24
2.4 Eigenvalues of Matrix M in Stability Analysis for Death State; $d = 1$ . . . 25
2.5 Eigenvalues of Matrix M in Stability Analysis for Life State; $d = 2$ 27
2.6 Eigenvalues of Matrix M in Stability Analysis for Transition State; $d = 2$. 28
2.7 Eigenvalues of Matrix M in Stability Analysis for Death State; $d = 2$ . . . 29
2.8 Illustration of the Fast Diffusion of the Reaction-Diffusion System; $d = 3$. 43
2.9 Diffusion Times for the Reaction-Diffusion System; $n = 2.5$, $d = 3$ 44
2.10 Death Times for the Reaction-Diffusion System; $n = 2, 2.5, 3$, $d = 3$ 48
2.11 Illustration of the Switch-Like Behavior; $d = 1$ 49
2.12 Illustration of the Switch-Like Behavior; $d = 2$ 50
2.13 Illustration of the Switch-Like Behavior; $d = 3$ 51
2.14 Traveling Wave Solution for the Reaction-Diffusion System; $n = 2.5$, $d = 1$ 53
2.15 Traveling Wave Solution for the Reaction-Diffusion System; $n = 2$, $d = 1$. 54
2.16 Traveling Wave Solution for the Reaction-Diffusion System; $n = 3$, $d = 1$. 54
2.17 Non-Monotone Traveling Wave Solution for Different Values of k_{di}; $d = 1$. 55
2.18 Traveling Wave Solution for Switched Initial Conditions; $n = 2.5$, $d = 1$ . . 56
2.19 Domain for the RDS on a Large Spatial Scale with Center on Cell Membrane 57
2.20 The Formation of a Traveling Wave Solution; $n = 2.5$, $d = 3$ 58
2.21 Illustration of the Switch-Like Behavior on a Large Scale; $n = 2$, $d = 2, 3$. 60
2.22 Illustration of the Switch-Like Behavior on a Large Scale; $n = 2.5$, $d = 2, 3$ 60
2.23 Illustration of the Switch-Like Behavior on a Large Scale; $n = 3$, $d = 2, 3$. 61

3.1 Two-Dimensional Simulation Domain for the Particle Model 66
3.2 Visualization of Three Different Particle Types 67
3.3 Function g_{M_i} for Death Receptor Monomers 79
3.4 Function g_{D_i} for Death Receptor Dimers 80
3.5 Function g_{T_i} for Death Receptor Trimers 82
3.6 Function g_{L_i} for Death Receptor Ligands 85

3.7 Function g_{U_i} for the Cluster Units 87
3.8 Decomposition of the Simulation Domain 94
3.9 Decomposition of the Simulation Domain with Boundary Conditions 95
3.10 Illustration of a List of Particles 96
3.11 Evolution of 'L-D-L' on a Time Scale of 1 s 110
3.12 Evolution of 'L-D-L' for #L = 4992 111
3.13 Evolution of 'L-M-M-L' for #L = 4992 112
3.14 Evolution of 'M-L' / 'D-L' and 'M-L' / 'M-M' for #L = 4992 113
3.15 Evolution of 'L-D-L' / 'D-L-D' and 'M-L-M' / 'L-M-M' for #L = 4992 . . 114
3.16 Evolution of 'L-M-M-L' / 'L-3M' for #L = 4992, #M = 4992 116
3.17 Evolution of 'L-D-L' for #M = 2496, #D = 2496 and Various #L 117
3.18 Evolution of 'L-D-L' for #M = 0, #D = 2496 and Various #L 118
3.19 Comparison of 'M-L' / 'D-L' (#M = 2496) and 'D-L' (#M = 2496, #M = 0) 119
3.20 Evolution of 'D-L-D' / 'L-D-L' for #M = 2496 and #M = 0 119
3.21 Evolution of 'M-M' for #M = 4992 and Various #L 120
3.22 Evolution of 'M-M' for #L = 4992 and Various #M 121
3.23 Evolution of 'T-L' for #T = 192 and Various #L 122
3.24 Evolution of 'T-L' for #T = 576 and Various #L 123
3.25 Evolution of 'T-L-T' / 'L-T-L' for #T = 192 and Various #L 123
3.26 Evolution of 'T-L-T' / 'L-T-L' for #T = 576 and Various #L 124
3.27 Evolution of 'U-U' for Various Numbers of Cluster Units 124
3.28 Evolution of 'L-D-L' for an Over-Expression of Dimers 125
3.29 Visualization of Clusters of Size Seven 126

4.1 Initial Condition for the Extended Reaction-Diffusion Model 135
4.2 Solution of the Extended Reaction-Diffusion Model after 10 Time Steps . . 136
4.3 Solution of the Extended Reaction-Diffusion Model after 50 Time Steps . . 137

A.1 Discretization of the Domain Ω for the Finite Difference Method; $d = 2$ . . 148

List of Tables

2.1 Zeros of the First Derivative of the Bessel Functions 26
2.2 Lower Bounds for the Decay Rate σ 45

3.1 List of Particle Bindings with Participation of Monomers 108
3.2 List of Particle Bindings with Participation of Dimers 109
3.3 List of Particle Bindings with Participation of Trimers 109
3.4 Binding between Cluster Units 110
3.5 Computation Times and Speed-Up for Monomers, Dimers and Trimers . . 129
3.6 Computation Times and Speed-Up for Dimers and Ligands 129
3.7 Computation Times and Speed-Up for Monomers and Ligands 130

A.1 Values for the Diffusion Coefficients of Caspases 140

Bibliography

[1] H. Amann. **Dynamic theory of quasilinear parabolic equations-II. reaction-diffusion systems**. *Differential Integral Equations*, 3(1):13–75, 1990.

[2] A. Ashkenazi and V. M. Dixit. **Death receptors: signaling and modulation**. *Science*, 281(5381):1305–1308, 1998.

[3] D. W. Banner, A. D'Arcy, W. Janes, R. Gentz, H. J. Schoenfeld, C. Broger, H. Loetscher, and W. Lesslauer. **Crystal structure of the soluble human 55 kd TNF receptor-human TNF beta complex: implications for TNF receptor activation.** *Cell*, 73(3):431–445, 1993.

[4] M. Bentele, I. Lavrik, M. Ulrich, S. Stößer, D. Heermann, H. Kalthoff, P. H. Krammer, and R. Eils. **Mathematical modeling reveals threshold mechanism in CD95-induced apoptosis.** *Journal of Cell Biology*, 166(6):839–851, 2004.

[5] H. Bisswanger. *Enzymkinetik*. Weinheim: Wiley-VCH, 2000.

[6] V. Boschert, A. Krippner-Heidenreich, M. Branschädel, J. Tepperink, A. Aird, and P. Scheurich. **Single chain TNF derivatives with individually mutated receptor binding sites reveal differential stoichiometry of ligand receptor complex formation for TNFR1 and TNFR2**. *Cellular Signalling*, 22(7):1088–1096, 2010.

[7] M. Branschädel, A. Aird, A. Zappe, C. Tietz, A. Krippner-Heidenreich, and P. Scheurich. **Dual function of cysteine rich domain (CRD) 1 of TNF receptor type 1: Conformational stabilization of CRD2 and control of receptor responsiveness**. *Cellular Signalling*, 22(3):404–414, 2010.

[8] C. Braun, M. Daub, A. Schöll, G. Schneider, and H.-J. Wunderlich. **Parallel simulation of apoptotic receptor-clustering on GPGPU architectures**. In *IEEE International Conference on Bioinformatics and Biomedicine (BIBM)*, pages 1–6. IEEE, 2012.

[9] R. Casten and C. Holland. **Stability properties of solutions to systems of reaction-diffusion equations**. *SIAM Journal on Applied Mathematics*, 33(2):353–364, 1977.

[10] F. Chan, H. Chun, L. Zheng, R. Siegel, K. Bui, and M. Lenardo. **A Domain in TNF Receptors That Mediates Ligand-Independent Receptor Assembly and Signaling**. *Science*, 288(5475):2351–2354, 2000.

[11] G. Cohen. **Caspases: the executioners of apoptosis**. *Biochem. J.*, 326(1):1–16, 1997.

[12] N. Danial and S. Korsmeyer. **Cell death: critical control points.** *Cell*, 116(2):205–219, 2004.

[13] M. Daub, S. Waldherr, F. Allgöwer, P. Scheurich, and G. Schneider. **Death wins against life in a spatially extended model of the caspase-3/8 feedback loop**. *BioSystems*, 108:45–51, 2012.

[14] T. Eissing, H. Conzelmann, E. Gilles, F. Allgöwer, E. Bullinger, and P. Scheurich. **Bistability Analyses of a Caspase Activation Model for Receptor-induced Apoptosis**. *Journal of Biological Chemistry*, 279(35):36892–36897, 2004.

[15] T. Eissing, S. Waldherr, F. Allgöwer, P. Scheurich, and E. Bullinger. **Steady state and (bi-)stability evaluation of simple protease signalling networks**. *BioSystems*, 90:591–601, 2007.

[16] L. Evans. *Partial Differential Equations*. Graduate Studies in Mathematics; 19. AMS, 1998.

[17] M. Falk, M. Daub, G. Schneider, and T. Ertl. **Modeling and visualization of receptor clustering on the cellular membrane**. In *Biological Data Visualization (BioVis), 2011 IEEE Symposium on*, pages 9–15. IEEE, 2011.

[18] P. A. Frey and A. D. Hegeman. *Enzymatic reaction mechanisms*. Oxford University Press, 2007.

[19] M. Fussenegger, J. Bailey, and J. Varner. **A mathematical model of caspase function in apoptosis**. *Nature Biotechnology*, 18(7):768–774, 2000.

[20] C. Gardiner. *Handbook of stochastic methods: for physics, chemistry & the natural sciences*. Series in synergetics; 13. Springer, 2004.

[21] D. Green. **Apoptotic Pathways: the Roads to Ruin**. *Cell*, 94(6):695–698, 1998.

[22] M. Grell, H. Wajant, G. Zimmermann, and P. Scheurich. **The type 1 receptor (CD120a) is the high-affinity receptor for soluble tumor necrosis factor**. *PNAS*, 95(2):570–575, 1998.

[23] M. Griebel, S. Knapek, and G. Zumbusch. *Numerical Simulation in Molecular Dynamics: Numerics, Algorithms, Parallelization, Applications*. Springer, 2007.

[24] C. Guo and H. Levine. **A Thermodynamic Model for Receptor Clustering**. *Biophysical Journal*, 77(5):2358–2365, 1999.

[25] C. Guo and H. Levine. **A Statistical Mechanics Model for Receptor Clustering**. *Journal of Biological Physics*, 26:219–234, 2000.

[26] M. Haidekker, T. Ling, M. Anglo, H. Stevens, J. Frangos, and E. Theodorakis. **New fluorescent probes for the measurement of cell membrane viscosity**. *Chemistry & Biology*, 8(2):123–131, 2001.

[27] M. Hengartner. **The biochemistry of apoptosis**. *Nature*, 407(6805):770–776, 2000.

[28] A. Henrot. *Extremum problems for eigenvalues of elliptic operators*. Birkhäuser, 2006.

[29] D. Henry. *Geometric Theory of Semilinear Parabolic Equations*. Lecture Notes in Mathematics; 840. Springer, 1981.

[30] D. Hoff. **Stability and Convergence of Finite Difference Methods for Systems of Nonlinear Reaction-Diffusion Equations**. *SIAM Journal on Numerical Analysis*, 15(6):1161–1177, 1978.

[31] H. Huber, M. Laussmann, J. Prehn, and M. Rehm. **Diffusion is capable of translating anisotropic apoptosis initiation into a homogeneous execution of cell death.** *BMC Systems Biology*, 4:9, 2010.

[32] N. Kern and D. Frenkel. **Fluid–fluid coexistence in colloidal systems with short-ranged strongly directional attraction**. *The Journal of Chemical Physics*, 118(21):9882–9889, 2003.

[33] B. Kholodenko, G. Brown, and J. Hoek. **Diffusion control of protein phosphorylation in signal transduction pathways**. *Biochemical Journal*, 350(3):901–907, 2000.

[34] P. Kloeden and E. Platen. *Numerical Solution of Stochastic Differential Equations*. Stochastic Modelling and Applied Probability; 23. Springer, 1992.

[35] P. Knabner and L. Angermann. *Numerik partieller Differentialgleichungen: Eine anwendungsorientierte Einführung*. Springer, 2000.

[36] A. Krippner-Heidenreich, F. Tübing, S. Bryde, S. Willi, G. Zimmermann, and P. Scheurich. **Control of Receptor-induced Signaling Complex Formation by the Kinetics of Ligand/Receptor Interaction**. *Journal of Biological Chemistry*, 277(46):44155–44163, 2002.

[37] M. Kruidering and G. Evan. **Caspase-8 in Apoptosis: The Beginning of "The End"?** *IUBMB Life*, 50(2):85–90, 2000.

[38] S. Kumar. **Mechanisms mediating caspase activation in cell death**. *Cell Death and Differentiation*, 6(11):1060–1066, 1999.

[39] M. Lamkanfi, N. Festjens, W. Declercq, V. T. Berghe, and P. Vandenabeele. **Caspases in cell survival, proliferation and differentiation**. *Cell Death and Differentiation*, 14(1):44–55, 2007.

[40] D. F. Legler, O. Micheau, M.-A. Doucey, J. Tschopp, and C. Bron. **Recruitment of TNF Receptor 1 to Lipid Rafts Is Essential for TNFα-Mediated NF-κB Activation**. *Immunity*, 18(5):655–664, 2003.

[41] B. Lewin. *Cells*. Jones & Bartlett Learning, 2007.

[42] A. K. Lewis, C. C. Valley, and J. N. Sachs. **TNFR1 signaling is associated with backbone conformational changes of receptor dimers consistent with overactivation in the R92Q TRAPS mutant**. *Biochemistry*, 51(33):6545–6555, 2012.

[43] N. Markevich, M. Tsyganov, J. Hoek, and B. Kholodenko. **Long-range signaling by phosphoprotein waves arising from bistability in protein kinase cascades**. *Molecular Systems Biology*, 2(1):61, 2006.

[44] A. Meager, L. Sampson, M. Grell, and P. Scheurich. **Development of resistance to tumour necrosis factor (TNFα) in KYM-1 cells involves both TNF receptors**. *Cytokine*, 5(6):556–563, 1993.

[45] D. Meintrup. *Stochastik: Theorie und Anwendungen*. Springer, 2005.

[46] J. Murray. *Mathematical Biology I: An Introduction*. Springer, 2002.

[47] G. Nuñez, M. Benedict, Y. Hu, and N. Inohara. **Caspases: the proteases of the apoptotic pathway**. *Oncogene*, 17(25):3237–3245, 1998.

[48] L. Payne and H. Weinberger. **An optimal Poincaré inequality for convex domains**. *Archive for Rational Mechanics and Analysis*, 5(1):286–292, 1960.

[49] A. S. Perelson. **Receptor clustering on a cell surface. III. Theory of receptor cross-linking by multivalent ligands: description by ligand states**. *Mathematical Biosciences*, 53(1-2):1–39, 1981.

[50] A. G. Porter and R. U. Jänicke. **Emerging roles of caspase-3 in apoptosis.** *Cell Death and Differentiation*, 6(2):99–104, 1999.

[51] M. Rehm, H. J. Huber, C. T. Hellwig, S. Anguissola, H. Dussmann, and J. H. Prehn. **Dynamics of outer mitochondrial membrane permeabilization during apoptosis.** *Cell Death and Differentiation*, 16(4):613–623, 2009.

[52] S. J. Riedl and Y. Shi. **Molecular Mechanisms of Caspase Regulation during Apoptosis**. *Nature Reviews Molecular Cell Biology*, 5:897–907, 2004.

[53] P. G. Saffman and M. Delbrück. **Brownian motion in biological membranes**. *PNAS*, 72(8):3111–3113, 1975.

[54] F. Schwabl. *Statistische Mechanik*. Springer, 2006.

[55] Y. Shi. **Clustering and signalling of cell receptors**. *Physica A: Statistical Mechanics and its Applications*, 311(1-2):199–212, 2002.

[56] Y. Shi. **Mechanisms of Caspase Activation and Inhibition during Apoptosis**. *Molecular Cell*, 9:459–470, 2002.

[57] J. Smoller. *Shock Waves and Reaction-Diffusion Equations*. A Series of Comprehensive Studies in Mathematics; 258. Springer, 1994.

[58] H. R. Stennicke, J. M. Jürgensmeier, H. Shin, Q. Deveraux, B. B. Wolf, X. Yang, Q. Zhou, H. M. Ellerby, L. M. Ellerby, and D. Bredesen. **Pro-caspase-3 is a major physiologic target of caspase-8**. *Journal of Biological Chemistry*, 273(42):27084–27090, 1998.

[59] H. R. Stennicke and G. S. Salvesen. **Catalytic properties of the caspases.** *Cell Death and Differentiation*, 6(11):1054–1059, 1999.

[60] L. Tartaglia, D. Pennica, and D. Goeddel. **Ligand passing: the 75-kDa tumor necrosis factor (TNF) receptor recruits TNF for signaling by the 55-kDa TNF receptor**. *Journal of Biological Chemistry*, 268(25):18542–18548, 1993.

[61] H. Triebel. *Höhere Analysis*. Deutscher Verlag der Wissenschaften, 1972.

[62] P. Vandenabeele, W. Declercq, R. Beyaert, and W. Fiers. **Two tumour necrosis factor receptors: structure and function**. *Trends in Cell Biology*, 5(10):392–399, 1995.

[63] S. Wiggins. *Introduction to applied nonlinear dynamical systems and chaos*. Texts in applied mathematics; 2. Springer, 2003.

[64] A. W. Wilber, J. P. K. Doye, A. A. Louis, E. G. Noya, M. A. Miller, and P. Wong. **Reversible self-assembly of patchy particles into monodisperse icosahedral clusters**. *The Journal of Chemical Physics*, 127:085106, 2007.

[65] M. L. Würstle, M. A. Laussmann, and M. Rehm. **The Caspase-8 Dimerization/Dissociation Balance Is a Highly Potent Regulator of Caspase-8, -3, -6 Signaling**. *Journal of Biological Chemistry*, 285(43):33209–33218, 2010.

[66] S. Yang, A. D. Thor, S. Edgerton, and X. H. Yang. **Caspase-3 mediated feedback activation of apical caspases in doxorubicin and TNF-α induced apoptosis**. *Apoptosis*, 11(11):1987–1997, 2006.